

Novel Degrees of Freedom for Design of Silicon Microring Resonators

Nieuwe vrijheidsgraden voor het ontwerp van microring-resonatoren in silicium

Ang Li



**UNIVERSITEIT
GENT**

Promotor: prof. dr. ir. W. Bogaerts
Proefschrift ingediend tot het behalen van de graad van
Doctor in de ingenieurswetenschappen: fotonica

Vakgroep Informatietechnologie
Voorzitter: prof. dr. ir. D. Dezutter
Faculteit Ingenieurswetenschappen en Architectuur
Academiejaar 2017 - 2018

ISBN 978-94-6355-108-3
NUR 950
Wettelijk depot: D/2018/10.500/26



Universiteit Gent
Faculteit Ingenieurswetenschappen en Architectuur
Vakgroep Informatietechnologie

Promotor: Prof. Dr. Ir. Wim Bogaerts

Examencommissie:

Prof. Dr. Ir. Daniël De Zutter (voorzitter)	Universiteit Gent, INTEC
Prof. Dr. Ir. Wim Bogaerts (promotor)	Universiteit Gent, INTEC
Prof. Dr. Ir. Roel Baets	Universiteit Gent, INTEC
Prof. Dr. Ir. Bart Kuyken	Universiteit Gent, INTEC
Dr. Ir. Stephane Clemmen	Universiteit Gent, INTEC
Dr. Ir. Peter De Heyn	IMEC
Dr. Ir. Francesco Morichetti	Politecnico di Milano
Dr. Ir. Thomas Van Vaerenbergh	Hewlett Packard Enterprise
Prof. Dr. Ir. Jeroen Beeckman	Universiteit Gent, ELIS

Universiteit Gent
Faculteit Ingenieurswetenschappen en Architectuur

Vakgroep Informatietechnologie
Technologiepark-Zwijnaarde 15, B-9052 Gent, België

Tel.: +32-9-264.33.41

Fax.: +32-9-264.35.93

Acknowledgement

Coming to this group for a Ph.D is one of the most important decisions in my life, as a 4.5-years Ph.D will definitely affect your future career and life. Now I am proud to say that it is also one of the smartest decisions I have made so far. This group is fantastic not only in adequate facilities and research sources, but also in daily atmosphere. So firstly I want to express my sincere gratitude to Wim for the opportunity he granted to me and the trust he placed in me back in 2013. He is a very special supervisor with diverse personalities, who can be as strict as a boss but also as easy-going as a peer colleague or even as funny as a friend. Basically, he is a person whom you want to communicate with in a very open and relaxing way. His smart intelligence, patient directions and insightful opinions make my research much easier. While his high standards and strict requirements taught me how to do research in a rigorous and patient way. Besides this, I need to particularly thank him for the tolerance and understanding as well as the freedom he gave to his students, which reflect in the facts that he allows me to make mistakes, fully understood my decision to change my research topics and respected our willingness to work in a flexible schedule.

As mentioned above, the overall atmosphere and general administration of our group are fantastic, which are important factors that make our group attract so many young talents and generate research outputs in an efficient way. I sincerely appreciate the efforts put by Prof. Roel Baets together with all other professors and administrative staff to build such an outstanding group. Specifically I'd like to express my gratitude to Michael Vanslembrouck, who is a very reliable friend and a solid support for the measurement labs, especially the semi-automatic setup, which I extensively used in past years. He has always been responsive to any request I asked. Also I'd like to thank Steven, Muhammad and Liesbet who offered the training and necessary support for my cleanroom activities, even if they don't occupy majority of my Ph.D but are very important parts. Besides, all other supportive staff including Jasper, Ilse V., Kristien, Bert, Ilse M., Mike and so on have helped me a lot either directly or indirectly. I am grateful to all of you.

Besides the professors and administrative staff, my gratitude shall also go to the intelligent and kind colleagues. Their expertise in respective topics have offered me a lot of knowledge through discussions or presentations. Many of them have helped me in different aspects, including Alfonso, Sarvagya, Antonio, Martin, Ab-

dul, Raphael, Jesper, Daan, Jeroen, Kasper, Soren, Amin, Anton, Paul, Sulakshna, Stephane and so on. Particularly I'd like to thank Dr. Thomas Van Vaerenbergh. This guy has a super cold face but super warm heart. I could write over three pages listing all the support and help he has given to me. During my very first year of Ph.D, he already started to guide me through many private discussions about my upcoming Ph.D and his experience. Also it is he who introduced me to a research intern position at this world-wide reputational Hewlett Packard Labs. Even quite recently, he also continuously offered his help in seeking job opportunities, writing recommendation letter, academic collaboration and so on.

Here I also want to express my gratitude to the jury members of my thesis, including Prof. Daniel De Zutter, Prof. Roel Baets, Prof. Wim Bogaerts, Prof. Bart Kuyken, Prof. Stephane Clemmen, Prof. Jeroen Beeckman, Dr. Francesco Morichetti, Dr. Peter De Heyn and Dr. Thomas Van Vaerenbergh. Your valuable time consumed in evaluating my these is greatly appreciated. Your careful reading and constructive comments are extremely important to make my thesis better.

This section goes to my previous colleagues at HP Labs, including Ray, Dave, Jason, Ranojoy, Thomas and Gabriel from the team of LSIP and people from other groups like Marco, Ashkan, Zhihong, Xiaoge, Shuren, Rui, Shengchang, Shaolei. They warmly welcomed me and helped me through my entire internship in both life and work. The working atmosphere over there is as wonderful as here in our group.

Of course, one big part of my gratitude should go to our intimate chinese community, including Yanlu, Zhechao, Yingtao, Bin, Weiqiang, Yunpeng, Ruijun, Chen, Lianyan, Xin, Haifeng, Jing, Haolan, Qiangsheng, Yingchen, Yufei, Yinghao, Ye, Yuxin, Yuting, Xiaomin, Guanyu, Jinghao, Keqi, Xiaoning, Zhenzhou, Yang, Qiang, Mi, Chonghuai, Naidi (forgive me if some names are missing). Our countless get-together contribute to most of my fun in the living at Gent and drive loneliness away. I wish everyone a bright career and happy life!

The biggest achievement in my Ph.D period is actually not related to my research, instead, it is to meet such a nice girl, and to know, to become familiar and gradually fall in love with each other. Ying, you have all the expectations I once had for a "perfect" girlfriend. Thank you for coming to my life, for comforting me, for encouraging me, for tolerating me and for bringing me happiness.

最后呢，借此机会由衷的、庄重的感谢我的家人，爸爸妈妈和弟弟，我知道正是你们的存在才使我永远不会孤单。感谢这些年来对我无私到过的理解、关心和包容。你们永远都是我遇到挫折后第一个想寻求慰藉的人，取得成绩后第一个想分享喜悦的人，你们是我奋斗的最可靠的后盾，也是最澎湃的动力。

Gent, April 2018
Ang Li

Table of Contents

Acknowledgement	i
Nederlandse samenvatting	xxxiii
Referenties	xliii
English summary	xlv
References	lv
1 Introduction	1-1
1.1 Silicon photonics integrated circuits	1-1
1.2 Parasitics in silicon photonics	1-5
1.3 Silicon ring resonators	1-8
1.4 Publications	1-11
1.4.1 International Journals	1-11
1.4.2 International conferences	1-12
References	1-14
2 Parasitics in Silicon Photonics Integrated Circuits	2-1
2.1 Grating coupler reflections	2-1
2.2 Substrate leakage and coupling	2-6
2.3 Radiation loss and Backscattering	2-8
2.3.1 Radiation loss	2-9
2.3.2 Backscattering	2-10
2.4 Evanescent coupling	2-15
2.5 Summary	2-21
References	2-22
3 Backscattering in silicon waveguides and ring resonators	3-1
3.1 Backscattering in silicon waveguides	3-1
3.1.1 Strong fluctuations in waveguide spectral transmission	3-1
3.1.2 PDF of waveguide transmission spectrum	3-4
3.1.3 Origins for strong fluctuations	3-5
3.1.4 Circuit model for waveguides with stochastic backscattering 3-5	
3.1.5 Mathematical model for waveguides with stochastic backscat- tering	3-8

3.1.6	Enhancement of the fluctuations by lumped parasitic reflections	3-9
3.2	Backscattering in silicon ring resonators	3-9
3.2.1	Problem description of backscattering in a silicon ring resonator	3-10
3.2.2	Improved tCMT model for ring resonator	3-14
3.2.3	Model validation by measurement fitting	3-20
3.2.4	Break down backscattering to individual contributions	3-26
3.2.4.1	Sidewall roughness-induced backscattering	3-26
3.2.4.2	Coupler-Induced Backscattering	3-28
3.2.4.3	Separation of Distributed and Lumped Backscattering	3-28
3.2.5	Quantitative analysis of backscattering	3-29
3.2.5.1	Extracting the Backscattering from model	3-29
3.2.5.2	Separating Distributed and Lumped Backscattering	3-30
3.2.6	Coupler-Induced Backscattering	3-31
3.2.7	Wavelength-dependent Model for Full-Spectrum Fitting	3-32
3.2.8	Phase response of rings with resonance splitting	3-38
3.2.9	Methods to suppress resonance splitting	3-38
3.3	Summary	3-40
	References	3-42
4	Engineered reflections in silicon ring resonator with one tunable reflector	4-1
4.1	Introduction	4-1
4.2	Fundamentally suppress backscattering by reflection engineering inside silicon ring resonator	4-2
4.2.1	An integrated tunable reflector	4-4
4.3	An ultra wide FSR and tuning range of a single silicon ring resonator by means of engineered reflections	4-19
4.3.1	Theoretical explanation based on tCMT	4-22
4.3.2	Design and simulation	4-26
4.3.3	Experimental characterization	4-35
4.3.4	Drawbacks of this structure	4-40
4.4	Other applications	4-40
4.4.1	Tunable microwave photonics filter	4-44
4.4.2	Tunable fast light	4-45
4.4.3	Novel sensing scheme based on Resonance Splitting	4-46
4.5	Summary	4-50
	References	4-51

5	Engineered reflections in silicon ring resonators with double tunable reflectors	5-1
5.1	General introduction of the device	5-1
5.2	Fano resonance	5-5
5.2.1	Introduction and background	5-5
5.2.2	Principle and simulation	5-9
5.2.3	Measurement	5-13
5.3	Optical analogue to electromagnetically induced transparency	5-16
5.3.1	Introduction	5-16
5.3.2	Simulation	5-17
5.3.3	Measurement	5-20
5.4	Contour plot presentation	5-23
5.5	Summary	5-26
	References	5-28
6	Backcoupling manipulation in silicon ring resonator	6-1
6.1	Introduction	6-1
6.2	Theory	6-2
6.3	Conceptual simulation	6-4
6.4	Practical circuit design and simulation	6-4
6.5	Experimental results	6-10
6.5.1	Ring with tunable reflector	6-10
6.5.2	Circular ring resonator	6-18
6.6	Summary	6-26
	References	6-26
7	Conclusion	7-1
7.1	Conclusion	7-1
7.2	Future work	7-4
	References	7-5

List of Figures

1	Het volledige circuit met de elektrische geïntegreerde circuits (EICs) en de fotonische circuits (PIC's) op een chip uit Ref. [1]. Dit circuit bevat 70 miljoen transistoren en 850 fotonische componenten.	xxxiii
2	Verschillende parasitaire effecten in PIC's uit ref. [2]. De brede diversiteit van de parasitaire effecten in PIC's maakt het moeilijk om deze effecten te bestuderen en modelleren in vergelijking met EICs.	xxxiv
3	SEM afbeelding van ref. [4] die de ruwheid weergeeft van de zijwanden van een standaard golfgeleider op silicium-op-isolator, gefabriceerd in een CMOS fab.	xxxv
4	Een opgemeten transmissiespectrum van een standaard golfgeleider met verschillende lengtes, gefabriceerd in IMEC. Alle golfgeleiders vertonen sterke fluctuaties, waarvan de intensiteit schaaft met de lengte van de golfgeleider.	xxxv
5	(a) schema voor een ideale ringresonator. (b) tCMT schema voor een realistische ringresonator met terugwaartse verstrooiing van het licht (r_{bs}) dat koppelt naar CW en CCW modes.	xxxvi
6	Een opgemeten spectrum van een echte, gefabriceerde silicium ringresonator. Verschillende resonanties vertonen splitsingen met verschillende vormen. Er zijn sterke verliezen naar de <i>add</i> poort.	xxxvi
7	Schema's van ringresonatoren met een reflector en de reflector zelf, respectievelijk.	xxxvii
8	(a) en (b) tonen het verwijderen van de resonantiesplitsing aan de <i>thru</i> en de <i>drop</i> poorten. (c) en (d) tonen het onderdrukken van verlies en reflecties aan de <i>add</i> poort en de <i>in</i> poort, respectievelijk.	xxxviii
9	(a) toont de experimentele demonstratie van een ultrabreed vrij spectraal bereik. (b) toont het grote afstembereik van de resonantie.	xxxviii
10	(a) en (c) conceptuele voorstelling van onze component en de Fabry-Perot caviteit die gevormd is door de twee reflectors, voorgesteld door de blauwe lijnen. (b) en (d) voorstelling met de in een lus eindigende, MZI gebaseerde reflectors.	xxxix
11	Opgemeten Fano resonantie die gegenereerd wordt door onze component. De maximale helling kan groter zijn dan 700 dB/nm.	xxxix
12	Opgemeten EIT piek. Dit toont een fazetransformatie rond 0.95π binnen een optisch bereik van 0.01 nm.	xl

13	Een ontworpen circuit om achterwaartse koppeling te introduceren en te manipuleren.	xl
14	Opgemeten spectra die de manipulatie van achterwaartse koppeling aantonen. De piek asymmetrie van een gesplitste resonantie kan aangepast worden en resonantiesplitsing kan dus compleet verwijderd worden.	xli
15	Een uitvergroting van enkele uitgemeten resonanties van een ringresonator met een koppelingsbrug van 400 nm. Alle resonanties tonen een Q-factor die groter is dan 300,000 en een grote ER. Het vrij spectraal bereik van een dergelijke resonator is ongeveer 2.5 nm. .	xlii
16	The full circuit with both EICs and PICs on a chip in Ref. [1]. This circuit contains 70 million transistors and 850 photonic components.	xlvi
17	An example figure showing different kinds of parasitics in PICs from Ref. [2]. This broad diversity imposes difficulty and complexity in studying and modelling parasitics in PICs compared to those in EICs.	xlvi
18	A SEM figure from Ref. [4] showing sidewall roughness of a standard strip waveguide on SOI substrate fabricated at a mature CMOS fab.	xlvi
19	Measured transmission spectra of standard strip waveguides with different lengths fabricated at IMEC. All show strong fluctuations, whose strength scales with waveguide length.	xlvi
20	(a) schematic for an ideal ring resonator. (b) tCMT schematic for a real ring resonator with backscattering (r_{bs}) that couples CW and CCW modes.	xlvi
21	A measured spectra of a real silicon ring resonator. Various resonances exhibit splitting with different shapes. And strong leakage to the <i>add</i> port is present.	xlvi
22	Schematics of the ring with a reflector and the reflector itself, respectively.	xlix
23	(a) and (b) show the resonance splitting elimination at the <i>thru</i> and <i>drop</i> ports. (c) and (d) show the suppression of leakage to the <i>add</i> port and reflection to the <i>in</i> port.	l
24	(a) shows the experimental demonstration of the ultra wide FSR spectrum. (b) presents the broad tuning range of this resonance. .	l
25	(a) and (c) give conceptual illustrations of our device and the Fabry-Perot cavity formed by two reflectors, which are represented by blue lines. (b) and (d) show the schematics where the loop-ended MZI based reflectors replace the blue lines.	li
26	Measured Fano resonance generated by our device. The maximum slope rate can be over 700 dB/nm.	li
27	Measured EIT peak. It shows a phase change around 0.95π within 0.01 nm optical range.	lii
28	A designed circuit in order to introduce and manipulation back-coupling in a realistic way.	lii

29	Measured spectra to show the manipulation of backcoupling. Peak asymmetry of a split resonance can be adjusted and resonance splitting can be eliminated.	liii
30	Some zoomview of resonances measured of a ring resonator with coupling gap at 400 nm. All resonances show Q factor larger than 300,000 and large ER. The FSR of such a resonator is about 2.5 nm.	liv
1.1	A mainstream SOI wafer consists of three layers: a bottom layer of silicon with a thickness around 800 μm ; a intermediate layer of SiO ₂ with a thickness around 2 μm ; a top layer of 220 nm thickness silicon, where the structures will be fabricated. The SiO ₂ serves as an intervening layer that prevents the substrate leakage. .	1-2
1.2	Absorption coefficient of silicon in cm ⁻¹ as a function of the wavelength at temperature of 300 K.	1-3
1.3	Silicon photonics 2013–2024 market forecast. Source: Silicon Photonics Report—Yole Development; Yole: 'Emerging optical data centers from big Internet companies (Google, Facebook, ...) will be triggering the market growth in 2018....'	1-4
1.4	A brief illustration of the potential parasitics of a capacitor(a) and parasitic capacitance in electronics integrated circuits(b).	1-4
1.5	An example figure showing different kinds of parasitics in PICs from Ref. [11]. This broad diversity imposes difficulty and complexity in studying and modelling parasitics in PICs compared to those in EICs.	1-5
1.6	The full circuit with both EICs and PICs on a chip in Ref. [34]. This circuit contains 70 million transistors and 850 photonic components.	1-7
1.7	One of our group's project to utilize thousands of photonic components on chip to provide re-configurable and robust PICs.	1-7
1.8	A couple of components in silicon photonics. Source: www.caliopa.com . 1-8	
1.9	(a) presents a schematic of an add-drop ring resonator. When one of the two bus waveguides are removed, it's called all-pass ring resonator. (b) gives the ideal output spectra of such a ring resonator. Lorentzian shaped resonances at the <i>pass</i> and <i>drop</i> ports with no transmission and reflection at the <i>add</i> and <i>in</i> port, respectively.	1-9
1.10	Figure from Ref. [46] showing some examples of silicon ring resonators. (a) Coupled ring resonators. (b) Circular ring resonators with symmetric coupling sections. (c) Racetrack ring resonators with extra straight coupling sections. (d) ring resonator with bend directional coupler for reduced wavelength dependency. (e) Ultra long spiral ring resonators.	1-10

2.1	(a) shows a simple circuit with only two grating couplers and one waveguide. It already exhibits clear parasitics effects. (b) gives the brief illustration of how grating coupler can couple light between waveguides and fibers.	2-2
2.2	Measured transmission spectra of three circuits shown in Fig. 2.1 with different waveguide lengths, all shorter than 1 cm. They are spiral shaped waveguides with standard 450 nm×220 nm cross-section. All show certain degree of regular ripples and rapid fluctuations.	2-2
2.3	A Fabry-Perot cavity and its transmission spectrum. It consists of two mirrors with certain reflectivity and a channel between them with loss τ^2 and physical length L_p . The transmission spectrum as a function of the wavevector k shows periodically located peaks	2-4
2.4	The Fourier transform of the transmission spectrum of a single Fabry-Perot cavity. It contains a series of peaks equally spaced with the period equaling the optical length of the cavity L_o . When the transmission spectrum is infinite (a), the peaks in the Fourier transform are delta functions (c). While if the transmission is measured within certain span (b), the peaks in the Fourier spectrum are broadened.	2-4
2.5	Simulated transmission spectra of circuits shown in Fig. 2.1 with and without parasitic reflections of the grating couplers. The parameters for the grating couplers' spectrum are extracted by fitting a real measurement.	2-5
2.6	Ripple strength as a function of power reflectivity of the grating couplers. Ripple strength is defined as the extinction ratio of the ripples shown in Fig. 2.5.	2-5
2.7	Fourier transforms of measured spectra in Fig. 2.2. Clearly, for each spectrum, there exists a peak standing at the optical length of the waveguide (the group index of a silicon strip waveguide is around 4.4). This indicates that the grating couplers introduce certain reflections. Moreover, for all the spectra there stand a peak located at around 2.65 mm. This matches well with the optical length of the substrate silicon, as it has a thickness between 700-800 μm and an index of 3.45.	2-6
2.8	2D simulation of a SOI grating coupler using Lumerical FDTD. Clearly, certain amount of light will be directed towards the substrate when it enters the grating coupler.	2-7
2.9	A brief illustration of the coupling from substrate leakage. This parasitic effect will contribute to the fluctuations in the transmission spectra of PICs.	2-7
2.10	Illustration of the measurements performed to investigate the substrate leakage.	2-8

-
- 2.11 A simple measurement to investigate the substrate leakage and coupling. When only input fiber is aligned to the grating coupler while output fiber is away from the output grating coupler, there should not exist any light path between two fibers. But still high transmission is observed, only 30 dB lower than a normal waveguide transmission and it shows the grating coupler spectrum. When the output fiber is aligned and input fiber is away from the grating coupler, much lower transmission is measured with strong noise. 2-8
- 2.12 A SEM figure from Ref. [15] showing sidewall roughness of a standard strip waveguide on SOI substrate fabricated at a mature CMOS fab. 2-9
- 2.13 Figure from Ref. [9] shows the good agreement between the radiation loss predicted by the n_w model (dashed lines) and by the traditional model in equation (2.3) (dots). (a) provides the results of slabs with different index contrast and fixed roughness parameters ($\sigma = 2nm$, $Lc = 50nm$) and (b) hives the results of different modes of the slab with $\Delta n = 30\%$ ($\sigma = 2nm$, $Lc = 50nm$). . . . 2-11
- 2.14 Measured reflection spectra from a standard strip waveguide using Optical Frequency Domain Reflectometry (OFDR) from Ref. [8]. The origin to the reflection is attributed to roughness induced backscattering and it shows stochastic nature in optical span with a relatively higher reflection for TE polarization than TM. 2-12
- 2.15 An optical circuit model built in Caphe with distributed backscattering included. The simulated results are plotted in Fig.2.16. WG refers to waveguide section, REFL represents reflector and GC stands for grating coupler. 2-12
- 2.16 Circuit simulation of circuit shown in Fig. 2.1 with parasitic reflections at the grating coupler as well as distributed reflectors along the waveguide. When parasitic reflections of the grating coupler and waveguide sidewall roughness induced backscattering are included, we can get a good predictive simulation of the circuit transmission. 2-13
- 2.17 Simulated mode profile of a silicon rib waveguide and strip waveguide from Ref. [26]. The rib waveguide leads to a smaller overlap between optical mode and waveguide vertical sidewall. 2-14
- 2.18 Simulated effective index of a silicon strip waveguide as a function of core width for different modes from Ref. [29]. 2-15
- 2.19 Simulated effective index of a silicon rib waveguide as a function of slab thickness or etch depth for TE polarization from Ref. [30]. 2-16
- 2.20 Simulated electric field distribution of TE polarization (a) and TM polarization (b) in a strip silicon waveguide. Clearly, due to the different resonant direction of the field, there is discontinuity at the vertical sidewall of TE polarization. While for TM light, it feels vertical sidewall much less. 2-16

-
- 2.21 Measured coupling spectra of a series of parallel strip waveguides with same width of 450 nm fabricated at Imec. Results indicate that the minimum spacing between two waveguides can be $1.6 \mu m$ to avoid any coupling between them. 2-17
- 2.22 Measured coupling spectra of two parallel waveguides with different waveguide width and constant spacing of 1200 nm. One width is fixed to 450 nm while the other one is swept from 400 nm to 500 nm. Results show that only 10 nm change in the waveguide width lead to no coupling between them even their spacing is as low as 1200 nm. 2-18
- 2.23 Power exchange between two waveguides as a function of propagation distance z . The curves are calculated based on equation (2.9). (a) shows the case of perfect phase matching $\delta = 0$. (b) gives the result when $\frac{\delta}{\kappa} = 0.5$ 2-19
- 2.24 Another circuit consisting of 3 waveguides with 450 nm width at the boundary and a different width in the center. The spacing between W1 and W3 are fixed at $1.2 \mu m$ and the coupling length is $140 \mu m$ 2-20
- 2.25 Measured spectra of circuits shown in Fig. 2.24 with different center waveguide widths. All show a strong coupling between W1 and W3 irrespective of the center waveguide width. But with increasing center waveguide width (thus smaller phase mismatch), the coupling becomes stronger. 2-21
- 3.1 Measured transmission spectra of standard strip waveguides with different lengths fabricated at IMEC. The spectra are normalized to the grating couplers spectra fitted from measurement by a forth order polynomial equation. There is no top oxide cladding for the waveguides. All show strong fluctuations, whose strength scales with waveguide length. For a 7 cm long waveguide, the spectrum shows dips with an extinction ratio over 14 dB. 3-2
- 3.2 Zoomed views of some dips from each of those two spectra shown in Fig. 3.1. Clearly, the dip gets narrower with longer waveguide. 3-2
- 3.3 Probability density function of the measured transmission spectra shown in Fig. 3.1. We could see the left shift of these distributions due to higher propagation loss of a longer waveguide. Moreover, the PDF gets broader with increasing waveguide length. In other words, more potential transmission values can happen for a longer waveguide. 3-4
- 3.4 Conceptual illustrations of waveguide with distributed scatterers. The contributions of the backscattering to the reflection of a waveguide have been thoroughly studied (a) but the their effects on transmission of a waveguide have been ignored (b). 3-6

-
- 3.5 Optical circuit simulations and measured transmission spectra of waveguides with distributed reflectors at the spacing of $25\ \mu\text{m}$. 1 cm is shown in blue while 7 cm in orange. 3-6
- 3.6 The fluctuations at the spectral transmission of a waveguide can be enhanced by lumped parasitic reflections of the grating couplers. The curve is generated from Caphe simulation. 3-7
- 3.7 A representation of waveguides with stochastic distributed backscattering by a mathematical model, called random walk problem. Each walk event represents a backscattering to the propagating light caused by the roughness. Its length refers to the power reflectivity of such a backscattering and its direction has the same meaning of phase of the backscattering. 3-8
- 3.8 (a) schematic for an ideal ring resonator. (b) tCMT schematic for a real ring resonator with backscattering (r_{bs}) that couples CW and CCW modes. 3-9
- 3.9 A measured spectra of a real silicon ring resonator. Various resonances exhibit splitting with different shapes. And strong leakage to the *add* port is present. 3-10
- 3.10 Histogram of split ratios of 6 sets of silicon ring resonators fabricated at IMEC; Each set contains 7 rings with variable lengths but the same coupling gap and coupling length. And each set has a different coupling gap. In total there are as many as 1080 resonances. When a resonance split is larger than half of 3dB bandwidth, it becomes visible and over 550 resonances exhibit visible splitting. 3-11
- 3.11 A pie chart clearly shows the dominance of asymmetric splitting among all of the splitting resonances we measured from 42 rings (in total more than 550 resonances exhibit splitting). Examples of asymmetric and symmetric resonance splitting are also given. 3-12
- 3.12 (a) A simplified schematic of a 2×2 directional coupler. Ideally, the backcoupling κ' and reflections r' are zero. (b) Illustration of the extra reflections caused by directional couplers in a ring. The directional coupler in a ring resonator can be physically divided into three parts, two scattering centers at the beginning and end, and a distributed scatterer in the straight section due to extra coupling length. Scatterers will cause unwanted backcoupling κ' to adjacent port as well as reflection to in port r' , while coupling length will bring roughness induced backscattering noted with r_c 3-13
- 3.13 A measured spectrum with 3 split resonances. We analyze these resonances in detail to get the proof of the origins for the asymmetry in resonance splitting, which we believe to be the backcoupling. 3-18
- 3.14 A sweep of different f factors using circuit simulator Caphe. When $f = 0$ and $\phi_\mu = 0$, the red line is generated, which is a symmetric split resonance; When magnitude of f is increased, the degree of asymmetry increases accordingly. 3-19

-
- 3.15 A sweep of different f factors using circuit simulator Caphe. When $f = 0$ and $\phi_\mu = 0$, the red line is generated, which is a symmetric split resonance; When magnitude of f is increased, the degree of asymmetry increases accordingly. 3-20
 - 3.16 Simulated spectra of 3 rings with the same length, loss and backscattering strength. The coupling coefficient κ of the directional coupler is increasing From top to bottom, with decreasing Q factor. The splitting distance keeps constant but the broadening of the resonance will gradually makes splitting invisible. 3-21
 - 3.17 Simulated resonances of ring resonators with and without backscattering. At the case with backscattering, even if the resonance is too broad to make the resonance splitting visible, still it's distorted from a Lorentzian shape. 3-22
 - 3.18 (a) and (b) present the amplitude transmission spectra and phase responses of a ring resonator under different coupling regions. (c) is the phasor plot. It clearly distinguishes these three coupling regions. 3-22
 - 3.19 Two inverse phasor plots of the resonances plotted in Fig. 3.17. The difference between them are amplified when it's very hard to distinguish them by purely looking at the amplitude transmissions. 3-23
 - 3.20 Fitting qualities of visible resonance splitting and invisible splitting, respectively. Both cases can be fitted accurately using our model, and the extracted values of the power reflectivity are all close to the simulation value. 3-24
 - 3.21 A measured spectrum with fitted amplitude of f factor at each resonance. Similar in other measured spectra, the amplitude of f is in the range of 0 to 0.4. 3-26
 - 3.22 FDTD simulations of mode profiles of directional couplers with 200 nm gap (blue) and 300 nm gap (green), as well as single-mode waveguide (red). Clearly, the electric field magnitude at the side-wall of a directional coupler is stronger than that of a waveguide. 3-27
 - 3.23 Power backscattering per roundtrip for rings with different roundtrip lengths and different directional coupler gaps. A linear increase of the backscattering for longer rings is observed, which corresponds to the distributed scattering H_0 . A decrease in backscattering for larger coupler gap is also shown, corresponding to the lumped scattering C_0 in the directional couplers. 3-31
 - 3.24 Fitted parameters H_0 and C_0 versus coupler gap. H_0 remains constant for different gaps, as it only depends on the ring waveguide roughness. And the value is well matched with formerly reported value. C_0 decreases for increasing gap, as the larger gap is, the smaller influence of directional coupler will be. 3-32
 - 3.25 Power backscattering as function of ring roundtrip length for different coupling lengths L_c . The backscattering increases with larger roundtrip lengths, and with larger coupling length. 3-33

3.26	Fitted backscattering contributions H_0 and C_0 for different coupling lengths L_c . C_0 increases with increasing L_c , indicating more backscattering caused by directional couplers. H_0 remains in the expected range of $6-8m^{-1}$	3-33
3.27	A directional coupler supports two supermodes, namely even and odd modes (or symmetric and anti-symmetric). The final output of a DC is a result of the interference between the two modes after the coupling length.	3-34
3.28	Fitting of a 75um long ring; here the circuit simulator caphe is used to fit a ring circuit, in other words, the complete spectrum is fitted instead of individual resonance.	3-36
3.29	Fitting of a 100um long ring, the good matching shows the reproducibility of this circuit fitting model.	3-37
3.30	Fitting of a 300um long ring; Larger mismatch is expected, due to the randomness of roughness induced backscattering, which is not included in this circuit model. However, there is still a good match and it clearly shows the variety in split resonance shapes caused by multi-scatterers in the ring circuit.	3-38
3.31	The backscattering will not only modify the resonance shape in amplitude spectrum, but also distorts the phase response.	3-39
4.1	(a) An example figure from Ref. [1] about a tungsten contact via and heater for silicon modulator as well as strip waveguide. (b) A brief layout from the same literature showing the heater used to tune a ring resonator.	4-2
4.2	Schematic (a) and experimental results (b) of the interferometric approach to eliminate resonance splitting induced by backscattering proposed in Ref. [7].	4-3
4.3	Schematics of the ring with a reflector and the reflector itself, respectively.	4-4
4.4	Simulated transmission spectrum of a MZI with (a) balanced arms and (b) length difference between two arms.	4-5
4.5	Schematic of a Sagnac mirror (a) and its reflectivity as a function of the coupling coefficient κ (b).	4-5
4.6	Simulated reflection spectrum of the tunable reflector. (a) $\Delta L = 0$ produces a flat spectrum. (b) $\Delta L = 50$ shows a strong, periodic wavelength dependence oscillating between 0 and 100%. Blue and red corresponds with an ideal directional coupler case and a realistic directional coupler case, respectively. The reflection does not reach 100% because of the small propagation loss of the waveguides which is taken into account. (c) The reflectivity also depends on the coupling coefficients κ of the two DCs. (d) Simulated tunability of such a reflector. When κ is in the range 0.15-0.85, Adding 0.5π phase shift in one arm can generate a change in reflectivity from 0 to 100%.	4-7

-
- 4.7 Measured reflection and transmission spectra of two different reflectors. (a) shows the balanced reflector with a flat spectra and (b) presents the results of a unbalanced reflector with periodic in spectra. The strong ripples in the reflection spectra are due to the reflection happening at the fiber/air facet as well as air/chip facet. . 4-8
- 4.8 A brief illustration showing that the measured spectrum is an interference pattern between the light reflected by the reflector (signal) and the parasitic reflections (noise), for instance, the fiber-air facet induced reflection. 4-9
- 4.9 Measured reflection and transmission spectra of different reflectors using index matching fluid to suppress the parasitic reflections and reveal the real reflection spectra of the reflectors. (a) shows the results without this fluid. (b) is the spectrum of the same reflector using fluid. (c) and (d) are measured spectra of two other reflectors. 4-9
- 4.10 Active measurement of the reflector with metal heater shows that 6 mW will change its reflectivity as much as 35 dB. 4-10
- 4.11 Simulated through port spectrum of a ring circuit with only backscattering and other parasitics in the circuit, including reflections and backcoupling at the directional couplers (a), and with both backscattering and tunable reflector (b) and (c). It shows clearly how the resonance shape evolves with phase shift. (d) gives the brief schematic of the device with a phase shifter. 4-12
- 4.12 During the one modulation period of the power reflectivity of the reflector (from 0 to 100%, then return to 0), the two peaks shift at different speed. If the DCs of the reflector are 50/50 splitter, then one peak doesn't shift at all as shown in the top figure. While if the DCs are not 50/50, for instance a 40/60 case in the bottom figure, the peak slightly shifts. 4-13
- 4.13 Microscopic images of the fabricated devices with in house processed metal heaters. (a) presents the overview of the chip and (b) provides zoomed view of one single device. 4-14
- 4.14 Two measured spectra of simple ring resonators (without reflectors) on the same chip, located close to the ring resonator with tunable reflector. Both rings, which have different coupling conditions, show clear resonance-splitting in most resonance peaks. . . 4-15
- 4.15 Experimental measurements of compensated backscattering. (a) demonstrates the control of all the resonances. (b) gives a zoomed-in view about how the resonance shapes evolve from clearly split to non-split. (c) shows the same compensation for the output at the drop port. 4-17

-
- 4.16 Measured spectra of the same device for the *in* (a) and the *add* ports (b). Clearly, under correct tuning condition, both the leakage to the *add* port and reflection to the *in* port can be significantly suppressed. There is still some residual transmission, but not due to internal backscattering. Instead it's caused by the parasitic reflections at the other parts outside the ring cavity as illustrated in (c). 4-18
- 4.17 A simulated intensity distribution of the fundamental TE mode in a bend silicon strip waveguide. It clearly shows the mode will be positioned closer to the outer wall. 4-19
- 4.18 Example figure from Ref. [19] about the performance of a two ring system utilizing Vernier effect to get a large FSR. 4-20
- 4.19 Example figure from Ref. [22] about the bragg grating assisted ultra wide FSR silicon ring resonator. (a) presents its conceptual illustration and microscopic image after the Ebeam fabrication. (b) is the overall spectrum at the through port and (c) is a zoomed view of other split resonance. The problem of using bragg grating lies in three aspects: demand of Ebeam lithography; non-predictable performance due to fabrication variation and hard to recover by dynamic tuning; limited tuning range. 4-21
- 4.20 At the critical coupling point, the extinction ratio drops dramatically with increasing reflection until it reaches an almost constant value. 4-24
- 4.21 The extinction ratio still changes significantly with increasing reflectivity when the MRR is configured as $\kappa_i = \kappa_o$, which is the general case and easy to guarantee. 4-25
- 4.22 These figures show how the extinction ratio as well as the side mode suppression changes with power coupling coefficient when the MRR is designed as $\kappa_i = \kappa_o$ 4-25
- 4.23 For the application to generate an ultra wide FSR ring resonator, the MZI of the tunable reflector is designed with a length difference ΔL 4-26
- 4.24 Simulated curves of the reflection spectra of the reflector. This unique spectrum provides only one zero reflection point in a very wide range. This is one of the basic principle to achieve an ultra wide FSR ring resonator. Larger order m leads to a sharper slope, but it can not be too large in order to avoid extra dips. 4-27
- 4.25 Simulated curves of the reflection spectra of the reflector under different coupling coefficients of the directional couplers. 4-27
- 4.26 A simulated through port spectra of our device under different coupling conditions, $\kappa_i^2 = 0.05$ (a), $\kappa_i^2 = 0.2$ (b) and $\kappa_i^2 = 0.5$ (c). The order m is chosen to be 23, and the MRR is set at the normal coupling condition $\kappa_i^2 = \kappa_o^2$ 4-29

-
- 4.27 In common tuning configuration, the zero-reflection wavelength of the reflector (a) and the resonance wavelength of the MRR (b) shift at the same rate, and thus the MRR remains single mode. n_g is designed to be 4.2, so maximum $\Delta n = 0.488\% n_g \approx 0.02$. . . 4-30
- 4.28 Instead of using one common phase shifter, we can implement two separate phase shifters to achieve individual tuning of the zero-reflection wavelength of the reflector and the resonance wavelength of the ring. 4-31
- 4.29 Brief illustration of the functionalities of PS1 and PS2 in Fig. 4.28. PS1 is in charge of shifting the zero reflection point of the reflector while PS2 performs the comb shift, to select one of the ring resonance to match the zero reflection point. 4-31
- 4.30 (a) Without PS2, tuning PS1 might result in degradation of the relocated single mode resonance as the local ring resonance doesn't match well with the zero reflection point. (b) With PS2 working, the performance of the relocated single mode resonance can be improved due to the good alignment between local resonance and zero reflection point. With the same index change, we achieve a 4 times larger wavelength shift compared to common tuning. 4-32
- 4.31 When optimizing for a larger tuning range (at the cost of smaller SMSR) we achieve a tuning range almost as wide as 100 nm with the same index change. 4-33
- 4.32 Tuning map for the two phase shifters PS1 and PS2 to achieve a continuous shift of the single mode resonance. Figures (a), (c) and (e) give the results of the first design, where the SMSR of each wavelength is larger than 28 dB while the tuning range is only 30 nm, 4 times wider than that of a normal silicon ring resonator; The results of the modified design are illustrated in figures (b), (d) and (f), where the design parameters are changed to achieve a much wider tuning range around 90 nm at the price of a smaller SMSR, but still, at each wavelength, a SMSR larger than 14 dB can be guaranteed. Note that, 85 nm tuning range comes with a $\Delta\phi_{ps1}$ that is less than $0.7 \times 2\pi$, an even wide range is feasible by increasing $\Delta\phi_{ps1}$ 4-34
- 4.33 Effect of unintentional backscattering on the performance of the MRR. (a) $L = 150 \mu m$, $\kappa_i^2 = 0.2$, $R_{bs} = 7 \times L$. (b) $L = 300 \mu m$, $\kappa_i^2 = 0.2$, $R_{bs} = 7 \times L$. (c) $L = 300 \mu m$, $\kappa_i^2 = 0.4$, $R_{bs} = 7 \times L$ and $m = 55$. When the ring roundtrip length increases from 150 μm to 300 μm , and the corresponding power reflectivity of backscattering grows to $7m^{-1} \times L = 0.0021$, the side mode suppression shows a significant decrease. But we could increase the κ_i and the resonant number m to compensate as in (c). 4-36
- 4.34 Microscope images of the fabricated device with two integrated phase shifters (metal heaters) (a) and a zoom view of a single device (b). 4-37

-
- 4.35 Measured spectra of our device. (a) shows the condition that the ring resonance doesn't match the zero-reflection point perfectly, so a resonance with small extinction ratio and side mode suppression ratio is observed. While (b) gives the results when PS2 is tuned such that one resonance is well aligned to the zero-reflection point. The performance gets improved. 4-38
- 4.36 By controlling PS1, the zero-reflection point can be shifted. Then tuning PS2 will again make one resonance match it to get a good ER and SMSR. 16 mW (around 0.0148 index change) can shift the single mode around 55 nm, which is $11\times$ more efficient than a normal silicon ring resonator. 4-39
- 4.37 A measured spectra of a device with ultra wide FSR. It shows strong reflection to the *in* port and the leakage to the *add* port is as high as the transmission at the *drop* port. 4-41
- 4.38 A brief illustration of the principle of a microwave photonics filter. When a microwave signal is applied to a modulator, there would be two sidebands generate at both sides of the optical carrier in the frequency spectrum. If this signal passes a notch filter, the two sidebands will be filtered out. 4-42
- 4.39 An example of making tunable microwave notch filter based on silicon PIC from Ref. [31]. 4-42
- 4.40 Static measurement of our device as a tunable MPF (a) and the whole spectrum (b). By tuning the metal heaters on top of one arm of the MZI reflector, the spacing between two adjacent peaks can be tuned over entire FSR. The asymmetry in two peaks is due to the ripples of the complete spectrum induced by parasitic reflections of the grating couplers and fiber/air facet. 4-43
- 4.41 Schematic of a ring resonator with sidewall grating (a). Resonance splitting can be induced (b). This resonance splitting can be used to generate pulse advancement, which is so called fast light (c). Source: ref. [35]. 4-45
- 4.42 The schematic of the ring based sensor. One of the MZI reflector's arm will be exposed to the sensing environment. 4-46
- 4.43 Field reflectivity r_0 as a function of index change. (a) $L_1 = L_2 = 200\mu m$ (b) $L_1 = L_2 = 400\mu m$. Increasing the arm length will lead to a smaller FSR but a sharper slope. 4-47
- 4.44 Simulated spectra of two devices, (a) $L_1 = L_2 = 100\mu m$. (b) $L_1 = L_2 = 250\mu m$. The red curve shows the original non-split resonance, while other colorful curves indicate how the split distance increases with increasing index change of the sensing arm. The result shows a efficiency around 350 nm/RIU. 4-48
- 4.45 Simulated $\Delta\lambda$ as a function of Δn_{eff} 4-49

5.1	(a) and (c) give the conceptual illustrations of our device and the Fabry-Perot cavity formed by two reflectors, which are represented by blue lines. (b) and (d) show the schematics where the loop-ended MZI based reflectors replace the blue lines.	5-2
5.2	Simulated outputs at the drop port of the device. Without any reflections, we see a Lorentzian-shaped resonance. Increasing one reflector's reflectivity leads to normal resonance splitting (a); When the second reflector also introduces reflection, a Fano resonance appears from the interference between a FP mode and a ring resonance (b); An EIT like spectrum can be generated by precisely adjusting the reflectors' reflectivities (c). A zoom view of one resonance (d).	5-3
5.3	Microscopic images of our devices (a) and a zoomed view of the heaters (b). (c) gives the designed layout for this device.	5-4
5.4	A basic introductory figure of a Fano resonance, with indication of its key parameters, including ER and slope rate.	5-5
5.5	An example illustration of the asymmetric Fano resonance from Ref. [1]. Clearly shown in this figure, the Fano resonance originates from the interaction between a sharp resonance mode and a smooth background mode. In Ref. [1], this sharp resonance mode comes from a resonator side coupled to a bus waveguide while the smooth background comes from a Fabry-Perot cavity formed by two partial transmitting element on two sides of the bus waveguide.	5-6
5.6	The conceptual schematic proposed by Fan for Fano resonance Ref. [1]. Two partial transmitting/reflecting elements are placed on the bus waveguide to form a Fabry-Perot cavity, which will interact with the ring resonance at the bus waveguide output.	5-7
5.7	An experimental implementation of the structure proposed in Ref. [1] in silicon photonics reported in Ref. [17]. Two partial transmitting/reflecting elements are realized by sidewall grating along the bus waveguide.	5-8
5.8	Simulated spectra of the embedded Fabry-Perot cavity (a),(b) and its schematic (c).	5-9
5.9	Simulated spectra of the complete device (a),(b), and its schematic (c). The tuning conditions are the same with those in Fig. 5.8.	5-10
5.10	This figure gives the conceptual illustration of the generation of a double Fano resonance pattern from the interference between a continuous mode and a split resonance.	5-11
5.11	Simulation shows the influence of the power coupling coefficient of the ring resonator on the performance of the Fano resonance.	5-12
5.12	Overall measured spectra of our device with different tuning conditions of the two phase shifters. The figure presents a one-to-one correspondence with the three stages explained in the simulation part and plotted in Fig. 5.2.	5-14

-
- 5.13 Measurements showing the tunability of the Fano resonance. One phase shifter is fixed with the other one receiving different power injection. The maximum ER can be larger than 40 dB with a corresponding slope rate over 400 dB/nm. While at other resonance, we observe a even sharper slope rate, which is over 700 dB/nm. 5-15
- 5.14 The spectral characteristics of EIT based on Fig. 1 from [22]. It will generate an ultra narrow window in the transmission or absorption spectrum. And the phase response or index profile shows an abrupt change within this window. 5-16
- 5.15 EIT level schemes can be sorted into three categories; vee, ladder, and lambda. 5-17
- 5.16 Tunability and phase response of the EIT peak generated by this ring with two reflectors. Left and right columns present the transmission in dB and the phase response normalized to π , respectively. By tuning the relative phase shift of the reflectors, we can get various EIT resonances. 5-18
- 5.17 By precisely controlling one of the reflectors, a clear EIT peak emerges. Note the tiny change in the power injection shown in the legend. 5-19
- 5.18 Measured phase response for the Lorentzian-shaped resonance (a) and normal resonance splitting (b). 5-20
- 5.19 Measured phase response for the spectrum with EIT peaks (c) and a zoom view of one of the EIT peak (d). When EIT is present, an abrupt phase change happen within its ultra narrow bandwidth. 5-21
- 5.20 Measured group delay of the spectrum shown in Fig. 5.19. At the EIT peak, there is a larger group delay at 4100 ps, compared to the background level at 3200 ps, the EIT slows light down at 1100 ps. We also notice some dips at the delay spectrum at the resonances showing splitting. This is the so-called fast light phenomenon. Due to our tunability of the internal reflections, we can achieve both tunable fast light and slow light. 5-22
- 5.21 Definition of the two parameters to be characterized by the contour plots, namely extinction ratio and slope rate. (a), (b) and (c) present the case of normal resonance splitting, Fano resonance and EIT, respectively. 5-23
- 5.22 Contour plots of extinction ratio and slope rate vs PS1 and PS2. The x and y axis refer to the tuning range from 0 to 0.5π of two phase shifters. They also present the reflectivity of the reflectors from 0 to 100%. 5-24
- 5.23 The two reflectors are now rearranged to make the two reflectors symmetric with respect to the center of the ring cavity. Now the two contour plots show certain symmetry with respect to the diagonal. 5-25

-
- 5.24 The two reflectors are now replaced with two dimensionless lumped reflectors, with constant reflection phase. The contour plots show similar pattern with those in Fig. 5.24. 5-27
- 6.1 Brief illustration of the concept of backcoupling. Left one shows the case of an ideal ring resonator, where the incoming light will only contribute to one of the two circulating modes. If backcoupling exists, both modes will be coupled from the incoming light as illustrated in the right part. 6-1
- 6.2 Simulated through port spectra of a circuit shown in Fig.6.1(b) with backcoupling induced at the directional coupler. (a) presents the results when $f=0, 0.2$ or 0.5 . When $f=0$, i.e. no backcoupling is present, the spectrum shows asymmetric resonance splitting. By varying the backcoupling strength ($f=0.2$ or 0.5), the peak asymmetry can be adjusted. (b) shows the case when $f=0.5$ and -0.5 . The minus sign indicates a π phase difference between κ and κ' . (c) gives the results when $f=1$ and -1 , namely the amplitude of backcoupling equals that of forward coupling. Under such condition, one peak will be suppressed. So resonance splitting will be eliminated even the backscattering is still present. 6-3
- 6.3 A designed circuit in order to introduce and manipulation backcoupling in a realistic way. A MZI is placed in front of a ring resonator to dynamically control the intensity of light at two inputs of a ring resonator. Each of the input will couple to one circulating mode in the ring. Thus the manipulation of the MZI split ratio will lead to the manipulation of the coupling ratio from input light to the two circulating modes of the ring resonator. A tunable reflector introduced in chapter 4 and 5 is implemented inside the ring cavity to couple the two circulating modes and induce resonance splitting. PS indicates phase shifter and DC refers to directional coupler. 6-5
- 6.4 Simulated spectra of the circuit in Fig.6.3 at the condition when the reflector introduces 0 reflectivity. Left column refers to out1 and right column presents the results at out2. Clearly, when there is no internal reflection thus no resonance splitting, manipulating backcoupling doesn't modify the resonance shape. The change in the transmission level is due to the change in the split ratio of the MZI. 6-7
- 6.5 When resonance splitting is present, the impacts of backcoupling will become visible. These figures show the results of manipulating PS1 with PS2=0. (a) and (b) show the outputs at out1 while (c) and (d) present the results at out2. 6-8

6.6	When backcoupling equals forward coupling ($\text{in1}=\text{in2}$), one of the two peaks in a split resonance can be suppressed. And by adding either 0.5π or 1.5π phase shift to PS1, we can also choose which peak to be suppressed.	6-9
6.7	We fix $\text{PS1}=0.2\pi$ and vary PS2 to change the phase difference between backcoupling and forward coupling. (a) and (b) show the output at out1 while (c) and (d) present the results at out2. . . .	6-11
6.8	Microscopic images of the devices to manipulate backcoupling. (a) is the circuit with a circular ring resonator, whose internal reflection is induced by stochastic backscattering. (b) presents the circuit with a ring resonator that has a tunable reflector inside. . .	6-12
6.9	Demonstration of the tunability of internal reflections using PS3 shown in Fig. 6.8(b). (a) and (b) present the tunability under different conditions of PS1.	6-13
6.10	Without internal reflections and resonance splitting, varying PS1 and PS2 do not impact the resonance shape, which is consistent with former simulation results.	6-14
6.11	Measured spectra at out1 and out2 at fixed $\text{PS2}=0$ with varying PS1. They show good match with simulation results plotted in Fig. 6.5.	6-15
6.12	Measured spectra at out1 and out2 at fixed $\text{PS1}=0$ with varying PS2. They show good match with simulation results plotted in Fig. 6.7.	6-16
6.13	Measured spectra with varying PS1 and fixed $\text{PS2}=0$ of two circuits. They both have circular ring resonators (without tunable reflector) but with different coupling coefficients ((a) low Q and (b) high Q). Resonance splitting due to stochastic backscattering is present in both case and it can suppressed by varying PS1. . . .	6-17
6.14	Measured spectra with varying PS2 and fixed $\text{PS1}=0$ of two circuits with circular ring resonators that have different coupling coefficients ((a) low Q and (b) high Q). Resonance splitting due to stochastic backscattering is present in both case and it can suppressed by varying PS2.	6-19
6.15	Some zoomview of resonances measured of a ring resonator with coupling gap at 400 nm. All resonances show Q factor larger than 300,000 and large ER. The FSR of such a resonator is about 2.5 nm. The calculated Finesse is around 600.	6-20
6.16	Quality factor as a function of cavity length for four propagation loss figures from Ref. [1].	6-20
6.17	Finesse as a function of cavity length for four propagation loss figures from Ref. [1].	6-21
6.18	FDTD simulation of the transmission of the directional coupler consisting of a circular arc with 35 μm bend radius and a bus waveguide with 400 nm gap in between. The coupling coefficient is less than 0.003.	6-24

- 6.19 FDTD simulation of the transmission of the directional coupler consisting of a circular arc with $35\ \mu m$ bend radius and a bus waveguide with 400 nm gap in between. The coupling coefficient is around 0.003. 6-25
- 6.20 Simulated outputs of the circuit shown in Fig. 6.3 but with the same parameters in the simulation of a pure circular ring above. Manipulating the backcoupling can increase the extinction ratio of the resonance. 6-26
- 7.1 The design of a generic programmable ring resonator. Top part shows the schematic and bottom part presents the designed layout. 7-3

List of Tables

- 3.1 The detailed data of above spectrum in Fig. 3.13. The existence of f can be inferred from a comparison of the first and third resonance. The peak with larger bandwidth has a higher peak power; comparing the first and second resonance, the relative difference in bandwidths of first resonance is only 6.7%, whereas that in second resonance is 31.6%, but the first one shows a even larger difference in peak power (47.5%) than the second one (42%); This decoupling relative peak power and bandwidth can only be explained with a non-zero f 3-18

List of Acronyms

I

AWG	Arrayed Waveguide Grating
-----	---------------------------

B

BW	Bandwidth
BS	Backscattering
BC	Backcoupling

C

CW	Clockwise
CCW	Counter-clockwise
CMOS	Complementary metal–oxide–semiconductor

D

DC	Directional Coupler
DUV	Deep Ultraviolet

E

EIC	Electronics Integrated Circuit
-----	--------------------------------

ER	Extinction Ratio
EIT	Electromagnetically Induced Transparency
EUV	Extreme Ultraviolet

F

FSR	Free Spectral Range
FWHM	Full Wave Half Maximum
FP	Fabry-Perot

G

GC	Grating Coupler
----	-----------------

I

IC	Integrated Circuit
----	--------------------

M

MZI	Mach Zenhder Interferometer
MMI	Multi-mode Interferometer
MPW	Multi-project Wafer
MPF	Microwave Photonics Filter

O

OFDR	Optical Frequency Domain Reflectometry
OVNA	Optical Vector Network Analyzer

P

PIC	Photonics Integrated Circuit
PDF	Probability Density Function
PS	Phase Shifter

R

RR	Ring Resonator
RIU	Refractive Index Unit

S

SOI	Silicon on Insulator
SMSR	Side Mode Suppression Ratio

T

tCMT	Temporal Coupled Mode Theory
------	------------------------------

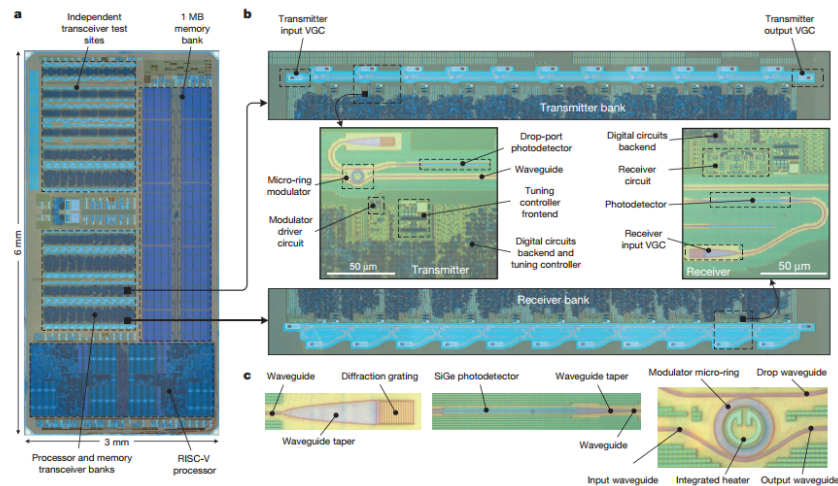
W

WG	Waveguide
WDN	Wavelength Division Multiplexing
WGM	Whispering Gallery Microcavity

Nederlandse samenvatting

–Summary in Dutch–

In de laatste tiental jaren is siliciumfotonica enorm gegroeid, met name in industriële toepassingen. Geïntegreerde fotonische circuits (PIC's) uit silicium beginnen meer en meer gebruikt te worden in datacenters, hoogperformante computers en in coherente communicatietechnieken dankzij de compatibiliteit met CMOS-technologie, die toelaat om dergelijke chips in hoog volume en tegen lage kostprijs te produceren. Het hoog indexcontrast van silicium laat toe om de componenten compact te schikken met een hoge densiteit, om zo meer complexe chips te krijgen. Recent werden silicium-gebaseerde PIC's gedemonstreerd met duizenden componenten op een enkele chip. Bijvoorbeeld, een geïntegreerde optische interconnectie tussen processor en geheugen werd gedemonstreerd door onderzoekers van MIT, UC Berkeley en Colorado Boulder, zoals weergegeven in figuur 1 [1].

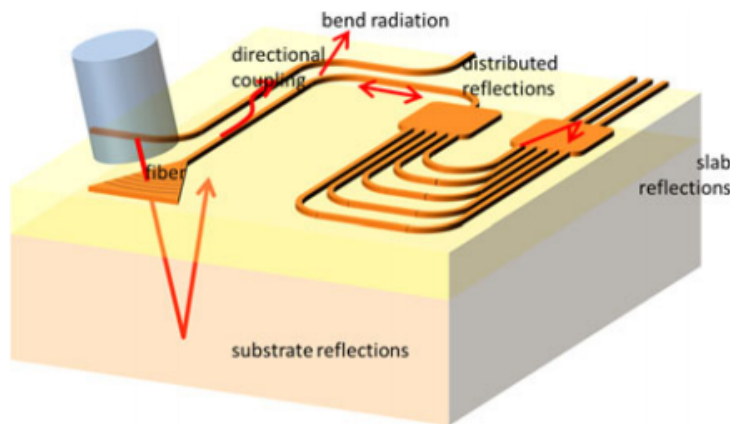


Figuur 1: Het volledige circuit met de elektrische geïntegreerde circuits (EICs) en de fotonische circuits (PIC's) op een chip uit Ref. [1]. Dit circuit bevat 70 miljoen transistoren en 850 fotonische componenten.

Parasitaire effecten

Met de toenemende densiteit van fotonische componenten op PIC's beginnen pa-

parasitaire effecten prominent te worden. Parasitaire effecten verwijzen naar onbedoelde effecten van het circuit of het systeem. Deze zijn in het verleden systematisch bestudeerd en gemodelleerd in elektronische geïntegreerde circuits (EICs) toen de dichtheid van de transistors een zeker niveau bereikte. De verschillende vormen van parasitaire effecten in EICs zijn rigoureus gestandaardiseerd. Ze manifesteren zich als weerstand, capaciteit en inductie. Daartegenover zijn deze effecten in siliciumfotonica veel complexer en meer uiteenlopend. Mogelijke parasitaire effecten in PIC's zijn: buigingsverliezen, substraatverliezen, overbodige reflecties, het inkoppelen van substraatverliezen naar andere delen van het circuit, terugwaartse verstrooiing door ruwheid van de wanden van de golfgeleider, ongewenste koppeling tussen golfgeleiders die niet logisch verbonden zijn, enz. [2, 3] Een korte illustratie van enkele van deze effecten is weergegeven in figuur 2. Daarenboven treden de parasitaire effecten in EICs gewoonlijk slechts op over een kleine afstand, zoals bijvoorbeeld de parasitaire capaciteit tussen naburige transistoren. Daartegenover kunnen de parasitaire effecten in PIC's over een groter bereik plaatsvinden, zelfs tussen verafgelegen delen van dezelfde chip. In deze thesis presenteren wij ons werk over de typische en meest frequente vormen van parasitaire effecten, zoals valse reflecties, substraatverliezen en -koppelingen, gedistribueerde terugwaartse verstrooiing van het licht en ongewenste evanescente koppeling. De experimentele observaties worden gegeven, in combinatie met gesimuleerde data en verdere bespreking van de oorsprong en impact van deze effecten.

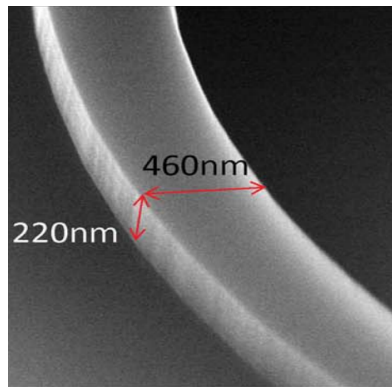


Figuur 2: Verschillende parasitaire effecten in PIC's uit ref. [2]. De brede diversiteit van de parasitaire effecten in PIC's maakt het moeilijk om deze effecten te bestuderen en modelleren in vergelijking met EICs.

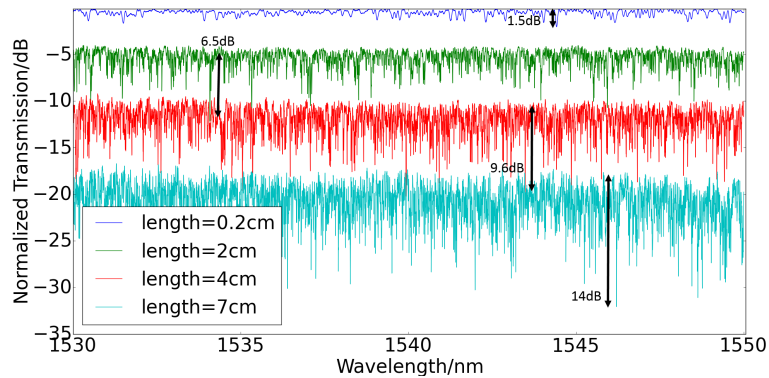
Achterwaartse verstrooiing in silicium golfgeleiders and ringresonatoren

Een vorm van parasitaire effect is de gedistribueerde achterwaartse verstrooiing van het licht, veroorzaakt door de ruwheid van de wanden van de golfgeleiders (Fig. 3), die onvermijdelijk is met de huidige fabricagetechnologie. Dusver is het

probleem uitvoerig bestudeerd en er heerst consensus dat extra buigingsverliezen en stochastische achterwaartse verstrooiing veroorzaakt zullen worden door deze ruwheid van de zijwanden van de golfgeleider. Maar ons onderzoek toont aan dat het transmissiespectrum van een silicium golfgeleider ook sterk gevoelig is aan dit probleem. Voor centimeter lange golfgeleiders vertoont het transmissiespectrum sterke en snelle fluctuaties zoals blijkt uit figuur 4. Wij presenteren een grondige analyse van de connectie tussen deze fluctuaties met de gedistribueerde achterwaartse verstrooiing van het licht, voortkomend uit de ruwheid van de zijwanden van de golfgeleider.



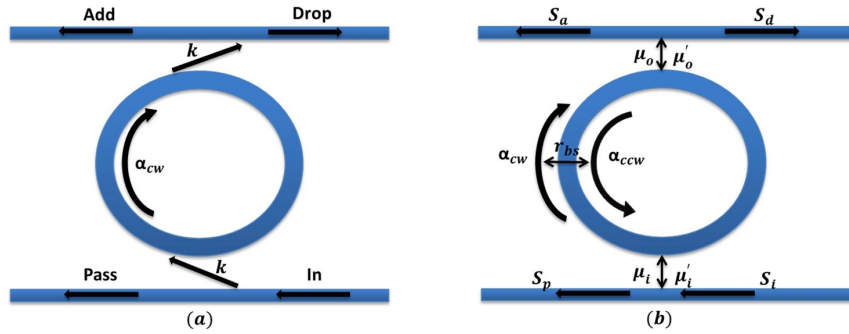
Figuur 3: SEM afbeelding van ref. [4] die de ruwheid weergeeft van de zijwanden van een standaard golfgeleider op silicium-op-isolator, gefabriceerd in een CMOS fab.



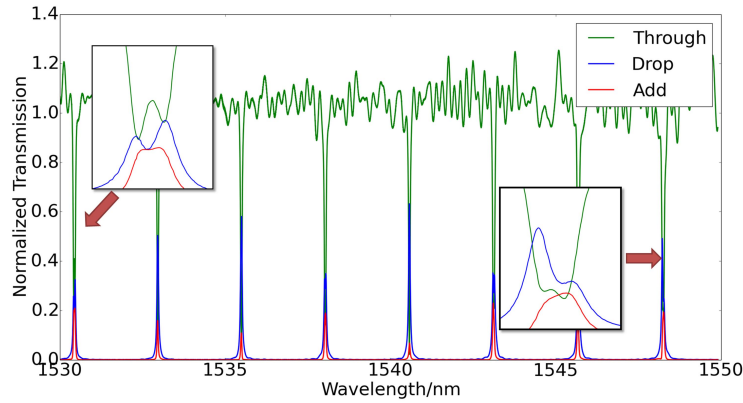
Figuur 4: Een opgemeten transmissiespectrum van een standaard golfgeleider met verschillende lengtes, gefabriceerd in IMEC. Alle golfgeleiders vertonen sterke fluctuaties, waarvan de intensiteit schaaft met de lengte van de golfgeleider.

De ruwheid van de zijwanden van de golfgeleider is nog nefaster voor resonerende structuren, zoals ringresonatoren (RRs). De terugwaartse verstrooiing van

het licht zal twee circulerende modes koppelen, waarvan een mode circuleert in wijzerzin (CW), en de andere mode in tegenwijzerzin (CCW) (Fig. 5). Oorspronkelijk zijn deze modes gedegenereerd en resonant met dezelfde golflengte. Maar door de koppeling van het licht wordt dit principe opgeheven en resonantiesplitsing zal optreden (Fig. 6). Daarenboven zullen ook ongewenste reflecties geïnduceerd worden naar de *in* poort en verliezen naar de *add* poort.



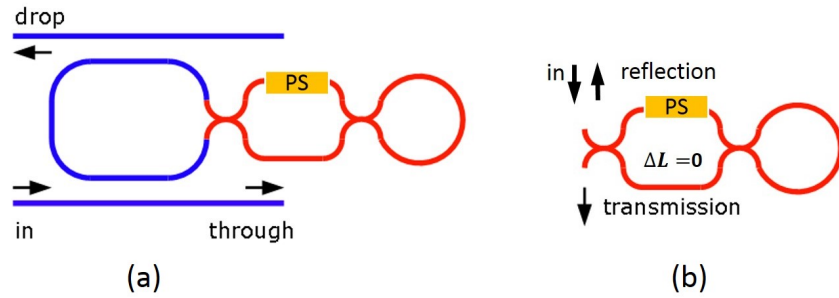
Figuur 5: (a) schema voor een ideale ringresonator. (b) tCMT schema voor een realistische ringresonator met terugwaartse verstrooiing van het licht (r_{bs}) dat koppelt naar CW en CCW modes.



Figuur 6: Een opgemeten spectrum van een echte, gefabriceerde silicium ringresonator. Verschillende resonanties vertonen splitsingen met verschillende vormen. Er zijn sterke verliezen naar de *add* poort.

Wij presenteren een uitgebreide analyse van ringresonatoren met terugwaartse verstrooiing van licht en tonen de oorzaak van de asymmetrische resonantiesplitsing aan, welke de terugkoppeling is aan de directionele koppelaars. Vervolgens bouwen wij een model, steunend op tijdsdomein gebaseerde gekoppelde modetheorie (tCMT), die alle vormen van resonantiesplitsing kan verklaren. Wij gebruiken

dit model om de meetdata van meer dan 1000 resonanties te fitten en zodoende een beschrijvende analyse te kunnen geven van de terugwaartse verstrooiing in functie van enkele fysische parameters van ringresonatoren.



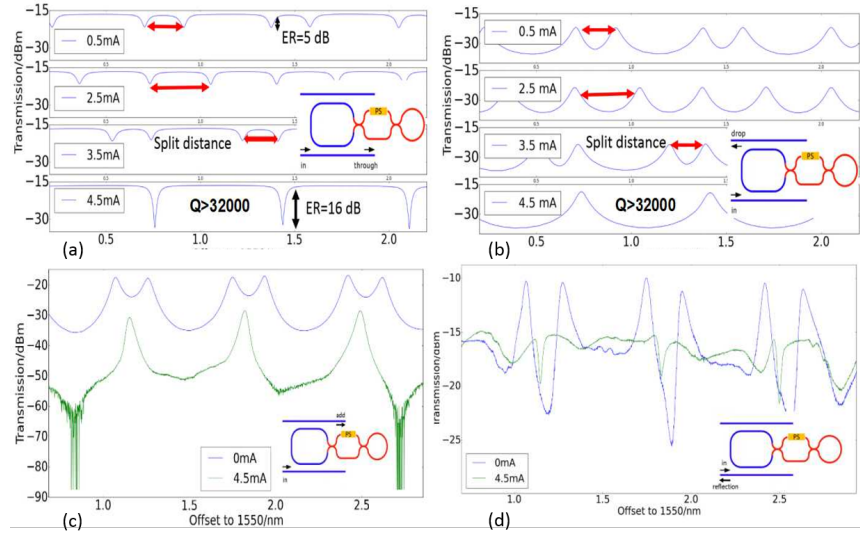
Figuur 7: Schema's van ringresonatoren met een reflector en de reflector zelf, respectievelijk.

Ontworpen reflecties in silicium ringresonatoren

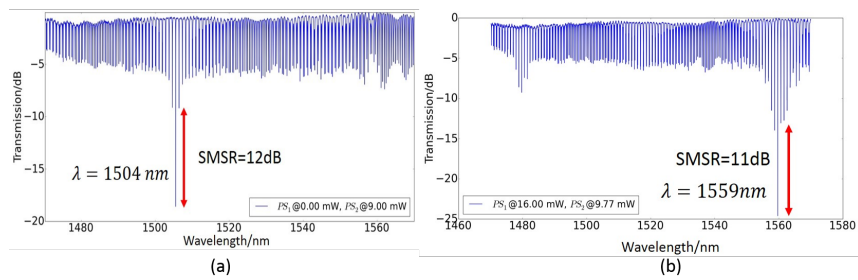
Tot dusver kunnen slechts twee parameters aangepast worden in het ontwerp van een silicium ringresonator, namelijk de koppelingscoëfficiënt κ van de directionele koppelaar en de total rondganglengte L . Echter, het is reeds aangetoond dat de terugstrooiing een negatief effect heeft op de prestaties van de ringresonator. Daarom kan het beschouwd worden als een oncontroleerbare ontwerpparameter van de ringresonator. Wij ontwerpen een nieuwe, afstembare reflector (Fig. 7), die ingewerkt kan worden in het ontwerp van een ringresonator om zo de interne reflecties controleerbaar te maken. Enkele toepassingen zijn experimenteel aangetoond. De allerbelangrijkste is dat we via deze methode de stochastische reflecties kunnen onderdrukken, aangezien de interne reflecties gecontroleerd kunnen worden via de reflector. Met correcte afstemming kunnen we niet alleen de resonantiesplitsing elimineren, maar ook de reflectie aan de *in* poort en het verlies aan de *add* poort onderdrukken (Fig. 8).

Deze component kan ook ontworpen worden om aan de ringresonator een ultrabreed vrij spectraal bereik (FSR) en afstembereik te geven. De reflector maakt gebruik van het principe dat de uitdoofverhouding (ER) van een resonantie enorm onderdrukt kan worden door middel van interne reflecties. De reflector kan zodanig ontworpen worden dat hij een reflectiespectrum heeft waar slechts één golflengtepunt uit een breed spectrum geen reflectie heeft. Daardoor heeft enkel deze 0-reflectiegolflengte een ultrabreed FSR (Fig. 9(a)). Bovendien, gebruik makend van het tweestaps afstelmechanisme, kan de zeer hoge ER resonantie afgestemd worden over een veel groter golflengtebereik dan de resonantie van een traditionele ringresonator (Fig. 9(b)).

De bovenvermelde toepassingen zijn gedemonstreerd met een ringresonator met een afstembare reflector in de resonator. Indien we twee identieke reflectors in

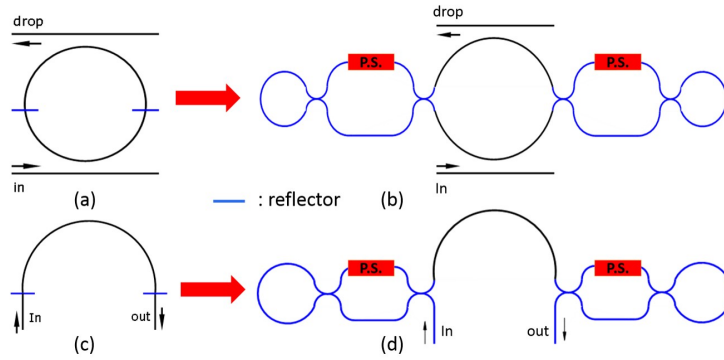


Figuur 8: (a) en (b) tonen het verwijderen van de resonantiesplitsing aan de thru en de drop poorten. (c) en (d) tonen het onderdrukken van verlies en reflecties aan de add poort en de in poort, respectievelijk.

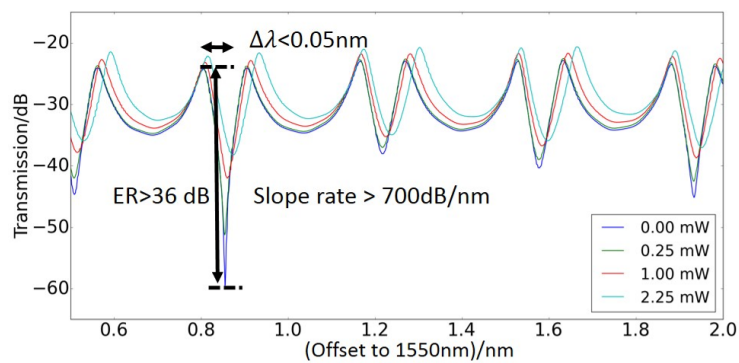


Figuur 9: (a) toont de experimentele demonstratie van een ultrabreed vrij spectraal bereik. (b) toont het grote afstembereik van de resonantie.

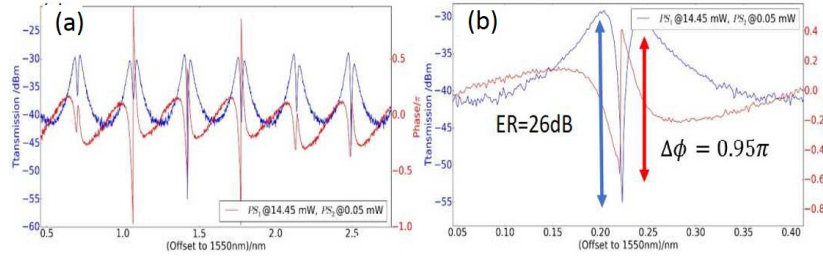
de ring plaatsen (Fig. 10), dan kunnen nog meer interessante verschijnselen plaatsvinden. In dit geval wordt een ingebedde Fabry-Perot (FP) caviteit gevormd tussen de twee reflectoren. Het uitgangssignaal is het resultaat van de interactie tussen de ringresonantie en de FP mode. De FP mode kan heel nauwkeurig afgestemd worden door de instelling van de twee reflectoren. Hetzelfde geldt voor de splitsing van de FP mode en de ring resonantie. Wanneer er een niet-nul ontstemming is tussen de ringresonantie en de FP resonantie dan ontstaat een Fano resonantie met een zeer steile helling. Deze mode is uitermate geschikt voor hooggevoelige sensors en schakelaars. Wij hebben experimenteel de afstembare Fano resonantie gedemonstreerd via deze methode. Een maximale helling van 700 dB/nm met een ER van meer dan 36 dB is opgemeten (Fig. 11).



Figuur 10: (a) en (c) conceptuele voorstelling van onze component en de Fabry-Perot caviteit die gevormd is door de twee reflectors, voorgesteld door de blauwe lijnen. (b) en (d) voorstelling met de in een lus eindigende, MZI gebaseerde reflectors.

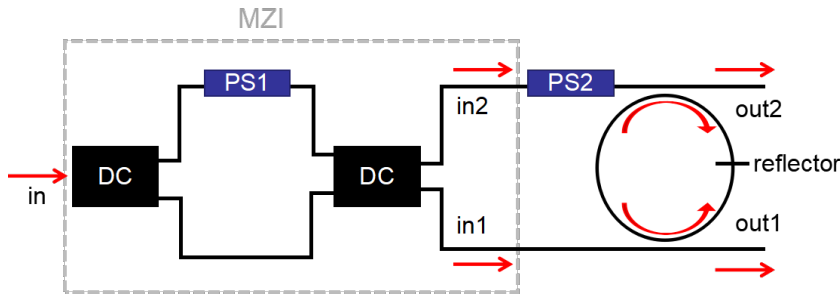


Figuur 11: Opgemeten Fano resonantie die gegenereerd wordt door onze component. De maximale helling kan groter zijn dan 700 dB/nm.



Figuur 12: Opgemeten EIT piek. Dit toont een fazetransformatie rond 0.95π binnen een optisch bereik van 0.01 nm.

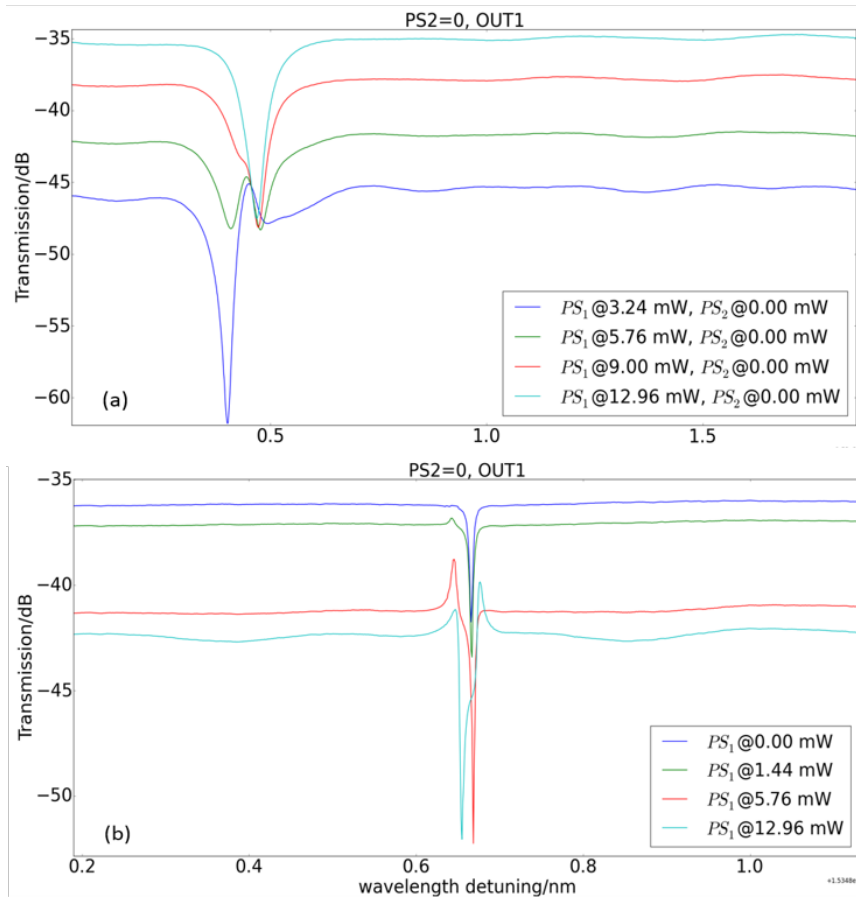
Wanneer de FP mode en de ringresonantie perfect zijn afgestemd op elkaar treedt er elektromagnetisch geïnduceerde transparantie op (EIT). De eigenschappen van EIT zijn onder meer een ultrasmaal venster in het transmissiespectrum en een abrupte faseverandering binnen dit ultrasmaal venster. Deze abrupte faseverandering weerspiegelt de sterke dispersie, m.a.w. een hoge groepindex en een lage groepsnelheid. Dat is waarom EIT tot dusver een van de meest belovende technieken is voor traag licht toepassingen, zoals optische buffers of optisch geheugen. Wij hebben experimenteel aangetoond dat EIT optreedt in onze component, met een faseverandering van 0.95π binnen een 0.01 nm golflengtebereik (Fig. 12).



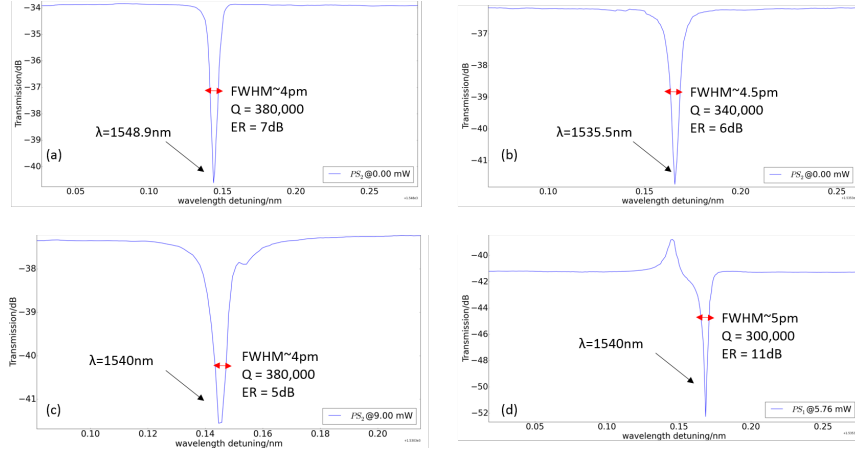
Figuur 13: Een ontworpen circuit om achterwaartse koppeling te introduceren en te manipuleren.

Manipulatie van de terugkoppeling van het licht in silicium ringresonatoren

Tijdens het onderzoek naar de terugstrooiing van licht begrepen we dat niet alleen de terugstrooiing bijdraagt tot de resonantiesplitsing; ook de terugkoppeling is belangrijk. De terugkoppeling dient dus beschouwd te worden als een bijkomende vrijheidsgraad in het ontwerp van een silicium ringresonator. Wij hebben bijgevolg ook een circuit ontworpen dat toelaat om deze terugkoppeling te manipuleren voor een ringresonator (Fig. 13). Een uitgebreide karakterisering door middel van simulaties en een experimentele demonstratie van dit circuit werden uitgevoerd.



Figuur 14: Opgemeten spectra die de manipulatie van achterwaartse koppeling aantonen. De piek asymmetrie van een gesplitste resonantie kan aangepast worden en resonantiesplitsing kan dus compleet verwijderd worden.



Figuur 15: Een uitvergroting van enkele uitgemeten resonanties van een ringresonator met een koppelingsbrug van 400 nm. Alle resonanties tonen een Q -factor die groter is dan 300,000 en een grote ER. Het vrij spectraal bereik van een dergelijke resonator is ongeveer 2.5 nm.

Deze karakterisering toont aan dat de assymetrie van een resonantiesplitsing kan aangepast worden, en dat de splitsing kan verwijderd worden (Fig. 14). Daarbovenop tonen we dat dit circuit een ultrahoge Q -factor heeft die dicht bij 400,000 ligt (Fig. 15). Dit is tot heden de grootste Q -factor voor een silicium ringresonator met een standaard stripgolfsgeleider.

Besluit

In deze thesis presenteren wij ten eerste ons onderzoek naar parasitaire effecten in siliciumfotonica met een focus op bepaalde, typische vormen van deze parasitaire effecten. Hun oorsprong en impact worden besproken met zowel simulatie- als meetresultaten. Daarna geven we een uitgebreide analyse van terugstrooiing van licht in silicium golfgeleiders en ringresonatoren, een van de belangrijkste vormen van parasitair effect. Vervolgens introduceren we een concept om interne reflecties te gebruiken als een additionele vrijheidsgraad in het ontwerp van silicium ringresonatoren en geven daarna een demonstratie van onze methode. Enkele applicaties die gebruik maken van de methode worden ook besproken. Ten slotte tonen wij ook de manipulatie van terugkoppeling van het licht aan en stellen dit voor als nog een extra vrijheidsgraad van silicium ringresonatoren.

Referenties

- [1] Chen Sun, Mark T Wade, Yunsup Lee, Jason S Orcutt, Luca Alloatti, Michael S Georgas, Andrew S Waterman, Jeffrey M Shainline, Rimas R Avizienis, Sen Lin, et al. *Single-chip microprocessor that communicates directly using light*. *Nature*, 528(7583):534–538, 2015.
- [2] Wim Bogaerts, Martin Fiers, and Pieter Dumon. *Design challenges in silicon photonics*. *IEEE Journal of Selected Topics in Quantum Electronics*, 20(4):1–8, 2014.
- [3] Daniele Melati, Francesco Morichetti, Gian Guido Gentili, and Andrea Melloni. *Optical radiative crosstalk in integrated photonic waveguides*. *Optics letters*, 39(13):3982–3985, 2014.
- [4] Wim Bogaerts and SK Selvaraja. *Compact single-mode silicon hybrid rib/strip waveguide with adiabatic bends*. *IEEE Photonics Journal*, 3(3):422–432, 2011.

English summary

The past decade has witnessed the rapid growth of silicon photonics, especially in industrial applications. Silicon photonics integrated circuits (PICs) start to become more and more widely employed in data centers, high performance computers and coherent communications thanks to its CMOS compatibility that makes large volume and low cost fabrication possible and its ultra high index contrast which allows compact components and high integration density. Recently, silicon photonics integrated circuits (PICs) with thousands of components have been continuously demonstrated. For instance, an on-chip interconnection circuit to communicate optically between processor and memories has been demonstrated in silicon photonics by researchers from MIT, UC Berkeley and Colorado Boulder, as exhibited in Fig. 16 [1].

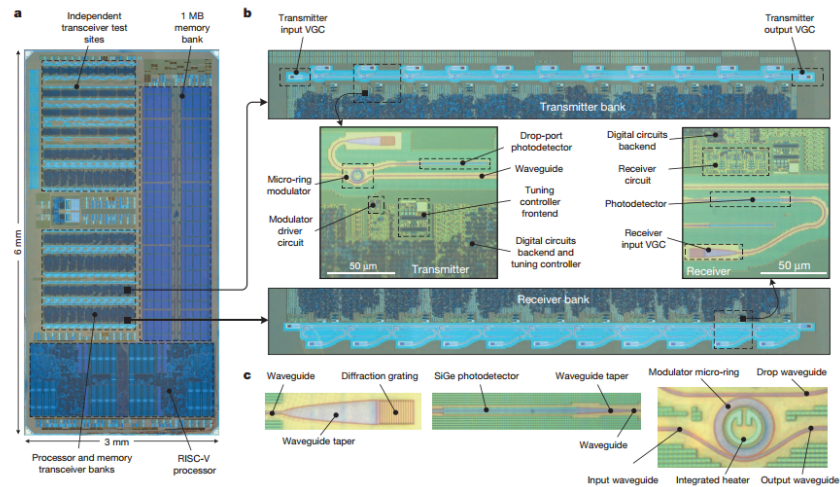


Figure 16: The full circuit with both EICs and PICs on a chip in Ref. [1]. This circuit contains 70 million transistors and 850 photonic components.

Parasitics

With the integration density growing, the parasitics in silicon PICs should draw attention. Parasitics refer to those unintended effects in a circuit or system. They have been systematically studied and modelled in electronics integrated circuits (EICs) when the integration density of transistors grew to a certain level. The

forms of parasitics in EICs are highly standardized. They appear as resistance, capacitance and inductance. While in silicon PICs, they are much more diverse and complicated. The potential parasitics in PICs include but are not limited to: bend losses, substrate leakage, coupling from substrate leakage to other parts of the circuit, spurious reflections, roughness induced backscattering, unwanted coupling between logically not coupled waveguides etc. [2, 3] A brief illustration of some photonics parasitics are given in Fig. 17. Moreover, usually the parasitics in EICs only exist in short range, for instance, the parasitic capacitance between adjacent transistors. While parasitics in PICs can be long range, even between distant parts of a chip. In this thesis, we present our work on some typical and most frequent forms of parasitics in silicon photonics, including spurious reflections, substrate leakage and coupling, distributed backscattering and unwanted evanescent coupling. Their experimental observations are provided, with further discussions and simulations about their origins and impacts.

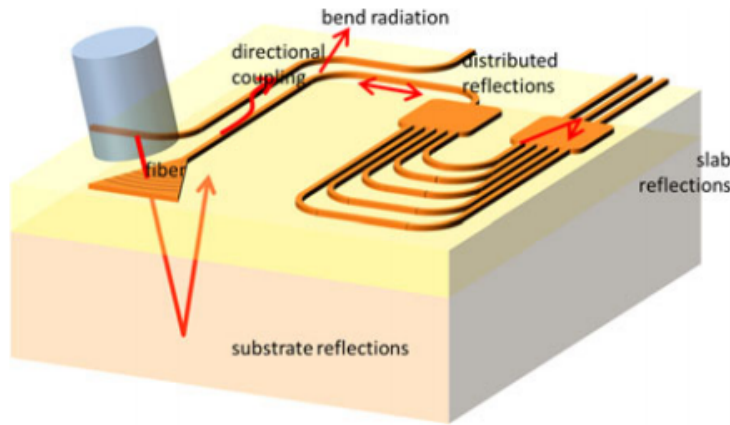


Figure 17: An example figure showing different kinds of parasitics in PICs from Ref. [2]. This broad diversity imposes difficulty and complexity in studying and modelling parasitics in PICs compared to those in EICs.

Backscattering in Silicon waveguides and ring resonators

One form of the parasitics in silicon photonics is the distributed backscattering caused by sidewall roughness of the waveguides (Fig. 18), which is inevitable due to current fabrication technology. So far, it has been intensively studied and it's concluded that extra radiation loss and stochastic backscattering will be induced by the sidewall roughness to a waveguide. But our research reveals that, the transmission spectrum of a silicon waveguide will also be strongly impacted. For centimeter long waveguides, the transmission spectra exhibit strong and rapid fluctuations as evident in Fig. 19. We present an in-depth analysis of the connection between these fluctuations with sidewall roughness induced backscattering.

The sidewall roughness induced backscattering is more detrimental to resonant

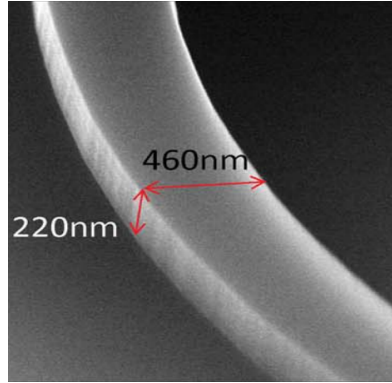


Figure 18: A SEM figure from Ref. [4] showing sidewall roughness of a standard strip waveguide on SOI substrate fabricated at a mature CMOS fab.

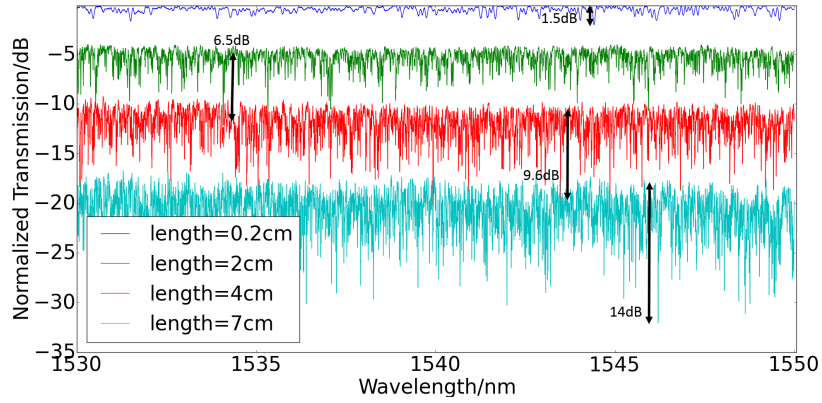


Figure 19: Measured transmission spectra of standard strip waveguides with different lengths fabricated at IMEC. All show strong fluctuations, whose strength scales with waveguide length.

devices like ring resonators (RRs). This backscattering will couple two circulating modes, one of which is circulating clockwise (CW) and the other one counter-clockwise (CCW) (Fig. 20). Originally they are degenerate and resonant at the same wavelength. Due to the coupling, their degeneracy is broken and resonance splitting will appear (Fig. 21). Moreover, unwanted reflection to the *in* port and leakage to the *add* port will also be induced.

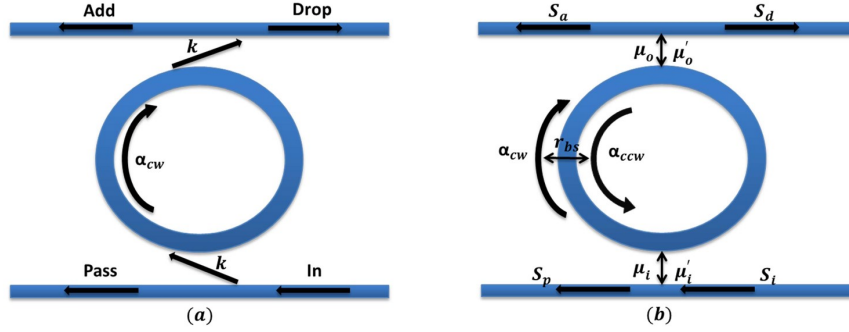


Figure 20: (a) schematic for an ideal ring resonator; (b) tCMT schematic for a real ring resonator with backscattering (r_{bs}) that couples CW and CCW modes.

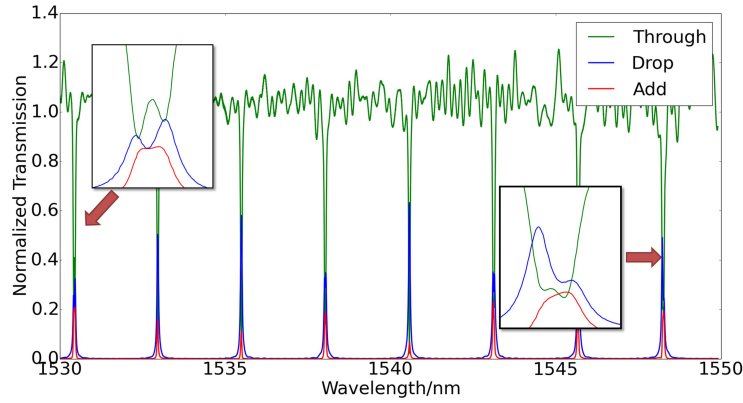


Figure 21: A measured spectra of a real silicon ring resonator. Various resonances exhibit splitting with different shapes. And strong leakage to the *add* port is present.

We present a comprehensive analysis of ring resonators with backscattering and prove the origin for asymmetric resonance splitting, which is the backcoupling at the directional couplers. Then a model based on temporal coupled mode theory (tCMT) that can explain all kinds of resonance splitting is built. We use this model to fit over 1000 resonances from measurements and give a quantitative analysis of the dependency of backscattering on some physical parameters of ring resonators.

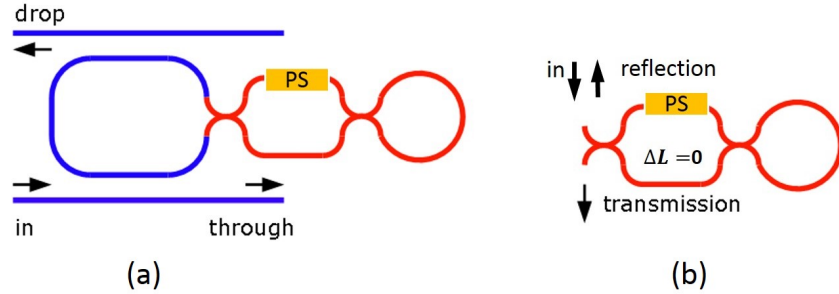


Figure 22: Schematics of the ring with a reflector and the reflector itself, respectively.

Engineered reflections in silicon ring resonators

So far, only two degree of freedoms can be manipulated at the design stage of a silicon ring resonator, namely coupling coefficient κ of the directional coupler and the total roundtrip length L . However, the backscattering is already proven to impact the ring resonators' performance significantly. Thus it can be considered as an uncontrollable degree of freedom for silicon ring resonators. We design a novel tunable reflector (Fig. 22), which can be incorporated into a ring resonator to provide tunable internal reflections. A couple of applications have been experimentally demonstrated. First of all, it can fundamentally suppress the stochastic backscattering, as now the internal reflections can be tuned through controlling the reflector. Under correct tuning condition, not only the resonance splitting can be eliminated, but also the reflection to the *in* port and leakage to the *add* port can be suppressed (Fig. 23).

This kind of structure can also be designed to provide a silicon RR with an ultra wide FSR and tuning range. It take advantages the principle that extinction ratio (ER) of a resonance can be dramatically suppressed by internal reflections. And the tunable reflector can be designed to provide a reflection spectrum where only one wavelength point in a broad span shows 0 reflection. Thus only the resonance that matches the 0 reflection point will have a large ER (Fig. 24(a)). Moreover, using two-step tuning mechanism, this large ER resonance can be tuned in a much broader range than a resonance of a normal silicon ring resonator (Fig. 24(b)).

The applications above are demonstrated using a ring resonator with one tunable reflector inside. Placing two identical reflectors inside a RR (Fig. 25) can give more interesting phenomenon. In this case, an embedded Fabry-Perot (FP) cavity is formed by the two reflectors. The outputs become the result of interaction between the ring resonance and the FP mode. The FP mode can be tuned to very smooth condition by controlling the two reflectors, so is the detuning between the FP mode and the ring resonance. When they have non-zero detuning, their interference will generate Fano resonance with very sharp slope, which is a great candidate for high efficiency sensors and switches. We experimentally demon-

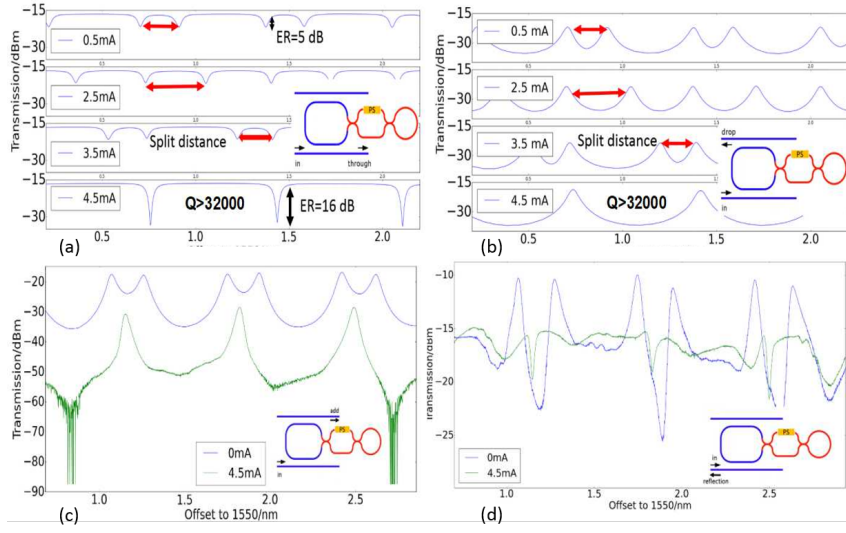


Figure 23: (a) and (b) show the resonance splitting elimination at the thru and drop ports. (c) and (d) show the suppression of leakage to the add port and reflection to the in port.

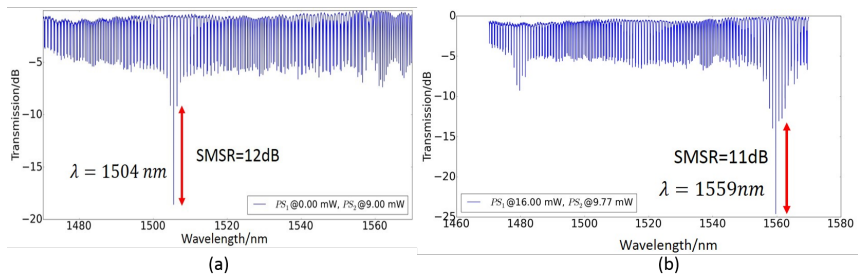


Figure 24: (a) shows the experimental demonstration of the ultra wide FSR spectrum. (b) presents the broad tuning range of this resonance.

strate the tunable Fano resonance using this approach. A maximum slope rate over 700 dB/nm with an ER over 36 dB was observed (Fig. 26).

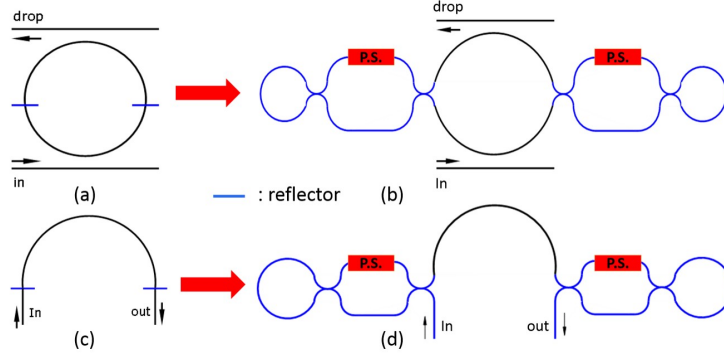


Figure 25: (a) and (c) give conceptual illustrations of our device and the Fabry-Perot cavity formed by two reflectors, which are represented by blue lines. (b) and (d) show the schematics where the loop-ended MZI based reflectors replace the blue lines.

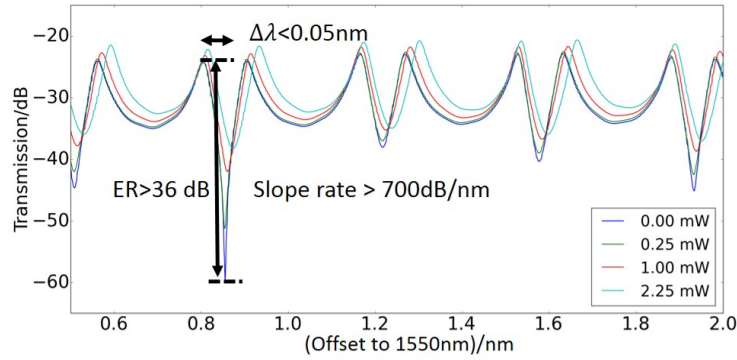


Figure 26: Measured Fano resonance generated by our device. The maximum slope rate can be over 700 dB/nm.

When the FP mode and the ring resonance have zero detuning, a phenomenon called electromagnetically induced transparency (EIT) will be generated. The features of EIT include an ultra narrow window in the amplitude transmission spectrum and an abrupt phase change within this ultra narrow window. This abrupt phase change within this narrow optical range reflects the strong dispersion, in other words, large group index and slow group velocity. That is why EIT is so far one of the most promising methods to demonstrate slow light applications, like optical buffer and storage. We experimentally demonstrate EIT in our device, with a phase change around 0.95π within 0.01 nm range (Fig. 27).

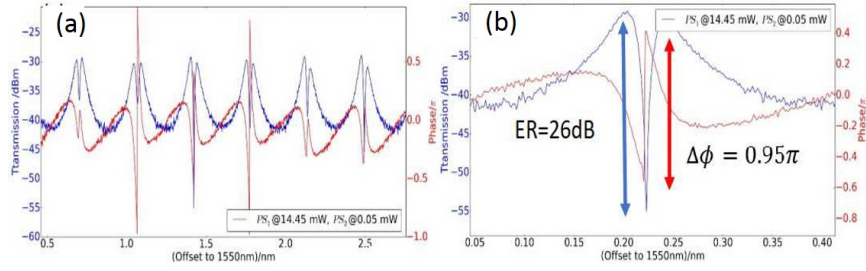


Figure 27: Measured EIT peak. It shows a phase change around 0.95π within 0.01 nm optical range.

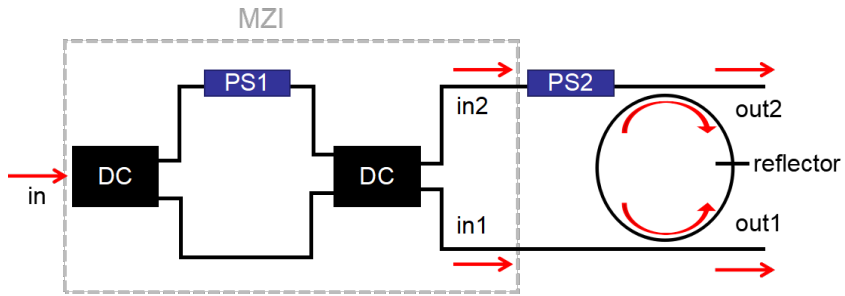


Figure 28: A designed circuit in order to introduce and manipulation backcoupling in a realistic way.

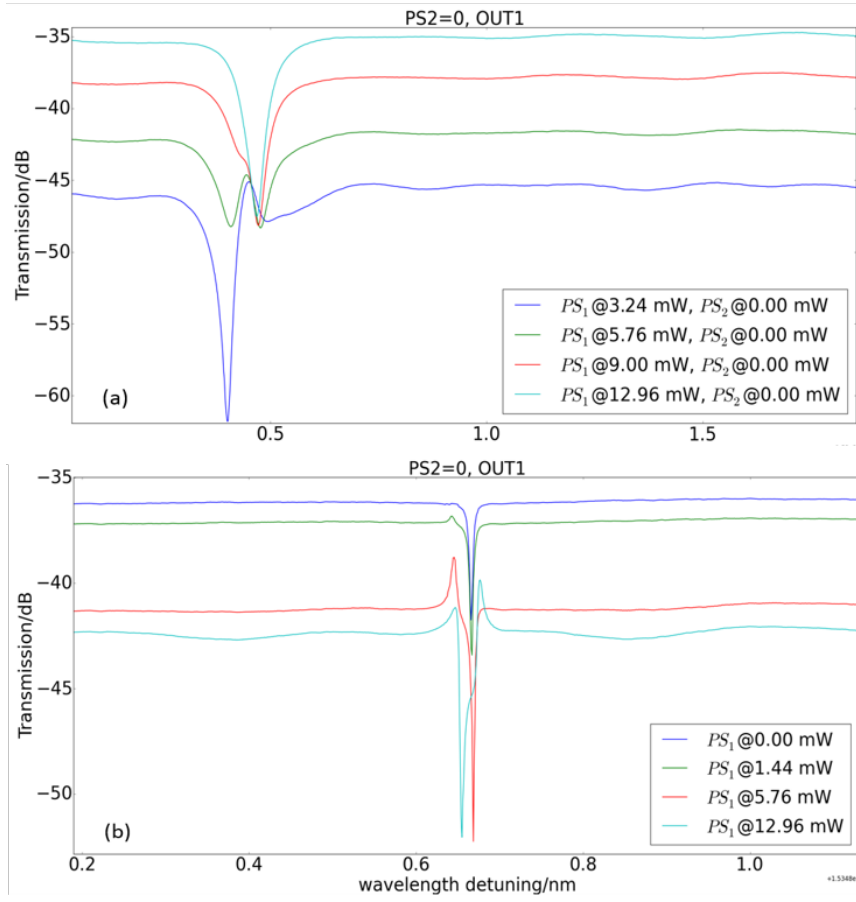


Figure 29: Measured spectra to show the manipulation of backcoupling. Peak asymmetry of a split resonance can be adjusted and resonance splitting can be eliminated.

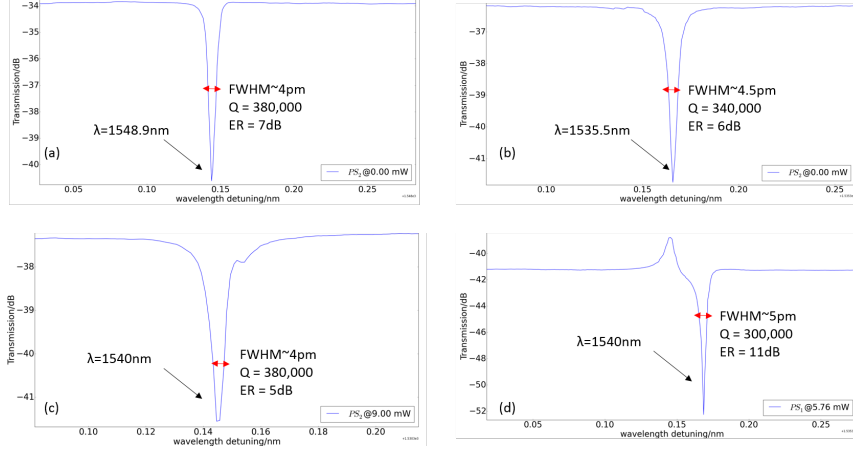


Figure 30: Some zoomview of resonances measured of a ring resonator with coupling gap at 400 nm. All resonances show Q factor larger than 300,000 and large ER. The FSR of such a resonator is about 2.5 nm.

Backcoupling manipulation of silicon ring resonators

In the study of backscattering in silicon ring resonator, we realize that not only the backscattering contributes to the resonance splitting, but also the backcoupling plays a role. So the backcoupling should be considered as another degree of freedom for silicon ring resonator. We also design a circuit that is capable to manipulate this factor for a silicon ring resonator (Fig. 28). A comprehensive simulation characterization and experimental demonstration of this circuit is given. It shows that, this method can be used to adjust peak asymmetry of a split resonance and elimination of resonance splitting can be achieved (Fig. 29). Moreover, we observed an ultra high Q factor that is close to 400,000 from this circuit (Fig. 30), which is so far the largest Q factor for silicon ring resonator with standard strip waveguide.

Conclusion

In this thesis, we first show our work on the parasitics in silicon photonics with focus on some typical forms of parasitics. Their origins and impacts are discussed both with simulation results and measurement results. Then we give a comprehensive analysis of backscattering in silicon waveguides and ring resonators, as it is inevitable and one of the most influential parasitics. After this, we propose the concept to treat the internal reflections as one degree of freedom for design of silicon ring resonators and give the demonstration of our method. A couple of applications are given using this method. Finally, we show the manipulation of the backcoupling and propose it to be another degree of freedom for silicon ring resonators.

References

- [1] Chen Sun, Mark T Wade, Yunsup Lee, Jason S Orcutt, Luca Alloatti, Michael S Georgas, Andrew S Waterman, Jeffrey M Shainline, Rimas R Avizienis, Sen Lin, et al. *Single-chip microprocessor that communicates directly using light*. *Nature*, 528(7583):534–538, 2015.
- [2] Wim Bogaerts, Martin Fiers, and Pieter Dumon. *Design challenges in silicon photonics*. *IEEE Journal of Selected Topics in Quantum Electronics*, 20(4):1–8, 2014.
- [3] Daniele Melati, Francesco Morichetti, Gian Guido Gentili, and Andrea Melloni. *Optical radiative crosstalk in integrated photonic waveguides*. *Optics letters*, 39(13):3982–3985, 2014.
- [4] Wim Bogaerts and SK Selvaraja. *Compact single-mode silicon hybrid rib/strip waveguide with adiabatic bends*. *IEEE Photonics Journal*, 3(3):422–432, 2011.

1

Introduction

1.1 Silicon photonics integrated circuits

Photonics is the branch of science that processes information by means of manipulating light. Light as the carrier for information can accommodate huge bandwidth (at the level of Terahertz) compared to electrical signal (at the level of gigahertz). Moreover, the extremely low propagation loss for light in optical fiber ($<1\text{dB/km}$) makes distant communications possible. It has grown to be influential in most aspects of life since the first practical component was born in 1960s. So far this field has become quite mature and many functional devices have been well developed. There exist light sources that generate light, optical isolators that protect light sources from back-reflected light, modulators that impose information onto light by modulating its intensity according to the information pattern sent to the modulator through electrical signal, optical amplifiers that boost the signal power against noise, photo detectors that convert incoming light into electrical signal for further processing and all the other passive components including resonators, splitters/combiners, filters, (de-)multiplexers and so on. Recently it has been officially recognized as a key enabling technology (KET) by the EU-Commission. Even if you might have not been directly exposed to this technology, without it your life quality will definitely be degraded. For instance, fiber-to-the-home (FTTH) transceivers which enable high speed internet surfing and high-resolution TV programs are employed throughout the world; all the communication channels between continents utilize optical fibers, where light, instead of electric current,

is propagating as it is able to carry much more information and has only a low propagation loss; huge data-centers supporting large companies like Google and Facebook are gradually switching to take advantage of optical fibers supporting optical signal instead of conventional copper cables guiding electrical signal; currently rapidly growing VR technology is also a field where photonics play a vital role; Optical medical microscopy is active in the medical field helping maintain and increase our health-care and so on.

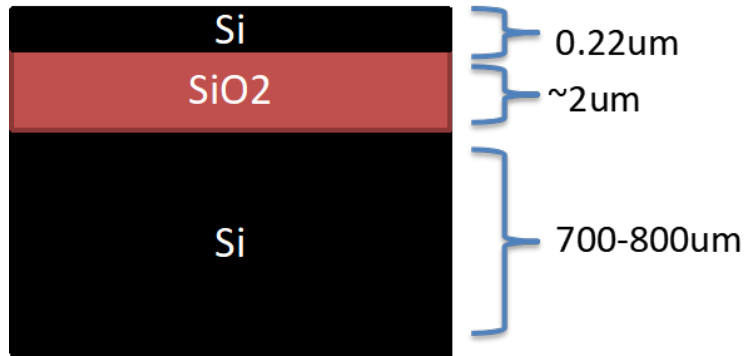


Figure 1.1: A mainstream SOI wafer consists of three layers: a bottom layer of silicon with a thickness around 800 μm ; a intermediate layer of SiO₂ with a thickness around 2 μm ; a top layer of 220 nm thickness silicon, where the structures will be fabricated. The SiO₂ serves as an intervening layer that prevents the substrate leakage.

Those photonics functionalities can either be implemented as bulky systems with discrete devices/equipment or as integrated circuits with many functionalities fabricated on small chips, which are called photonic integrated circuits (PICs). And just like the importance of electronics integrated circuits (EICs) in all the electric applications, PICs are also key parts in the photonics technologies. The integration of multiple components onto a single chip can not only dramatically reduce the cost and size of the device but also significantly improve their performance sometimes, for instance an integrated Raman spectroscopy is reported to have a detected signal with 4 orders of magnitude higher than confocal Raman, which is both bulky and expensive [1]. Among all the material platforms for PICs, silicon-on-insulator (SOI) is one of the most promising and widely used. It consists of three layers shown in Fig. 1.1. The main advantages are listed as following:

- **CMOS compatibility.** Photonics on SOI, or silicon photonics, utilizes silicon as the structure layer, which is also commonly used for EICs. Thus it can enjoy the mature fabrication technology developed for EICs, called Complementary metal–oxide–semiconductor (CMOS) technology. Using this technology can dramatically increase the manufacture volume and decrease the cost per chip.

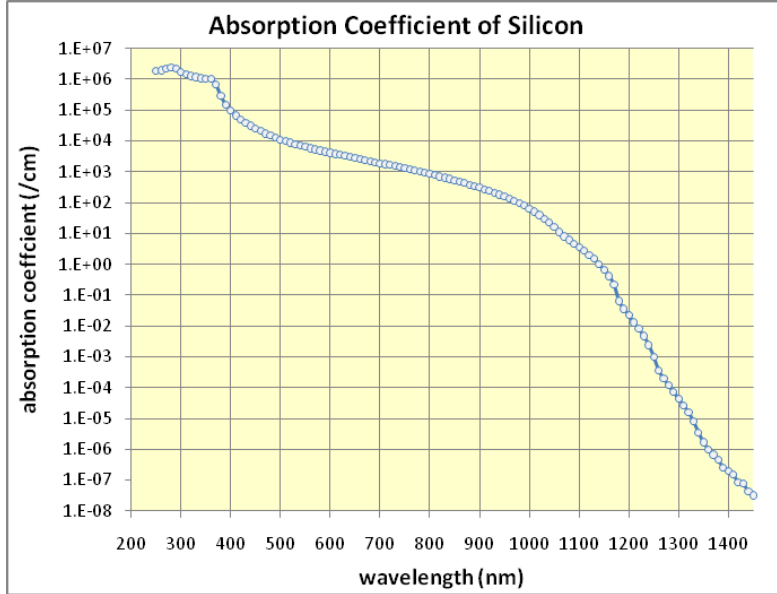


Figure 1.2: Absorption coefficient of silicon in cm^{-1} as a function of the wavelength at temperature of 300 K.

- Ultra high index contrast. Silicon has an refractive index around 3.45 while the refractive index of SiO_2 is only 1.45. This large index contrast allows very tight confinement of optical field in silicon waveguides. In other words, the waveguide cross section can be made very compact (hundreds of nanometer) without significant loss and the bend radius can also be quite tight ($< 5 \mu\text{m}$) without noticeable radiation loss. These features allow compact components and high integration density compared to other platforms
- Low loss. It is transparent for wavelength longer than $1.1 \mu\text{m}$ due to its large band-gap (around 1.1 eV) as evident in Fig. 1.2 [2]. And it can only guide light shorter than $4 \mu\text{m}$ due to the absorption of SiO_2 . This wavelength range covers the telecommunications bands used in fiber optic communications.
- Silicon is very sensitive to temperature variation. This is both a blessing and a curse. Due to the large thermo-optic coefficient ($1.8 \times 10^{-4}/\text{K}$), it's very efficient to use heaters to tune the optical properties of silicon photonics components. But at the same time, it makes silicon photonics very vulnerable to background temperature variation, which is a main source of noise, especially for resonant devices, where the light intensity is quite high to induce temperature change.

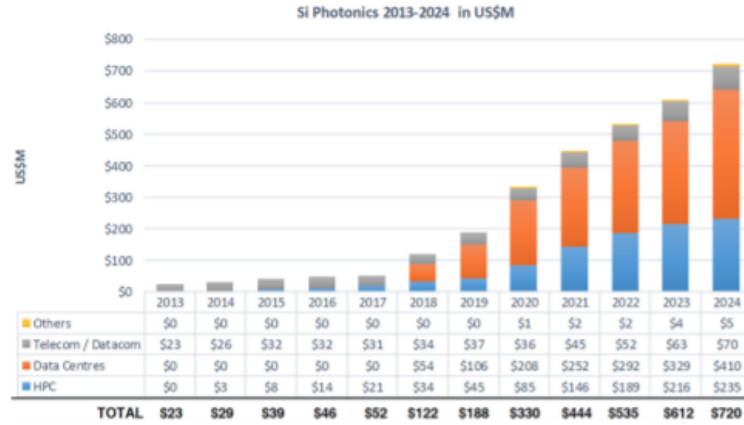


Figure 1.3: Silicon photonics 2013–2024 market forecast. Source: Silicon Photonics Report—Yole Development; Yole: 'Emerging optical data centers from big Internet companies (Google, Facebook, ...) will be triggering the market growth in 2018....'

The first proposal to use silicon as the material to demonstrate on-chip optical functionalities can be traced back to the 1980s. Richard Soref and Klaus Petermann pioneered in this field with their work on silicon waveguides and switches [3–6]. The past decade witnessed the explosive growth of silicon photonics, especially in the industrial field. Silicon photonics is a disruptive technology in applications like data centers, coherent communications and high performance computing (HPC) [7–10], some giant companies including Intel, Cisco, Mellanox, Facebook, have invested huge sources to develop silicon photonics as an enabling technology for those applications, and they start to massively deploy silicon photonics products like 100 Gbs optical transceiver modules. The market forecast for silicon photonics in Fig. 1.3 shows that the total market volume of silicon photonics will grow to almost 200 million USD in 2019.

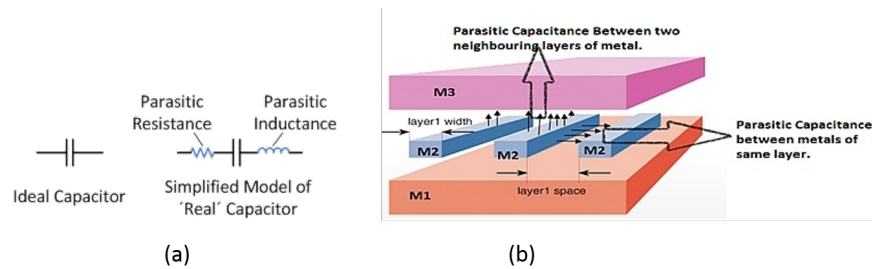


Figure 1.4: A brief illustration of the potential parasitics of a capacitor(a) and parasitic capacitance in electronics integrated circuits(b).

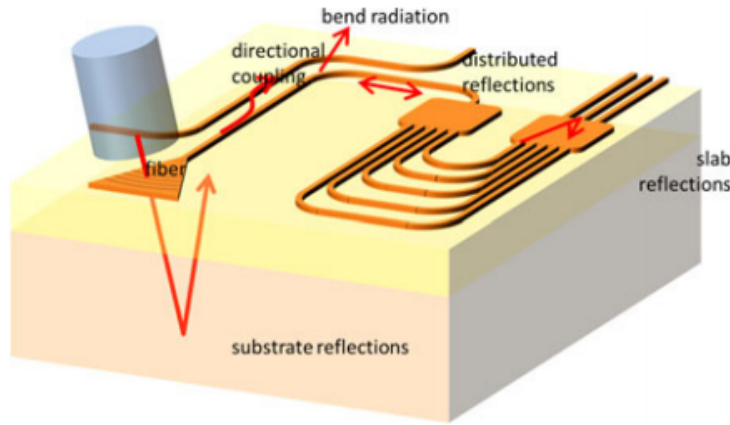


Figure 1.5: An example figure showing different kinds of parasitics in PICs from Ref. [11]. This broad diversity imposes difficulty and complexity in studying and modelling parasitics in PICs compared to those in EICs.

1.2 Parasitics in silicon photonics

Along with the rapid development of silicon photonics, there are still some remaining issues to be modelled or solved. Parasitics is one of them. Parasitics refer to those unintended effects in a circuit or system [12–14]. In electronic integrated circuits (EICs), they appear as resistance, capacitance and inductance, which have already been in-depth studied and perfectly modelled [15, 16]. Fig. 1.4 gives an example of parasitics of a capacitor and parasitic capacitance between metal layers in a simplified circuit. A good understanding and model of those parasitics are vital especially for large scale integrated circuits. Without taking them into consideration, the fabricated circuits might show deviated or unpredictable performance compared with design. Parasitics become more and more performance limiting with increasing integration density [17]. Nowadays, even if PICs are not yet having similar integration density as EICs, the parasitics start to attract attention due to three reasons:

- The difference between photonics parasitics and electronics parasitics. Parasitics in PICs are much more complicated and diverse than those in EICs. They are not so standardized that they can be simply divided into a couple of categories (like resistance, capacitance and inductance in EICs). The potential parasitics in PICs include but are not limited to: bend losses, bend induced mode conversion, substrate leakage, coupling from substrate leakage to other part of the circuit, spurious reflections, roughness induced backscattering, unwanted coupling between logically not coupled waveguides, radi-

ation that might be accidentally captured by other components etc. [11, 18] A brief illustration of some photonics parasitics are given in Fig. 1.5. Moreover, usually the parasitics in EICs only act over short range, for instance, the parasitic capacitance only takes place between adjacent transistors. While parasitics in PICs happen over long range, even between distant parts of a chip.

Effects mentioned above are just examples of linear parasitics. If nonlinearities are considered, the parasitic library can be expanded significantly including nonlinear absorption, thermally induced index change, self phase modulation etc. Moreover, the nature of coherence of light makes parasitics worse and more complicated to model in PICs as the light can be constructively or destructively interfered. So far only some of those parasitics have attracted attention to some extent, and only in an independent way instead of global modelling and standardization. All these difficulties require that the parasitics in PICs should be systematically studied as early as possible, for us to be well prepared for large scale PICs.

- Unlike EICs, where parasitics can be safely ignored when a circuit only contains a few components, even a few integrated optical components can suffer significantly from parasitics. For instance, the most fundamental building blocks in PICs, namely waveguides, can deviate from their ideal performance drastically due to sidewall roughness induced backscattering [19–23]. Our research found that centimeter long silicon waveguides behave like random cavities instead of a wavelength-independent guiding channel [21, 22]. This has been so far ignored and will cause serious problems for optical circuits using long waveguides, for instance, optical sensors, delay lines, reservoir computing based on long spiral waveguides and so on. Another example is silicon ring resonators. We will discuss in chapter 3 about how strongly the parasitic reflection inside a ring resonator can distort its spectrum and cause problems for circuits that use ring resonators [24–29]. Also literature reports that parasitics will degrade performance of devices like Mach-Zehnder-Modulators (MZM), Multi-Mode-Interferometers (MMI), arrayed-waveguide-gratings (AWG), Fabry-Perot cavities (FP) and so on [30–33].
- With the rapid growing of silicon photonics, large scale PIC in silicon photonics may be just around the corner. Many groups are now dedicated to design and fabricate complicated PICs with thousands of optical components. Researchers at MIT, UC Berkeley and Colorado Boulder gave the first demonstration of an on-chip interconnection circuit to communicate optically between processor and memories as exhibited in Fig. 1.6 [34]. This heralds the future of photonics processors. Sun et.al. successfully imple-

mented a large-scale nanophotonic phased array with 64×64 (4096) optical nanoantennas [35]. And our group is also working hard on the way of designing robust and programmable PICs where light will be distributed into tens or hundreds of pathways as shown in Fig. 1.7. Moreover, the integration of PICs with other technologies are also emerging. For instance, the existence of MEMS components or circuits on PICs have been intensively evaluated [36–38].

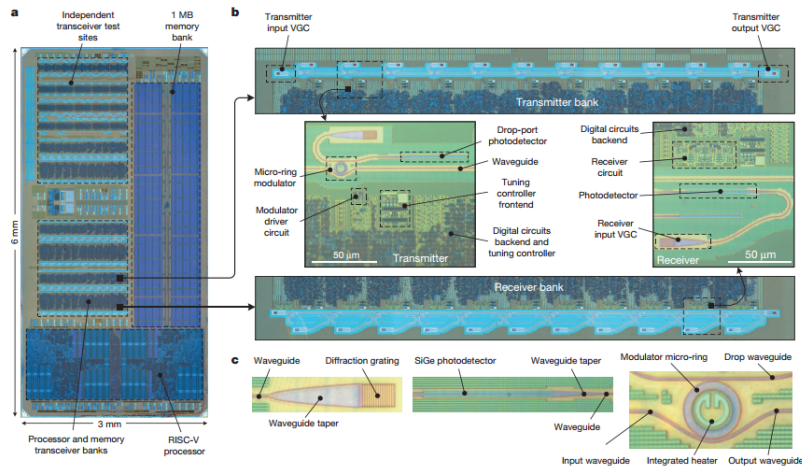


Figure 1.6: The full circuit with both EICs and PICs on a chip in Ref. [34]. This circuit contains 70 million transistors and 850 photonic components.

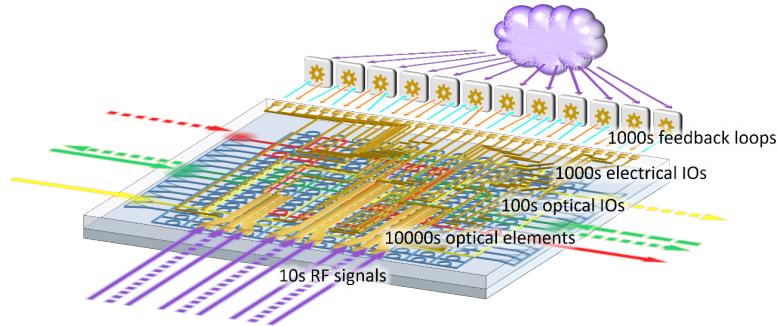


Figure 1.7: One of our group's project to utilize thousands of photonic components on chip to provide re-configurable and robust PICs.

In chapter 2, we will present our study of some typical parasitics in silicon photonics, including spurious reflections, substrate leakage and coupling, radiation

loss and distributed backscattering etc.

1.3 Silicon ring resonators

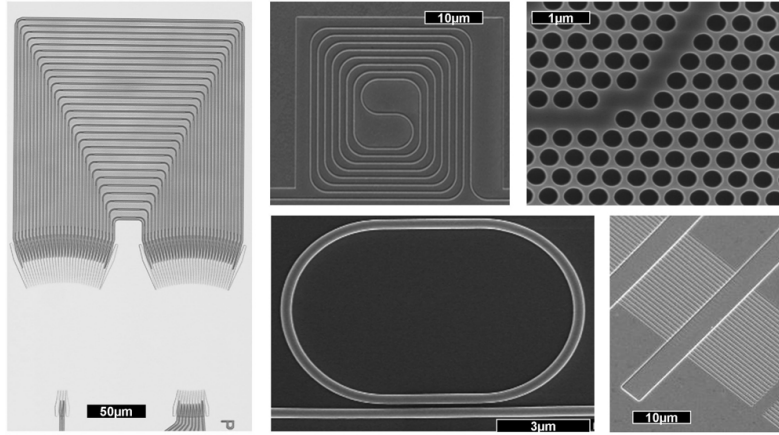


Figure 1.8: A couple of components in silicon photonics. Source: www.caliopa.com.

As a mature platform for PICs, there are many components developed in silicon photonics to enable various functionalities. Fig. 1.8 gives a couple of examples. Ring resonators are one of the most important building blocks. They can be used in various applications, including wavelength division multiplexing (WDM) filters, (de-)multiplexers, laser cavities, high speed modulators and switches in telecommunications and datacomms [39–43]. In bio-photonics field they are widely developed for high resolution sensors as the resonances of ring resonators are extremely sensitive to external environment change [44]. Microwave photonics also rely heavily on ring resonators to achieve efficient microwave generation or processing [45].

A comprehensive explanation of ring resonators is given in Ref. [46]. Briefly speaking, a ring resonator consists of a waveguide looped back to itself with one or two bus waveguide(s) next to it as shown in Fig. 1.9. Depending on the number of bus waveguides and thus the total ports of a ring resonator, it's named either all-pass ring resonator or add-drop ring resonator. Light injected to the in port of one bus waveguide will be partially coupled into the looped waveguide and partially coupled back to the bus waveguide after each roundtrip. Under the circumstances where the optical roundtrip of the looped waveguide equals multiple of wavelengths λ , there will be resonances. Thus a ring resonator supports numerous resonances. Resonances at the *pass* (or *through*) port are Lorentzian shaped notches while they appear as peaks at the *drop* port as plotted in Fig. 1.9. Ide-

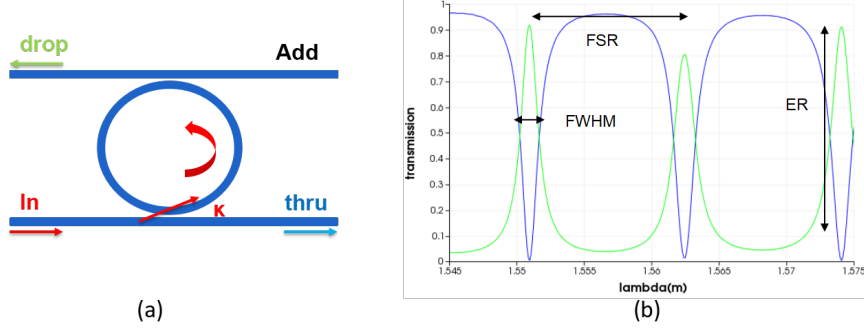


Figure 1.9: (a) presents a schematic of an add-drop ring resonator. When one of the two bus waveguides are removed, it's called all-pass ring resonator. (b) gives the ideal output spectra of such a ring resonator. Lorentzian shaped resonances at the pass and drop ports with no transmission and reflection at the add and in port, respectively.

ally there should exist no transmission to the *add* port and no reflection to the *in* port. The optical spacing between two resonances is defined as *free spectral range* (FSR), which is determined by the length of the looped waveguide following equation $FSR = \frac{\lambda^2}{n_g L}$, where λ is the resonance wavelength, n_g and L are the group index and physical length of the looped waveguide, respectively. The difference between the peak transmission and background transmission of one resonance is called *extinction ratio* (ER). Another parameter called *quality factor* (Q) is to evaluate how long light can be confined in such a resonator, mathematically it's defined as $Q = \frac{\lambda}{BW}$, where BW is the abbreviation for bandwidth, it can also be called *full-width-half-maximum* (FWHM).

Generally speaking, it's desirable to make all these three parameters as large as possible. Larger FSR allows more channels for ring resonator based WDM filters and (de-)multiplexers. It also means wider operation range of ring resonator based sensors and single mode laser cavities. High ER will give a large on-off contrast of ring modulators and de-multiplexers, thus low cross-talk of the communication channel. While large Q factor means a narrow resonance, which is beneficial for ring based sensors and laser cavities, even if at certain cases it is detrimental. For instance, high Q will limit the modulation speed of a ring based modulator. Moreover, ring resonators with larger Q factors will confine light for a longer time. This is very attractive for ring based nonlinear optics.

Silicon photonics as a platform for ring resonators has unique advantages and drawbacks compared to other platforms. It has a very large index contrast (3.45 for silicon and 1.45 for silicon dioxide) that enables good confinement of light even with very small waveguide cross-section. Thus ultra compact ring resonators are possible in silicon photonics. And this will facilitate ring resonators with large FSR, as it is inversely proportional to total length of a ring resonator. So far, there

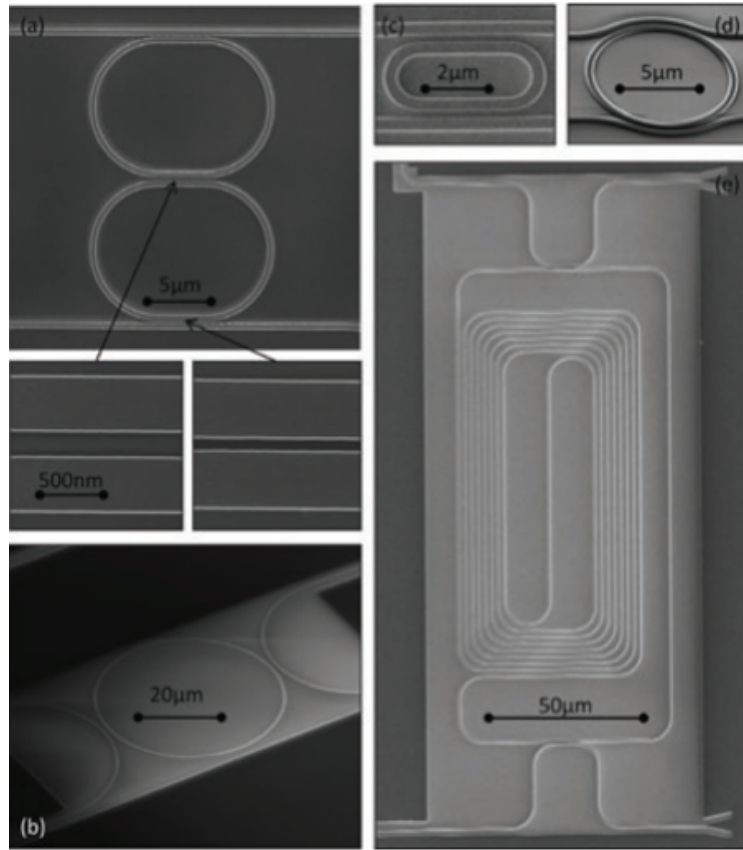


Figure 1.10: Figure from Ref. [46] showing some examples of silicon ring resonators. (a) Coupled ring resonators. (b) Circular ring resonators with symmetric coupling sections. (c) Racetrack ring resonators with extra straight coupling sections. (d) ring resonator with bend directional coupler for reduced wavelength dependency. (e) Ultra long spiral ring resonators.

exist only two degrees of freedom when design silicon ring resonators, namely coupling coefficient κ and total roundtrip length L . Ideally, they determine the performance indicators of a ring resonator, like FSR, ER and Q factor. However, in chapter 3 we will demonstrate that there exist another two factors that impact the outputs of ring resonators significantly, which are internal reflections and backcoupling. In chapters 4 and 5, we will propose our methods to manipulate the internal reflections, while in chapter 6, the methods to manipulate backcoupling will be introduced. Overall, we want to make these two factors as new degrees of freedom when designing silicon ring resonators.

1.4 Publications

1.4.1 International Journals

1. Yufei Xing, Domenico Spina, Ang Li, Tom Dhaene, and Wim Bogaerts. *Stochastic collocation for device-level variability analysis in integrated photonics*. Photonics Research, 4(2):93–100, 2016.
2. Ang Li, Qiangsheng Huang, and Wim Bogaerts. *Design of a single all-silicon ring resonator with a 150 nm free spectral range and a 100 nm tuning range around 1550 nm*. Photonics Research, 4(2):84–92, 2016.
3. Ang Li, Thomas Van Vaerenbergh, Peter De Heyn, Peter Bienstman, and Wim Bogaerts. *Backscattering in silicon microring resonators: a quantitative analysis*. Laser & Photonics Reviews, 10(3):420–431, 2016.
4. Ang Li and Wim Bogaerts. *Fundamental suppression of backscattering in silicon microrings*. Optics Express, 25(3):2092–2099, 2017.
5. Ang Li and W Bogaerts. *An actively controlled silicon ring resonator with a fully tunable Fano resonance*. APL Photonics, 2(9):096101, 2017.
6. Ang Li and Wim Bogaerts. *Experimental demonstration of a single silicon ring resonator with an ultra-wide FSR and tuning range*. Optics Letters, 42(23):4986–4989, Dec 2017.
7. Ang Li and Wim Bogaerts. *Tunable electromagnetically induced transparency in integrated silicon photonics circuit*. Optics express, 25(25):31688–31695, 2017.
8. Ang Li and Wim Bogaerts. *Manipulation of backcoupling in silicon ring resonator*. Photonics Research (accepted)
9. Ang Li and Wim Bogaerts. *Nonreciprocal transmission in silicon photonics by means of electromagnetically induced transparency*. In progress

10. Ang Li and Wim Bogaerts. *Power silicon ring resonators with novel degree of freedoms*. Laser & Photonics Reviews (In progress)

1.4.2 International conferences

1. Ang Li, Thomas Van Vaerenbergh, Peter De Heyn, Yufei Xing, Peter Bienstman, and Wim Bogaerts. *Experimentally demonstrate the origin for asymmetric resonance splitting and contributions from couplers to backscattering in SOI microrings*. In Advanced Photonics 2015, page IM2B.6. Optical Society of America, 2015.
2. Ang Li, Yufei Xing, and Wim Bogaerts. *A novel sensing scheme based on resonance splitting in silicon microrings*. In 20th Annual Symposium of the IEEE Photonics Society Benelux Chapter, pages 187–190, 2015.
3. Ang Li and Wim Bogaerts. *A simple and novel method to obtain an FSR free silicon ring resonator*. In Proceedings of SPIE: Silicon Photonics and Photonics Integrated Circuits V, volume 9891, pages 1–7, 2016.
4. Yufei Xing, Domenico Spina, Ang Li, Tom Dhaene, and Wim Bogaerts. *Variability analysis of device-level photonics using stochastic collocation (Conference Presentation)*. In SPIE Photonics Europe, pages 989117–989117. International Society for Optics and Photonics, 2016.
5. Yufei Xing, Ang Li, Raphaël Van Laer, Roel Baets, and Wim Bogaerts. *Backscatter Model for Nanoscale Silicon Waveguides*. In 24th International Workshop on Optical Wave & Waveguide Theory and Numerical Modelling (OWTNM 2016), 2016.
6. Ang Li, Yufei Xing, Raphaël Van Laer, Roel Baets, and Wim Bogaerts. *Extreme Spectral Transmission Fluctuations in Silicon Nanowires Induced by Backscattering*. In IEEE International Conference on Group IV Photonics, 2016.
7. Yufei Xing, Ang Li, Raphaël Van Laer, Roel Baets, and Wim Bogaerts. *Backscatter-induced transmission noise and length-dependent attenuation in silicon waveguides*. In Proceedings Symposium IEEE Photonics Society Benelux, pages 279–282, 2016.
8. Ang Li, Yufei Xing, and Wim Bogaerts. *An integrated tunable reflector*. In 19th European Conference on Integrated Circuits, 2017.
9. Ang Li and Wim Bogaerts. *Fundamentally cancel backscattering in silicon microrings*. In Lasers and Electro-Optics Europe & European Quantum Electronics Conference (CLEO/Europe-EQEC, 2017 Conference on), pages 1–1. IEEE, 2017.

10. Ang Li and Wim Bogaerts. *A novel approach to create a tunable Fano resonance with an extinction ratio over 40 dB*. In Group IV Photonics (GFP), 2017 IEEE 14th International Conference on, pages 27–28. IEEE, 2017.
11. Ang Li and Wim Bogaerts. *Engineered Reflections in Silicon Ring Resonator: A New Degree of Freedom for Design*. In Proceedings Symposium IEEE Photonics Society Benelux, 2017.

References

- [1] Ashim Dhakal, Pieter C Wuytens, Frédéric Peyskens, Karolien Jans, Nicolas Le Thomas, and Roel Baets. *Nanophotonic waveguide enhanced Raman spectroscopy of biological submonolayers*. ACS Photonics, 3(11):2141–2149, 2016.
- [2] Martin A Green and Mark J Keevers. *Optical properties of intrinsic silicon at 300 K*. Progress in Photovoltaics: Research and Applications, 3(3):189–192, 1995.
- [3] Richard Soref and J Lorenzo. *All-silicon active and passive guided-wave components for $\lambda = 1.3$ and $1.6 \mu\text{m}$* . IEEE Journal of Quantum Electronics, 22(6):873–879, 1986.
- [4] Richard A Soref and Brian R Bennett. *Kramers-Kronig analysis of electro-optical switching in silicon*. In Integrated Optical Circuit Engineering IV, volume 704, pages 32–38. International Society for Optics and Photonics, 1987.
- [5] B Schuppert, J Schmidtchen, and K Petermann. *Optical channel waveguides in silicon diffused from GeSi alloy*. Electronics Letters, 25(22):1500–1502, 1989.
- [6] Richard A Soref, Joachim Schmidtchen, and Klaus Petermann. *Large single-mode rib waveguides in GeSi-Si and Si-on-SiO₂/sub 2*. IEEE Journal of Quantum Electronics, 27(8):1971–1974, 1991.
- [7] Yurii A Vlasov. *Silicon CMOS-integrated nano-photonics for computer and data communications beyond 100G*. IEEE Communications Magazine, 50(2), 2012.
- [8] Dessislava Nikolova, Sébastien Rumley, David Calhoun, Qi Li, Robert Hendry, Payman Samadi, and Keren Bergman. *Scaling silicon photonic switch fabrics for data center interconnection networks*. Optics express, 23(2):1159–1175, 2015.
- [9] Po Dong, Xiang Liu, S Chandrasekhar, Lawrence L Buhl, Ricardo Aroca, and Young-Kai Chen. *Monolithic silicon photonic integrated circuits for compact 100 Gbs coherent optical receivers and transmitters*. IEEE Journal of Selected Topics in Quantum Electronics, 20(4):1–8, 2014.
- [10] Marc A Taubenblatt. *Optical interconnects for high-performance computing*. Journal of Lightwave Technology, 30(4):448–457, 2012.

- [11] Wim Bogaerts, Martin Fiers, and Pieter Dumon. *Design challenges in silicon photonics*. IEEE Journal of Selected Topics in Quantum Electronics, 20(4):1–8, 2014.
- [12] Freddy Magnussen and Heinz Lendenmann. *Parasitic effects in PM machines with concentrated windings*. IEEE transactions on industry applications, 43(5):1223–1232, 2007.
- [13] B Puers, E Peeters, Aa Van Den Bossche, and Willy Sansen. *A capacitive pressure sensor with low impedance output and active suppression of parasitic effects*. Sensors and Actuators A: Physical, 21(1-3):108–114, 1990.
- [14] Y Michalakis and ME Hochberg. *Parasitic effects on host life-history traits: a review of recent studies*. Parasite, 1(4):291–294, 1994.
- [15] Do W Baker and EA Herr. *Parasitic effects in microelectronic circuits*. IEEE Transactions on electron devices, 12(4):161–167, 1965.
- [16] Duy-Phach Vu and Ngwe K Cheong. *Reduction of parasitic effects in floating body mosfets*, November 26 1996. US Patent 5,578,865.
- [17] William H Kao, Chi-Yuan Lo, Mark Basel, and Raminderpal Singh. *Parasitic extraction: Current state of the art and future trends*. Proceedings of the IEEE, 89(5):729–739, 2001.
- [18] Daniele Melati, Francesco Morichetti, Gian Guido Gentili, and Andrea Melloni. *Optical radiative crosstalk in integrated photonic waveguides*. Optics letters, 39(13):3982–3985, 2014.
- [19] Francesco Morichetti, Antonio Canciamilla, and Andrea Melloni. *Statistics of backscattering in optical waveguides*. Optics letters, 35:1777–1779, 2010.
- [20] Francesco Morichetti, Antonio Canciamilla, Carlo Ferrari, Matteo Torregiani, Andrea Melloni, and Mario Martinelli. *Roughness induced backscattering in optical silicon waveguides*. Physical Review Letters, 104(January):1–4, 2010.
- [21] Ang Li, Yufei Xing, Raphaël Van Laer, Roel Baets, and Wim Bogaerts. *Extreme spectral transmission fluctuations in silicon nanowires induced by backscattering*. In Group IV Photonics (GFP), 2016 IEEE 13th International Conference on, pages 160–161. IEEE, 2016.
- [22] Y. Xing, A. Li, R. Van Laer, R. Baets, and W. Bogaerts. *Backscattering induced transmission noise and length dependent attenuation in silicon waveguides*. In Proceedings of the 21th Annual Symposium of the IEEE Photonics Society Benelux Chapter, 2016.

- [23] Bo Peng, Jessie Rosenberg, Wesley D Sacher, Asger S Jensen, Marwan Khater, William MJ Green, and Tymon Barwicz. *Distributed backscattering in production O-band Si nanophotonic waveguides*. Optics Express, 25(19):23477–23485, 2017.
- [24] F. Morichetti, a. Canciamilla, M. Martinelli, a. Samarelli, R. M. De La Rue, M. Sorel, and a. Melloni. *Coherent backscattering in optical microring resonators*. Applied Physics Letters, 96(May):13–15, 2010.
- [25] G C Ballesteros, J Matres, J Mart, and C J Oton. *Characterizing and modeling backscattering in silicon microring resonators*. Optics Express, 19(25):24980–24985, 2011.
- [26] B E Little, J P Laine, and S T Chu. *Surface-roughness-induced contradirectional coupling in ring and disk resonators*. Optics letters, 22:4–6, 1997.
- [27] Sam Werquin, Steven Verstuyft, and Peter Bienstman. *Integrated interferometric approach to solve microring resonance splitting in biosensor applications*. Optics express, 21(14):16955–16963, 2013.
- [28] K Iwatsuki, Kazuo Hotate, and Minoru Higashiguchi. *Effect of Rayleigh backscattering in an optical passive ring-resonator gyro*. Applied Optics, 23(21):3916–3924, 1984.
- [29] TJ Kippenberg, SM Spillane, and KJ Vahala. *Modal coupling in traveling-wave resonators*. Optics letters, 27(19):1669–1671, 2002.
- [30] Emil Kleijn, Meint K Smit, and Xaveer JM Leijtens. *Analysis of parasitic effects in PICs using circuit simulation*. In Proc. SPIE, volume 8781, page 878104, 2013.
- [31] Gayle Murdoch, Alexey Milenin, Christie Delvaux, Patrick Ong, Shibnath Pathak, Diedrik Vermeulen, Gunther Sterckx, Gustaf Winroth, Peter Verheyen, Guy Lepage, et al. *Advanced 300-mm waferscale patterning for silicon photonics devices with record low loss and phase errors*. In 17th Opto-Electronics and Communications Conference (OECC-2012), pages 15–16. IEEE, 2012.
- [32] Weiming Yao, Giovanni Gilardi, Meint K Smit, and Michael J Wale. *Performance degradation of integrated optical modulators due to electrical crosstalk*. Journal of Lightwave Technology, 34(13):3080–3086, 2016.
- [33] Giovanni Gilardi, Weiming Yao, Meint K Smit, and Micheal J Wale. *Observation of dynamic extinction ratio and bit error rate degradation due to thermal effects in integrated modulators*. Journal of Lightwave Technology, 33(11):2199–2205, 2015.

- [34] Chen Sun, Mark T Wade, Yunsup Lee, Jason S Orcutt, Luca Alloatti, Michael S Georgas, Andrew S Waterman, Jeffrey M Shainline, Rimas R Avizienis, Sen Lin, et al. *Single-chip microprocessor that communicates directly using light*. Nature, 528(7583):534–538, 2015.
- [35] Jie Sun, Erman Timurdogan, Ami Yaacobi, Ehsan Shah Hosseini, and Michael R Watts. *Large-scale nanophotonic phased array*. Nature, 493(7431):195, 2013.
- [36] Ming C Wu, Sangyoon Han, Tae Joon Seok, and Niels Quack. *Large-port-count MEMS silicon photonics switches*. In Optical Fiber Communications Conference and Exhibition (OFC), 2015, pages 1–3. IEEE, 2015.
- [37] Tae Joon Seok, Niels Quack, Sangyoon Han, Richard S Muller, and Ming C Wu. *Large-scale broadband digital silicon photonic switches with vertical adiabatic couplers*. Optica, 3(1):64–70, 2016.
- [38] Sangyoon Han, Tae Joon Seok, Niels Quack, Byung-Wook Yoo, and Ming C Wu. *Large-scale silicon photonic switches with movable directional couplers*. Optica, 2(4):370–375, 2015.
- [39] P. De Heyn, J. De Coster, P. Verheyen, G. Lepage, M. Pantouvaki, P. Absil, W. Bogaerts, J. Van Campenhout, and D. Van Thourhout. *Fabrication-Tolerant Four-Channel Wavelength-Division-Multiplexing Filter Based on Collectively Tuned Si Microrings*. Lightwave Technology, Journal of, 31(16):2785–2792, Aug 2013.
- [40] Kristof Vandoorne, Pauline Mechet, Thomas Van Vaerenbergh, Martin Fiers, Geert Morthier, David Verstraeten, Benjamin Schrauwen, Joni Dambre, and Peter Bienstman. *Experimental demonstration of reservoir computing on a silicon photonics chip*. Nature communications, 5, 2014.
- [41] Stephan Gulde, Asma Jebali, and Nikolaj Moll. *Optimization of ultrafast all-optical resonator switching*. Optics express, 13:9502–9515, 2005.
- [42] Qianfan Xu, Vilson R Almeida, and Michal Lipson. *Micrometer-scale all-optical wavelength converter on silicon*. Optics letters, 30:2733–2735, 2005.
- [43] Tao Chu, Nobuhide Fujioka, and Masashige Ishizaka. *Compact, lower-power-consumption wavelength tunable laser fabricated with silicon photonic-wire waveguide micro-ring resonators*. Optics express, 17:14063–14068, 2009.
- [44] Katrien De Vos, Irene Bartolozzi, Etienne Schacht, Peter Bienstman, and Roel Baets. *Silicon-on-Insulator microring resonator for sensitive and label-free biosensing*. Optics express, 15:7610–7615, 2007.

- [45] Haifeng Shao, Xiaoqing Jiang, Jianyi Yang, Yingtao Hu, Gunther Roelkens, and Hui Yu. *Photonic-Assisted Microwave Frequency Doubling based on Silicon Ring Modulator*. In IEEE Photonics Conference 2014, pages 222–223, 2014.
- [46] Wim Bogaerts, Peter De Heyn, Thomas Van Vaerenbergh, Katrien De Vos, Shankar Kumar Selvaraja, Tom Claes, Pieter Dumon, Peter Bienstman, Dries Van Thourhout, and Roel Baets. *Silicon microring resonators*. *Laser & Photonics Reviews*, 6(1):47–73, 2012.

2

Parasitics in Silicon Photonics Integrated Circuits

In this chapter, we will focus on some unwanted effects (usually problematic) in silicon photonics integrated circuits called parasitics, which are defined as "changes in behavior due to the connection/proximity of other components. Here, we will focus on some most important cases, including backreflections, backscattering, substrate leakage, radiative coupling etc. Their origins will be explained and their influences on the performance of waveguides and ring resonators will be comprehensively studied.

2.1 Grating coupler reflections

The introduction of parasitics and the importance to model them in silicon photonics have already been given in chapter 1. To provide a better understanding, here we present some experimental observations of circuits/components with parasitics and compare them with ideal cases. We start with a simple circuit as shown in Fig. 2.1(a). It just contains two grating couplers and one straight waveguide in between. The grating coupler is one of the most popular methods to couple light between fibers and optical chips as indicated in Fig. 2.1(b) [1]. Ideally it's considered to be a component with a relatively flat optical spectrum within certain bandwidth, and importantly without reflection. And a waveguide is believed to guide light without any wavelength dependency in its transmission spectrum.

So the ideal power transmission spectrum of such a circuit looks like a Gaussian-shape curve (or polynomial in log-scale). However, for short waveguides (shorter than 1 cm) we observe regular ripples with different periods and sharp fluctuations on top of this Gaussian-shape curve as also shown in Fig. 2.2.

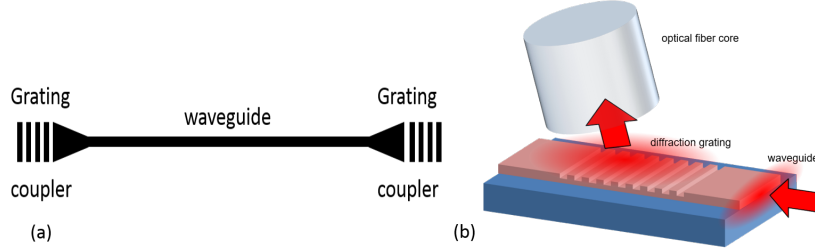


Figure 2.1: (a) shows a simple circuit with only two grating couplers and one waveguide. It already exhibits clear parasitics effects. (b) gives the brief illustration of how grating coupler can couple light between waveguides and fibers.

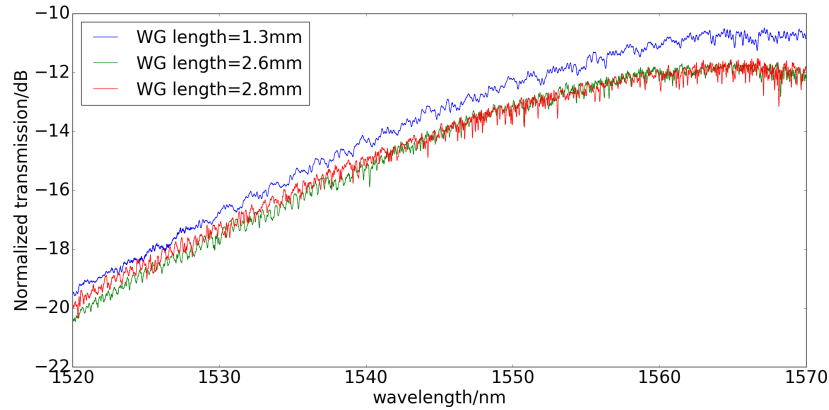


Figure 2.2: Measured transmission spectra of three circuits shown in Fig. 2.1 with different waveguide lengths, all shorter than 1 cm. They are spiral shaped waveguides with standard $450 \text{ nm} \times 220 \text{ nm}$ cross-section. All show certain degree of regular ripples and rapid fluctuations.

To analyze the contributions to the ripples and fluctuations, we performed a Fourier transform of the measured transmission spectrum. To understand the value of doing Fourier transform analysis of an optical transmission spectrum, we take a single Fabry-Perot cavity as an example. The conceptual schematic is shown in Fig. 2.3(a). It consists of two mirrors with certain reflectivity $R_1 = R_2 = R$ and a channel between them with loss τ^2 and physical length L_p . The transmission as a function of wavevector $k_0 = \frac{2\pi n_{eff}}{\lambda}$ can be mathematically represented as

equation (2.1) [2].

$$T(k_0) = \frac{(1 - R)^2 \tau^2}{(1 - R\tau^2)^2 + 4R\tau^2 \sin^2(k_0 L_p)} \quad (2.1)$$

Apparently, it shows a periodic feature as a function of k_0 , as evident in Fig. 2.3(b). The transmission contains a series of peaks periodically located with spacing of $\Delta k = \frac{\pi}{L_p}$. Alternatively, we can say that the transmission as a function of k_0 has a frequency of $\frac{L_p}{\pi}$. Therefore, we can use the optical length $L_o = L_p n_g$ as the measure for frequency in the Fourier transform of a transmission spectrum. A Fourier transform of such a transmission is given in equation (2.2) [2].

$$FT(L) = \int T(k) e^{j\pi L k} dk \quad (2.2)$$

If we plot its Fourier transform as a function of optical length, we get a series of peaks located at multiples of L_o as shown in Fig. 2.4. Each peak at mL_o corresponds with m roundtrips the light has travelled. So by looking at the Fourier transform of an optical transmission spectrum, we can retrieve the hidden cavities within a circuit by analyzing the locations of peaks. Note that, the peaks in the Fourier transform spectrum are ideally delta functions with ultra narrow widths if the measured optical spectrum is infinite (ultra wide span, from almost 0 μm til $\infty \mu m$). However, for a real case, the optical spectrum is usually tens of nanometers. As a consequence, the peaks at the Fourier transform spectrum show certain widths as illustrated in Fig. 2.4. This is easy to understand, as for a standard Fourier transform pair (time-frequency), the longer is the signal in time, the higher resolution will be achieved in its frequency (narrower peaks in its Fourier transform). Note that, the example is chosen to be a cavity, while in reality, an interference path between two signals can also lead to a peak in its Fourier transform. The interference can happen between two physical pathways, or two waveguide modes etc.

The Fourier transforms of the spectra in Fig. 2.2 are presented in Fig. 2.7. Obviously, for each circuit with different waveguide length there is a peak located at the optical length of the waveguide if we assume the group index to be around 4.4. These peaks indicate that the reflections happen at the grating couplers standing at two ends of the waveguides. We use our optical circuit simulator-Caphe [3] to do some simulations for the effects of grating couplers' reflections. Clearly shown in Fig. 2.5, by adding only 2% power reflectivity to each grating coupler, significant ripples already appears and the strengths of these ripples grow with grating coupler reflectivity as evident in Fig. 2.6. Now such a circuit becomes a Fabry-Perot cavity instead of a wavelength independent guiding channel.

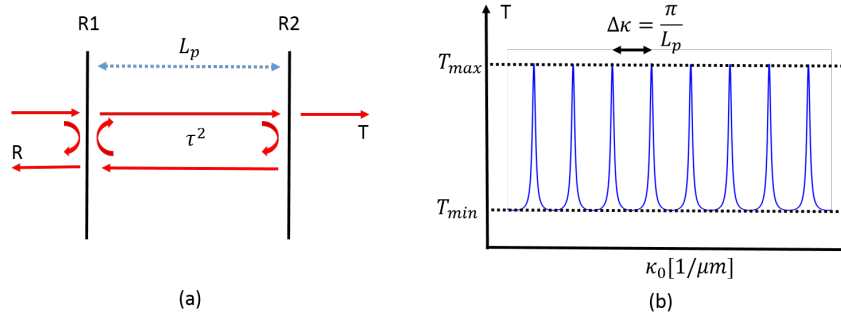


Figure 2.3: A Fabry-Perot cavity and its transmission spectrum. It consists of two mirrors with certain reflectivity and a channel between them with loss τ^2 and physical length L_p . The transmission spectrum as a function of the wavevector k shows periodically located peaks .

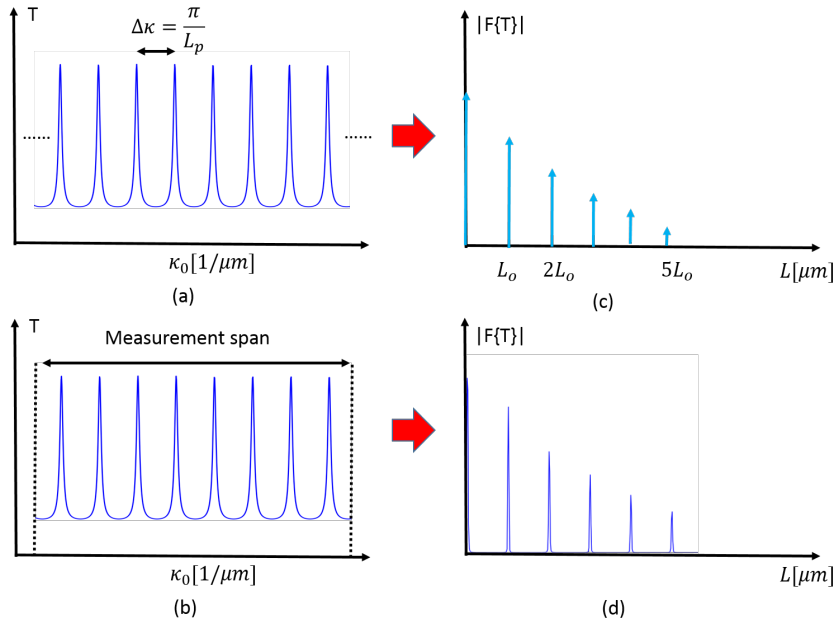


Figure 2.4: The Fourier transform of the transmission spectrum of a single Fabry-Perot cavity. It contains a series of peaks equally spaced with the period equaling the optical length of the cavity L_o . When the transmission spectrum is infinite (a), the peaks in the Fourier transform are delta functions (c). While if the transmission is measured within certain span (b), the peaks in the Fourier spectrum are broadened.

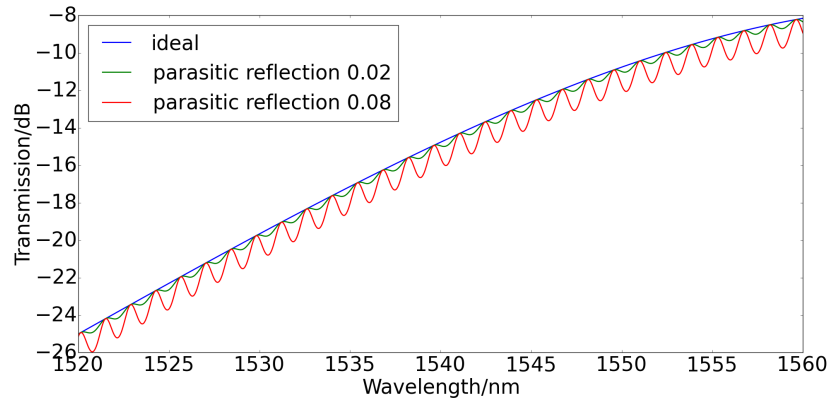


Figure 2.5: Simulated transmission spectra of circuits shown in Fig. 2.1 with and without parasitic reflections of the grating couplers. The parameters for the grating couplers' spectrum are extracted by fitting a real measurement.

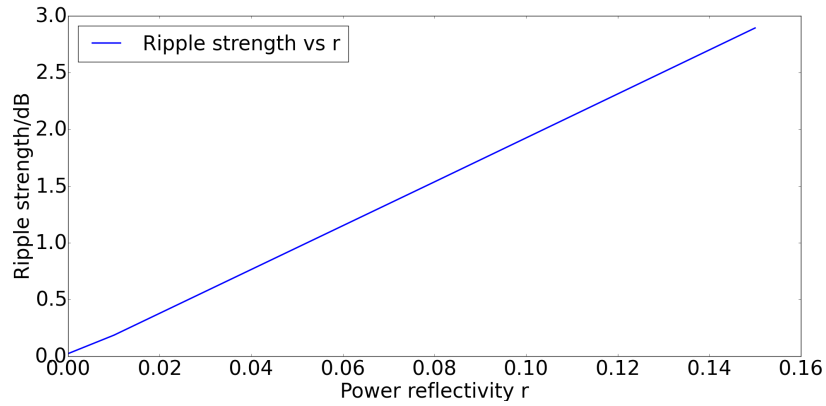


Figure 2.6: Ripple strength as a function of power reflectivity of the grating couplers. Ripple strength is defined as the extinction ratio of the ripples shown in Fig. 2.5.

2.2 Substrate leakage and coupling

Moreover, for all the three circuits, we can always observe a peak standing at 2.65 mm. Our first thought tells that this might be attributed to the substrate coupling, as the substrate silicon usually has a thickness between 700-800 μm with an index of 3.45. The mechanism can be explained in the following way: light from fiber entering the grating coupler might be partially guided to the substrate silicon (as evident in the FDTD simulation plotted in Fig. 2.8) and will be reflected again at the bottom of the substrate. Due to the roughness of the substrate bottom surface, the reflected light can propagate to many directions and be captured by other components on the chip as shown in Fig. 2.9.

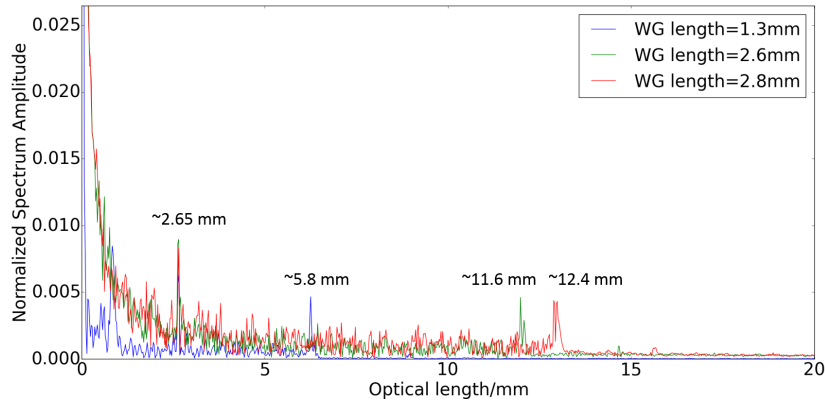


Figure 2.7: Fourier transforms of measured spectra in Fig. 2.2. Clearly, for each spectrum, there exists a peak standing at the optical length of the waveguide (the group index of a silicon strip waveguide is around 4.4). This indicates that the grating couplers introduce certain reflections. Moreover, for all the spectra there stand a peak located at around 2.65 mm. This matches well with the optical length of the substrate silicon, as it has a thickness between 700-800 μm and an index of 3.45.

To verify this, we performed a simple measurement. The schematic is given in Fig. 2.10 and the results are presented in Fig. 2.11. We align the input fiber well to the grating coupler while randomly move the output fiber somewhere distant enough from the output grating coupler. Still you could get as high as -35 dBm power transmission, which is only 30 dB lower than a waveguide transmission spectrum (laser output power is 4 dBm, setup loss is 3.5 dB, each grating coupler has a loss about 4 dB). And the spectrum exhibits similar shape with a waveguide transmission spectrum, meaning it is the spectrum of the grating coupler, which indicates that the input grating coupler plays a role in this parasitic light path. If we keep the output fiber aligned to the output grating coupler and move the input fiber away from the input grating coupler, you get a much lower transmission with

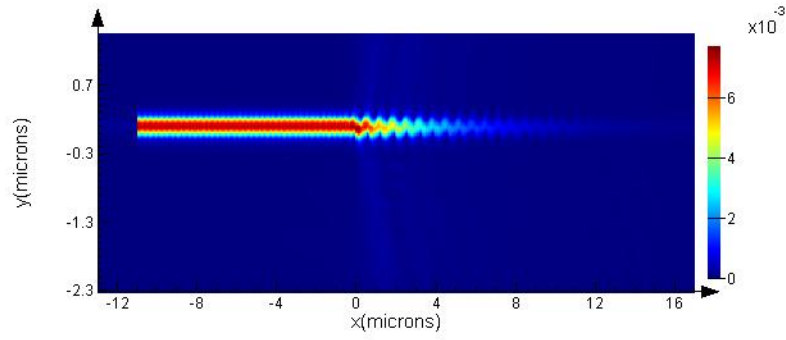


Figure 2.8: 2D simulation of a SOI grating coupler using Lumerical FDTD. Clearly, certain amount of light will be directed towards the substrate when it enters the grating coupler.

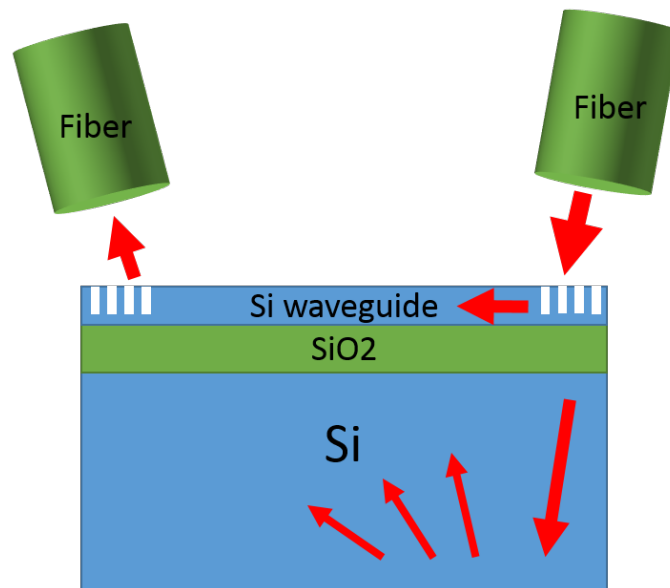


Figure 2.9: A brief illustration of the coupling from substrate leakage. This parasitic effect will contribute to the fluctuations in the transmission spectra of PICs.

stronger noise. This is reasonable as in our hypothesis, the input grating coupler helps the leakage to the substrate, without the input grating coupler, most of the light coming out of the input fiber will be reflected back at the silicon layer.

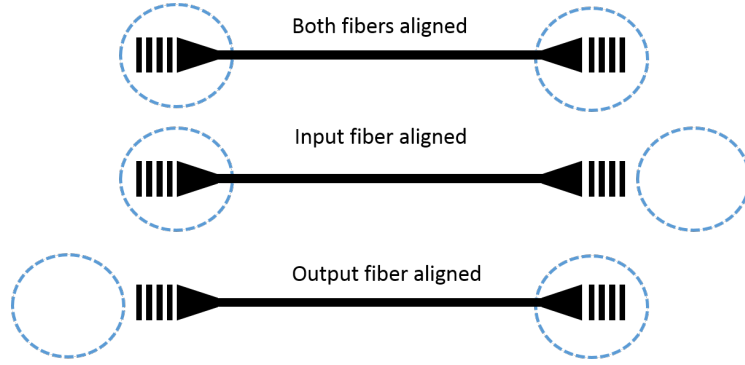


Figure 2.10: Illustration of the measurements performed to investigate the substrate leakage.

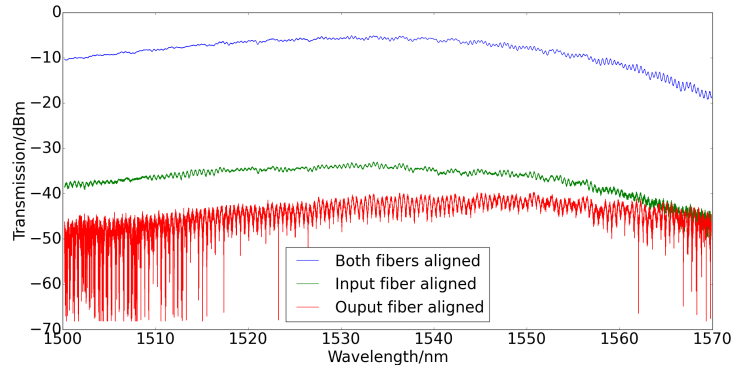


Figure 2.11: A simple measurement to investigate the substrate leakage and coupling. When only input fiber is aligned to the grating coupler while output fiber is away from the output grating coupler, there should not exist any light path between two fibers. But still high transmission is observed, only 30 dB lower than a normal waveguide transmission and it shows the grating coupler spectrum. When the output fiber is aligned and input fiber is away from the grating coupler, much lower transmission is measured with strong noise.

2.3 Radiation loss and Backscattering

The two kinds of parasitics mentioned above, namely grating couplers reflections and substrate coupling, only contribute to ripples with single and deterministic periods (a single peak in the Fourier transform spectrum gives a periodic signal with

single frequency). What is responsible for the rapid fluctuations in the transmission spectrum and those distributed peaks in the Fourier transform spectrum? The answer is sidewall roughness induced backscattering of the waveguide. Fig. 2.12 gives a SEM picture of a standard SOI waveguide fabricated at a mature CMOS fab. Clearly the sidewall exhibits roughness, which is inevitable based on current fabrication technology. It has been intensively studied in past years and the consequences of this sidewall roughness can be classified into two categories, that are extra loss and distributed stochastic backscattering [4–11].

2.3.1 Radiation loss

The extra loss is due to the coupling from the guided mode in the waveguide to those radiation modes caused by the perturbation of the roughness and it's called radiation loss. It has been theoretically studied and modelled by Payne and Lacey [12] and is believed to be the main loss source of current silicon waveguides fabricated at mature CMOS fab [6, 13] as the intrinsic loss of undoped silicon is very low for photon energies below its band gap ($\approx 1.1\text{eV}$) or wavelength longer than $1.1\text{ }\mu\text{m}$. Equation (2.3) gives an upper bound of the radiation loss caused by sidewall roughness [9, 14].

$$\alpha_r = \frac{gf\sigma^2}{\sqrt{2}k_0d^4n_{eff}} \quad (2.3)$$

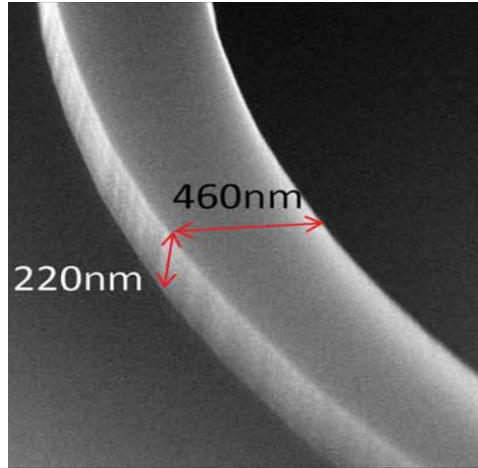


Figure 2.12: A SEM figure from Ref. [15] showing sidewall roughness of a standard strip waveguide on SOI substrate fabricated at a mature CMOS fab.

k_0 , d and n_{eff} are wavevector in vacuum, half width of the waveguide core and effective index of a silicon slab with the same thickness of the waveguide core, re-

spectively. Functions g and f present in this model help understand the impacts of waveguide parameters on this radiation loss. Their complete expressions can be found in Ref. [12, 16]. Briefly speaking, g purely depends on the waveguide geometry while f is related to the statistical distribution of the roughness (Gaussian, exponential etc.) with correlation length L_c included and it is also dependent on the waveguide geometry. It is usually in the same order of unity [12]. σ refers to the root-mean square of the roughness profile. Clearly, the most influential parameter is the waveguide core width. The scattering loss scales inversely proportionally to the forth power of d . For a silicon strip waveguide with 400 nm width and 200 nm thickness, a roughness with a root-mean square at 5 nm can generate 60 dB/cm loss [17], which is unacceptable to silicon PIC. Luckily, current CMOS technology usually generates a root-mean square smaller than 2 nm, corresponding with an upper bound of the scattering loss at 1.58 dB/cm [18], which is consistent with measured waveguide propagation loss at the level of 2 dB/cm or less. Silicon strip waveguides with overall losses smaller than 1 dB/cm have been reported [19].

This model provides a rigorous explanation of the radiation loss caused by sidewall roughness. But it's too complicated to be directly applied for engineering purpose. D.Melati et al. proposed a more straightforward model for radiation loss induced by sidewall roughness, which is given in equation (2.4) [9]:

$$\alpha_r = A \frac{\delta n_{eff}}{\delta w} \quad (2.4)$$

Here A is a factor that takes into account only the roughness standard deviation and correlation length while being independent on the slab width as long as it's far away from the mode cut-off. This so-called n_w model gives information on the "sensitivity" of the mode to the width variations produced by the sidewall roughness and consequently on the amount of power coupled out to the radiative modes. The good agreement between this model with the traditional model provided in equation (2.3) is shown in Fig. 2.13. It provides an easier understanding of the interaction between optical fields and sidewall roughness. A straightforward design rule about how to reduce the radiation loss by playing with waveguide geometry and its optical parameters (n_{eff} for instance) can be developed based on this model.

The consequence of extra loss brought by sidewall roughness has been discussed. However with our research on silicon waveguides going on, we start to realize that the influence of sidewall roughness on the transmission is more complicated, which we will comprehensively discuss in chapter 3.

2.3.2 Backscattering

Besides the extra radiation loss, another consequence of sidewall roughness is the stochastic backscattering. Logically speaking, sidewall roughness can be consid-

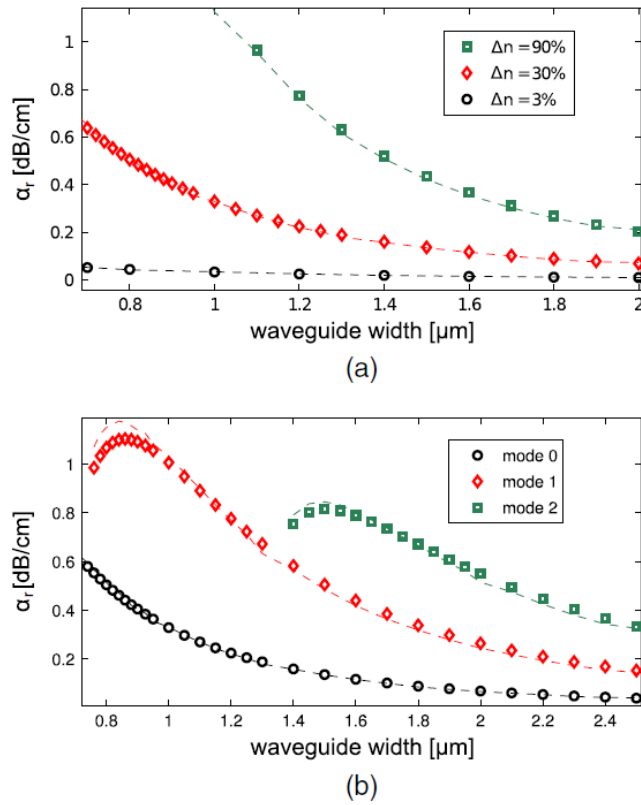


Figure 2.13: Figure from Ref. [9] shows the good agreement between the radiation loss predicted by the n_w model (dashed lines) and by the traditional model in equation (2.3) (dots). (a) provides the results of slabs with different index contrast and fixed roughness parameters ($\sigma = 2\text{nm}$, $L_c = 50\text{nm}$) and (b) gives the results of different modes of the slab with $\Delta n = 30\%$ ($\sigma = 2\text{nm}$, $L_c = 50\text{nm}$).

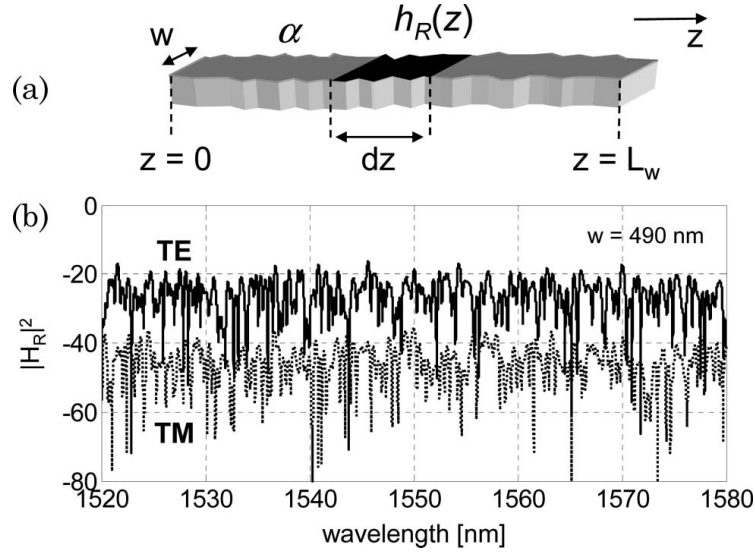


Figure 2.14: Measured reflection spectra from a standard strip waveguide using Optical Frequency Domain Reflectometry (OFDR) from Ref. [8]. The origin to the reflection is attributed to roughness induced backscattering and it shows stochastic nature in optical span with a relatively higher reflection for TE polarization than TM.

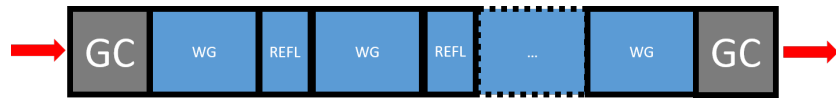


Figure 2.15: An optical circuit model built in Caphe with distributed backscattering included. The simulated results are plotted in Fig.2.16. WG refers to waveguide section, REFL represents reflector and GC stands for grating coupler.

ered as distributed lumped scatterers along the waveguide. The scatterers will scatter incoming light (forward propagating) to many directions. Directions that are outside the waveguide core can be considered as coupling to radiation modes, or radiation loss. While light can also be scattered backwards, this is the so-called backscattering. According to Ref. [7, 8, 20], the backscattering shows a stochastic nature in optical domain as shown in Fig.2.14, with a waveguide cross-section dependent and polarization dependent strength. According to Ref. [8], for TE polarization, the backscattering strength is 4.1 m^{-1} for 490 nm width and 12.8 m^{-1} for 350 nm width, which is reasonable as the narrower is the waveguide width, more sidewall roughness the light feels. While we observed a strength of $6\text{-}8 \text{ m}^{-1}$ for 450 nm wide waveguide [20], which is consistent with literature. By adding some distributed reflectors along the waveguide to model the backscattering as plotted in Fig. 2.15, we are able to get a simulated spectrum matching the measurement data better as illustrated in Fig. 2.16. Each lumped reflector is constant in reflectivity but random in phase to provide a good behavior model of distributed backscattering [21]. Ideally the placement of the distributed reflectors should follow the correlation length of the sidewall roughness and the reflectivity should be dependent on the root mean square of the sidewall roughness. Here it is just a quick demo to show the influence of backscattering.

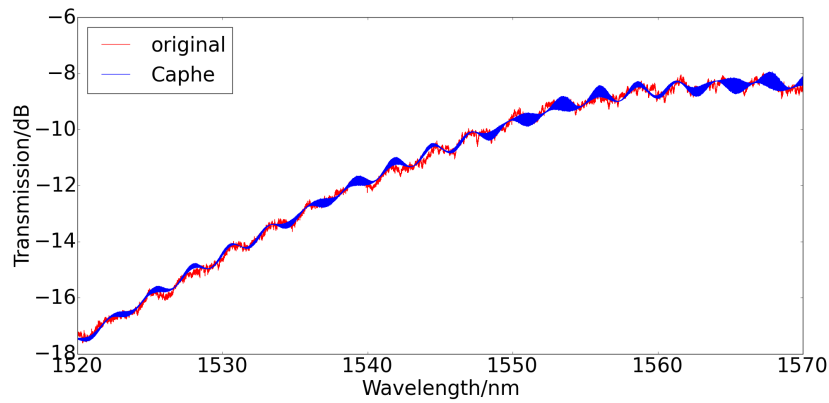


Figure 2.16: Circuit simulation of circuit shown in Fig. 2.1 with parasitic reflections at the grating coupler as well as distributed reflectors along the waveguide. When parasitic reflections of the grating coupler and waveguide sidewall roughness induced backscattering are included, we can get a good predictive simulation of the circuit transmission.

Here we'd like to provide some discussions about multiple factors that influence the effects induced by sidewall roughness to light, based on which potential solution towards backscattering insensitive devices can be developed.

- Platforms: The sidewall roughness is a bigger concern to high index con-

trast platforms like silicon photonics, as the electric field of the light will feel roughness more due to the ultra compact waveguide cross-section and consequently strong electric field discontinuity at the sidewall. Middle or low index contrast platforms like silica, silicon nitride and III-V have been reported to suffer much less from sidewall roughness [22–25]. Thus ultra low propagation loss waveguide and high Q resonator can be realized as backscattering is now the biggest loss source.

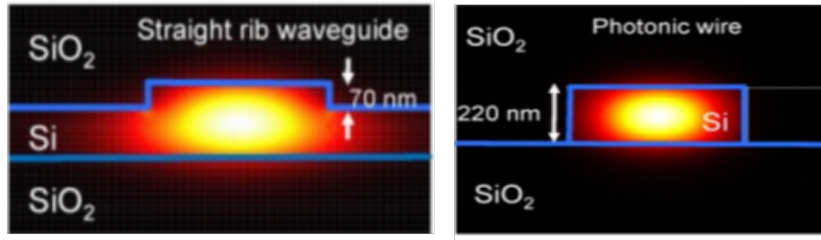


Figure 2.17: Simulated mode profile of a silicon rib waveguide and strip waveguide from Ref. [26]. The rib waveguide leads to a smaller overlap between optical mode and waveguide vertical sidewall.

- Waveguide cross-section: The principle is similar with platforms as they all determine the electric field profile at the sidewall. Given the standardized silicon thickness (220 nm), the way to manipulate cross-section is to change the width of strip waveguide or use rib waveguide. Narrower waveguide will lead to a weaker confinement thus stronger overlap between optical mode and sidewall roughness as evident in Fig. 2.17. That is why waveguides are usually tapered to a wider width in devices like AWG and long waveguide MZI sensors, which are very sensitive to phase errors [27–29]. This is because the effective index of a waveguide n_{eff} is very sensitive to waveguide core width w . $\frac{\Delta n_{eff}}{\Delta w}$ can be as large as $3 \times 10^{-3}/nm$ for light in fundamental TE polarization as shown in Fig. 2.18 [29]. And sidewall roughness can bring significant phase errors. Recent research reported in Ref. [30] shows that, the coherence lengths for single mode strip and rib waveguides in silicon photonics fabricated at mature CMOS fab are limited to around 4.17 mm and 1.61 mm respectively. Using broad waveguide is an effective method to reduce impacts of sidewall roughness. But broad waveguide will support multiple modes and raise the modal cross talk issue, so for bend sections, they are usually tapered back to standard 450 nm waveguide width to avoid higher mode activation. While the use of rib waveguides will also effectively reduce the overlap between optical mode and sidewall roughness. But it brings an issue of component footprint. For strip waveguide, the bend radius can be down to sub $5\text{-}\mu m$ without problem, while for rib waveguide,

it has to be larger than $20\mu\text{m}$ to avoid significant bend loss. Moreover, for rib waveguide there exists another issue that needs to be well controlled, namely etch depth. Variation in this parameter also significantly impacts the effective index as evident in Fig. 2.19 [30].

- **Polarization:** All the effects brought by sidewall roughness we mentioned above are about TE polarized mode by default, which is the most popular modes used in silicon photonics area. But using TM mode significantly reduces the effects of sidewall roughness by a factor of 35 [31]. This is due to the different direction of the electric field of different polarizations as evident in Fig. 2.20. For TE mode, electric field is resonating perpendicularly to the sidewall, while for TM mode, it's resonating parallel to the sidewall, resulting no discontinuity at the sidewall thus less field feels the roughness. Silicon ring resonators using TM mode have been successfully demonstrated with a Q factor over 300,000, almost 4 times of a TE ring resonator [32].

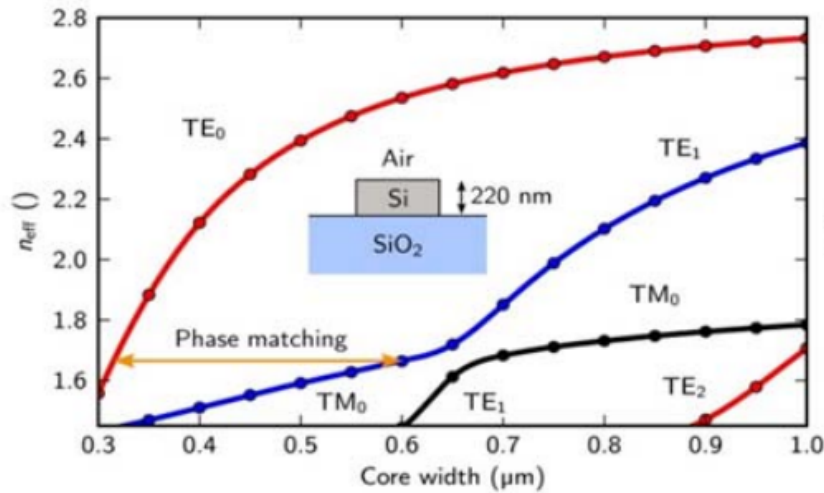


Figure 2.18: Simulated effective index of a silicon strip waveguide as a function of core width for different modes from Ref. [29].

2.4 Evanescent coupling

Another important form of parasitics is the potential evanescent coupling between two adjacent waveguides/elements, which are designed not to feel each other. The coupling can be triggered because that there is certain portion of electric field of the guided mode presenting outside the waveguide core and this tail can be

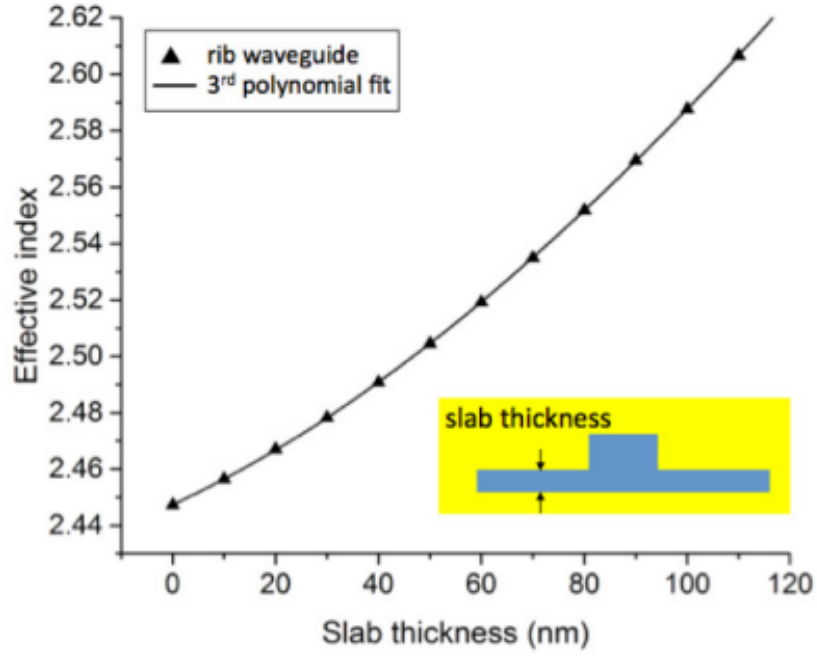


Figure 2.19: Simulated effective index of a silicon rib waveguide as a function of slab thickness or etch depth for TE polarization from Ref. [30].

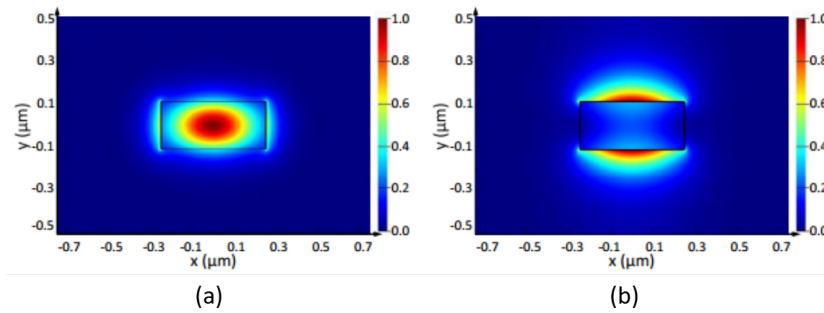


Figure 2.20: Simulated electric field distribution of TE polarization (a) and TM polarization (b) in a strip silicon waveguide. Clearly, due to the different resonant direction of the field, there is discontinuity at the vertical sidewall of TE polarization. While for TM light, it feels vertical sidewall much less.

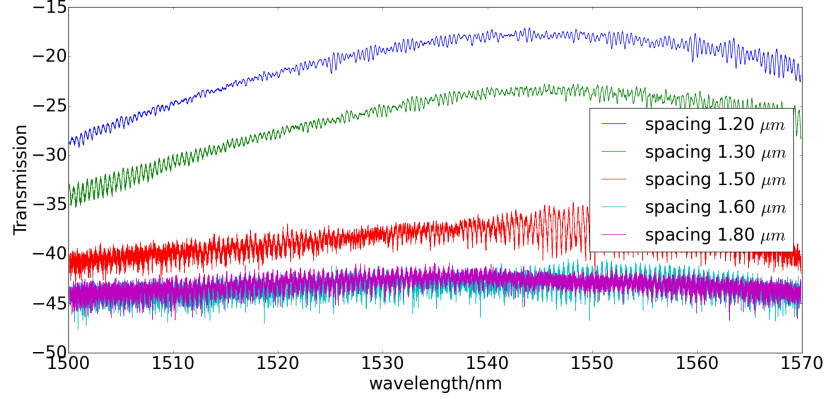


Figure 2.21: Measured coupling spectra of a series of parallel strip waveguides with same width of 450 nm fabricated at Imec. Results indicate that the minimum spacing between two waveguides can be 1.6 μm to avoid any coupling between them.

captured by nearby components when the phase matching condition is achieved. This effect is vital for large scale integrated optics as it determines the minimum safe distance between two components, which in turn sets an upper limit to the highest integration density of a PIC where waveguide arrays are widely employed, for instance, optical interconnect and phased arrays. It also sets certain limit on devices using arrayed waveguides like AWG and dense waveguide superlattice [28, 33].

Current experiments indicate that the waveguides need to be at least 4 μm spaced away in order to avoid low crosstalk at a single wavelength or tens of μm away for broad wavelength range [34, 35]. To study this, we designed a set of directional couplers with constant coupling length (400 μm) but varying spacing between their centers. The waveguides all have the same cross-section that is 450 nm width and 220 nm thickness fabricated at IMEC. The results plotted in Fig. 2.21 show that, coupling becomes negligible when spacing is larger than 1.6 μm . Note that our chip has no dioxide cladding, so for silicon dioxide protected structures the minimum safe spacing should be larger than 1.6 μm . This is also true for narrower waveguide as light will be less confined (more electric field outside core) thus easily coupled for both cases.

Meanwhile, we want to investigate the influence of the waveguide width on coupling as the key factor that matters is the phase matching between two waveguides. Phase matching is a fundamental concept to explain devices like directional couplers and it is also frequently used for some nonlinear effects like four-wave-mixing. Basically speaking, light is guided as mode in a waveguide and due to the difference in mode profile (for instance, confinement factor), each mode has its own propagation constant $\beta = \frac{2\pi n_{eff}}{\lambda}$. β is dependent on both wavelength of

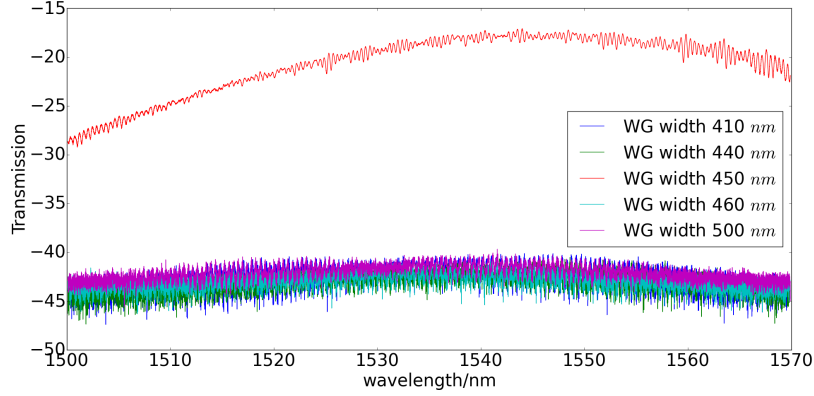


Figure 2.22: Measured coupling spectra of two parallel waveguides with different waveguide width and constant spacing of 1200 nm. One width is fixed to 450 nm while the other one is swept from 400 nm to 500 nm. Results show that only 10 nm change in the waveguide width lead to no coupling between them even their spacing is as low as 1200 nm.

the light as well as properties of the waveguide, including its geometry and material. This propagation constant, as its name suggests, plays an important role in the properties of light during its propagation as it determines the phase evolution during the propagation. If β doesn't change along the propagation direction, then the phase is a product of β and propagation length L . Ideally, modes in a waveguide are orthogonal to each other, which means no power transfer among them. However, when a perturbation is present, for instance, a side waveguide WG_b standing in parallel close enough to the original waveguide WG_a , the light in WG_a will start to feel WG_b and power exchange will gradually take place between these two waveguides. This is the basic concept of a directional coupler. And it can be modelled in a mathematical way based on coupled mode theory (CMT). According to Ref. [36–38], the two modes in two adjacent waveguides can be expressed as equations (2.5) and (2.6):

$$\frac{da_1}{dz} = -j\beta_1 a_1 + \kappa_{12} a_2 \quad (2.5)$$

$$\frac{da_2}{dz} = -j\beta_2 a_2 + \kappa_{21} a_1 \quad (2.6)$$

Where a_1 and a_2 are the electric field strengths of the two modes in each waveguide. β_x is the propagation constant of mode a_x . κ_{12} and κ_{21} refer to the coupling coefficients between the two modes. They are identical for linear and passive circuits and in following context they will be replaced with κ . z is the propagation distance in space. Note that these equations are only valid when $\kappa \ll \beta$, which

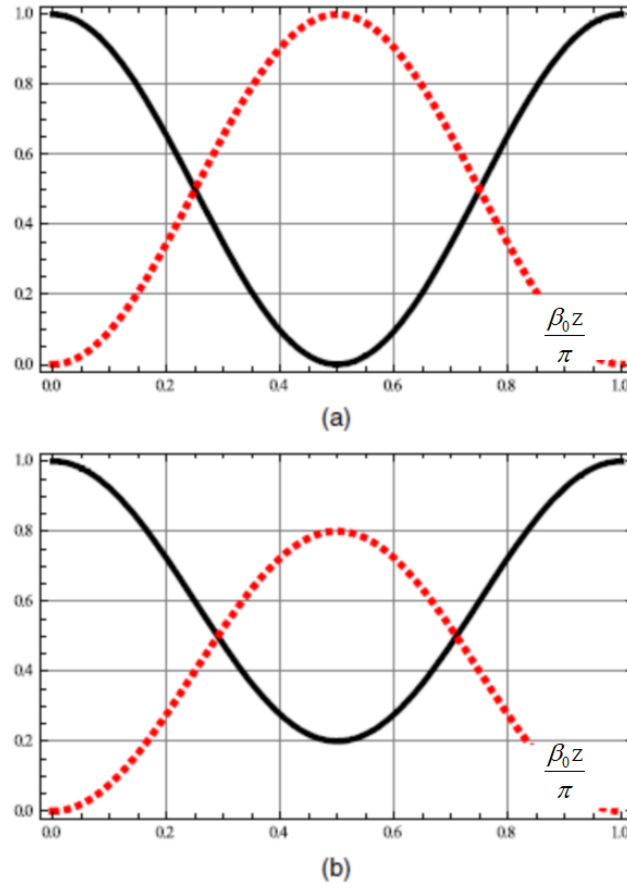


Figure 2.23: Power exchange between two waveguides as a function of propagation distance z . The curves are calculated based on equation (2.9). (a) shows the case of perfect phase matching $\delta = 0$. (b) gives the result when $\frac{\delta}{\kappa} = 0.5$.

is often the case for a typical directional coupler. If we start with 0 amplitude at the input of WG_2 ($a_2(z = 0) = 0$) and unit amplitude at the input of WG_1 ($a_1(z = 0) = 1$) we get following equation for a_2 :

$$a_2(z) = \frac{\kappa}{\beta_0} a_1(0) \sin(\beta_0 z) \exp(-j \frac{\beta_1 + \beta_2}{2} z) \quad (2.7)$$

$$\beta_0 = \sqrt{\delta^2 + \kappa^2} \quad (2.8)$$

Where $\delta = \frac{\beta_1 - \beta_2}{2}$ is the so-called phase mismatch factor between the two waveguides. Then after the propagation length L , the output power in WG_2 is:

$$P_2(L) = \frac{\kappa^2}{\kappa^2 + \delta^2} \sin^2(\sqrt{\kappa^2 + \delta^2} L) \quad (2.9)$$

Clearly, the maximum power transfer from WG_1 to WG_2 is limited by the factor phase mismatch factor δ as illustrated in Fig. 2.23. When $\delta = 0$, namely $\beta_1 = \beta_2$, the phase matching is met, a 100% power exchange can be achieved.

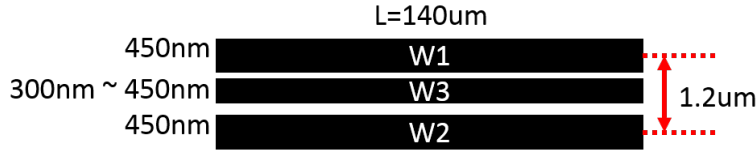


Figure 2.24: Another circuit consisting of 3 waveguides with 450 nm width at the boundary and a different width in the center. The spacing between W1 and W3 are fixed at 1.2 μm and the coupling length is 140 μm .

We also designed and measured another sets of similar devices. They have the same coupling length and varying spacing but one of the two waveguides has a different width than 450 nm. The measurements tell us that a 10 nm change in the waveguide width will significantly break the phase matching condition and lead to negligible coupling between them even at the spacing of 1200 nm. Knowing this fact will effectively reduce the footprint of integrated optics and arrayed waveguides based devices. Using mismatched waveguides to reduce cross-talk has now been widely adopted in dense waveguide superlattice [33].

Besides these normal directional coupler structures, we also performed some other related experiments to further study the coupling between waveguides. The circuits we measured are shown in Fig. 2.24. It contains three waveguides, with two outside ones having the same width, namely 450 nm, while the middle one's width is swept from 300 nm to 500 nm. The spacing between centers of two boundary waveguides are fixed at 1200 nm to limit the variables. We input light from one of the three ports and measured the transmission at each output. If we assume no

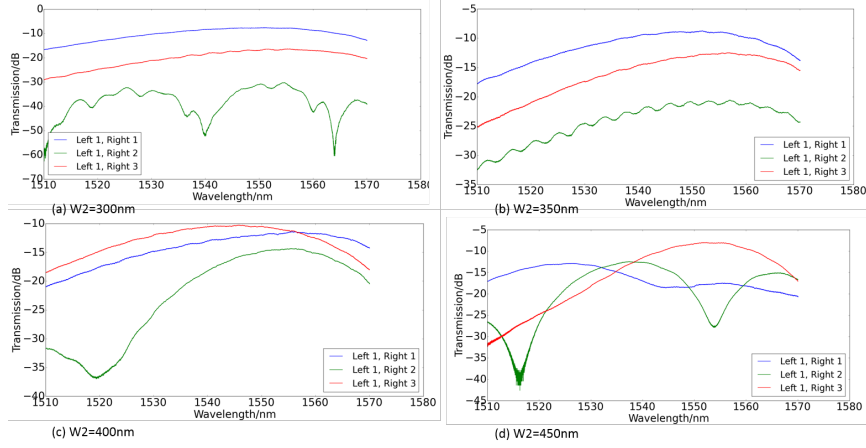


Figure 2.25: Measured spectra of circuits shown in Fig. 2.24 with different center waveguide widths. All show a strong coupling between W1 and W3 irrespective of the center waveguide width. But with increasing center waveguide width (thus smaller phase mismatch), the coupling becomes stronger.

coupling between WG1 (WG3) and WG2 due to the large phase mismatch, then naturally we would also expect no coupling between WG1 and WG3. However, when injecting light to WG1, we observed high transmission at WG3 irrespective of the center waveguide width as shown in Fig. 2.25. It seems that WG1 and WG3 can feel each other bypassing the "transparent" center waveguide as they are perfectly phase matched. And with the center waveguide width approaching 450 nm, the coupling between WG1 and WG3 also grows. This phenomenon imposes more attention when designing dense waveguide arrays but it can also be taken advantage of towards novel devices, for instance, novel three waveguide couplers and switches are theoretically proposed in Ref. [39].

2.5 Summary

In this chapter, we give an overview of some of the most popular forms of parasitics in silicon PICs, including lumped reflections, substrate leakage and coupling, stochastic backscattering, evanescent coupling, radiative coupling and loss etc. Their respective origins and impacts have been discussed in detail. However, this is just partial picture of the complete parasitics in silicon PICs. The diversity and complexity of the parasitics in photonics urge us to make a comprehensive research and systematic model of them as soon as possible in order to be well prepared to the large scale silicon PICs.

References

- [1] Diedrik Vermeulen, Yannick De Koninck, Yanlu Li, Emmanuel Lambert, Wim Bogaerts, Roel Baets, and Günther Roelkens. *Reflectionless grating couplers for Silicon-on-Insulator photonic integrated circuits*. Optics express, 20(20):22278–22283, 2012.
- [2] Wim Bogaerts. *Nanofotonische golfgeleiders en fotonische kristallen in Silicium-op-Isolator / Wim Bogaerts*. PhD thesis, Ghent University, 2004.
- [3] Martin Fiers, Thomas Van Vaerenbergh, Ken Caluwaerts, Dries Vande Ginste, Benjamin Schrauwen, Joni Dambre, and Peter Bienstman. *Time-domain and frequency-domain modeling of nonlinear optical components at the circuit-level using a node-based approach*. JOSA B, 29(5):896–900, 2012.
- [4] Pieter Dumon, Wim Bogaerts, Vincent Wiaux, Johan Wouters, Stephan Beckx, Joris Van Campenhout, Dirk Taillaert, Bert Luyssaert, Peter Bienstman, Dries Van Thourhout, et al. *Low-loss SOI photonic wires and ring resonators fabricated with deep UV lithography*. IEEE Photonics Technology Letters, 16(5):1328–1330, 2004.
- [5] Wim Bogaerts, Roel Baets, Pieter Dumon, Vincent Wiaux, Stephan Beckx, Dirk Taillaert, Bert Luyssaert, Joris Van Campenhout, Peter Bienstman, and Dries Van Thourhout. *Nanophotonic waveguides in silicon-on-insulator fabricated with CMOS technology*. Journal of Lightwave Technology, 23(1):401–412, 2005.
- [6] Kuan Pei Yap, André Delâge, Jean Lapointe, Boris Lamontagne, Jens H Schmid, Philip Waldron, Barry A Syrett, and Siegfried Janz. *Correlation of scattering loss, sidewall roughness and waveguide width in silicon-on-insulator (SOI) ridge waveguides*. Journal of Lightwave Technology, 27(18):3999–4008, 2009.
- [7] Francesco Morichetti, Antonio Canciamilla, Carlo Ferrari, Matteo Torregiani, Andrea Melloni, and Mario Martinelli. *Roughness induced backscattering in optical silicon waveguides*. Physical Review Letters, 104(January):1–4, 2010.
- [8] Francesco Morichetti, Antonio Canciamilla, and Andrea Melloni. *Statistics of backscattering in optical waveguides*. Optics letters, 35:1777–1779, 2010.
- [9] Daniele Melati, Andrea Melloni, and Francesco Morichetti. *Real photonic waveguides: guiding light through imperfections*. Advances in Optics and Photonics, 6(2):156–224, 2014.

- [10] Y. Xing, A. Li, R. Van Laer, R. Baets, and W. Bogaerts. *Backscattering induced transmission noise and length dependent attenuation in silicon waveguides*. In Proceedings of the 21th Annual Symposium of the IEEE Photonics Society Benelux Chapter, 2016.
- [11] Bo Peng, Jessie Rosenberg, Wesley D Sacher, Asger S Jensen, Marwan Khater, William MJ Green, and Tymon Barwicz. *Distributed backscattering in production O-band Si nanophotonic waveguides*. Optics Express, 25(19):23477–23485, 2017.
- [12] FP Payne and JPR Lacey. *A theoretical analysis of scattering loss from planar optical waveguides*. Optical and Quantum Electronics, 26(10):977–986, 1994.
- [13] Kevin K Lee, Desmond R Lim, Hsin-Chiao Luan, Anuradha Agarwal, James Foresi, and Lionel C Kimerling. *Effect of size and roughness on light transmission in a Si/SiO₂ waveguide: Experiments and model*. Applied Physics Letters, 77(11):1617–1619, 2000.
- [14] Siegfried Janz. *Silicon-based waveguide technology for wavelength division multiplexing*. Silicon Photonics, pages 2000–2000, 2004.
- [15] Wim Bogaerts and SK Selvaraja. *Compact single-mode silicon hybrid rib/strip waveguide with adiabatic bends*. IEEE Photonics Journal, 3(3):422–432, 2011.
- [16] JPR Lacey and FP Payne. *Radiation loss from planar waveguides with random wall imperfections*. IEE Proceedings J-Optoelectronics, 137(4):282–288, 1990.
- [17] Koji Yamada. *Silicon photonic wire waveguides: fundamentals and applications*. In Silicon Photonics II, pages 1–29. Springer, 2011.
- [18] F Grillot, L Vivien, S Laval, D Pascal, and E Cassan. *Size influence on the propagation loss induced by sidewall roughness in ultrasmall SOI waveguides*. IEEE Photonics Technology Letters, 16(7):1661–1663, 2004.
- [19] Jaime Cardenas, Carl B Poitras, Jacob T Robinson, Kyle Preston, Long Chen, and Michal Lipson. *Low loss etchless silicon photonic waveguides*. Optics express, 17(6):4752–4757, 2009.
- [20] Ang Li, Thomas Vaerenbergh, Peter Heyn, Peter Bienstman, and Wim Bogaerts. *Backscattering in silicon microring resonators: a quantitative analysis*. Laser & Photonics Reviews, 10(3):420–431, 2016.

- [21] Antonio Canciamilla, Matteo Torreggiani, Carlo Ferrari, Francesco Morichetti, Raffaella Costa, and Andrea Melloni. *Backscatter in integrated optical waveguides and circuits*. In Proc. SPIE, volume 7218, page 72180N, 2009.
- [22] Ehsan Shah Hosseini, Siva Yegnanarayanan, Amir Hossein Atabaki, Mohammad Soltani, and Ali Adibi. *High quality planar silicon nitride microdisk resonators for integrated photonics in the visiblewavelength range*. Optics express, 17(17):14543–14551, 2009.
- [23] Alexander Gondarenko, Jacob S Levy, and Michal Lipson. *High confinement micron-scale silicon nitride high Q ring resonator*. Optics express, 17(14):11366–11370, 2009.
- [24] AZ Subramanian, Pieter Neutens, Ashim Dhakal, Roelof Jansen, Tom Claes, Xavier Rottenberg, Frédéric Peyskens, Shankar Selvaraja, Philippe Helin, Bert Du Bois, et al. *Low-loss singlemode PECVD silicon nitride photonic wire waveguides for 532–900 nm wavelength window fabricated within a CMOS pilot line*. IEEE Photonics Journal, 5(6):2202809–2202809, 2013.
- [25] Molly Piels, Jared F Bauters, Michael L Davenport, Martijn JR Heck, and John E Bowers. *Low-loss silicon nitride AWG demultiplexer heterogeneously integrated with hybrid III–V/silicon photodetectors*. Journal of Lightwave Technology, 32(4):817–823, 2014.
- [26] Shankar Kumar Selvaraja, Wim Bogaerts, Philippe Absil, Dries Van Thourhout, and Roel Baets. *Record low-loss hybrid rib/wire waveguides for silicon photonic circuits*. Group IV Photonics, 2010, 2010.
- [27] Yuanliang Chu, Xiaoping Zheng, Hanyi Zhang, Xueming Liu, and Yili Guo. *The impact of phase errors on arrayed waveguide gratings*. IEEE Journal of selected topics in quantum electronics, 8(6):1122–1129, 2002.
- [28] Shibnath Pathak, Michael Vanslambrouck, Pieter Dumon, Dries Van Thourhout, and Wim Bogaerts. *Optimized silicon AWG with flattened spectral response using an MMI aperture*. Journal of Lightwave Technology, 31(1):87–93, 2013.
- [29] Sarvagya Dwivedi, Herbert D’heer, and Wim Bogaerts. *A compact all-silicon temperature insensitive filter for WDM and bio-sensing applications*. IEEE Photonics Technology Letters, 25(22):2167–2170, 2013.
- [30] Yisu Yang, Yangjin Ma, Hang Guan, Yang Liu, Steven Danziger, Stewart Ocheltree, Keren Bergman, Tom Baehr-Jones, and Michael Hochberg. *Phase coherence length in silicon photonic platform*. Optics express, 23(13):16890–16902, 2015.

- [31] Tymon Barwicz and Hermann A Haus. *Three-dimensional analysis of scattering losses due to sidewall roughness in microphotonic waveguides*. Journal of Lightwave Technology, 23(9):2719, 2005.
- [32] Peter J De Heyn, Bart Kuyken, Diedrik Vermeulen, Wim Bogaerts, and Dries Van Thourhout. *High-performance low-loss silicon-on-insulator microring resonators using TM-polarized light*. In Optical Fiber Communication Conference, page OThV2. Optical Society of America, 2011.
- [33] Weiwei Song, Robert Gtdula, Siamak Abbaslou, Ming Lu, Aaron Stein, Warren YC Lai, J Provine, R Fabian W Pease, Demetrios N Christodoulides, and Wei Jiang. *High-density waveguide superlattices with low crosstalk*. Nature communications, 6:7027, 2015.
- [34] David Kwong, Amir Hosseini, John Covey, Xiaochuan Xu, Yang Zhang, Swapnajit Chakravarty, and Ray T Chen. *Corrugated waveguide-based optical phased array with crosstalk suppression*. IEEE Photonics Technology Letters, 26(10):991–994, 2014.
- [35] Fuad E Doany, Benjamin G Lee, Solomon Assefa, William MJ Green, Min Yang, Clint L Schow, Christopher V Jahnes, Sheng Zhang, Jonathan Singer, Victor I Kopp, et al. *Multichannel high-bandwidth coupling of ultradense silicon photonic waveguide array to standard-pitch fiber array*. Journal of Lightwave Technology, 29(4):475–482, 2011.
- [36] Akihiro Takagi, Kaname Jingui, and Masao Kawachi. *Wavelength characteristics of (2* 2) optical channel-type directional couplers with symmetric or nonsymmetric coupling structures*. Journal of lightwave technology, 10(6):735–746, 1992.
- [37] CR Doerr, M Cappuzzo, E Chen, A Wong-Foy, L Gomez, A Griffin, and L Buhl. *Bending of a planar lightwave circuit 2/spl times/2 coupler to desensitize it to wavelength, polarization, and fabrication changes*. IEEE photonics technology letters, 17(6):1211–1213, 2005.
- [38] Yann G Boucher. *Analytical model for the coupling constant of a directional coupler in terms of slab waveguides*. Optical Engineering, 53(7):071810–071810, 2014.
- [39] Richard Soref. *Mid-infrared 2× 2 electro-optical switching by silicon and germanium three-waveguide and four-waveguide directional couplers using free-carrier injection*. Photonics Research, 2(5):102–110, 2014.

3

Backscattering in silicon waveguides and ring resonators

In Chapter 2 we briefly discussed backscattering and its effects on short waveguide circuits, which are the sharp fluctuations on top of the grating coupler spectrum and stochastic reflections. However its effects are more complicated to be summarized in one sentence. In this chapter, we will give a more comprehensive and in-depth characterization of backscattering and its effects on silicon waveguides¹ as well as ring resonators².

3.1 Backscattering in silicon waveguides

3.1.1 Strong fluctuations in waveguide spectral transmission

The work presented in this section is done in close collaboration with my colleague, Yufei Xing. The waveguide is the most basic building block in any integrated optics platform. Thus the complete understanding and accurate model of its behavior is vital for PIC design especially for large scale circuits where waveguides can be the most dominant elements. Similarly in EICs, the interconnect wires start to be the most performance limiting element instead of the transistors when the integration density grows to a certain level. Waveguides are also critical to

¹in collaboration with Yufei Xing

²in collaboration with Thomas Van Vaerenbergh

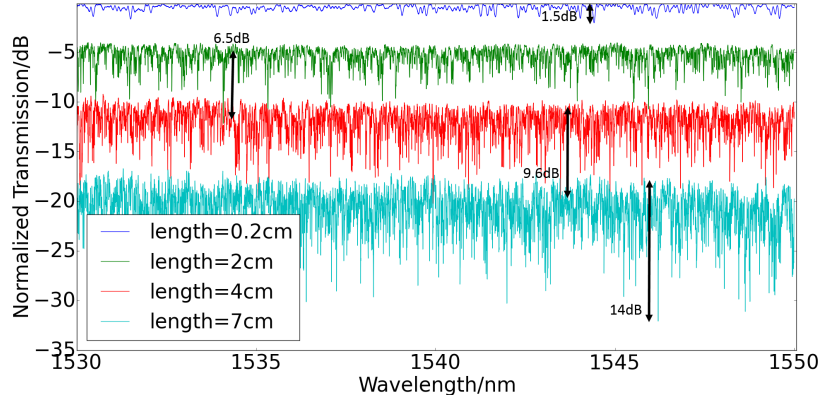


Figure 3.1: Measured transmission spectra of standard strip waveguides with different lengths fabricated at IMEC. The spectra are normalized to the grating couplers spectra fitted from measurement by a forth order polynomial equation. There is no top oxide cladding for the waveguides. All show strong fluctuations, whose strength scales with waveguide length. For a 7 cm long waveguide, the spectrum shows dips with an extinction ratio over 14 dB.

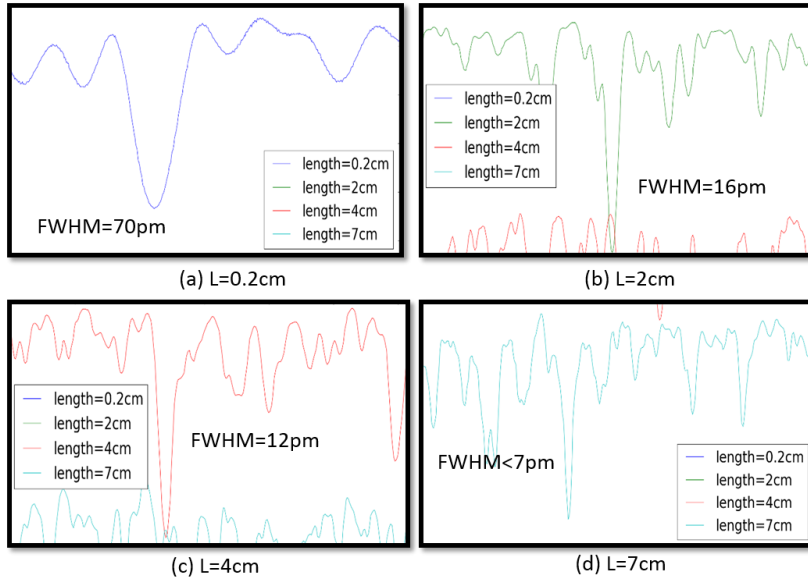


Figure 3.2: Zoomed views of some dips from each of those two spectra shown in Fig. 3.1. Clearly, the dip gets narrower with longer waveguide.

the performance of some devices, for instance, long spiral waveguides based photonic reservoir computing, MZI based biosensors, waveguide based delay lines, microwave photonics devices utilizing very long waveguide cavities etc.

So far, waveguides are considered as a light guiding channel with loss coefficient that is wavelength independent and a wavelength dependent phase response due to dispersion. The study of sidewall roughness makes its model more accurate with stochastic reflections included. Still, the transmission spectrum is by default not affected. However, the measurements of short waveguides in last chapter already showed the distortion of the transmission spectra due to sidewall roughness, even if the fluctuations are weak, in the order of 1 dB. Silicon strip waveguides start to behave weird when they are longer than 1 cm. Fig.3.1 plots our measurements of transmission spectra of some centimeter long waveguides with standard strip cross-section ($450 \text{ nm} \times 220 \text{ nm}$) fabricated at IMEC. Three main observations can be extracted from these measurements:

- The strong fluctuations. For 7 cm long waveguide, we observe fluctuations with an extinction ratio almost 14 dB. This is absolutely unacceptable for any waveguide based devices or circuits. 14 dB is even larger than extinction ratio of most filters, sensors or modulators. Such strong fluctuations will seriously degrade or even kill the performance of entire circuits, especially when this feature is not considered in the circuit model at the design stage. Moreover, this phenomenon is detrimental for waveguide characterization. Currently most popular method to characterize waveguide propagation loss is the cut-back method. In detail, a couple of waveguides with different lengths will be measured in transmission. Then the loss is simply extracted by linearly fitting the curve of transmission vs waveguide length. Apparently, if waveguide shows strong fluctuations like this, this method won't be accurate for propagation loss extraction, which is the most fundamental performance indicator of a waveguide.
- The fluctuation strength scales with waveguide length. As shown in Fig.3.1, for a 0.2 cm long waveguide, the ripples are slightly larger than 1 dB. It grows to 6.5 dB for a 2 cm long waveguide, 9.6 dB for a 4 cm long waveguide and reaches 14 dB when waveguide length is 7 cm. This implies the reason behind these fluctuations has something to do with the waveguide length. And the waveguide model somehow should also be length dependent.
- The dips get narrower with waveguide length. It drops from over 70 pm of a 2 mm long waveguide til only 7 pm of a 7 cm long waveguide as shown in Fig. 3.2.

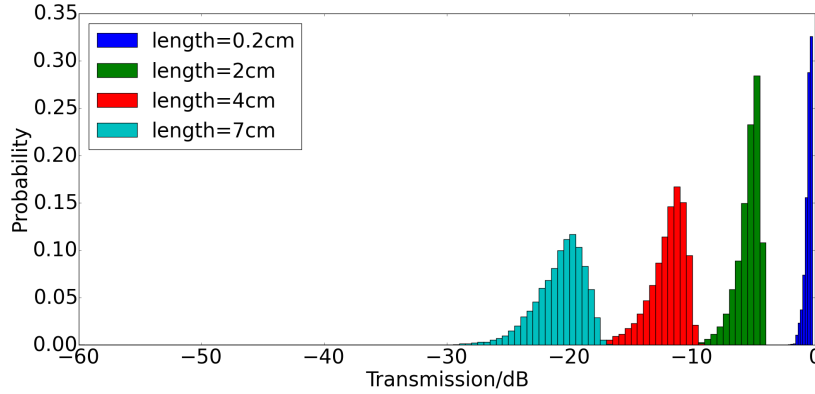


Figure 3.3: Probability density function of the measured transmission spectra shown in Fig. 3.1. We could see the left shift of these distributions due to higher propagation loss of a longer waveguide. Moreover, the PDF gets broader with increasing waveguide length. In other words, more potential transmission values can happen for a longer waveguide.

3.1.2 PDF of waveguide transmission spectrum

Another indirect observation from the measured transmission spectra is presented in Fig. 3.3. It shows the probability density function (PDF) of the transmission spectrum of each waveguide. Studying the PDF can give us a lot of information. For an ideal waveguide, its PDF should be a Dirac function with a peak of 1 at the position corresponding with its total propagation loss (loss per unit $\alpha \times$ waveguide length L) as the loss should be wavelength independent. However, due to the sidewall roughness and parasitic reflections at the grating couplers, the transmission spectrum is a distribution centered at the mean value of its spectrum. And the highest value should correspond with its total propagation loss. To understand this, we take a simplified example with only parasitic reflections at the grating couplers. So the circuit now behaves like a Fabry-Perot cavity with two "mirrors" at two ends as shown in Fig. 2.5. Clearly, it is the upper envelope of the spectrum with ripples that correspond with the real waveguide transmission, i.e., its total propagation loss. The existence of scatterers will only add dips to the transmission spectrum of a waveguide.

Due to higher loss of a longer waveguide, the center of the PDF is blue shifted, which is expected. However, something surprising is the broadening of the PDF with increasing waveguide length. In other words, for longer waveguide, the transmission of the waveguide may have more possible values. This is quite a detrimental feature as a waveguide, because now its behavior will become more and more non-deterministic and unpredictable. Moreover, the PDF shows asymmetry with respect to its center. We found the PDF fits well into generalized extreme value

distribution given in equation (3.1), where a limit distribution needs not to exist. It is often used to model a sequence of independent and identically distributed random variables which is also the case for waveguides with stochastic distributed backscattering.

$$PDF = \frac{1}{\sigma} (1 + \epsilon s)^{(-1/\epsilon)-1} \exp(-(1 + \epsilon s)^{-1/\epsilon}) \quad (3.1)$$

Where, $s = \frac{x-\mu}{\sigma}$. x refers to the original data, in this case, it's the data of the transmission spectra. σ μ represent the deviation and mean value of this distribution respectively. ϵ is a factor only about the distribution shape. So using this distribution to characterize a waveguide transmission is more robust and accurate than using a loss coefficient.

3.1.3 Origins for strong fluctuations

Now we start to focus on the origins of those fluctuations and try to clarify its dependency on waveguide length. We attribute the fluctuations to the sidewall roughness induced stochastic backscattering. As briefly explained in section 2, the sidewall roughness can be considered as distributed scatterers along the waveguide. The light propagating along the waveguide will be weakly reflected by each scatterer as shown in Fig. 3.4(a) and those numerous reflections contribute to the stochastic backscattering discussed in former literature [1–8]. But what has been neglected is the fact that this backscattered light will be reflected again by the scatterers and propagate to the output of the waveguide. Due to their coherence, the output of the waveguide is actually an interference pattern between numerous beams including those reflected multiple times and one always forward propagating without being reflected at all as illustrated in Fig. 3.4(b). This explains why the dips get sharper with increasing waveguide length. As longer waveguide contains more scatterers thus more beams are interfering at the output leading to a sharper interference pattern.

3.1.4 Circuit model for waveguides with stochastic backscattering

We use the optical circuit simulator Caphe to verify our hypothesis. To model the distributed scatterers we use a series of weak reflectors along the waveguide. The spacing between two reflectors are chosen to be $25 \mu m$ as an approximation because the measured optical span is 20 nm , such a span corresponds with a spatial resolution around $28 \mu m$ according to equation $f_{sr} = \frac{\lambda^2}{n_g L}$. In other words, the transmission measured at 20 nm span can only contain full information of a spatial cavity longer than $28 \mu m$. Features of any cavity shorter than this value can not be fully captured within a 20 nm wavelength range. The section length can be

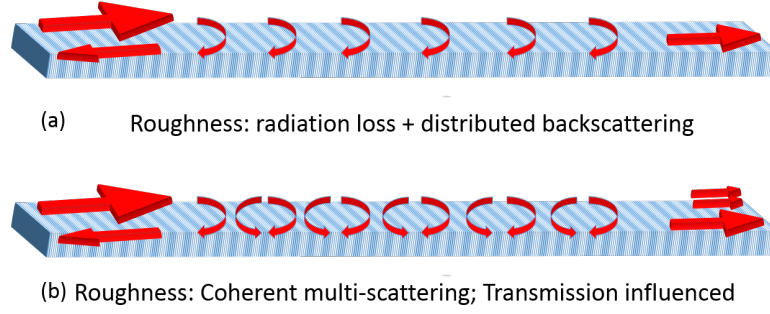


Figure 3.4: Conceptual illustrations of waveguide with distributed scatterers. The contributions of the backscattering to the reflection of a waveguide have been thoroughly studied (a) but the their effects on transmission of a waveguide have been ignored (b).

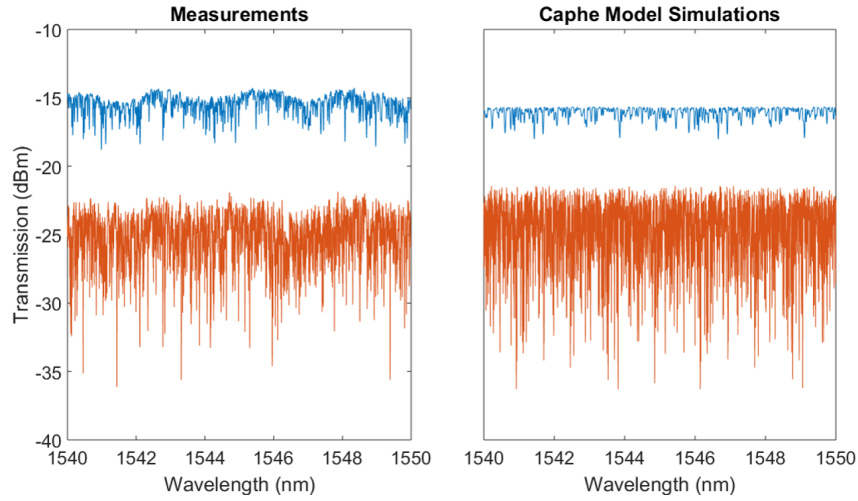


Figure 3.5: Optical circuit simulations and measured transmission spectra of waveguides with distributed reflectors at the spacing of $25\ \mu\text{m}$. 1 cm is shown in blue while 7 cm in orange.

chosen shorter for improved accuracy but at the price of more time and memory consumption for the simulation. And according to Ref. [9], the reflector can be designed with constant reflectivity and random phase to model roughness scatterers. This is reasonable as within this $25\ \mu\text{m}$, the reflections caused by each point roughness will be averaged out and generate a constant reflection if it's considered as a black box. While the random phase between two reflectors reflects the stochastic nature of roughness. The simulations of a 1 cm and 7 cm waveguides are plotted in Fig. 3.5. The corresponding measurements are also placed for comparison. This circuit model can give a good reproduction of the strong fluctuations and the waveguide length dependency of the fluctuations also exists. This circuit model not only helps understand the principle behind the fluctuations, but also enables more accurate performance prediction of PIC where long waveguide might be involved at the design/simulation stage.

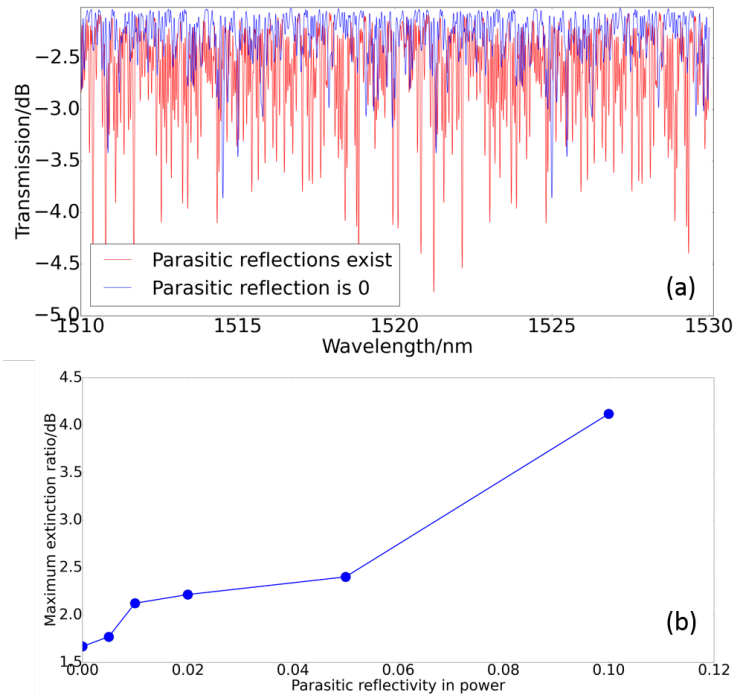


Figure 3.6: The fluctuations at the spectral transmission of a waveguide can be enhanced by lumped parasitic reflections of the grating couplers. The curve is generated from Caphe simulation.

3.1.5 Mathematical model for waveguides with stochastic backscattering

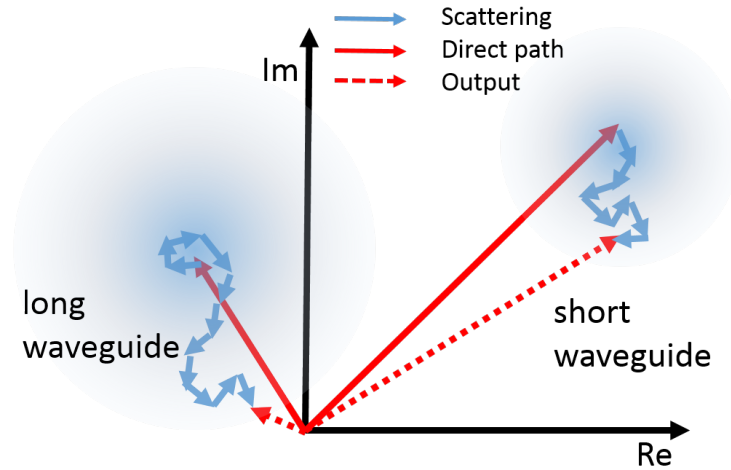


Figure 3.7: A representation of waveguides with stochastic distributed backscattering by a mathematical model, called random walk problem. Each walk event represents a backscattering to the propagating light caused by the roughness. Its length refers to the power reflectivity of such a backscattering and its direction has the same meaning of phase of the backscattering.

This phenomenon can also be intuitively explained in a mathematical way with the help of a random walk model evident in Fig. 3.7. Imagine a "drunk" guy starting to conduct a series of random walks from a specific location pointed by the solid red arrow and ending up at a position pointed by the dashed red arrow after those walks. Each walk has the same distance but can point at any directions. Then this model can represent the waveguide with sidewall roughness very well. The starting point corresponds with the light beam travelling directly from input to output without reflected at all. And the end location should represent the output power of a waveguide. Each random walk stands for a reflection caused by distributed scatterers. The walking distance is a representation of the beam that is scattered forward to the output of the waveguide, while the direction represents the phase of the reflection which is random. The gradient circles drawn in blue cover all the potential end positions, namely all the potential transmission of a waveguide. Not difficult to understand, longer waveguide will bring two consequences: a starting position closer to origin due to higher propagation loss and more random walks as the number of scatterers scale with waveguide length. These two consequences will result in a larger gradient blue circle. Optically speaking, this

means more potential values at the output of longer waveguide, thus the PDF will be broader. And there will be higher chance for the end position of a longer waveguide to reach the origin (i.e. zero transmission) and that's why we see the longer tail extending towards low power of the PDF shown in Fig. 3.3. Based on the study, we highly recommend to use broader waveguide for long range routing.

3.1.6 Enhancement of the fluctuations by lumped parasitic reflections

As a complete circuit, the grating couplers are always at both ends of a waveguide so the parasitic reflections of them shall not be isolated from the study of waveguide backscattering. We add two reflectors with certain amount of power reflectivity at both ends of a waveguide in the circuit model and find the maximum extinction ratio of these fluctuations gets enhanced by lumped parasitic reflections as evident in Fig. 3.6. This is reasonable as the grating coupler at the input will reflect back those backscattering and help them contribute to the output. It is therefore essential to reduce any kind of parasitic reflections in the circuit, for instance, use of off-axis grating coupler with significantly weakened reflections [10], improved Multi-Mode-Interferometer (MMI) with optimized isolation [11], carefully designed waveguide crossing [12] etc.

3.2 Backscattering in silicon ring resonators

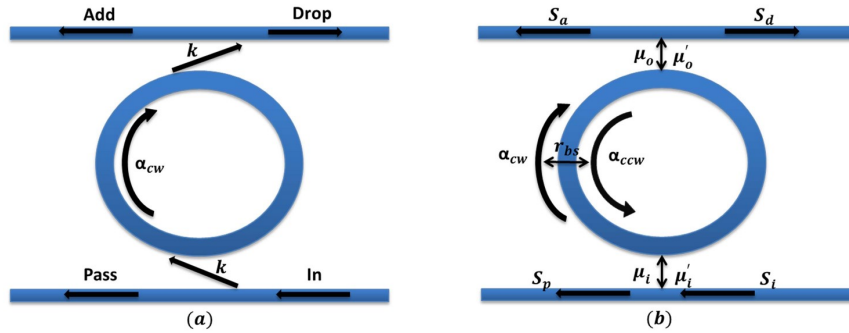


Figure 3.8: (a) schematic for an ideal ring resonator. (b) tCMT schematic for a real ring resonator with backscattering (r_{bs}) that couples CW and CCW modes.

Backscattering is responsible for stochastic reflections and fluctuations in transmission spectra of silicon waveguides or any waveguide based devices without feedback. Its detrimental effect is amplified for devices with feedback, for instance resonators, as light will be confined for multiple roundtrips. Even weak

reflections per roundtrip will be coherently built up due to their usually high Finesse. We will take silicon microring resonators as an example to evaluate the impact of backscattering.

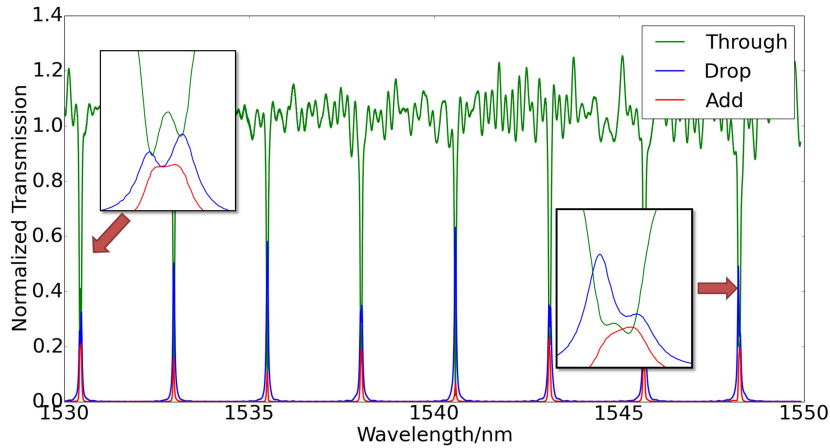


Figure 3.9: A measured spectra of a real silicon ring resonator. Various resonances exhibit splitting with different shapes. And strong leakage to the add port is present.

3.2.1 Problem description of backscattering in a silicon ring resonator

The basic introduction of a ring resonator has been given in chapter 1. And its ideal output spectra are plotted in Fig. 1.9. The nature of a looped waveguide makes a ring resonator inherently support two propagating modes, namely clockwise (CW) and counter-clockwise (CCW) modes as illustrated in Fig. 3.8. Depending on the direction of the input light, there should be only one of them being activated for an ideal case. Even if they are both activated (for instance, two beams injected from both ends of the bus waveguide simultaneously), they still resonate at the same wavelength due to their degeneracy which is only valid when they are independent from each other. However, the existence of sidewall roughness will cause backscattering of the light propagating along the ring waveguide, and the backreflected light will propagate in a reverse direction. Thus the backscattering can be considered as a coupling element between CW and CCW mode. And this coupling will break the degeneracy. As a consequence, their resonance frequency will start to split and peak splitting will start to appear in the spectra at *drop* and *pass* ports if the split distance is large enough compared to its FWHM. This is very analogous to quantum systems where two quantum particles (for instance, they can be electrons, atoms, molecules, or harmonic oscillators) are originally degenerate at

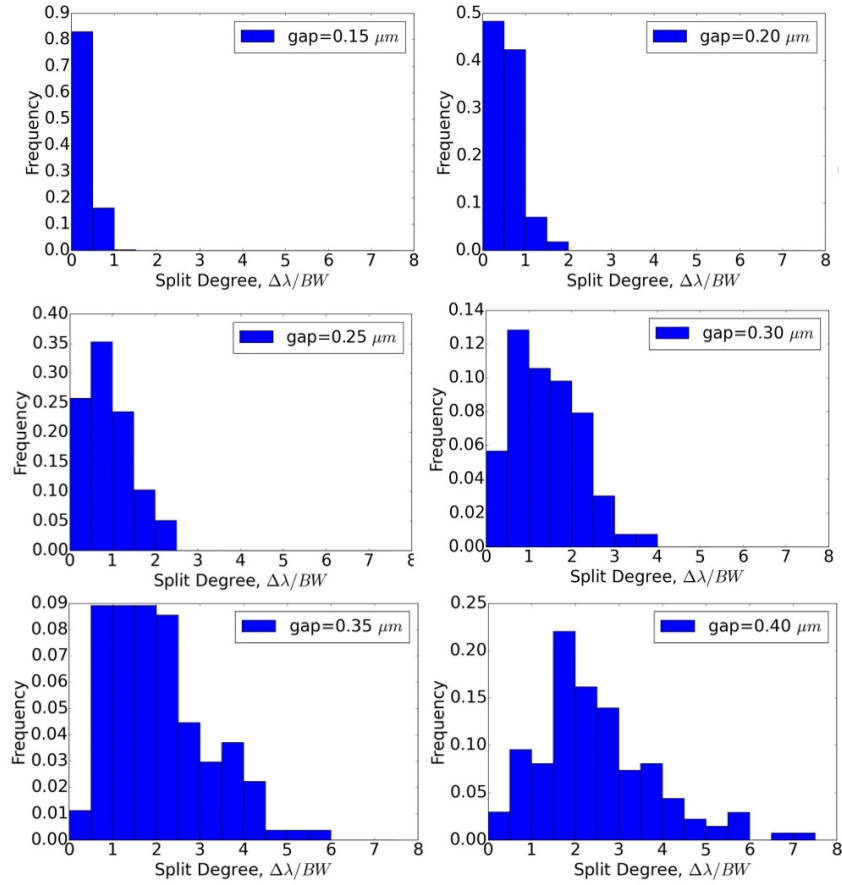


Figure 3.10: Histogram of split ratios of 6 sets of silicon ring resonators fabricated at IMEC; Each set contains 7 rings with variable lengths but the same coupling gap and coupling length. And each set has a different coupling gap. In total there are as many as 1080 resonances. When a resonance split is larger than half of 3dB bandwidth, it becomes visible and over 550 resonances exhibit visible splitting.

the same energy level. When an external magnetic field or electric field is applied to them, their energy levels or spectral lines will be split. These are well known the Stark effect and the Zeeman effect. Moreover, due to the activation of another mode, there will be significant leakage to the *add* port and reflection to the *in* port. These various irregular resonance shapes together with the leakage and reflection are problematic for most of ring resonator based applications.

- In ring-based sensors the shift of the resonance wavelength might not be correctly detected [13].
- In ring-resonator-based tunable lasers, the reflection at *in* port and the leakage to the *add* port as well as the distortion of the ring's transmission spectrum may cause laser instabilities.
- In ring-resonator-assisted loss characterization techniques, wrong model parameters will be extracted from an imperfect fitting of split resonances [14].
- Ring-resonator-based wavelength-division multiplexing (WDM) filters will deviate from the designed filter specifications as the Q-factor cannot be well controlled.
- Ring-assisted microwave detection circuits could result in the wrong peak power extracted from a split resonance [15].

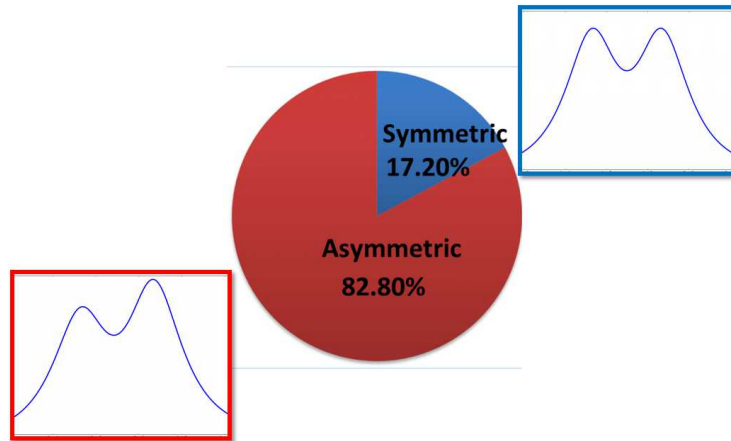


Figure 3.11: A pie chart clearly shows the dominance of asymmetric splitting among all of the splitting resonances we measured from 42 rings (in total more than 550 resonances exhibit splitting). Examples of asymmetric and symmetric resonance splitting are also given.

But how frequent can this splitting happen? We measured 6 sets of silicon add-drop ring resonators fabricated at IMEC with air cladding, each set contains 7

ring resonators with variable roundtrip lengths, and each set is different with each other in terms of coupling gaps. In total there are as many as 1080 resonances. To quantitatively characterize the problem of resonance splitting, we make a figure of merit called split degree, that is the ratio of optical spacing between two peaks of a split resonance and optical bandwidth of this resonance $\frac{\Delta\lambda}{BW}$. When the split degree is greater than 1, i.e. split distance is larger than its bandwidth, the splitting starts to be visible. For all the 1080 resonances, those exhibiting visible splitting amounts to over 550. And the split degree can be sometimes larger than 4, under such circumstances, the split resonance is resolved to two clearly distinguished peaks. This serves a strong proof of the severity of this problem in current silicon photonics. We also note the clear tendency of strong split degree with increasing coupling gap. It is reasonable as the bandwidth of the resonance will decrease with increasing coupling gap, thus given the same splitting distance, the split degree shall increase. This gives a hint that increasing resonance bandwidth is an option to avoid resonance splitting at the sacrifice of low Q factor.

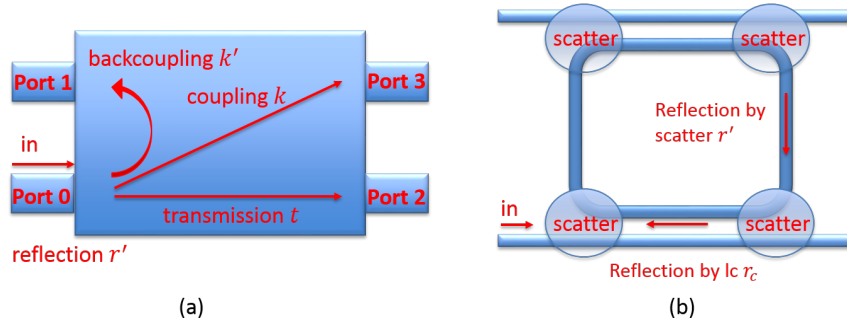


Figure 3.12: (a) A simplified schematic of a 2x2 directional coupler. Ideally, the backcoupling κ' and reflections r' are zero. (b) Illustration of the extra reflections caused by directional couplers in a ring. The directional coupler in a ring resonator can be physically divided into three parts, two scattering centers at the beginning and end, and a distributed scatterer in the straight section due to extra coupling length. Scatterers will cause unwanted backcoupling κ' to adjacent port as well as reflection to in port r' , while coupling length will bring roughness induced backscattering noted with r_c .

There have been quite some efforts made to analyze and model ring resonators with backscattering inside. The peak splitting is already attributed to the sidewall roughness induced backscattering both theoretically and by fitting measurement results with a model for ring resonator including backscattering. But the research is not yet fully complete. So far these models can only successfully explain symmetric resonance splitting [14, 16–18], which means the two peaks split from a resonance have the same height. While the asymmetric resonance splitting can not be well fitted thus thoroughly understood. To highlight the importance of suc-

cessfully modelling asymmetric resonance splitting, we analyzed the frequency of asymmetric splitting in all the measured resonances that exhibit splitting. Result is plotted in Fig. 3.11, it's astonished to realize that over 80% resonance splittings are asymmetric. What's more, the reason for the extreme diversity in resonance splitting is also not yet fully understood. Even if the sidewall roughness induced backscattering is indeed stochastic, but it is not the only reason for those various splitting shapes.

3.2.2 Improved tCMT model for ring resonator

To analyze this problem we first build a theoretical model for ring resonator with backscattering included. The model is based on temporal coupled mode theory (tCMT), which has proven to be a great tool for normal ring resonators or coupled resonators [19]. This model is analyzing a resonator in time domain, with time scale related to its roundtrip time (around 1 ps). It has certain requirements to assure its accuracy when applied to a ring resonator, namely the loss rate of the resonator shall be much less than Our model is based on the existing tCMT model for ring resonator but improves it in two aspects:

- an element serving as a model for backscattering is included. This element is responsible for the coupling between CW and CCW modes in this model.
- the concept of backcoupling κ' is proposed and added into our model. In contrast to the normal forward coupling of a directional coupler, backcoupling is the term describing the unwanted coupling from in port to its adjacent port as shown in Fig.3.12(a).

The two factors above grant the ability of successfully explaining and accurately fitting all kinds of resonances to our model. As mentioned above, a ring resonator naturally supports two modes, i.e. CW and CCW modes. Ideally only one of them is activated by its corresponding in port. If we assume CW mode is the one to be activated by the input, the amplitudes of these two modes are given by following equations:

$$\frac{d\alpha_{cw}}{dt} = j(\omega_0 + j\frac{1}{\tau_{tot}})\alpha_{cw} - j\mu_i S_i - j\mu_{12}\alpha_{ccw} \quad (3.2)$$

$$\frac{d\alpha_{ccw}}{dt} = j(\omega_0 + j\frac{1}{\tau_{tot}})\alpha_{ccw} - j\mu'_i S_i - j\mu_{21}\alpha_{cw} \quad (3.3)$$

And the outputs at each port are given in equations (3.4)-(3.7)

$$S_r = -j\mu_i\alpha_{ccw} - j\mu'_i\alpha_{cw} \quad (3.4)$$

$$S_p = S_i - j\mu_i\alpha_{cw} - j\mu'_i\alpha_{ccw} \quad (3.5)$$

$$S_a = -j\mu_o\alpha_{ccw} - j\mu'_o\alpha_{cw} \quad (3.6)$$

$$S_d = -j\mu_o\alpha_{cw} - j\mu'_o\alpha_{ccw} \quad (3.7)$$

- α_{cw} and α_{ccw} are the two modes energy amplitudes respectively. They are normalized in such a way that their square represent the energy in the resonator.
- ω_0 is the intrinsic resonant frequency of this resonator, purely depends on the physical parameter of the ring resonator, for instance, total roundtrip length and effective index.
- τ_{tot} is the total decay rate of this resonator. It consists of five contributions $\frac{1}{\tau_{tot}} = \frac{1}{\tau_l} + \frac{1}{\tau_i} + \frac{1}{\tau_o} + \frac{1}{\tau_i'} + \frac{1}{\tau_o'}$, namely decay rate due to propagation loss τ_l , decay rate due to coupling (both forward coupling and backcoupling) at two directional couplers of the ring resonator $\tau_i + \tau_i'$ and $\tau_o + \tau_o'$. We can assume $\tau_i + \tau_i'$ and $\tau_o + \tau_o'$ to be the same if the two directional couplers are designed to be identical, which is often the case, as it is very easy to design and obtain for an add-drop ring resonator. As this model is in temporal domain, so it's always temporal term "rate" instead of spatial terms like loss, coupling coefficient etc. But they can be linked following equations (3.8) and (3.9).

$$\mu_x^2 = \frac{2}{\tau_x} \quad (3.8)$$

- μ_i and μ_o stand for the mutual coupling of the two directional couplers. Their dependency on the spatial field coupling coefficient κ are given in equation (3.9). Where v_g and n_g refer to the group velocity and group index of the ring waveguide while L stands for the physical length.

$$\mu_i^2 = \mu_o^2 = \kappa_i^2 \frac{v_g}{L} = \kappa_i^2 \frac{c}{n_g L} \quad (3.9)$$

- μ_{12} and μ_{21} are the element representing backscattering, which can be considered as a lumped reflector inside the ring cavity. As shown in equations (3.2) and (3.3), they are responsible for the coupling between these two modes. Without them is the case for a normal ring resonator. The strength of the backscattering that couples CW and CCW should be independent on the propagation direction of light, thus μ_{12} and μ_{21} should have the same amplitudes. For linear and passive device, they are also expected to have opposite phase due to the reciprocity and in later paragraph we will show that our fitting results from measurement also confirm this. But at this moment, we still consider them to have their own phases. Similar to μ_o and μ_i , they also depend on some spatial parameters, in this case, it is the reflectivity of the backscattering r_{bs} as shown in equation (3.10).

$$\mu_{12} = r_{bs} \frac{v_g}{L} = r_{bs} \frac{c}{n_g L} \quad (3.10)$$

r_{bs} should also be wavelength dependent according to Ref. [4]. However, within one resonance, it can be considered as constant due to the ultra narrow FWHM.

- μ'_i μ'_o are two terms describing the so-called backcoupling at the directional couplers. It is also dependent on the spatial field backcoupling coefficient κ' as given in equation (3.11).

$$\mu_i'^2 = \mu_o'^2 = \kappa_i'^2 \frac{v_g}{L} = \kappa_i'^2 \frac{c}{n_g L} \quad (3.11)$$

- S_x refers to the wave amplitude at each port. S_x^2 has the unit of power. For an ideal ring resonator, reflection to *in* port S_r and transmission at *add* port S_a should be 0.

Now we can solve equations (3.4)-(3.7) based on formula (3.2) and (3.3). We take the transmission at *drop* port for example, transmissions at other ports can also be derived. Both ideal case and the case with backscattering and backcoupling are given in following equations:

$$\begin{aligned} \frac{S_d}{S_i} |_{ideal} &= A_0 \frac{\frac{2}{\tau_i}}{j(\omega - \omega_0) + (\frac{2}{\tau_i} + \frac{1}{\tau_l})} \\ &= A_0 \frac{\frac{BW_0}{2}}{j(\omega - \omega_0) + \frac{BW_0}{2}} \end{aligned} \quad (3.12)$$

$$\begin{aligned} \frac{S_d}{S_i} |_{bs} &= \frac{A_0}{2} \left[\frac{(\mu_i - \mu'_i)^2}{j(\omega - \omega_0 - \mu_r \cos \frac{\phi_\mu}{2}) + (\frac{2}{\tau_i} + \frac{2}{\tau_r} + \frac{1}{\tau_l} + \mu_r \sin \frac{\phi_\mu}{2})} \right. \\ &\quad \left. + \frac{(\mu_i + \mu'_i)^2}{j(\omega - \omega_0 + \mu_r \cos \frac{\phi_\mu}{2}) + (\frac{2}{\tau_i} + \frac{2}{\tau_r} + \frac{1}{\tau_l} - \mu_r \sin \frac{\phi_\mu}{2})} \right] \\ &= \frac{A_0}{2} \left[\frac{(\mu_i - \mu'_i)^2}{j(\omega - \omega_1) + \frac{BW_1}{2}} + \frac{(\mu_i + \mu'_i)^2}{j(\omega - \omega_2) + \frac{BW_2}{2}} \right] \\ &= \frac{A_0}{2} \left[\frac{\frac{BW_0}{2}(1-f)^2}{j(\omega - \omega_1) + \frac{BW_1}{2}} + \frac{\frac{BW_0}{2}(1+f)^2}{j(\omega - \omega_2) + \frac{BW_2}{2}} \right] \end{aligned} \quad (3.13)$$

Here:

- A_0 is a dimensionless factor, scaled by potential losses outside the ring cavity. Using this factor helps fit the measured results which might include other losses for instance, the grating coupler loss, bus waveguide propagation loss etc.

- BW_0 and ω_0 are the intrinsic resonance frequency and bandwidth of the resonator without any parasitics. They are determined by the physical configurations of this resonator, including roundtrip length, propagation loss and coupling coefficients of the directional couplers. Strictly speaking, $\frac{BW_0}{2} = \frac{1}{\tau_{tot}}$, where $\frac{1}{\tau_{tot}} = \frac{1}{\tau_l} + \frac{2}{\tau_i}$ for the ideal ring and $\frac{1}{\tau_{tot}} = \frac{1}{\tau_l} + \frac{2}{\tau_i} + \frac{2}{\tau_i'}$ for ring with backcoupling. In those equations above, $\mu_i = \frac{2}{\tau_i}$ is approximated to $\frac{BW_0}{2}$.
- f shown in equation (3.13) is a dimensionless factor which equals the ratio of forward coupling κ over backcoupling κ' . Introducing this factor helps reduce the freedoms (or parameters) in this equation.
- (ω_1, BW_1) and (ω_2, BW_2) represent the respective (resonance frequency, bandwidth) of these two modes.

Also:

$$\omega_1 = \omega_0 + \mu_0 \cos \frac{\phi_\mu}{2} \quad (3.14)$$

$$\omega_2 = \omega_0 - \mu_0 \cos \frac{\phi_\mu}{2} \quad (3.15)$$

$$BW_1 = BW_0 + 2\mu_0 \sin \frac{\phi_\mu}{2} \quad (3.16)$$

$$BW_2 = BW_0 - 2\mu_0 \sin \frac{\phi_\mu}{2} \quad (3.17)$$

$\mu_0 = \sqrt{|\mu_{12}\mu_{21}|}$ and $\phi_\mu = \angle \mu_{12}\mu_{21}$. Our measurement fitting results indicate ϕ_μ is close to 0, this means that $\phi_{\mu_{12}} = -\phi_{\mu_{21}}$, which verifies our hypothesis. This also implies that the coupling between these two modes is conservative instead of dissipative because now the scatter matrix of the lumped reflector is conservative to 1.

Now it becomes quite clear that, instead of a single Lorentzian shaped resonance with central frequency ω_0 and bandwidth BW_0 at the ideal case, there are two Lorentzian shaped resonances standing at their own frequencies ω_1 and ω_2 with different bandwidths BW_1 and BW_2 due to the presence of backscattering. The difference in resonance frequency is linear to the backscattering strength μ_0 which is in good correspondence with former literature [20]. If backscattering is strong enough to make their separation become comparable with their bandwidths, a visible splitting shall appear. While their peak heights are determined by two factors according to equation (3.13), including their respective bandwidth BW_x and the f factor that related to the backcoupling. The former one stands in the denominator of the equation while the second one is in the numerator. However, based on careful analysis of our measured data, we conclude that the main

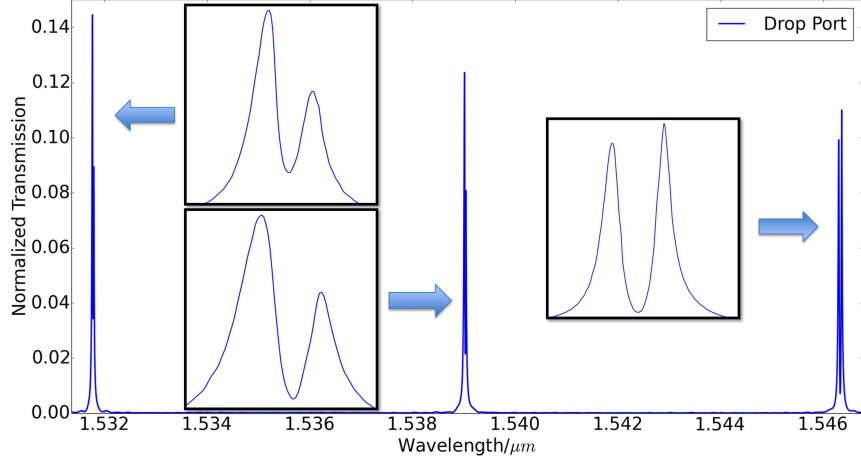


Figure 3.13: A measured spectrum with 3 split resonances. We analyze these resonances in detail to get the proof of the origins for the asymmetry in resonance splitting, which we believe to be the backcoupling.

responsibility for their peak height asymmetry should be taken by the latter one, namely backcoupling.

	Resonance 1	Resonance 2	Resonance 3
BW_1/pm	16.7188	14.1098	21.0971
BW_2/pm	15.6252	19.4137	22.5090
$\frac{\Delta BW}{BW_0}$	6.76%	31.6%	6.47%
P_1	0.1447	0.1236	0.099
P_2	0.0892	0.0807	0.110
$\frac{\Delta P}{P_0}$	47.5%	42.0%	10.5%

Table 3.1: The detailed data of above spectrum in Fig. 3.13. The existence of f can be inferred from a comparison of the first and third resonance. The peak with larger bandwidth has a higher peak power; comparing the first and second resonance, the relative difference in bandwidths of first resonance is only 6.7%, whereas that in second resonance is 31.6%, but the first one shows a even larger difference in peak power (47.5%) than the second one (42%); This decoupling relative peak power and bandwidth can only be explained with a non-zero f .

To perform the analysis, we focus on a measured spectrum with some asymmetric resonance splitting as shown in Fig. 3.13. And Table 3.1 shows the characteristics of those split resonances. If there were no backcoupling at all ($f = 0$),

the only reason that there could be an asymmetry in the peak power of the two modes is that their bandwidths are different, as can be seen in the denominator of equation (3.13). Two natural conclusions can be derived consequently:

- a larger bandwidth should lead to a lower peak power.
- a large difference between peak power should correspond with a large difference in bandwidth.

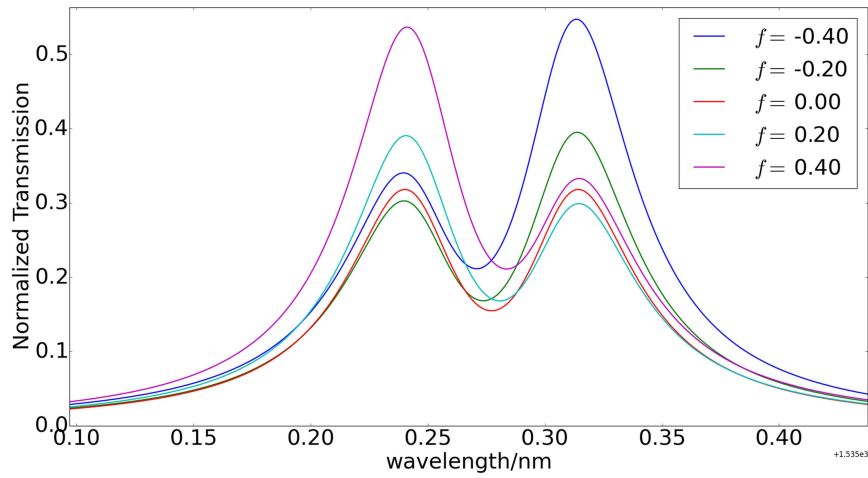


Figure 3.14: A sweep of different f factors using circuit simulator Caphe. When $f = 0$ and $\phi_\mu = 0$, the red line is generated, which is a symmetric split resonance; When magnitude of f is increased, the degree of asymmetry increases accordingly.

However, something different is observed in the measured spectra shown in Table 1. For the first and third resonances, the peak with the larger bandwidth actually has a higher peak power. In addition, when comparing the first and second resonances, we also find a discrepancy: in the first resonance, the two peaks have a much smaller difference in bandwidth (6.7%) than in the second resonance (31.6%), but at the same time the two peaks of the first resonance have a larger difference in power (47.5%) than those of the second one (42%). Moreover, as mentioned above, our fitting of the measured spectra tell us ϕ_μ is very close to 0, meaning the difference in their bandwidths should be negligible. All of these observations and analysis reveal that, besides bandwidth, there must be another factor introducing an asymmetry and we believe it to be the backcoupling.

To further confirm this, we build a circuit model in Caphe. The very big advantage of using optical circuit simulator is its behavior parameter sweep at a very fast speed compared to other physics simulations. In this model, we include the backcoupling (f factor) into the directional couplers and by comparing the results

when $f = 0$ and $f \neq 0$ we can get a straightforward view how backcoupling influences the relative peak height of those two peaks in a split resonance as evident in Fig. 3.14. When no backcoupling is present ($f = 0$), only symmetric resonance splitting appears. While keeping the backscattering strength constant and varying the magnitude of f , asymmetry start to emerge. One interesting condition is when $f = \pm 1$, according to equation (3.13), under such condition, one peak will have 0 transmission. This can be utilized to eliminate backscattering induced resonance splitting.

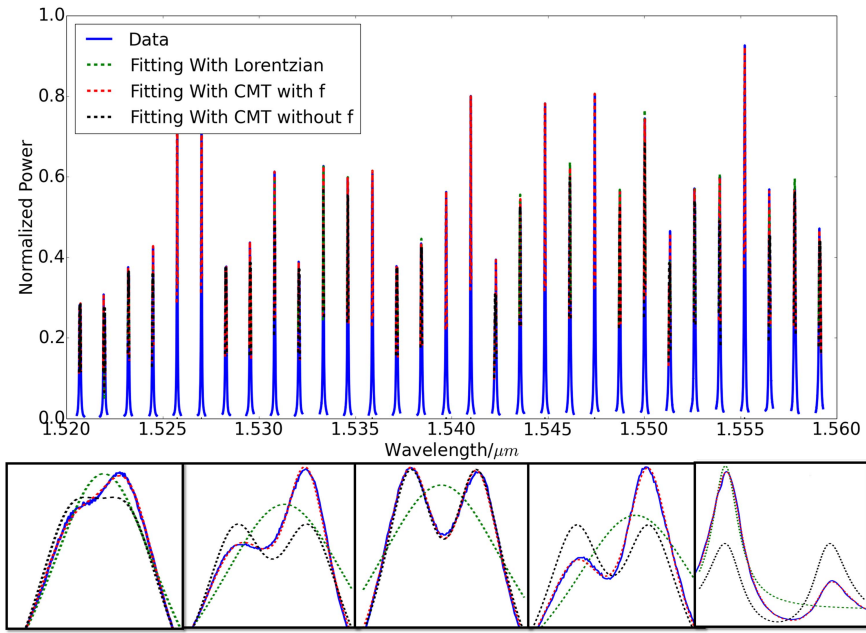


Figure 3.15: A sweep of different f factors using circuit simulator Caphe. When $f = 0$ and $\phi_\mu = 0$, the red line is generated, which is a symmetric split resonance; When magnitude of f is increased, the degree of asymmetry increases accordingly.

3.2.3 Model validation by measurement fitting

After a comprehensive explanation of our model for ring resonator with backscattering and backcoupling, we'd like to show the fitting of measured ring spectra using this model. We implement equation (3.13) into Python and use least square method to perform the fitting of *drop* port spectra. With minor revisions, transmission at *pass* port can also be fitted with corresponding mode equation derived from tCMT. The parameters fed into the fitting procedure are $[A_0, \omega_0, BW_0, \mu_0, f, \phi_\mu]$, which can be translated into [amplitude factor, resonance frequency, in-

trinsic bandwidth, amplitude of backscattering, backcoupling coefficient, phase of backscattering]. Since least square is a relatively simple fitting algorithm used to find local minimum instead of global minimum, which is very fast in speed but also quite sensitive to the initial guess of the parameters. We implement an algorithm into our code that can automatically and very accurately guess all the initial parameters from the measured spectra.

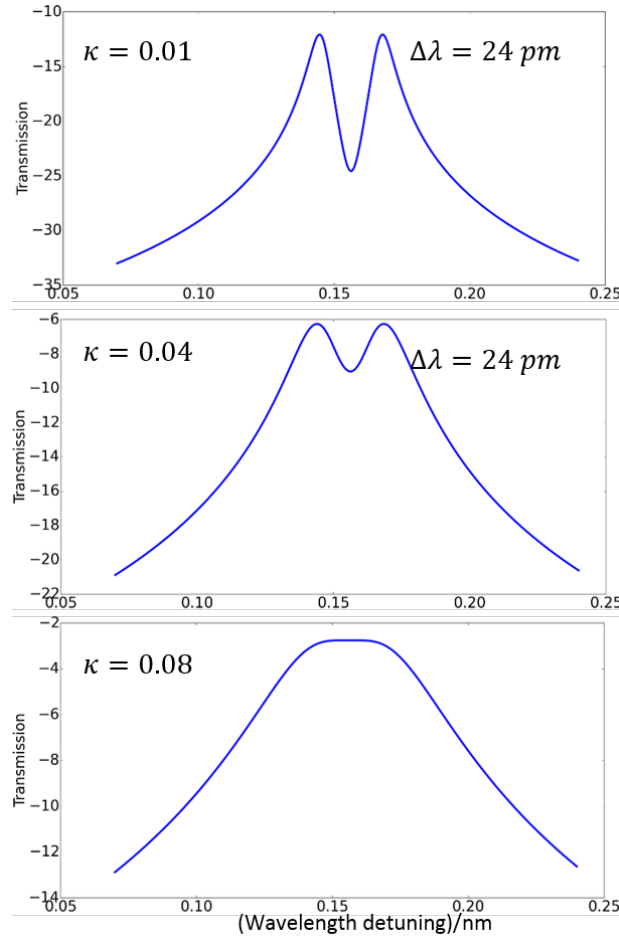


Figure 3.16: Simulated spectra of 3 rings with the same length, loss and backscattering strength. The coupling coefficient κ of the directional coupler is increasing From top to bottom, with decreasing Q factor. The splitting distance keeps constant but the broadening of the resonance will gradually makes splitting invisible.

Figure 3.15 gives examples of 3 different ring models. The green line is the result of a traditional Lorentzian model. It fails to fit resonances with even a small

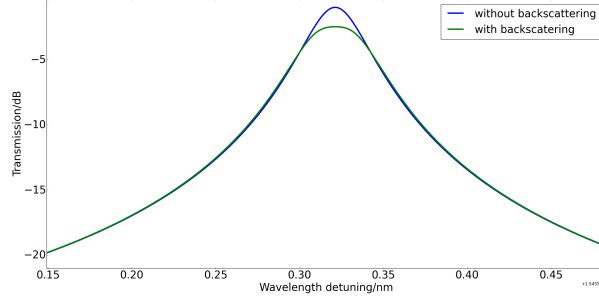


Figure 3.17: Simulated resonances of ring resonators with and without backscattering. At the case with backscattering, even if the resonance is too broad to make the resonance splitting visible, still it's distorted from a Lorentzian shape.

amount of splitting. The black curve fits the resonances with a t-CMT model with backscattering, but without backcoupling ($f = 0$). Only symmetrically split resonances can be handled by this model, and it performs poorly for asymmetric peaks. Our improved t-CMT model with a non-zero backcoupling factor f is plotted in a red dashed line. It accurately fits non-split, symmetrically split and asymmetrically split resonances.

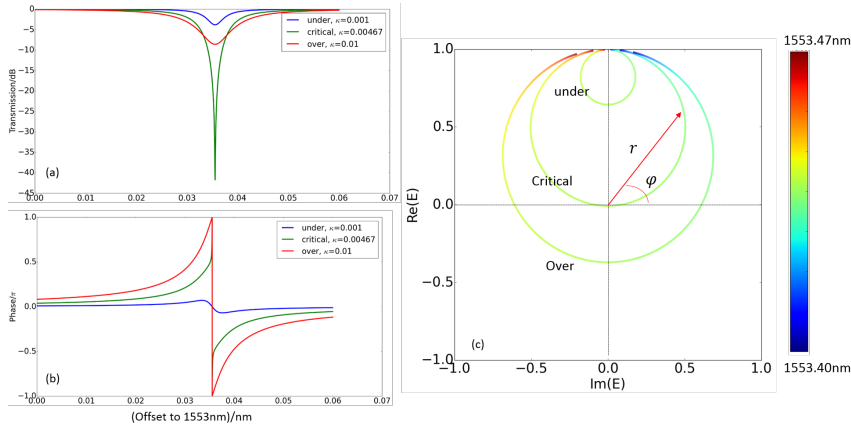


Figure 3.18: (a) and (b) present the amplitude transmission spectra and phase responses of a ring resonator under different coupling regions. (c) is the phasor plot. It clearly distinguishes these three coupling regions.

The paragraph above verifies the ability of our model to successfully handle any kind of resonance splitting. But in reality, the case with invisible resonance splitting also happens occasionally. As for a given backscattering strength, the splitting distance between the two peaks is constant no matter what the Q factor

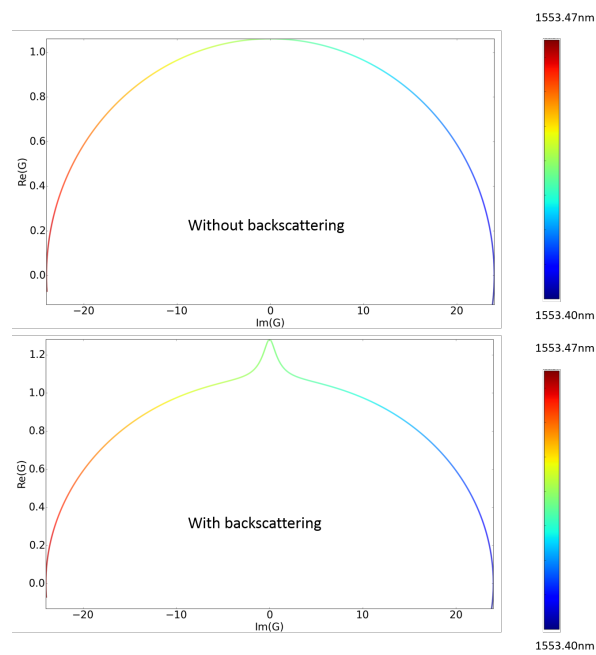


Figure 3.19: Two inverse phasor plots of the resonances plotted in Fig. 3.17. The difference between them are amplified when it's very hard to distinguish them by purely looking at the amplitude transmissions.

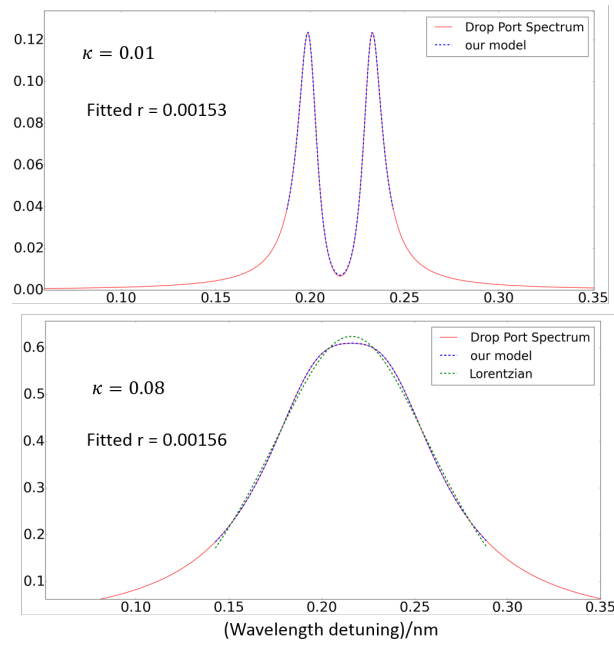


Figure 3.20: Fitting qualities of visible resonance splitting and invisible splitting, respectively. Both cases can be fitted accurately using our model, and the extracted values of the power reflectivity are all close to the simulation value.

(FWHM of the resonance) is as evident in Fig. 3.16, where the resonances of ring resonators with fixed backscattering strength but variable Q factors are simulated. So if the Q factor is not very high, in other words, the resonance is relatively broad compared to the backscattering induced splitting distance, then the splitting may be invisible under the envelope of the resonance. But the resonance is still slightly distorted from a pure Lorentzian shape without any backscattering and splitting as evident in Fig. 3.17. The parameters in the simulations: propagation loss $\alpha = 2 \text{ dB/cm}$, ring roundtrip length $L = 2\pi * 35 \mu\text{m}$, group index $n_g = 4.2$, the backscattering strength (power reflectivity) $r = 7 * L = 0.00154$, the power coupling coefficients $\kappa = 0.01$ for the visible resonance splitting and $\kappa = 0.08$ for the invisible split resonance. The simulated FSR is around 2.6 nm.

By only looking at the amplitude transmission spectrum, it's hard to distinguish this with a normal Lorentzian resonance. However, using modified phasor plot can directly amplify the difference. Phasor plot is a representation of the phase response together with the amplitude response by plotting the real part of the electric field $ReE = |E|\cos(\phi)$ vs its imaginary part $ImE = |E|\sin(\phi)$. Circular curves of normal Lorentzian resonance will be generated in this phasor plot as illustrated in Fig. 3.18. The length of the arrow pointing from the origin (0,0) to one specific point on the curve is the amplitude of the electric field at this point while the angle between this arrow and the x-axis contains the effective phase shift at this wavelength point. It has been adopted to analyze the response of a ring resonator or WGM, especially to recognize the coupling condition [21, 22], as the curves of resonance at different coupling conditions (critical-, under-, over- coupling) show different feature as also illustrated in Fig. 3.18. For this invisible resonance splitting (but not a Lorentzian resonance), the phasor plot is still a pseudo-circular curve with only slight difference with that of a normal Lorentzian resonance. But the phasor plot of the inverse of the electric field ($G = \frac{1}{E}$), which is called inverse phasor plot [22], can clearly amplify this difference. Fig. 3.19 shows the inverse phasor plots of the resonances in Fig. 3.17. Obviously, the peak in the bottom phasor plot identifies the invisible resonance splitting. While for a pure Lorentzian resonance, it's still a circular curve without this kind of peak.

So this situation is worthy investigating to validate our model as handling such a resonance with a Lorentzian function is inaccurate and unreliable. We use our model to fit the two resonances plotted in Fig. 3.17. The fitting qualities are provided in Fig. 3.20. First of all, both resonance patterns can be fitted accurately using our model while the fitting for the invisible resonance splitting using Lorentzian model is poor. Secondly, the fitted value of the power reflectivity r all show a good match with the value we choose in the simulation. This further validates the ability of our model to handle all kinds of resonances in a reliable manner.

We proposed the concept of backcoupling so we want to provide a solid proof

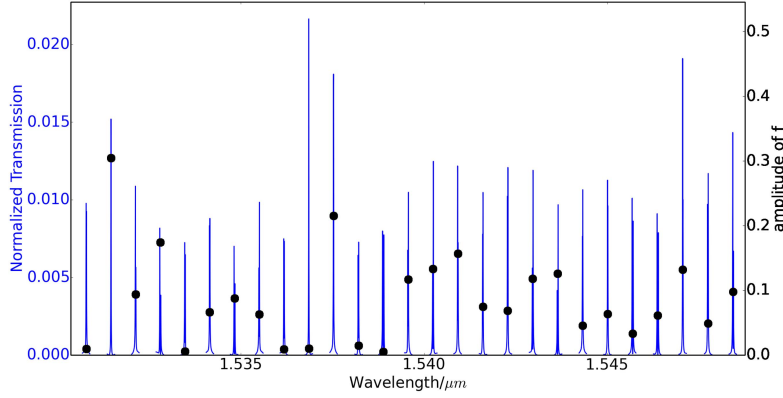


Figure 3.21: A measured spectrum with fitted amplitude of f factor at each resonance. Similar in other measured spectra, the amplitude of f is in the range of 0 to 0.4.

and give a basic guideline of its typical value. Figure 3.21 plots the f -factor for a typical example of measured rings. The amplitude of f factor varies from 0 to 0.4, which means that there can be as much as 40% of the cross-coupled field (16% of the power) coupled back to the adjacent port of *in* port. Such a large value explains the significant difference in peak power in some split resonances.

3.2.4 Break down backscattering to individual contributions

Since our model is capable to fit various resonance shapes and extract the key parameters of each resonance, so we want to do more with this model. Among the fitting parameters, μ_0 can be used to retrieve the backscattering strength of a ring resonator at specific resonance according to equation (3.10). So we target a comprehensive analysis of the backscattering in silicon ring resonators, trying to break it down to all the individual contributions and provide a guideline about the dependency of backscattering strength on physical parameters of ring resonators. Generally speaking, a ring resonator consists of a looped waveguide and one or two directional couplers. So each component can potentially introduce unwanted reflection or scattering, contributing to the total backscattering in ring. It's essential to have a good understanding of all the individual contributions so that we might conclude with a quantitatively predictable equation for backscattering.

3.2.4.1 Sidewall roughness-induced backscattering

For the ring waveguide itself, roughness-induced backscattering is the only contribution to backscattering in the ring that has been verified and analyzed in detail.

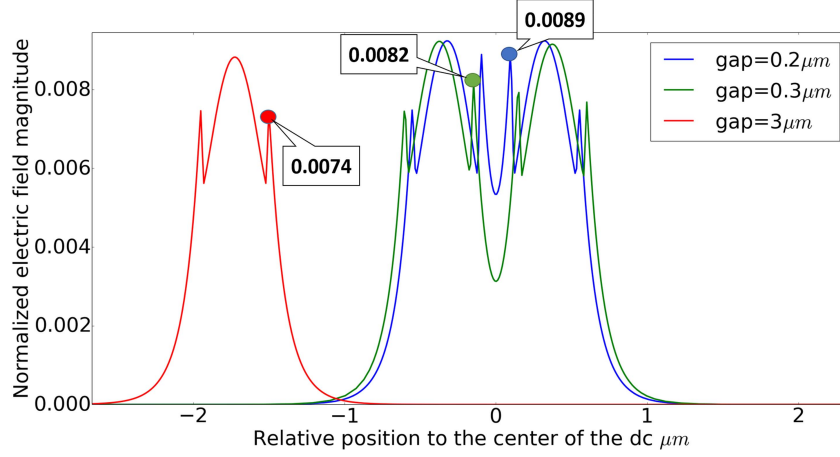


Figure 3.22: FDTD simulations of mode profiles of directional couplers with 200 nm gap (blue) and 300 nm gap (green), as well as single-mode waveguide (red). Clearly, the electric field magnitude at the sidewall of a directional coupler is stronger than that of a waveguide.

Other potential contributions from the ring waveguide could include the interface between a bend and a straight waveguide. In [23], the bend radius of ring resonator is chosen to be as large as $20\mu m$. At such large radii, the transition between bend and straight waveguide is almost perfect in silicon wire waveguides [24], which might explain why only roughness induced backscattering was observed. For sharper bend radii, $5\mu m$ or even smaller, the interface between bend and straight section can introduce additional reflections.

According to [5], roughness-induced backscattering can be considered as a statistical process, where the reflectivity's spectral characteristics (mean value, standard deviation and correlation length) depend on the waveguide length. Using *optical frequency-domain reflectometry* (OFDR), Morichetti [4, 5] demonstrated a linear relationship between reflected power R_w and waveguide length if the waveguide is short compared to the decay length of the propagation losses. For a ring resonator, the same technique clearly shows how a coherent addition of the reflections for each roundtrip in the ring increases the reflected power around resonance wavelength. This linear relationship is:

$$R_w = r_w^2 = H_w \times L_w \quad (3.18)$$

Here, H_w is a parameter dependent on waveguide dimension and sidewall quality.

3.2.4.2 Coupler-Induced Backscattering

In addition to the waveguide roughness, the directional couplers should also be considered as a source of backscattering. Ideally, a directional coupler shown in Fig. 3.12(a) does not have any reflection r' and backcoupling k' , leaving only forward coupling k and transmission t . But this is not always the case: the experimentally determined increase in loss in coupling sections [25] indicates that this reflection component can be non-negligible in microrings.

There can be two different types of backscattering associated to a directional coupler (Fig. 3.12(b)):

1. The existence of an adjacent waveguide is actually a perturbation to the effective index of the original waveguide. So the beginning and end interface of a directional coupler can behave like scatterers due to an abrupt change in effective index. This scattering can couple to the backward propagating waveguide modes, i.e. an unwanted field backreflection r' to the input port and a backcoupling k' to the adjacent port. The more abrupt this transition from an isolated waveguide to a pair is, the stronger the scattering can be. The abruptness increases for smaller gap, so we can expect a larger backscattering of the coupling sections in rings with a smaller gap.
2. For directional couplers with long (straight) coupling section, the power is exchanged back and forth between the two waveguides, increasing the local field intensity at the internal walls, which is verified by a commercial FDTD simulator provided by Lumerical as illustrated in Fig. 3.22. Therefore, for the same waveguide length, there can be significantly higher backscattering by sidewall roughness compared to a single waveguide. The coupler roughness-induced backscattering is indicated as r_c . Similar to waveguides (equation (3.18)), the total reflected power $R_c = r_c^2$ has a form of:

$$R_c = H_c \times L_c, \quad \text{where} \quad H_c > H_w \quad (3.19)$$

3.2.4.3 Separation of Distributed and Lumped Backscattering

In our t-CMT model for a ring resonator, both backscattering r_{bs} and backcoupling k' are included. The backscattering r_{bs} consists of distributed backscattering caused by waveguide roughness (r_w), whose power reflectivity has a linear dependence on ring length L , and lumped reflection introduced by couplers (r' and r_c), whose power reflectivity should be independent on ring length, but dependent on couplers parameters, for instance, gap and coupling length. Based on this knowledge, assuming a low average total reflectivity during one roundtrip, only first order reflection contributions are taken into account. When the ring length

$L \ll \frac{1}{2\alpha_{loss}}$ we propose for low-field reflectivity r_{bs} a simple linear approximation of power reflectivity $R_{bs} = r_{bs}^2$:

$$R_{bs} = H_0 L + C_0 \quad (3.20)$$

$H_0 L_0$ refers to the distributed backscattering caused by roughness and C_0 covers the contribution from the couplers.

3.2.5 Quantitative analysis of backscattering

In previous section we proposed a quantitative prediction model for backscattering in ring resonator as in equation (3.20). According to this equation, the average backscattering strength is waveguide length and coupler section dependent with respective coefficients H_0 and C_0 . To make it valuable, these two coefficients have to be determined from measurements.

A set of rounded rectangular *add-drop* microrings (fixed $6.5\mu\text{m}$ coupling length and $4.5\mu\text{m}$ bend radius) with 7 different total ring lengths (150-1000 μm) and 6 different coupling gaps (150-400 nm) were measured in order to verify the model proposed in equation (3.20) and to extract these two coefficients. With this, we intend to verify that the sources of backscattering include circular waveguide roughness as well as directional couplers. All resonances between 1520 nm and 1560 nm are analyzed, using a 1pm resolution wavelength scan with a continuous-wave tunable laser and power meter in a vertical coupling setup. The devices were designed with the IPKISS framework [26] and fabricated at IMEC in a passive silicon photonics technology. The waveguide dimensions are $450\text{ nm} \times 220\text{ nm}$, embedded in oxide and excited with TE polarization using fiber grating couplers.

3.2.5.1 Extracting the Backscattering from model

With an accurate peak-fitting model we can now look deeper into the actual backscattering in SOI microrings. First of all, the strength of the backscattering will be mathematically extracted from measured spectra. By analyzing the transmission spectra at the *drop* port and the *add* port, the field backreflectivity r_{bs} for each individual resonance can be calculated. As the r_{bs} variation with wavelength has a strong stochastic component, we look at the mean and standard deviation of r_{bs} over the different resonances within the transmission spectrum of a single ring. For resonances that are visibly split, r_{bs} is calculated as:

$$R_{bs} = r_{bs}^2 = \mu_0^2 \frac{n_g L}{c} = \mu_0^2 \frac{\lambda_0^2}{c \times FSR_\lambda} \quad (3.21)$$

where FSR_λ is the free spectral range in wavelength domain, λ_0 is the central wavelength of the fitted resonance. All of these parameters, λ_0 , FSR_λ and μ_0 can

be directly extracted from the fit of the peak. From equations (3.14) and (3.15) equation (3.22) can be generated:

$$\Delta\omega_{bs} = \omega_1 - \omega_2 = 2\mu_0 \cos \frac{\phi_\mu}{2} = \frac{2\pi c}{\lambda_0^2} \Delta\lambda_{bs} \quad (3.22)$$

And as discussed in previous section, the ϕ_μ is always very close to 0, it's further simplified as:

$$\mu_0 = \frac{\pi c}{\lambda_0^2} \Delta\lambda_{bs} \quad (3.23)$$

Now in combination with equation (3.10), equation (3.24) can be generated.

$$\frac{\Delta\lambda_{bs}}{BW_\lambda} = \frac{\mathcal{F}r_{bs}}{\pi}, \quad (3.24)$$

Here $\Delta\lambda_{bs}$ refers to the wavelength spacing between the two peaks of a split resonance. $\mathcal{F} = \frac{FSR_\lambda}{BW_\lambda}$ is the finesse of the ring, where $\mathcal{F}/2\pi$ is the number of roundtrips light makes during the cavity lifetime. This equation mathematically describes the coherent addition of the backreflection contribution for each of the $\mathcal{F}/2\pi$ roundtrips.

However, for non-split peaks, the fitted parameter μ_0 is not always reliable, as the effect of the envelope shape on the properties of the individual peaks can be ambiguous: there are often multiple solutions for the resonance modes α_{cw} and α_{ccw} . Instead, the relative peak intensity at the *add* and *drop* port can be used to calculate r_{bs} . After some transformations of equations (3.7) and (3.6), we get

$$\frac{P_A}{P_D} = \frac{(\frac{\Delta\lambda_{bs}}{BW_\lambda})^2}{1 + (\frac{\Delta\lambda_{bs}}{BW_\lambda})^2} = \frac{(\frac{\mathcal{F}r_{bs}}{\pi})^2}{1 + (\frac{\mathcal{F}r_{bs}}{\pi})^2} \quad (3.25)$$

Similar to equation (3.24), the dependency on $\mathcal{F}r_{bs}$ reflects the coherent addition of reflection per roundtrip at resonance.

3.2.5.2 Separating Distributed and Lumped Backscattering

In equation (3.20) the total backscattering is separated into contributions by lumped scatterers (C_0) and by distributed scatterers (H_0), like sidewall roughness. H_0 depends on the electric field strengths at the sidewalls and the quality of sidewall. A lower value of H_0 can be obtained by using a better etch process, broader waveguides, or the TM polarization [4, 27].

We applied our model and extraction procedures to rings with different roundtrip length and coupling gaps. The propagation losses in the measured waveguides are of the order of $< 2dB/cm$ [28]. This makes, even if the additional losses in the coupling sections of small gap resonators are considered, the linear approximation in equation (3.20) a valid assumption.

The power reflectivity R_{bs} is plotted in Fig. 3.23, which confirms that the highest power reflection R_{bs} per roundtrip is of the order of 0.01, and therefore higher order reflection contributions can indeed be safely neglected in equation (3.20).

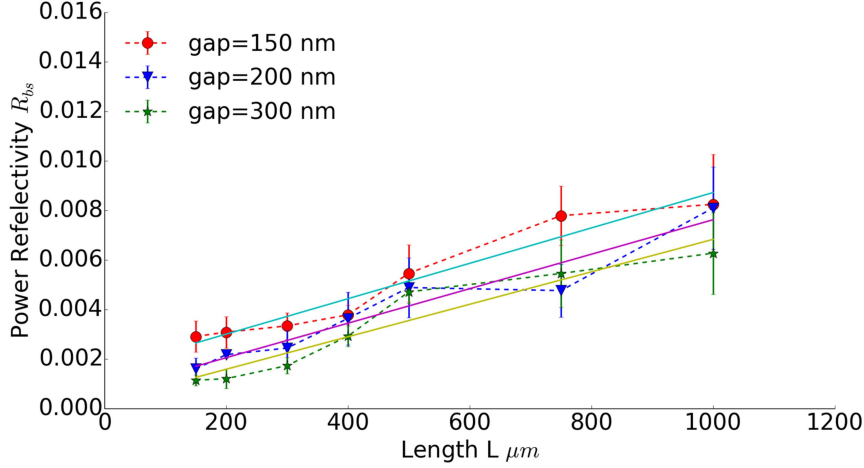


Figure 3.23: Power backscattering per roundtrip for rings with different roundtrip lengths and different directional coupler gaps. A linear increase of the backscattering for longer rings is observed, which corresponds to the distributed scattering H_0 . A decrease in backscattering for larger coupler gap is also shown, corresponding to the lumped scattering C_0 in the directional couplers.

It's clearly observable that the reflected power increases linearly with the ring length, confirming the length-dependent model from equation (3.20). It is also shown that for a larger coupler gap, the curve shifts down. This confirms that the directional coupler plays an important role in the lumped scattering contribution C_0 , and that smaller gaps will lead to stronger discontinuities and backscattering.

This is again confirmed in Fig. 3.24 where dependencies of C_0 and H_0 on the coupler gap are plotted. For all gaps, H_0 is quite stable around $6-8 \text{ m}^{-1}$, which corresponds well with the value reported in [5]. As H_0 represents the backscattering caused by sidewall roughness, it is indeed expected to be independent of the gap. In terms of C_0 , it is clearly shown in the same figure that rings with larger gap have smaller C_0 , meaning less backscattering induced by the couplers.

3.2.6 Coupler-Induced Backscattering

C_0 is more complicated to understand than H_0 . In reality, besides couplers the bend/straight transition might also introduce extra lumped reflections. These reflections could add a small contribution to C_0 that is independent of the coupling

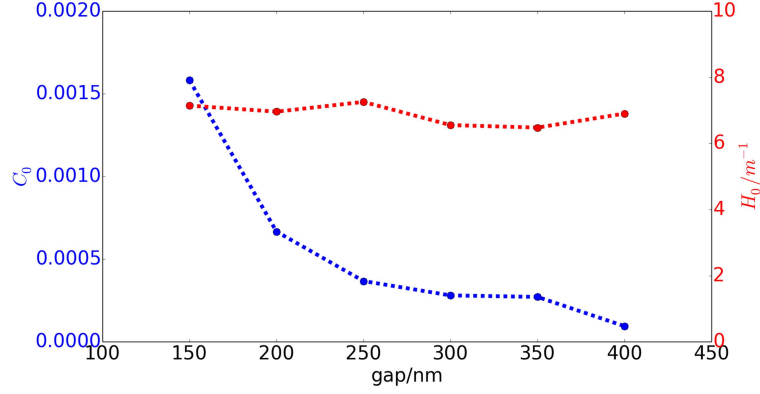


Figure 3.24: Fitted parameters H_0 and C_0 versus coupler gap. H_0 remains constant for different gaps, as it only depends on the ring waveguide roughness. And the value is well matched with formerly reported value. C_0 decreases for increasing gap, as the larger gap is, the smaller influence of directional coupler will be.

parameters. For simplicity, let's assume that the lumped contributions to backscattering solely originate in the directional couplers. The effect of the couplers is investigated by measuring another sets of rings with a fixed coupler gap (200 nm), 7 different ring roundtrip lengths (150-1000 μm), and 6 different coupling lengths (5-15 μm).

Figure 3.25 again plots R_{bs} as function of ring length, but now for directional couplers with 3 different coupler lengths. The curves with the longer coupling lengths L_c show a higher backscattering. Figure 3.26 quantifies how C_0 increases with coupling length L_c . H_0 also shows a slight increase, but less pronounced, and still within the range reported in [5]. The change in H_0 can also be due to a secondary effect: longer coupler lengths increase the ring linewidth, which affects the quality of the fit due to the existence of noise in the spectrum.

All of the data shown tell us that the coupler sections indeed introduce considerable reflections, and the strength of that reflection depends on both gap and coupling length.

3.2.7 Wavelength-dependent Model for Full-Spectrum Fitting

With the model discussed in the previous section, we could accurately fit every individual resonance separately.

However, in reality, there should be a constant set of parameters for the ring circuit instead of a unique set of parameters for each resonance. By claiming that each resonance has different parameters, i.e. backcoupling and backscattering, the

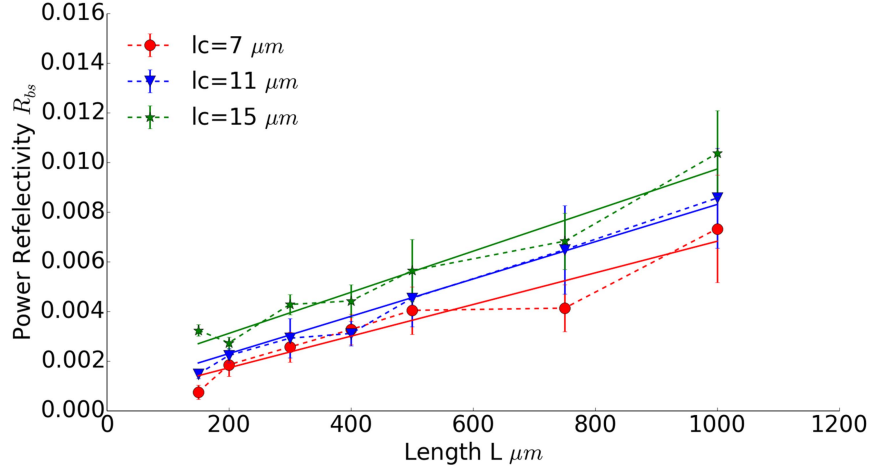


Figure 3.25: Power backscattering as function of ring roundtrip length for different coupling lengths L_c . The backscattering increases with larger roundtrip lengths, and with larger coupling length.

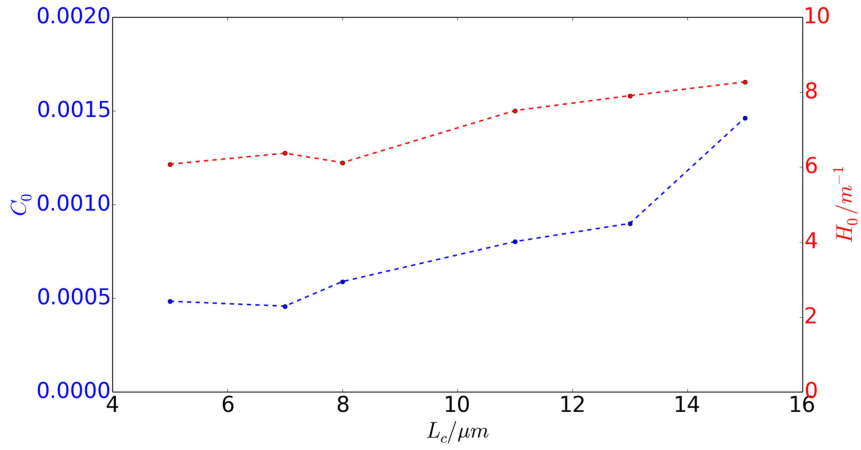


Figure 3.26: Fitted backscattering contributions H_0 and C_0 for different coupling lengths L_c . C_0 increases with increasing L_c , indicating more backscattering caused by directional couplers. H_0 remains in the expected range of $6-8m^{-1}$.

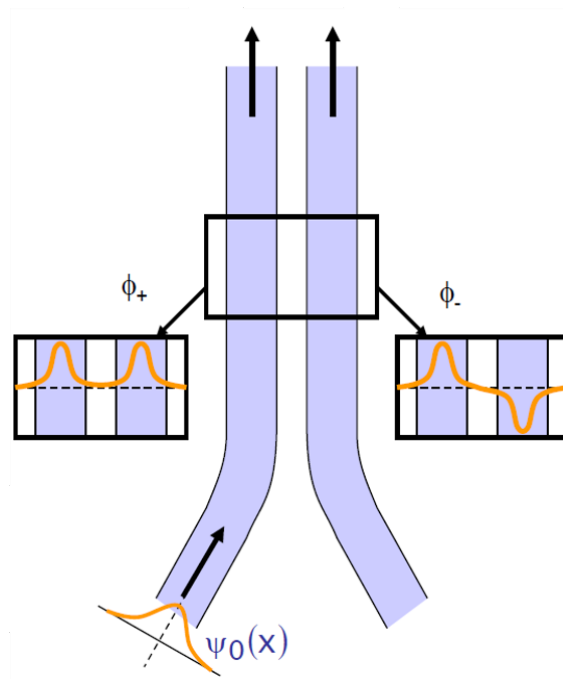


Figure 3.27: A directional coupler supports two supermodes, namely even and odd modes (or symmetric and anti-symmetric). The final output of a DC is a result of the interference between the two modes after the coupling length.

differences between resonances in a single spectrum could be explained. The question how to physically explain the differences between the parameters of different resonances within the same spectrum still remains.

Back to our former analysis, we remind ourselves that there are two individual contributions: roughness-induced backscattering and directional couplers. It has already been reported in [5] that the roughness-induced backscattering exhibits a degree of randomness, which might be a reason for the different shapes of resonances in a single spectrum. This is also analyzed in the previous section about backscattering in the waveguide. We show that the a waveguide with distributed backscattering is like a random walk model. Even each reflection event has the same amplitude, due to the random phase, the final transmission or reflection of the waveguide might end up at different values. So for different resonances, the same ring waveguide might generate quite different reflectivity. However, our analysis and measurement results in previous sections reveal that the strength of backscattering only influences the spectral separation of the two split peaks. In other words, the large differences in peak powers of each split-resonance cannot be explained by the randomness in backscattering.

When the layout of the system is considered, we see that for an add-drop filter, there are two couplers, so four scatterers in total. These four scatterers plus backscattering will form a complicated multi-cavity system in the ring circuit, which will show a certain wavelength dependency. In order to verify this, the circuit simulator Caphe with a detailed model for the ring circuit is used to fit the measured data. The objective function for the fitting is differential evolution [29], which is much more time consuming but rigorous than other simple algorithm using objective functions like least square. The wavelength span of the fitting procedure as well as the measured spectrum is chosen to be 20 nm with a 1 pm resolution, in order to incorporate enough resonances and include adequate data points within one single resonance. In this model, a basic directional coupler contains two independent 'waveguides' corresponding with the even and odd supermodes. The effective indexes are simulated using FIMMWAVE. The scatterers at the input and output stages of a directional coupler couple the individual waveguide mode to the supermodes as shown in Fig.3.27, and also add parasitic reflection and backcoupling. Thus, the parameters to be fitted include:

- Coefficients of a third-order polynomial equation describing the effective index of the ring waveguide versus wavelength.
- Coefficients of two second-order polynomial equations for the effective indexes of the two supermode waveguides.
- Reflection and backcoupling of these scatterers. They are assumed to be constant among all of these scatterers.

- Roughness induced backscattering strength for even and odd modes of the directional coupler.

Moreover, for the sake of both accuracy and efficiency, we'd prefer to implement a multi-stage fit, rather than a single fitting procedure that is fed with all parameters simultaneously. In detail, the effective index of the ring waveguide is first fitted to find the correct positions of the resonances. Then the effective indexes of the supermode waveguides are fitted to get the proper coupling strength of the directional couplers. Subsequently comes the fitting of these parasitics, including backscattering of the waveguide as well as backreflection and backcoupling of the scatterers. Usually it takes around 10 hours to finish all these fitting procedures.

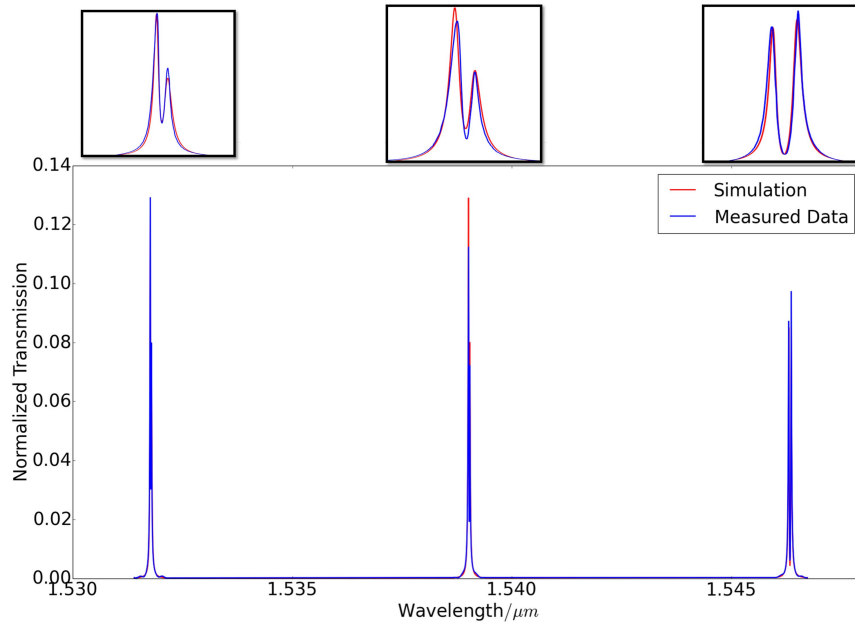


Figure 3.28: Fitting of a 75 μm long ring; here the circuit simulator caphe is used to fit a ring circuit, in other words, the complete spectrum is fitted instead of individual resonance.

Figure 3.28 and 3.29 show the fitting of two relatively short rings. Due to the limited number of resonances in the spectrum, the randomness of the backscattering does not play a significant role. Even if in our model backscattering is considered to be wavelength independent, a relatively good match between simulation and measured data can still be achieved, and the fitted parameters are consistent with previously fitting results or simulated values. For example, the power coupling ratio is in the order of 1×10^{-3} , similar to the value simulated by Lumerical FDTD Solutions, which is 3.6×10^{-3} . The fitted value of backcoupling of the

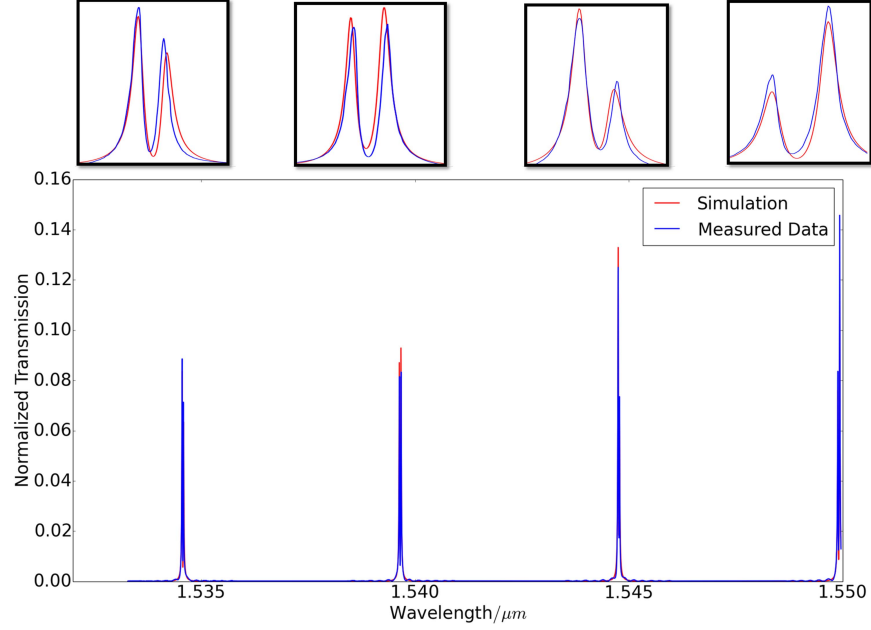


Figure 3.29: Fitting of a 100μm long ring, the good matching shows the reproducibility of this circuit fitting model.

directional coupler is in the order of 10^{-5} , in good correspondence with the previously reported f -factor for the electric field, which is from 0 to 0.3, i.e. from 0 to 0.09 for power.

Figure 3.30 shows the fitting result of a longer ring, with more than 10 resonances. Due to the large number of resonances here, the randomness of the backscattering can become quite influential and will have an impact on the fitting quality. As expected, the fitting mismatch increases, which can actually be considered as a measure for randomness of the distributed backscattering. Still, we can extract trends from this fitting.

In summary, we identify two reasons in order to explain why individual resonances in the same ring can be quite different, not only in split ratio, but also in asymmetry and bandwidths. The first one is due to the previously reported randomness in waveguide-roughness-induced backscattering, and this will affect the split ratio of the resonances. The second contribution is from the complicated directional couplers, which contain not only lumped multi-scatterers that introduce extra reflection and backcoupling but also distributed backscattering due to the sidewall roughness of the extra coupling length.

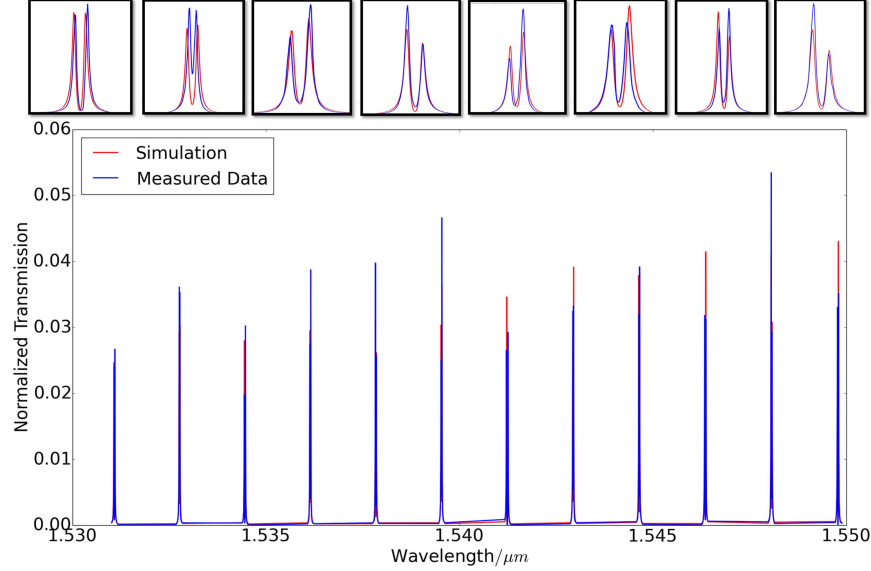


Figure 3.30: Fitting of a 300um long ring; Larger mismatch is expected, due to the randomness of roughness induced backscattering, which is not included in this circuit model. However, there is still a good match and it clearly shows the variety in split resonance shapes caused by multi-scatterers in the ring circuit.

3.2.8 Phase response of rings with resonance splitting

Besides the distortion in the amplitude transmission spectrum, backscattering is also supposed to impact the phase response of a ring resonator. To investigate this, we performed a series of simulation using caphe. Fig. 3.31 shows the simulated phase response at the *drop* port. With increasing reflectivity that couples CW and CCW modes, the resonance splitting becomes more and more obvious. In the meantime, we observe the change in the phase response. For an ideal ring resonator, the phase shows a continuous change around the resonance. While for a resonance with splitting, the phase change around the resonance becomes non-continuous.

3.2.9 Methods to suppress resonance splitting

After understanding the origin of the resonance splitting, a number of techniques to reduce or avoid resonance splitting can be suggested. Generally, the methods to suppress resonance splitting can be classified into four categories:

1. Improving the lithography and etching technology to reduce the sidewall roughness [4].

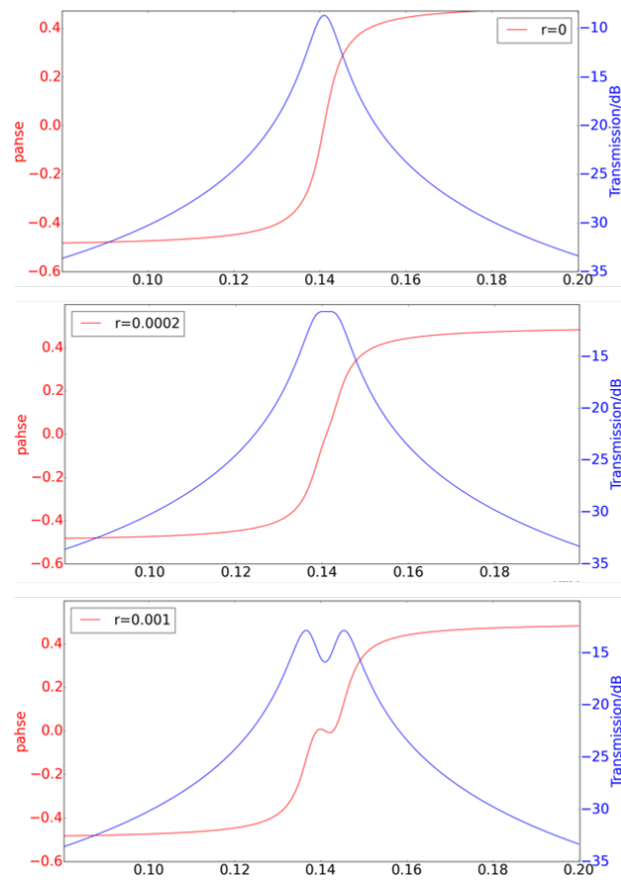


Figure 3.31: The backscattering will not only modify the resonance shape in amplitude spectrum, but also distorts the phase response.

2. Using TM polarisation or rib waveguides so that the sidewall sees weaker electric field [4, 27].
3. Lowering the Q factor, i.e. strengthening the coupling coefficient of the directional coupler(s). Among the 6 measured sets of rings with gaps from $0.15\ \mu\text{m}$ to $0.4\ \mu\text{m}$, there is a clear observable trend that resonance splitting is very rare in rings with gap of $0.15\ \mu\text{m}$. On the other hand, rings with a gap larger than $0.25\ \mu\text{m}$, almost invariably exhibit severe resonance splitting due to a narrower bandwidth/higher Q factor, as illustrated in Fig. 3.10. This is also confirmed by the simulation results plotted in Fig. 3.16.
4. Active compensation: either the backscattering r_{bs} or the backcoupling (f factor) of the whole ring circuit could be tailored. The former method relies on an intentional reflector inside the ring, whose reflectivity as well as phase could be tuned, to compensate the parasitic backscattering r_{bs} . As a consequence, the total ring circuit can be made to suffer no backscattering at all. The second method tunes the f factor to be 1, so that the input wave contributes equally to CW and CCW modes. As in equation (3.13), when $f = 1$, one peak of a split resonance disappears. In such a case, the parasitic backscattering as well as the resonance splitting still occurs, but one peak is suppressed at the output.

3.3 Summary

In this chapter we provide a comprehensive and in-depth analysis of backscattering in silicon waveguides and ring resonators, respectively. The impacts of backscattering on individual component observed through measurements are given. We found that the existence of backscattering makes silicon waveguides not wavelength independent elements any more. Their transmission spectra show strong and rapid fluctuations, and the fluctuation strength grows with waveguide length. We successfully build an optical circuit model with backscattering included to produce the transmission spectra similar with measurements and we also propose to explain a waveguide with backscattering using a mathematical model-random walk problem.

While for the ring resonators, we figure out the impacts of backscattering on the ring output spectra and the origins for asymmetric resonance splitting, which is the backcoupling at the directional couplers. We build a thorough theoretical model based on temporal coupled mode theory (tCMT) that is capable to fit all kinds of resonances. With this model, we further make a quantitative analysis of backscattering in silicon ring resonators with respect to the physical parameters of a ring, including roundtrip length, coupling gap and coupling length. Finally a circuit model that incorporates many parasitics of a ring resonator is built and

it can fit a complete ring spectrum with a common set of parameters for the ring instead of fitting resonance one by one with different sets of parameters for each resonance.

With this study on backscattering in silicon ring resonators, we are going to introduce an effective method based on reflection engineering to actively compensate the backscattering in next chapter.

References

- [1] Pieter Dumon, Wim Bogaerts, Vincent Wiaux, Johan Wouters, Stephan Beckx, Joris Van Campenhout, Dirk Taillaert, Bert Luyssaert, Peter Bienstman, Dries Van Thourhout, et al. *Low-loss SOI photonic wires and ring resonators fabricated with deep UV lithography*. IEEE Photonics Technology Letters, 16(5):1328–1330, 2004.
- [2] Wim Bogaerts, Roel Baets, Pieter Dumon, Vincent Wiaux, Stephan Beckx, Dirk Taillaert, Bert Luyssaert, Joris Van Campenhout, Peter Bienstman, and Dries Van Thourhout. *Nanophotonic waveguides in silicon-on-insulator fabricated with CMOS technology*. Journal of Lightwave Technology, 23(1):401–412, 2005.
- [3] Kuan Pei Yap, André Delâge, Jean Lapointe, Boris Lamontagne, Jens H Schmid, Philip Waldron, Barry A Syrett, and Siegfried Janz. *Correlation of scattering loss, sidewall roughness and waveguide width in silicon-on-insulator (SOI) ridge waveguides*. Journal of Lightwave Technology, 27(18):3999–4008, 2009.
- [4] Francesco Morichetti, Antonio Canciamilla, Carlo Ferrari, Matteo Torregiani, Andrea Melloni, and Mario Martinelli. *Roughness induced backscattering in optical silicon waveguides*. Physical Review Letters, 104(January):1–4, 2010.
- [5] Francesco Morichetti, Antonio Canciamilla, and Andrea Melloni. *Statistics of backscattering in optical waveguides*. Optics letters, 35:1777–1779, 2010.
- [6] Daniele Melati, Andrea Melloni, and Francesco Morichetti. *Real photonic waveguides: guiding light through imperfections*. Advances in Optics and Photonics, 6(2):156–224, 2014.
- [7] Y. Xing, A. Li, R. Van Laer, R. Baets, and W. Bogaerts. *Backscattering induced transmission noise and length dependent attenuation in silicon waveguides*. In Proceedings of the 21th Annual Symposium of the IEEE Photonics Society Benelux Chapter, 2016.
- [8] Bo Peng, Jessie Rosenberg, Wesley D Sacher, Asger S Jensen, Marwan Khater, William MJ Green, and Tymon Barwicz. *Distributed backscattering in production O-band Si nanophotonic waveguides*. Optics Express, 25(19):23477–23485, 2017.
- [9] Antonio Canciamilla, Matteo Torregiani, Carlo Ferrari, Francesco Morichetti, Raffaella Costa, and Andrea Melloni. *Backscatter in integrated*

- optical waveguides and circuits*. In Proc. SPIE, volume 7218, page 72180N, 2009.
- [10] Diedrik Vermeulen, Yannick De Koninck, Yanlu Li, Emmanuel Lambert, Wim Bogaerts, Roel Baets, and Günther Roelkens. *Reflectionless grating couplers for Silicon-on-Insulator photonic integrated circuits*. Optics express, 20(20):22278–22283, 2012.
- [11] Yanlu Li and Roel Baets. *Improved multi-mode interferometers (MMIs) on silicon-on-insulator with the optimized return loss and isolation*. In 16th Annual Symposium of the IEEE Photonics Benelux Chapter, Belgium, 2011.
- [12] Wim Bogaerts, Pieter Dumon, Dries Van Thourhout, and Roel Baets. *Low-loss, low-cross-talk crossings for silicon-on-insulator nanophotonic waveguides*. Optics letters, 32(19):2801–2803, 2007.
- [13] Sam Werquin, Steven Verstuyft, and Peter Bienstman. *Integrated interferometric approach to solve microring resonance splitting in biosensor applications*. Optics express, 21(14):16955–16963, 2013.
- [14] Michele Moresco, Marco Romagnoli, Stefano Boscolo, Michele Midrio, Matteo Cherchi, Ehsan Shah Hosseini, Douglas Coolbaugh, Michael R Watts, and Birendra Dutt. *Method for characterization of Si waveguide propagation loss*. Optics express, 21(5):5391–400, March 2013.
- [15] Haifeng Shao, Xiaoqing Jiang, Jianyi Yang, Yingtao Hu, Gunther Roelkens, and Hui Yu. *Photonic-Assisted Microwave Frequency Doubling based on Silicon Ring Modulator*. In IEEE Photonics Conference 2014, pages 222–223, 2014.
- [16] Ziyang Zhang, Matteo Dainese, Lech Wosinski, and Min Qiu. *Resonance-splitting and enhanced notch depth in SOI ring resonators with mutual mode coupling*. Optics express, 16:4621–4630, 2008.
- [17] G C Ballesteros, J Matres, J Mart, and C J Oton. *Characterizing and modeling backscattering in silicon microring resonators*. Optics Express, 19(25):24980–24985, 2011.
- [18] Siddharth Tallur and Sunil a Bhawe. *Rayleigh scattering boosted multi-GHz displacement sensitivity in whispering gallery opto-mechanical resonators*. Opt. Express, 21(23):27780–27788, 2013.
- [19] B.E. Little, S.T. Chu, H.a. Haus, J. Foresi, and J.-P. Laine. *Microring resonator channel dropping filters*. Journal of Lightwave Technology, 15(6):998–1005, June 1997.

- [20] Miloš A Popović. *Theory and Design of High-Index-Contrast Microphotonic Circuits*. PhD thesis, 2008.
- [21] Qiang Li, Ziyang Zhang, Jing Wang, Min Qiu, and Yikai Su. *Fast light in silicon ring resonator with resonance-splitting*. Optics express, 17(2):933–940, 2009.
- [22] Fabio Turri. *Experiments and modelling of vertically coupled Microresonators*. PhD thesis, University of Trento, 2017.
- [23] F. Morichetti, a. Canciamilla, M. Martinelli, a. Samarelli, R. M. De La Rue, M. Sorel, and a. Melloni. *Coherent backscattering in optical microring resonators*. Applied Physics Letters, 96(May):13–15, 2010.
- [24] Wim Bogaerts, Pieter Dumon, D Van Thourhout, Dirk Taillaert, Patrick Jaenen, Johan Wouters, Stephan Beckx, Vincent Wiaux, and Roel G Baets. *Compact wavelength-selective functions in silicon-on-insulator photonic wires*. Selected Topics in Quantum Electronics, IEEE Journal of, 12(6):1394–1401, 2006.
- [25] Fengnian Xia, Lidija Sekaric, and Yurii a Vlasov. *Mode conversion losses in silicon-on-insulator photonic wire based racetrack resonators*. Optics express, 14(9):3872–86, May 2006.
- [26] Martin Fiers, Emmanuel Lambert, Shibnath Pathak, Bjorn Maes, Peter Bienstman, Wim Bogaerts, and Pieter Dumon. *Improving the design cycle for nanophotonic components*. Journal of Computational Science, 4(5):313–324, 2013.
- [27] Peter J De Heyn, Bart Kuyken, Diedrik Vermeulen, Wim Bogaerts, and Dries Van Thourhout. *High-performance low-loss silicon-on-insulator microring resonators using TM-polarized light*. In Optical Fiber Communication Conference, page OThV2. Optical Society of America, 2011.
- [28] Wim Bogaerts, Peter De Heyn, Thomas Van Vaerenbergh, Katrien De Vos, Shankar Kumar Selvaraja, Tom Claes, Pieter Dumon, Peter Bienstman, Dries Van Thourhout, and Roel Baets. *Silicon microring resonators*. Laser & Photonics Reviews, 6(1):47–73, 2012.
- [29] P Rocca, G Oliveri, and A Massa. *Differential evolution as applied to electromagnetics*. Antennas and Propagation Magazine, IEEE, 53(1):38–49, 2011.

4

Engineered reflections in silicon ring resonator with one tunable reflector

4.1 Introduction

In the previous chapter, we thoroughly explained and modeled the problem of backscattering in silicon waveguides and ring resonators. We show the origins and impacts of backscattering on these components. Generally speaking, stochastic backscattering behaves like a lumped reflector inside a ring cavity. So if we were able to fully control the total reflections inside the ring resonator, we should be able to control its output spectra. And under the condition that the reflection approaches 0, the backscattering can be fundamentally suppressed.

To achieve a full control of the reflections, we need an intentional reflector inside the ring cavity, whose reflectivity and phase are tunable. In this chapter, we will discuss about such a reflector and how we realize reflections engineering in silicon ring resonator with such a tunable reflector. Two applications of this kind of device will be shown. The first one is the fundamental suppression of stochastic backscattering while the second one is to make a silicon ring resonator with an ultra wide FSR and tuning range.

4.2 Fundamentally suppress backscattering by reflection engineering inside silicon ring resonator

Given the severity and high frequency of backscattering in silicon ring resonators, many efforts have been done to explain, originate and model backscattering in silicon ring resonators. However, there have been very few effective approaches reported to fundamentally suppress it or eliminate its impacts. Based on former discussion, we are aware that lowering the Q factor (broadening the resonance) will efficiently avoid resonance splitting. But this method lacks control of reflection to the *in* port and leakage to the *add* port. Moreover, the Q factor is actually a very key factor for ring resonator based devices and usually it's desirable to have a high Q factor. For instance, ring resonator based sensors require a high Q for the sake of high efficiency and resolution. So this method is only a compromise approach that is simple in design but poor in performance and may not be a good idea for most ring based applications.

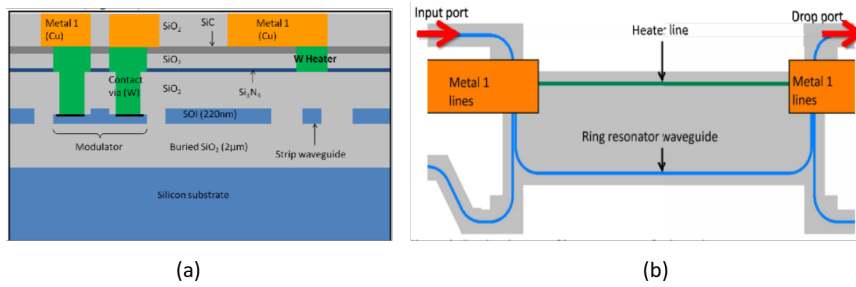


Figure 4.1: (a) An example figure from Ref. [1] about a tungsten contact via and heater for silicon modulator as well as strip waveguide. (b) A brief layout from the same literature showing the heater used to tune a ring resonator.

Using TM polarization on the other hand, can fundamentally avoid backscattering inside the ring cavity. But it also has some key drawbacks. The use of TM polarization makes the light less confined, thus the minimum bend radius (around $25 \mu m$) should be quite large compared to the ring with TE polarized light ($4.5 \mu m$) to avoid bend radiation loss. This sacrifices the compact footprint of the silicon ring resonator, which is one of key advantages brought by silicon photonics. Another disadvantage is about the tuning of a ring resonator. One reason why ring resonators are so popular is that their resonance is very sensitive to environment, so the tuning can be easily and efficiently achieved. Metal heaters on top of the ring resonators are one of the most popular approaches to tune the ring resonators as briefly illustrated in Fig. 4.1 [2–6]. However, metal can absorb light significantly so there should be certain distance between the heaters and waveguides to avoid loss. But this distance, on the other hand, affects the tuning efficiency. Since the

electric field of TM polarized light is vertically polarized making it more sensitive to the upper cladding as shown in Fig. 2.20. Consequently, the heaters should be further away for rings with TM polarization and this will increase the power consumption of the heaters to achieve the same tuning range. Moreover, TM light is less confined than TE polarization in a waveguide with the same cross-section. As a result, light in TM polarization is less sensitive to the index change in the waveguide core. This fact also lowers the tuning efficiency for waveguides with TM polarization.

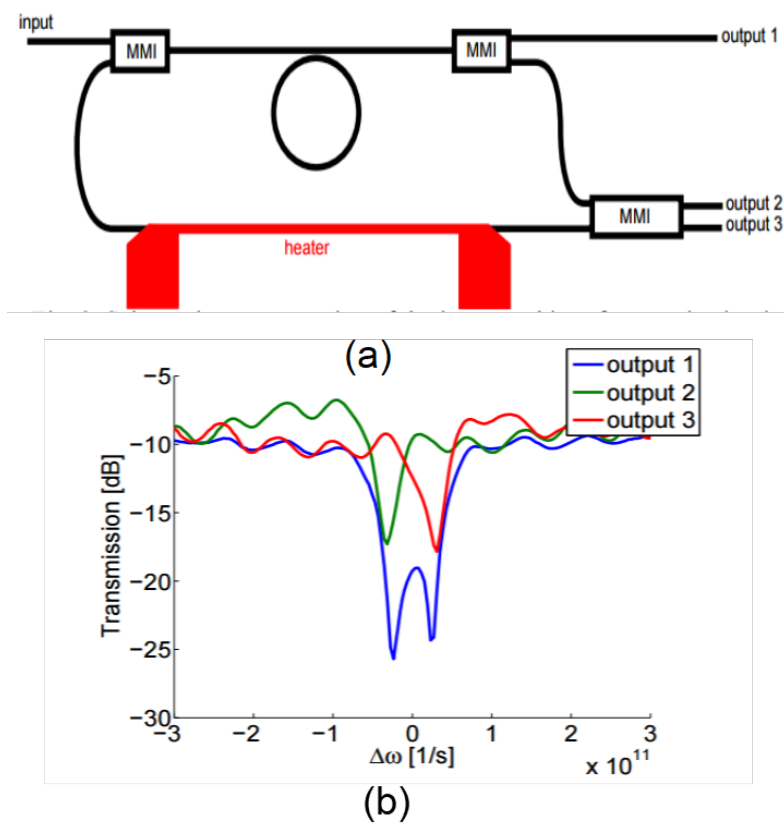


Figure 4.2: Schematic (a) and experimental results (b) of the interferometric approach to eliminate resonance splitting induced by backscattering proposed in Ref. [7].

Werquin et al. [7] have proposed an approach based on the interference of light from the pass port and the reflection of the ring resonator as shown in Fig. 4.2. By tuning the relative optical length of these two paths, one peak of the split-resonance will be suppressed. However, it works only for an individual resonance as each resonance splitting condition may be notably different. Besides, the cor-

rected resonance, even if it's non-split, has a lower quality compared to the original resonance in terms of extinction ratio. What's more, the backreflection cannot be fixed in this way. Another drawback is that this solution only works for the *through* port, thus for the all-pass ring resonator configuration.

In this section we will give a theoretical characterization and experimental demonstration of one method briefly introduced in the last section, that is using an intentional reflector to compete with stochastic backscattering r_{bs} . This method, instead of post-processing resonances out of ring resonators, can fundamentally suppress backscattering inside the ring cavity. Thus all impacts brought by backscattering can be handled. Not only resonance splitting will be eliminated but also the reflection to the *in* port and leakage to the *add* port can be reduced.

4.2.1 An integrated tunable reflector

The idea follows our study of backscattering in silicon ring resonator. It's concluded that total backscattering in a ring resonator including sidewall roughness induced backscattering as well as directional coupler induced backreflections can be simply represented by a reflector with a given reflectivity and phase. Naturally if we can take control of the total reflectivity inside the ring, we can then fully control the impacts brought by reflections and under correct condition, all the impacts shall be cancelled out if the total reflectivity can be fully suppressed. In order to do so, we need an integrated reflector to be put inside the ring that can be dominant over the backscattering. The reflector should be widely tunable as the backscattering itself is quite stochastic, making it impossible to accurately know its reflectivity and phase. Actually there have already been quite some studies about implementing Bragg reflectors inside ring resonators to achieve certain control of reflectivity [8, 9]. However, backscattering suppression can not be realized based on these structures due to the poor tunability of the Bragg reflectors.

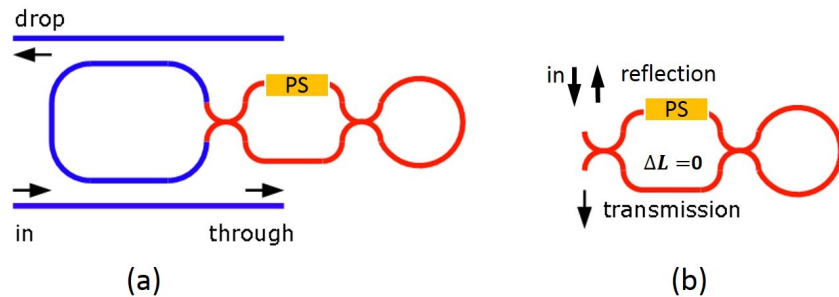


Figure 4.3: Schematics of the ring with a reflector and the reflector itself, respectively.

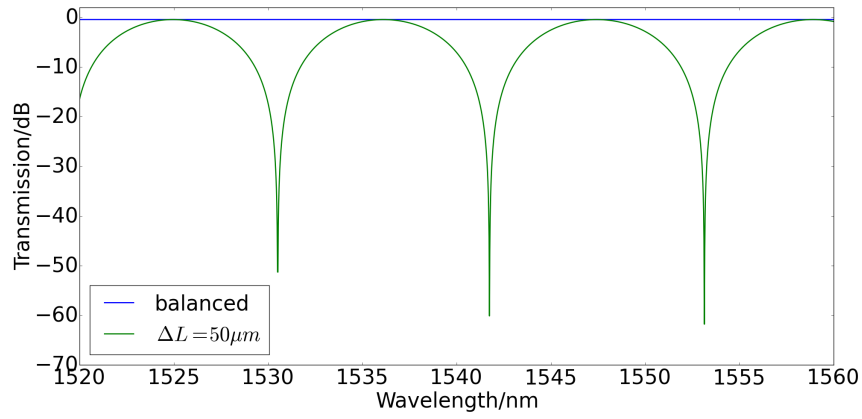


Figure 4.4: Simulated transmission spectrum of a MZI with (a) balanced arms and (b) length difference between two arms.

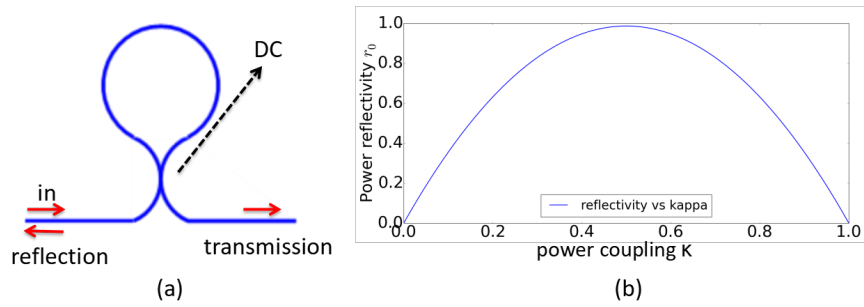


Figure 4.5: Schematic of a Sagnac mirror (a) and its reflectivity as a function of the coupling coefficient κ (b).

We propose a novel type of integrated tunable reflector as shown in Fig. 4.3(b). The reflector itself is a sub-circuit consisting of a Mach-Zehnder-Interferometer (MZI) with a loop end. MZI is another very popularly used device in various photonics applications. It consists of one splitter that splits incoming light into two beams and they will propagate through two arms whose lengths determine the relative phase conditions of the two beams when they arrive at the combiner. The outputs at two ports of the combiner depend on the phase difference between the two beams. If two arms are identical, it's usually called a balanced MZI, which can produce a relatively flat optical transmission spectrum. When length difference ΔL is introduced between two arms, the output spectrum will show a periodic wavelength response as shown in Fig. 4.4. In integrated optics, the splitter and combiner are usually chosen to be directional couplers (DC) or multi-mode-interferometers (MMI). The former one has an advantage of compact footprint. In silicon photonics, it typically has the length around 10s of μm or even shorter, depending on the gap. But it is very sensitive to the fabrication variation. According to Ref. [10], a normal silicon directional coupler has a sensitivity to fabrication variation at $\frac{\Delta L_{3dB}}{\Delta g} \approx 300nm/nm$, where L_{3dB} is the length required to get a 3 dB split ratio, i.e. 50/50 splitter, and g represents the gap. In other words, for a designed 50/50 splitter with a gap at 230 nm. A gap change of ± 20 nm around 230 nm which is quite realistic in silicon photonics, the split ratio will change from 65% to 35%. The MMI, on the other hand, outperforms DC in terms of robustness to fabrication variation. But this comes at the price of higher insertion loss (typically 0.3-0.5 dB [10]) and larger footprint (over $100\mu m$ long for a 2×2 MMI). In this reflector, we choose DC in order to keep the total roundtrip length of the ring resonator short.

Our reflector can be treated as a MZI whose two outputs are connected with a loop. Alternatively it can be considered as a special Sagnac mirror whose directional coupler is replaced by a MZI. This way helps to understand its principle easier. A Sagnac mirror shown in Fig. 4.5 is a 2-port device that provides fixed reflectivity at a certain wavelength. It is a loop ended directional coupler, whose coupling coefficient determines the reflectivity of the mirror as evident in Fig. 4.5(b). And a MZI is just a "tunable" 2×2 directional coupler with a tunable split ratio between its two outputs. Thus by tuning the MZI's split ratio, the reflectivity of the Sagnac mirror also becomes tunable. The reflection and transmission coefficients of a Sagnac mirror is given in equation (4.1):

$$r = 2j\kappa t E_0 e^{j\phi_L}, t = (t^2 - \kappa^2) E_0 e^{j\phi_L} \quad (4.1)$$

Where E_0 represents the input electric field strength, κ and t are the field coupling and transmission coefficients of the directional coupler, respectively. ϕ_L refers to the phase induced by the loop waveguide. Clearly, when $\kappa = t$, all the light will be reflected.

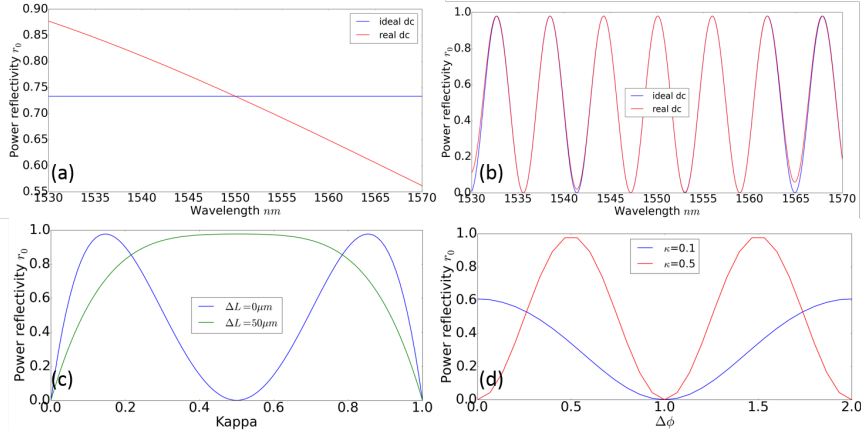


Figure 4.6: Simulated reflection spectrum of the tunable reflector. (a) $\Delta L = 0$ produces a flat spectrum. (b) $\Delta L = 50$ shows a strong, periodic wavelength dependence oscillating between 0 and 100%. Blue and red corresponds with an ideal directional coupler case and a realistic directional coupler case, respectively. The reflection does not reach 100% because of the small propagation loss of the waveguides which is taken into account. (c) The reflectivity also depends on the coupling coefficients κ of the two DCs. (d) Simulated tunability of such a reflector. When κ is in the range 0.15-0.85, Adding 0.5π phase shift in one arm can generate a change in reflectivity from 0 to 100%.

The key parameters that determine the reflection spectrum of our reflector are listed :

- The armlength of the phase shifter L_1 .
- The length difference $\Delta L = L_1 - L_2$ between two arms.
- The coupling coefficients κ_1 and κ_2 .

L_1 should not be too short in order to provide sufficient phase shift to tune the reflectivity. And it shouldn't be too long either, as it contributes to the ring cavity roundtrip length. In terms of the length difference ΔL , it is mainly responsible for the FSR of the reflection spectrum, as $FSR = \frac{\lambda^2}{n_g \Delta L}$. When $\Delta L = 0$, it's a relatively flat spectrum similar to the MZI as shown in Fig. 4.6(a), while the spectrum starts to become wavelength dependent when ΔL grows as also evident in Fig. 4.6(b). In these figures, both two curves corresponding with "ideal DC" and "real DC" are drawn. Ideal DC means the directional couplers in the circuit model are wavelength independent. While real DC represents the real world where each wavelength has a slightly different coupling coefficient of the same DC. In our circuit model, it's approximately to linear dependency. In reality, the wavelength dependency of a DC is more complicated than linear. But a linear dependency here

is accurate enough to show the influence of DC on the reflector's performance. Any higher-order dependence does not affect our analysis in any substantial way.

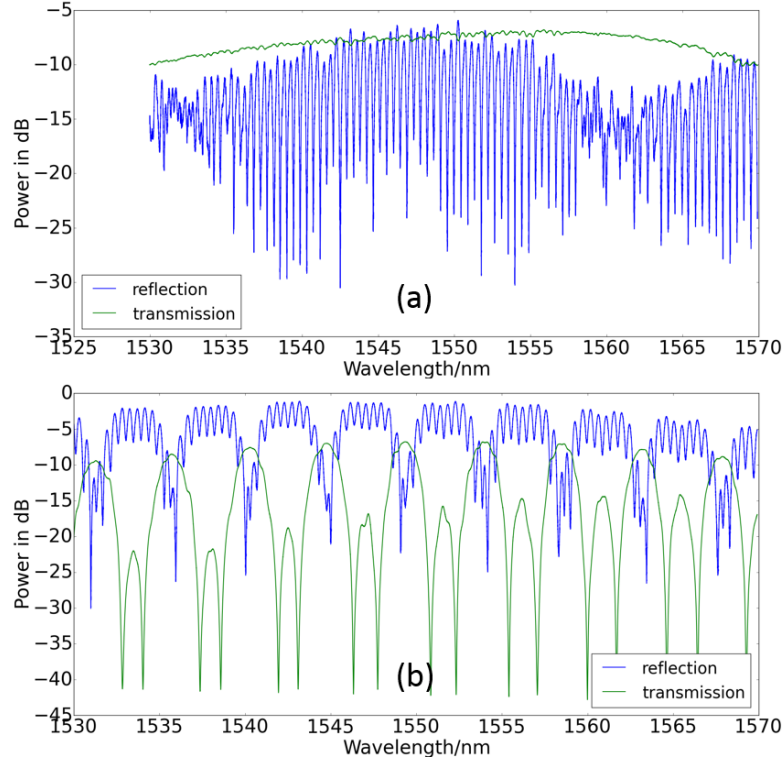


Figure 4.7: Measured reflection and transmission spectra of two different reflectors. (a) shows the balanced reflector with a flat spectra and (b) presents the results of an unbalanced reflector with periodic in spectra. The strong ripples in the reflection spectra are due to the reflection happening at the fiber/air facet as well as air/chip facet.

Static measurements of the reflector's spectra confirm the simulations. In Fig. 4.7, both flat and strongly wavelength dependent reflection spectra are observed with different ΔL . The measurement is performed using vertical coupling setup and it has a severe problem for the reflection spectrum, which are the strong ripples. They are due to the interference between signal and those parasitic reflections happening at different interfaces including fiber/air, air/chip and grating coupler/waveguide as briefly illustrated in Fig. 4.8. The former two are the main contributions due to large index difference. We also notice the difference in the amplitudes of the ripples in Fig. 4.7(a) and (b). This is due to the difference in their reflectivity. When the signal strength (reflector's reflectivity) has the similar magnitude as the parasitic reflections, their interference generate a larger extinction ratio. While if two beating signals have very different strength, their interference

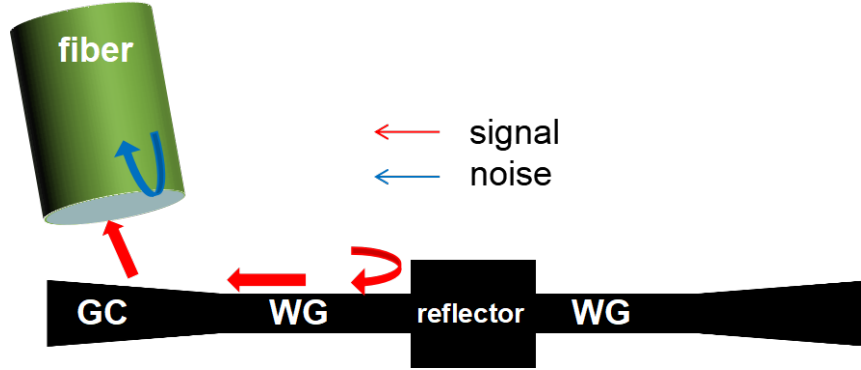


Figure 4.8: A brief illustration showing that the measured spectrum is an interference pattern between the light reflected by the reflector (signal) and the parasitic reflections (noise), for instance, the fiber-air facet induced reflection.

only generates small ripples.

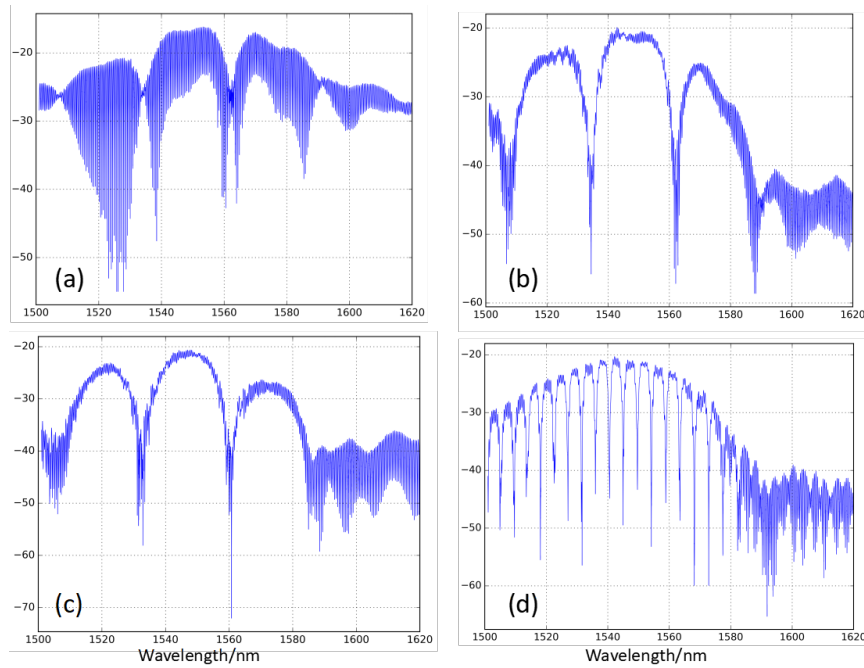


Figure 4.9: Measured reflection and transmission spectra of different reflectors using index matching fluid to suppress the parasitic reflections and reveal the real reflection spectra of the reflectors. (a) shows the results without this fluid. (b) is the spectrum of the same reflector using fluid. (c) and (d) are measured spectra of two other reflectors.

Another experiment is performed in order to suppress the parasitic reflections by filling the gap between fiber and chip with index matching fluid. It has an index around 1.52 which is very close to the fiber core index. Clearly, the results plotted in Fig. 4.9 are much cleaner.

The influence of coupling coefficient κ on its reflectivity can be more straightforward observed from Fig. 4.6(c) and (d), which shows the reflectivity at 1550 nm as a function of κ and the tunability of the reflectivity under different κ . We notice that κ has to be in the range of 15% to 85% in order for the reflector to provide the reflectivity range from 0 to 100%. This is similar and in consistence with former research about MZIs, where it shows that κ has to be in the same range in order for a 3 stage cascaded MZI to be able to operate at 50/50 split ratio [11]. The reason behind this is simple: if the κ is less than 15% or more than 85%, a MZI can not provide an extinction ratio larger than 3 dB in its transmission spectrum.

The simulated tunability of the reflector shows that only $\frac{\pi}{2}$ radians added to the phase shifter could lead to a reflectivity change from 0 to 100%. This can be easily achieved by thermo-optic tuning with relatively low power consumption. And the active measurement proves that 6 mW consumed by the metal heater can lead to a 35 dB change in its reflectivity/transmission as evident in Fig. 4.10. Use of more efficient heater can further reduce the power consumption. The broad tuning range and simple tuning mechanism are the key features that make it possible to compensate the stochastic backscattering in ring resonator.

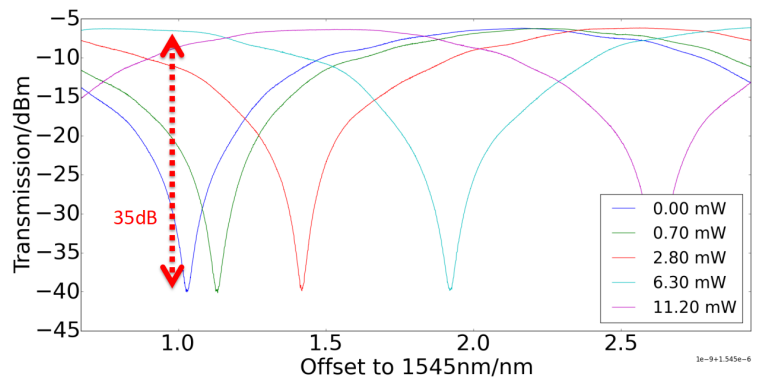


Figure 4.10: Active measurement of the reflector with metal heater shows that 6 mW will change its reflectivity as much as 35 dB.

In order to test our hypothesis, we built a circuit model for a ring resonator with backscattering in *caphe*. According to our model presented in [12], backscattering can be treated as a lumped reflector with a constant reflectivity but a random phase. So such a lumped reflector is added in the ring circuit for the stochastic backscattering. Moreover, additional parasitic reflections and backcoupling at the

directional couplers are also included. The results of this circuit without and with our reflector are shown in Fig. 4.11. Obviously, without the intentional reflector, the spectrum shows resonance-splitting due to the existence of backscattering and other parasitics. The asymmetry in some split resonances and the diversity in these resonances can be attributed to additional parasitic effects, namely reflections and backcoupling at the directional couplers [12].

By introducing our reflector and adjusting the phase in one arm, the total reflectivity inside the ring can be controlled, and as a consequence, the resonance shape evolves from visibly split to non-split. And note that, during the modulation period, one peak of the split resonance wavelengths hardly changes with only the other one keeping moving. The principle behind this is simple: the resonance splitting will create two peaks on both sides of the original resonance. One is blue shifted (R_b) and the other one is red shifted (R_r), with a separation that depends linearly on the coupling strength between the CW and CCW propagating modes, and this is given by the reflectivity of the cavity reflector [12]. The phase shift of the tuner in the MZI reflector will add an increment to the total optical length of the ring cavity, thus leading to a redshift of the entire spectrum (both R_b and R_r). At the same time this phase shift will increase the reflectivity, and thus R_b will experience an additional blueshift due to the increase of the separation, effectively cancelling the redshift and keeping R_b in place. For the redshifted resonance R_r , the two effects add up.

When the phase shift in the MZI induces the maximum, near-100% reflectivity (or 0% transmission), the peak separation is maximum, at half the FSR of the original ring resonator: the shifted resonance R_r is now exactly in between its corresponding R_b and the R_b of the adjacent resonance. This can be easily understood as now the ring cavity is cut in one place, turning it into a Fabry-Perot cavity with twice the roundtrip length. This confirms that now the travelling wave cavity is turned into a standing wave cavity. Increasing the phase shift further will start to decrease the reflectivity, but with a flip in phase. This will continue to shift the R_r peak, now reducing the separation with the next resonance's R_b , eventually merging with the resonances. At that point, the phase shifters have added 2π phase shift to the circumference of the ring, effectively increasing the order of each resonance with 1. Note that, the phase shifter in the MZI only controls the relative positions of the split peaks. To control the absolute position of the resonances, an additional thermal tuner can be added in the main loop of the ring, or a global temperature control can be used.

To further investigate the phenomenon of this shift pattern and show it more clearly, we performed other simulations and realize that it depends on the directional couplers of the reflector. If it's a perfect 50/50 splitter, the left peak R_b of the split resonance doesn't shift at all during one modulation period of the reflectivity provided by the reflector (from 0 to 100%, then back to 0), as shown in the top

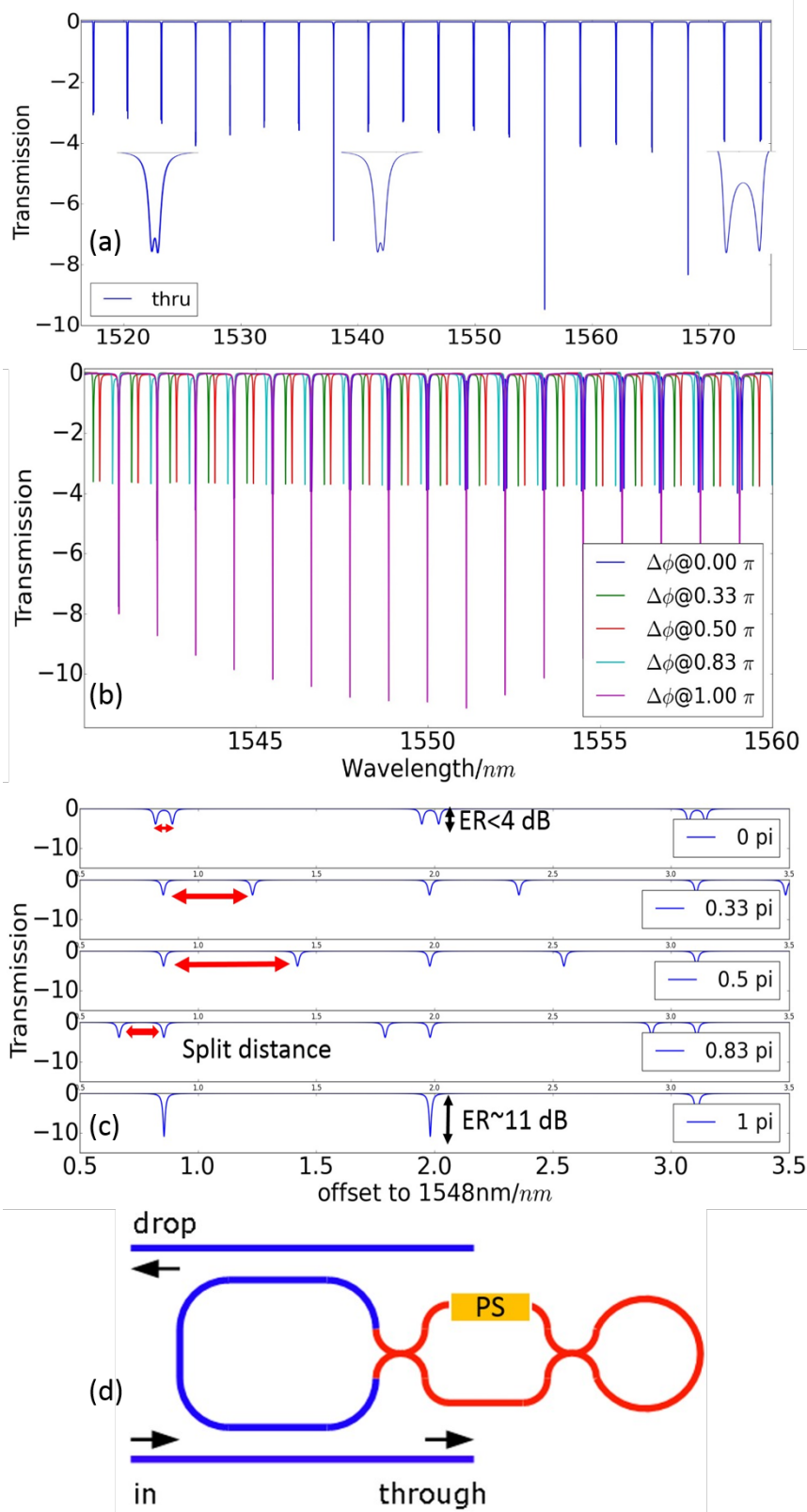


Figure 4.11: Simulated through port spectrum of a ring circuit with only backscattering and other parasitics in the circuit, including reflections and backcoupling at the directional couplers (a), and with both backscattering and tunable reflector (b) and (c). It shows clearly how the resonance shape evolves with phase shift. (d) gives the brief schematic of the device with a phase shifter.

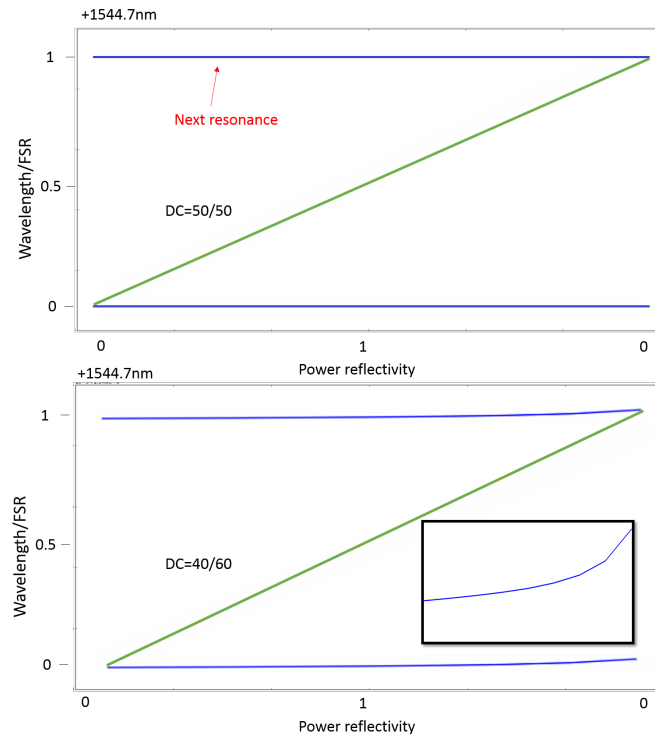


Figure 4.12: During the one modulation period of the power reflectivity of the reflector (from 0 to 100%, then return to 0), the two peaks shift at different speed. If the DCs of the reflector are 50/50 splitter, then one peak doesn't shift at all as shown in the top figure. While if the DCs are not 50/50, for instance a 40/60 case in the bottom figure, the peak slightly shifts.

figure in Fig. 4.12. If it's not a 50/50 splitter, for instance a 40/60 splitter due to fabrication variation, the left peak R_b slightly shifts as evident in the bottom figure in Fig. 4.12. The inset in the bottom figure is a zoom view of the blue curve, to show that it increases slightly.

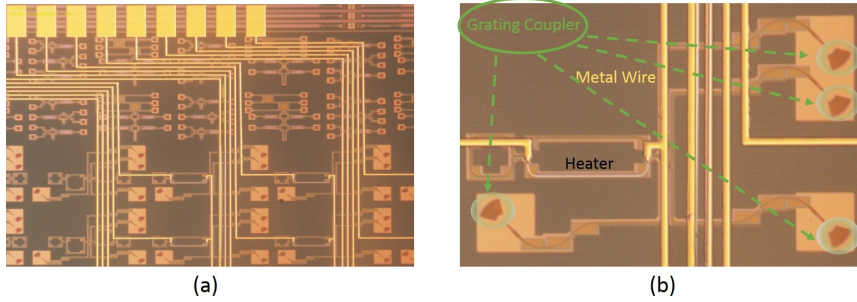


Figure 4.13: Microscopic images of the fabricated devices with in house processed metal heaters. (a) presents the overview of the chip and (b) provides zoomed view of one single device.

To demonstrate our method, we designed and fabricated these structures through IMEC 200 mm CMOS technology line via Europractice MPW service. The waveguide cross-section is designed to be $450 \text{ nm} \times 220 \text{ nm}$. The sample is covered by a planarized oxide cladding for the convenience of metal heaters we are going to process, as shown in Fig. 4.13. The heaters consist of a titanium resistive element connected with gold contact electrodes. The Ti heater has a $2 \mu\text{m}$ width and 100 nm thickness. A $200 \mu\text{m}$ long Titanium heater usually has a measured resistance $\approx 1 \text{ K}\Omega$. For the device, we choose the two arms of the MZI reflector to be identical, with a length of $200 \mu\text{m}$, to make sure sufficient phase shift can be achieved. The measurement results show that 15 mW can give a π phase shift of our heater. This is over-dimensioned to demonstrate the concept: experimental results show that the length of the MZI arms can be shortened to $70\text{-}100 \mu\text{m}$, even without the use of more efficient heaters.

As a reference to our actively compensated ring resonator we use two ring resonators without reflectors inside, located close to our device on the same chip to prove the existence and influence of actual backscattering. This is necessary as backscattering, especially those from sidewall roughness, is fabrication quality dependent. To demonstrate our method of suppressing backscattering, we need first to assess the backscattering statistics of this run. These rings are configured at different coupling conditions, and therefore their resonances have different line widths. The measured spectra in Fig. 4.14 clearly show how frequent the backscattering-induced resonance splitting can be and the suppression of extinction ratio of split resonances when comparing those non-split resonances with

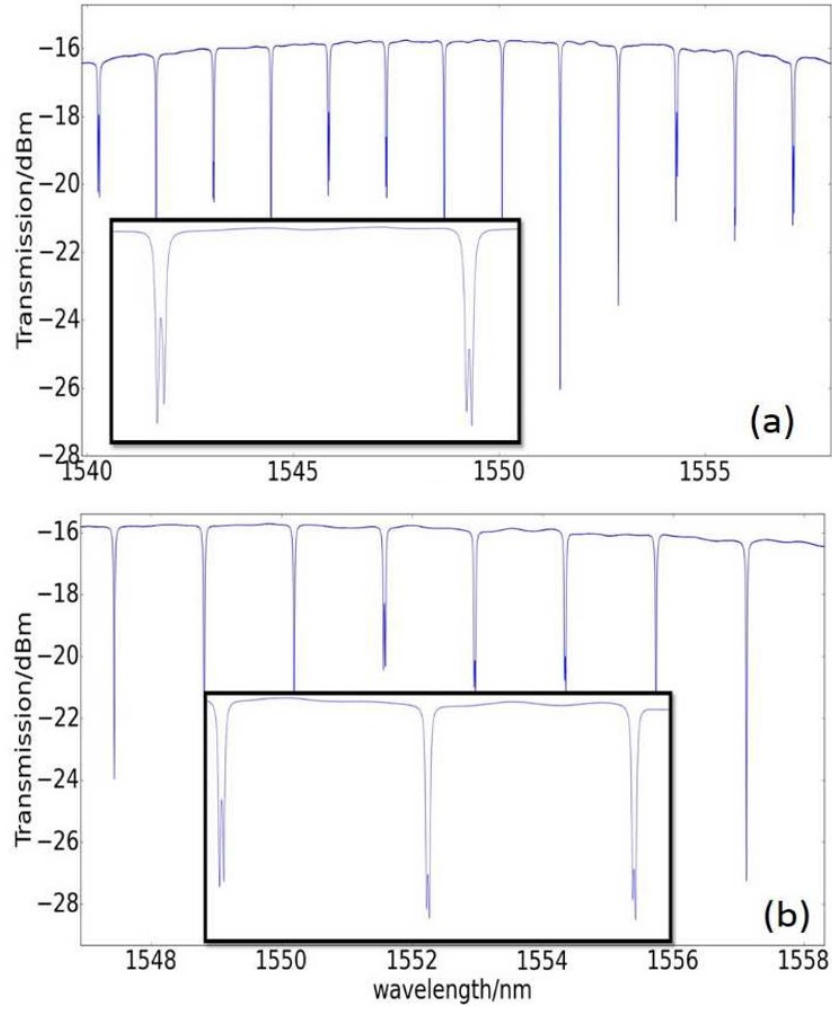


Figure 4.14: Two measured spectra of simple ring resonators (without reflectors) on the same chip, located close to the ring resonator with tunable reflector. Both rings, which have different coupling conditions, show clear resonance-splitting in most resonance peaks.

split resonances. These spectra once again confirms the existence of backscattering. Note that these test rings have a much shorter total length compared to our device, thus our device is expected to suffer from much stronger backscattering as the backscattering strength grows linearly with ring roundtrip length [12].

The active measurement of our device is shown in Fig. 4.15 and Fig. 4.16. For the measurement, an Agilent tunable laser (TL) is used as the optical source. It can perform wavelength sweep from 1465 nm til 1570 nm with a resolution of 1 pm. The scan of 20 nm with 1 pm resolution takes less than half a minute. The minimum input power is limited to 4 mW so an additional attenuator is connected with the laser output to suppress the input power into the ring resonator in order to avoid any nonlinear effects. After the attenuator is the polarization controller to tune the light into TE polarization which is supported by our on chip structures. Fiber at 10 degree angle is used to vertically shine light onto the grating coupler which couples light into the waveguides. Output coupling structure is similar with a grating coupler and an angled fiber. The light coming out of the output fiber goes into a 50/50 splitter. One arm is connected to a HP8163A power meter for fiber alignment while the other one is connected to Agilent photodiode to collect data. A Keithley 2400 is used to provide a DC current to a probe that touches the on chip metal contact pads connected to a Titanium heater.

As evident in Fig. 4.15, by injecting current, under correct condition all of the resonance shapes at the *drop* and *thru* ports become non-split, and the shift pattern of the two peaks observed in the simulation is also reproduced in the measurement, that is one peak hardly moves while the other one is moving much rapidly in the tuning period.

Besides recovered resonance shape, the extinction ratio is also increased dramatically compared to the original split resonance. This is because the extinction ratio gets suppressed by reflection inside the ring [13], details and mathematical deviation of this phenomenon will be given in next chapter.

We also characterized how the unwanted transmission at *in* and *add* ports will be influenced. Both spectra show a clear suppression in power and a change in shape. In detail, for the *add* port spectrum, after injecting proper current, instead of a split resonance the shape becomes non-split. But this residual transmission is not a sign of remaining backscattering in the ring resonator, instead, it is actually caused by the parasitic reflections at the input and output grating couplers, which excites the clockwise ring mode from the *through* port. From another point of view, this actually can be considered as an additional confirmation of the elimination of backscattering in the ring since the resonance shape has become a clear Lorentzian-line. A similar analysis can be applied to the reflection spectrum at the *in* port, which has originally a clearly split resonance pattern, while after current injection, the resonances disappear, with just parasitic random reflections remaining.

The measurement results at the drop port are also plotted in Fig. 4.15. The res-

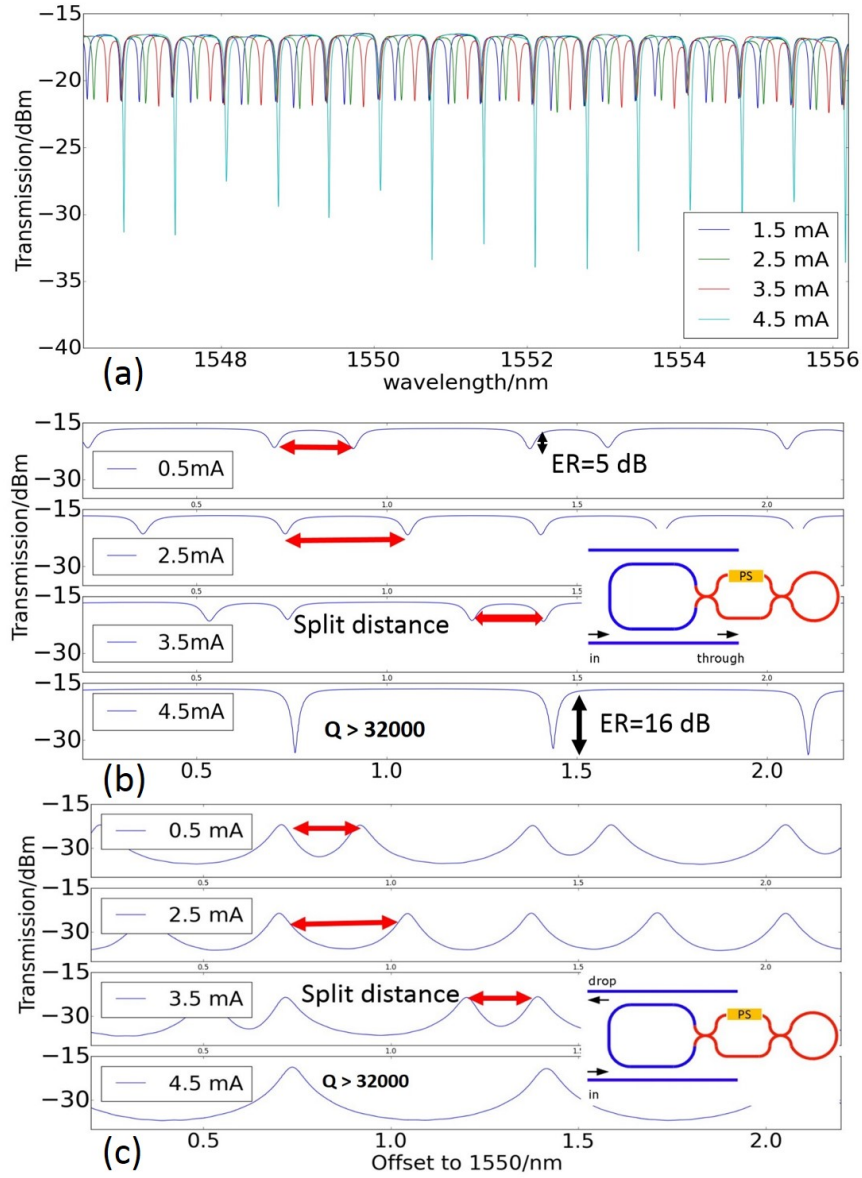


Figure 4.15: Experimental measurements of compensated backscattering. (a) demonstrates the control of all the resonances. (b) gives a zoomed-in view about how the resonance shapes evolve from clearly split to non-split. (c) shows the same compensation for the output at the drop port.

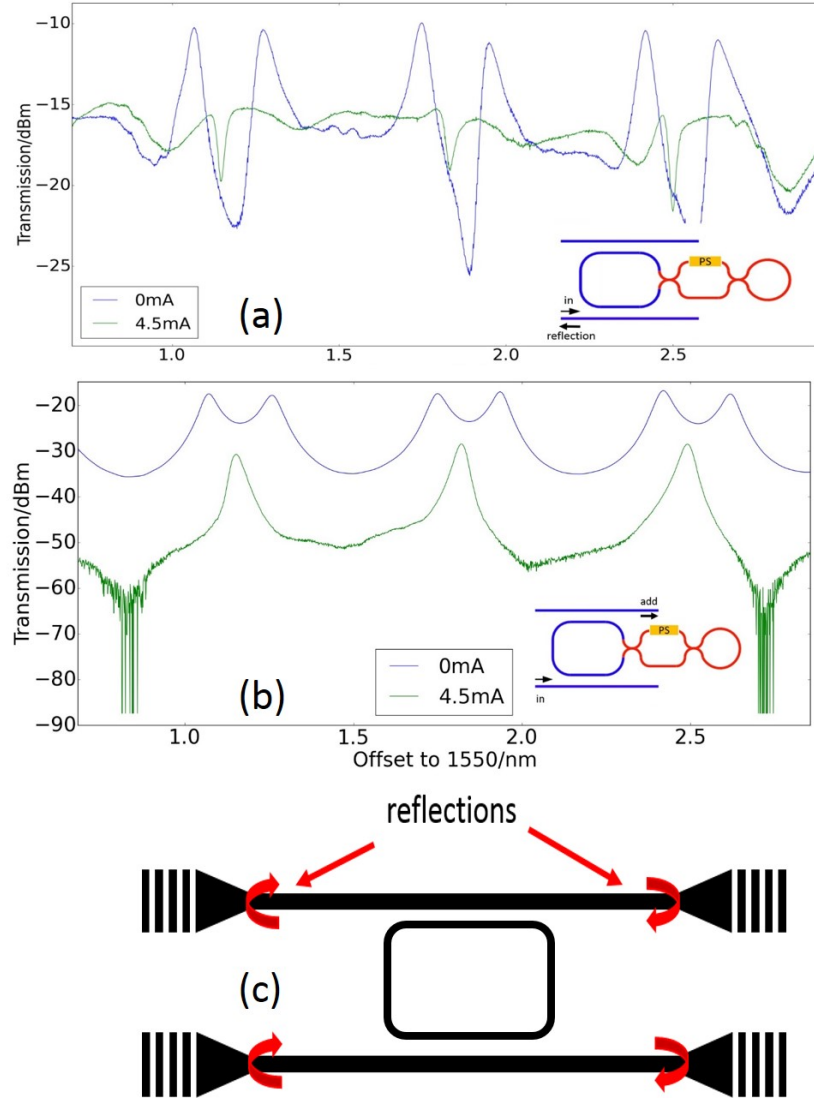


Figure 4.16: Measured spectra of the same device for the in (a) and the add ports (b). Clearly, under correct tuning condition, both the leakage to the add port and reflection to the in port can be significantly suppressed. There is still some residual transmission, but not due to internal backscattering. Instead it's caused by the parasitic reflections at the other parts outside the ring cavity as illustrated in (c).

onance splitting exhibits the same trend in both ports of an add-drop filter, which again confirms the fact that, our solution indeed fundamentally compensates the backscattering inside the ring resonator.

A key limitation of our device is the long ring length, or in other words, the small *free spectral range* (FSR). But the currently demonstrated device is not yet optimized in its total length. For instance, the MZI reflector's arm length can be safely reduced to 80-100 μm without sacrificing performance. This will bring a 200 μm reduction in the total ring length. Still, the lower boundary of the roundtrip length is around 350 μm , which translates to a maximum FSR of 1.7 nm. This will limit its application as WDM filter. But it can still be valuable for applications like microwave filters, integrated optical sensors or multi-mode laser cavities.

4.3 An ultra wide FSR and tuning range of a single silicon ring resonator by means of engineered reflections

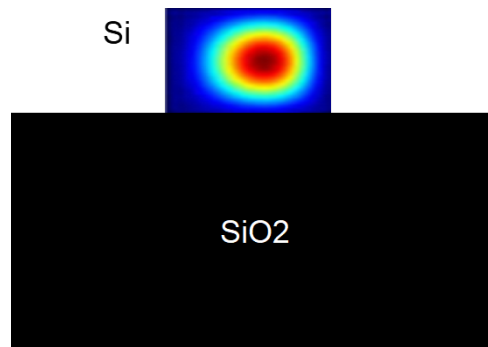


Figure 4.17: A simulated intensity distribution of the fundamental TE mode in a bend silicon strip waveguide. It clearly shows the mode will be positioned closer to the outer wall.

The use of such a tunable reflector in ring resonator can bring another interesting application besides backscattering suppression, which is a single silicon ring resonator with an ultra wide FSR and tuning range.

As we already emphasized in previous chapter, it is very desirable for a ring resonator to have a large FSR as this is very beneficial for most ring based applications. For instance, a larger FSR for a ring resonator based (de-)multiplexers in telecommunications allows more signal channels can be processed. Or it means a wider sensing and detection range for ring resonator based sensors. Also ring resonators are widely used as single mode laser cavities. Such a large FSR will

provide a wider operation span of this laser. FSR of a single ring resonator is mainly determined by its roundtrip length L as $FSR = \frac{\lambda^2}{n_g L}$, where n_g is the group index of the waveguide. This is why silicon photonics is very attractive for ring resonators. Its ultra high index contrast allows very tight bend radius thus compact ring roundtrip length. But the length can not indefinitely go short as multiple problems will be raised for very tight bend radius (smaller than $4 \mu m$):

- In a bend section, the mode will be pushed towards the outer wall of the waveguide as evident in Fig. 4.17. This will bring two consequences: extra radiation loss and stronger backscattering [14, 15].
- A very sharp bend usually has a different effective index of the optical mode. Or in other words, the mode profile looks different with that in a straight waveguide. Thus the interface between bend and straight section could induce backreflections.
- For the coupling section of a circular ring resonator, the coupling coefficient is also bend radius dependent. These extremely sharp bends make it difficult to engineer the coupling section for a specific coupling strength without resorting to impractically narrow gaps [16, 17] that are hard to fabricate and will cause extra coupling loss and coupler induced backscattering to the circuit [12, 18]

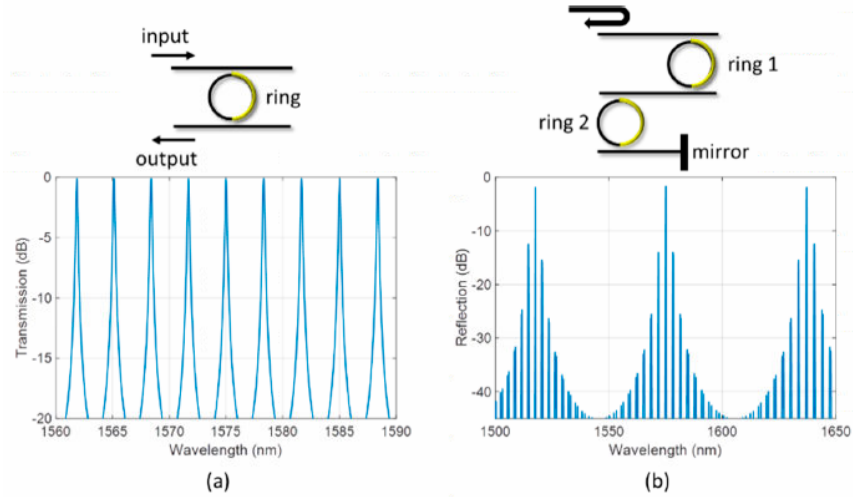


Figure 4.18: Example figure from Ref. [19] about the performance of a two ring system utilizing Vernier effect to get a large FSR.

So far, the smallest silicon ring resonator fabricated with acceptable performance has a radius of $1.5 \mu m$ with a FSR around 45 nm [17]. Further increase

of the FSR can only be realized through more complicated methods. One of them is to take advantage of Vernier effect brought by two or multiple ring resonators [19–21], each of them with a slightly different FSR. Only the resonance that matches all resonances of these resonators will show a larger extinction ratio, other resonances will be suppressed as shown in Fig. 4.18. Mathematically, the new FSR of such a circuit is expressed in equation (4.2).

$$FSR = \frac{FSR_1 * FSR_2}{|FSR_1 - FSR_2|} \quad (4.2)$$

However, multiple rings will impose additional requirements to the design accuracy and fabrication tolerance as resonances of each ring need to be precisely matched, not only in the resonance wavelength, but also preferably in their bandwidth. It also complicates the stabilization mechanism, as the rings need to be independently controlled. Besides, the tuning efficiency of the Vernier circuit is relatively poor and the resonance mode is hard to move continuously in the spectrum. Moreover, the well known problem of backscattering induced splitting is not considered and cannot be compensated.

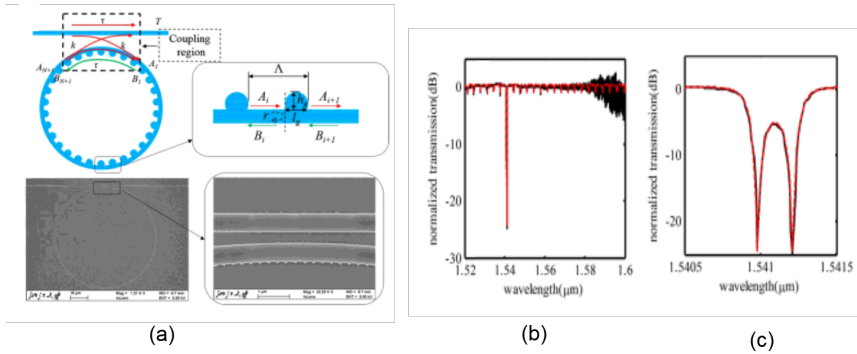


Figure 4.19: Example figure from Ref. [22] about the bragg grating assisted ultra wide FSR silicon ring resonator: (a) presents its conceptual illustration and microscopic image after the Ebeam fabrication. (b) is the overall spectrum at the through port and (c) is a zoomed view of other split resonance. The problem of using bragg grating lies in three aspects: demand of Ebeam lithography; non-predictable performance due to fabrication variation and hard to recover by dynamic tuning; limited tuning range.

An alternative is to add intentional reflections inside the ring cavity to suppress or cancel the side resonances, except for one resonance [22–24]. Bragg gratings can be used to implement this effect [22, 23], but the need for high-resolution e-beam lithography negates some of the advantages of current silicon photonics technologies. Moreover, the Bragg grating is not simple to design such that it needs to be correctly aligned with the required resonances of the ring. Even a small fabrication variation can make the Bragg grating perform different from its design

and it can not be easily recovered by tuning. Urbonas et al. deposited metal nanodisks along the ring waveguide, but this introduces material incompatibilities to silicon photonics. Moreover, metal particles will bring significant absorption loss. As clearly shown in [24], the Q factor as well as the extinction ratio of the resonance are limited to less than 3 dB and 300, respectively, which are quite inadequate for most ring based applications. Even if the grating assisted ultra-wide FSR ring resonators could have a good performance in terms of extinction ratio and Q factor, as present in Fig. 4.19, maximum tuning range of this resonance is the same as that of a normal silicon ring resonator, which is around 7 nm if metal heaters are applied as the temperature variation induced by a heater is generally less than 100 K and the thermo-optic coefficient of Silicon is $1.8 \times 10^{-4} \text{ K}^{-1}$ [25, 26], which is not enough to take full advantage of the FSR.

In our work, we also count on the internal reflection engineering to achieve an ultra wide FSR. But instead of using Bragg grating or metal particles, we use the tunable reflector introduced in previous section. The fundamental principle we rely on for an ultra wide FSR is the fact that internal reflections inside a ring resonator will not only cause splitting to a resonance, but also suppress its ER significantly. So if we manage to get a reflection pattern inside the ring cavity, where only one wavelength point λ_0 in a broad range has zero reflectivity with the rest span suffering from strong reflection, then this resonance located at λ_0 will have a very large ER while all the others are suppressed by strong reflections. Under these circumstance, this ring can be considered as a pseudo single mode ring with an ultra wide FSR.

4.3.1 Theoretical explanation based on tCMT

We first mathematically prove how the internal reflections will lead to suppression of ER. To do this, we re-use the tCMT model for a ring resonator with internal reflections, and now we solve the equations at the *thru* port according to equation (3.5) in chapter 3, and get the output at the *thru* port as following:

$$\begin{aligned} \frac{S_t}{S_i} &= 1 - \frac{2}{\tau_i} \frac{j(\omega - \omega_0) + (\frac{1}{\tau_i} + \frac{1}{\tau_o} + \frac{1}{\tau_l})}{[j(\omega - \omega_0) + (\frac{1}{\tau_i} + \frac{1}{\tau_o} + \frac{1}{\tau_l})]^2 + |\mu_r|^2} \\ &= 1 - \frac{2}{\tau_i} \left(\frac{0.5}{j(\omega - \omega_1) + (\frac{1}{\tau_i} + \frac{1}{\tau_o} + \frac{1}{\tau_l})} + \frac{0.5}{j(\omega - \omega_2) + (\frac{1}{\tau_i} + \frac{1}{\tau_o} + \frac{1}{\tau_l})} \right) \end{aligned} \quad (4.3)$$

$\omega_1 = \omega_0 + |\mu_r|$, $\omega_2 = \omega_0 - |\mu_r|$. Here the backcoupling related terms μ_i' and f are ignored for simplicity. All other terms shown in this equation have been systematically explained in chapter 3. Naturally we see two Lorentzian shaped resonances with their own frequency and bandwidth. When $\mu_r = 0$, i.e. no internal reflections, we get the output at the *thru* port of an ideal ring resonator, that is:

$$\frac{S_t}{S_i} = 1 - \frac{\frac{2}{\tau_i}}{j(\omega - \omega_0) + (\frac{1}{\tau_i} + \frac{1}{\tau_o} + \frac{1}{\tau_l})} \quad (4.4)$$

This is a pure Lorentzian shaped resonance with central frequency ω_0 . The power transmission is the square of the output S_t :

$$\frac{|S_t|^2}{|S_i|^2} = 1 - \frac{\frac{2}{\tau_i}(\frac{2}{\tau_o} + \frac{2}{\tau_l})}{(\omega - \omega_0)^2 + (\frac{1}{\tau_i} + \frac{1}{\tau_o} + \frac{1}{\tau_l})^2} \quad (4.5)$$

Now let's look at the transmission P_r at the resonance $\omega = \omega_0$.

$$P_r = 1 - \frac{\frac{2}{\tau_i}(\frac{2}{\tau_o} + \frac{2}{\tau_l})}{(\frac{1}{\tau_i} + \frac{1}{\tau_o} + \frac{1}{\tau_l})^2} \quad (4.6)$$

When $\frac{1}{\tau_i} = \frac{1}{\tau_o} + \frac{1}{\tau_l}$, then $P_r \approx 0$, or physically speaking, when the power coupled into the MRR from the input port i equals the roundtrip loss plus the power coupled to the output port d , we get critical coupling, which gives us the largest extinction ratio as $ER = 1 - 10\log_{10}P_r$. For an all-pass ring, where $\frac{1}{\tau_o} = 0$, the critical coupling condition is changed to $\kappa_i^2 = a_l^2$. It is in good correspondence with former literature which describes critical coupling in the space domain [27]. In [27], the critical coupling condition for an all-pass MRR has the same formula, while for an add-drop MRR it is written as $(1 - \kappa_i^2) = (1 - \kappa_o^2)(1 - a_l^2)$. After some transformation we get $\kappa_i^2 = \kappa_o^2 + a_l^2 - \kappa_o^2 a_l^2$, where the term $\kappa_o^2 a_l^2$ is generally two orders of magnitudes smaller, and therefore negligible. at that point it becomes the same as our condition, which is $\kappa_i^2 = \kappa_o^2 + a_l^2$.

The point is, the transmission at the resonance frequency ω_0 will be strongly modified when there is internal reflection present. Let's get the equation for P_r in the case of internal reflections:

$$\begin{aligned} P_r &= \left(\frac{\frac{2}{\tau_o} + \frac{2}{\tau_l}}{\frac{2}{\tau_i} + \frac{2}{\tau_o} + \frac{2}{\tau_l}}\right)^2 + \frac{(\frac{2}{\tau_i})^2 - 2\frac{2}{\tau_i}(\frac{2}{\tau_o} + \frac{2}{\tau_l})}{(\frac{2}{\tau_i} + \frac{2}{\tau_o} + \frac{2}{\tau_l})^2 + 16|\mu_r|^2} \\ &= \left(\frac{\kappa_o^2 + a_l^2}{\kappa_i^2 + \kappa_o^2 + a_l^2}\right)^2 + \frac{(\kappa_i^2)^2 - 2\kappa_i^2(\kappa_o^2 + a_l^2)}{(\kappa_i^2 + \kappa_o^2 + a_l^2)^2 + 16r^2} \end{aligned} \quad (4.7)$$

Here, all the terms in temporal domain (τ, μ_i, μ_r) are replaced with their corresponding spatial domain terms (κ, α, r) . When $r = 0$, this equation becomes identical with equation (4.6). Now it is apparently too complicated to directly analyze in a quantitative way. If we assume that the ring resonator is still configured at its critical coupling condition, that is $\kappa_i^2 = \kappa_o^2 + a_l^2$, we get a simplified equation for P_r :

$$P_r|_{cp} = \frac{1}{4} - \frac{|\kappa|^4}{4|\kappa|^4 + 16r^2} \quad (4.8)$$

Now we plot how the reflectivity r will impact the transmission at resonance frequency P_r , thus the ER of this resonance in Fig. 4.20. When the ring is critically coupled, even a tiny reflectivity that is not able to cause resonance splitting, could suppress its ER dramatically. To make the analysis more practical, we investigate how the extinction ratio changes with reflectivity when the MRR is not critically coupled. This is necessary because in reality, it's very difficult to fabricate a ring where all coupling factors and losses are matched at the correct wavelength, due to fabrication variability. So exploring the behavior of the ring in the non-critical-coupling regime can also be considered as a fabrication tolerance analysis of the device. In Fig. 4.21 the dependency of the extinction ratio on reflectivity $|r|$ under different coupling strength is given. In contrast to Fig. 4.20, the MRR is not configured at the critical coupling point. The loss factor α_l^2 is set to be constant at 0.0114 corresponding with a 0.05 dB roundtrip power loss and κ_i is set to be identical with κ_o , which is often the case and much easier to ensure than an absolute coupling coefficient.

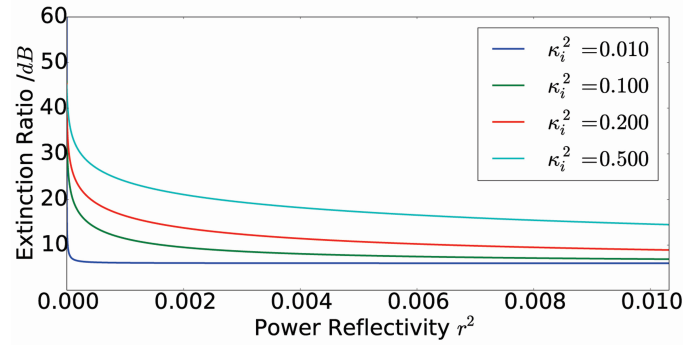


Figure 4.20: At the critical coupling point, the extinction ratio drops dramatically with increasing reflection until it reaches an almost constant value.

It's natural to expect a performance degradation due to the deviation from the critical coupling condition, which appears in the smoother slope and the smaller side mode suppression ratio (SMSR), here SMSR is defined as $SMSR = ER_0 - ER_r$, where ER_0, ER_r refers to the extinction ratio of the resonance that suffers zero reflection and the resonance that suffers strong reflection, respectively. However, the extinction ratio still drops significantly with increasing reflectivity, and it's noteworthy that the extinction ratio of the remaining resonance (ER_0) as well as the side mode suppression ratio (SMSR) can be improved simply by increasing the coupling coefficient, as illustrated in Fig. 4.22. This device is then quite practical, as we require no exact configuration such as critical coupling. Another advantage is that in this configuration the MRR becomes less sensitive to stochastic backscattering, which we will discuss in detail in a later section.

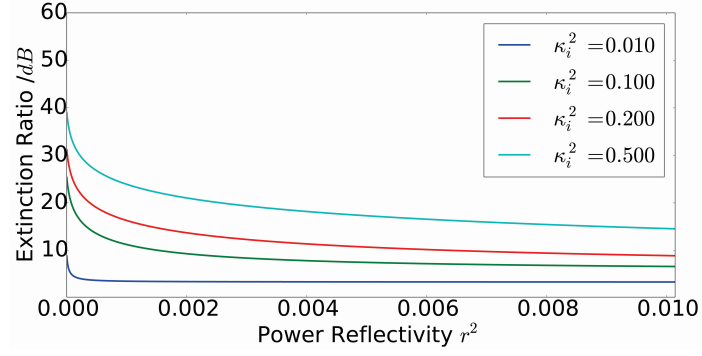


Figure 4.21: The extinction ratio still changes significantly with increasing reflectivity when the MRR is configured as $\kappa_i = \kappa_o$, which is the general case and easy to guarantee.

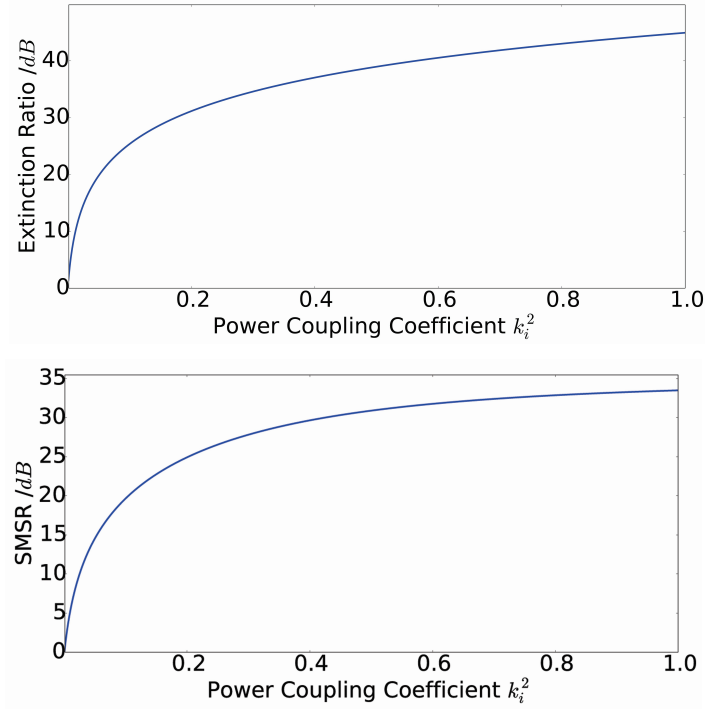


Figure 4.22: These figures show how the extinction ratio as well as the side mode suppression changes with power coupling coefficient when the MRR is designed as $\kappa_i = \kappa_o$.

$$\frac{2\pi\Delta L n_{eff}}{\lambda_0} = m\pi \quad (4.9)$$

4.3.2 Design and simulation

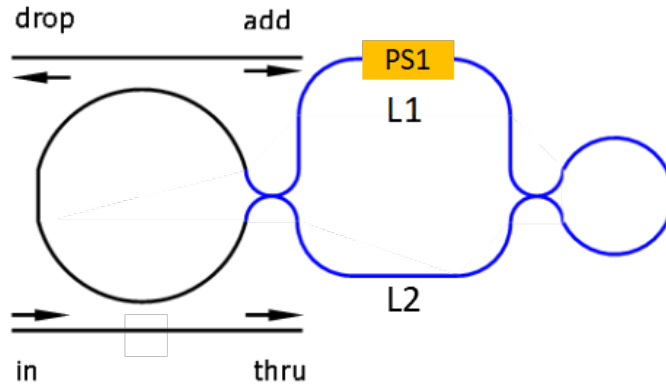


Figure 4.23: For the application to generate an ultra wide FSR ring resonator, the MZI of the tunable reflector is designed with a length difference ΔL .

With this knowledge in mind, we need to design a reflector that can provide a satisfying reflection spectrum described above. We still use the same reflector introduced in previous section. And our complete device for this application looks very similar with that used for backscattering suppression shown in Fig. 4.3(a). The difference lies in the design of the loop ended MZI reflector. For this applications, the MZI of the reflector is designed to operate with a length difference ΔL between its two arms as shown in Fig 4.23. Following equation (4.9), where m is an integer named interference order. ΔL is defined in such a way that, at wavelength λ_0 , the reflectivity is 0, while all the other wavelength suffer from strong reflections as plotted in Fig. 4.24, which is a simulated reflection spectrum of this reflector. The specialty of such a spectrum is that within a very wide range, there is only one point with zero reflectivity, while the rest of the span exhibits strong reflections. Increasing m will bring some benefit as it has a sharper slope, but in return, a very large m will add additional zero reflection points to the spectrum. Ideally the directional couplers of the reflector are designed to be 50/50 which is also applied in the simulation shown in Fig. 4.24. But a DC is very sensitive to fabrication variation, which is inevitable and usual in silicon photonics. To investigate this issue, we simulate the reflection spectrum of the reflector with different coupling coefficients of the DCs. Results plotted in Fig. 4.25 proves that even with a 30/70 splitter this unique reflection spectrum still remains.

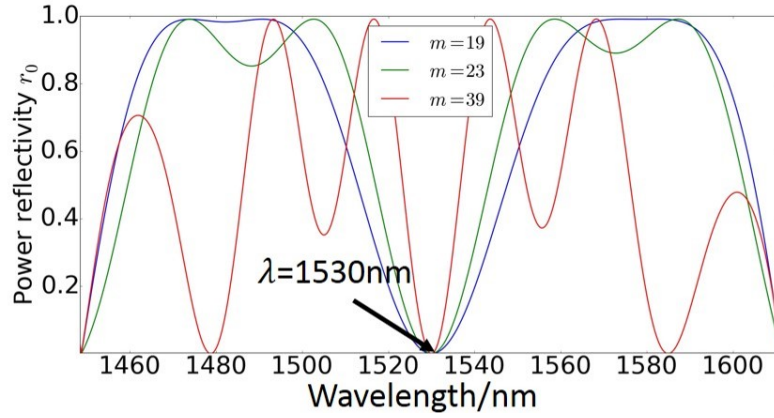


Figure 4.24: Simulated curves of the reflection spectra of the reflector. This unique spectrum provides only one zero reflection point in a very wide range. This is one of the basic principle to achieve an ultra wide FSR ring resonator. Larger order m leads to a sharper slope, but it can not be too large in order to avoid extra dips.

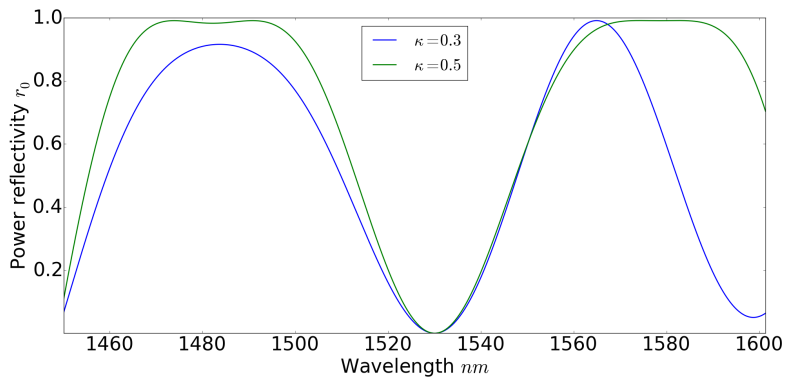


Figure 4.25: Simulated curves of the reflection spectra of the reflector under different coupling coefficients of the directional couplers.

Fig. 4.26 presents the simulated transmission spectra of the *thru* port. Here, $L_2 = 10 \mu m$, $m = 23$, thus $\Delta L = 7.44 \mu m$, and the total roundtrip length is set to be around $150 \mu m$ and a resonance appears at 1540 nm . The roundtrip loss is set to be 0.05 dB (corresponding with a loss coefficient of 330 dB/m), and $\kappa_i = \kappa_o$. In consistence with the theory, only the resonance of zero reflection shows a large extinction ratio in the ring spectrum, while the other resonances all have very small extinction ratio and clear resonance splitting.

Besides, we notice that, another part of the theory is also verified, which is, the SMSR and ER of the surviving resonance could be increased simply by coupling more power into the ring, as also shown in Fig.4.26. Even though for large coupling coefficient, for instance, $\kappa_i^2 = 0.5$, the adjacent resonance modes start to arise, we can again suppress it by increasing the interference number m as this will sharpen the slope of the reflector spectrum. Just be careful not to make m too large for extra zero reflection points to appear. However, we need to bear in mind that by increasing the power coupling coefficient, the bandwidth and the Q factor of the resonance will be broadened and decreased respectively, which is not so desirable in many applications.

Tunability of such a device is also worthy studying as optical sensors are one of its potential applications. Good news is that the zero reflection point λ_0 of the reflector shifts at the same pace with the ring spectrum if the index change happens globally instead of locally (evident in Fig. 4.27), which means during the index modulation period, this single mode holds. Thus it can be safely implemented as an optical sensor with wide detection range. Unfortunately for current structure, the global tuning efficiency or tuning range is the same as a normal silicon ring resonator. In detail, a global temperature change at 1 K or an index change in the waveguide core at 1.8×10^4 will lead to the resonance shifts the same amount as a resonance of single silicon ring resonator does. Both follow following equation:

$$\frac{\Delta\lambda}{\lambda_0} = \frac{\Delta n}{n_g} \quad (4.10)$$

So 100 K change in the temperature will only lead to around 7 nm . This isn't very good if it is used as a wavelength tunable filter. However, instead of global tuning the temperature or index, a two-step local tuning method can be adopted to increase the tuning range and efficiency of this single mode notably. The schematic is given in Fig. 4.28, where two separate phase shifters (PS1 and PS2) are used to independently tune the local index. PS1 is on top of one arm of the MZI reflector. Logically speaking, it performs the function of choosing the location of this single mode by shifting the zero reflection point of the reflector, whose mathematical representation is given in equation (4.11). While PS2 is responsible for the comb shifting the complete ring spectrum by adding incremental to its total roundtrip length. The graphical illustration is given in Fig. 4.29. The quantitative description

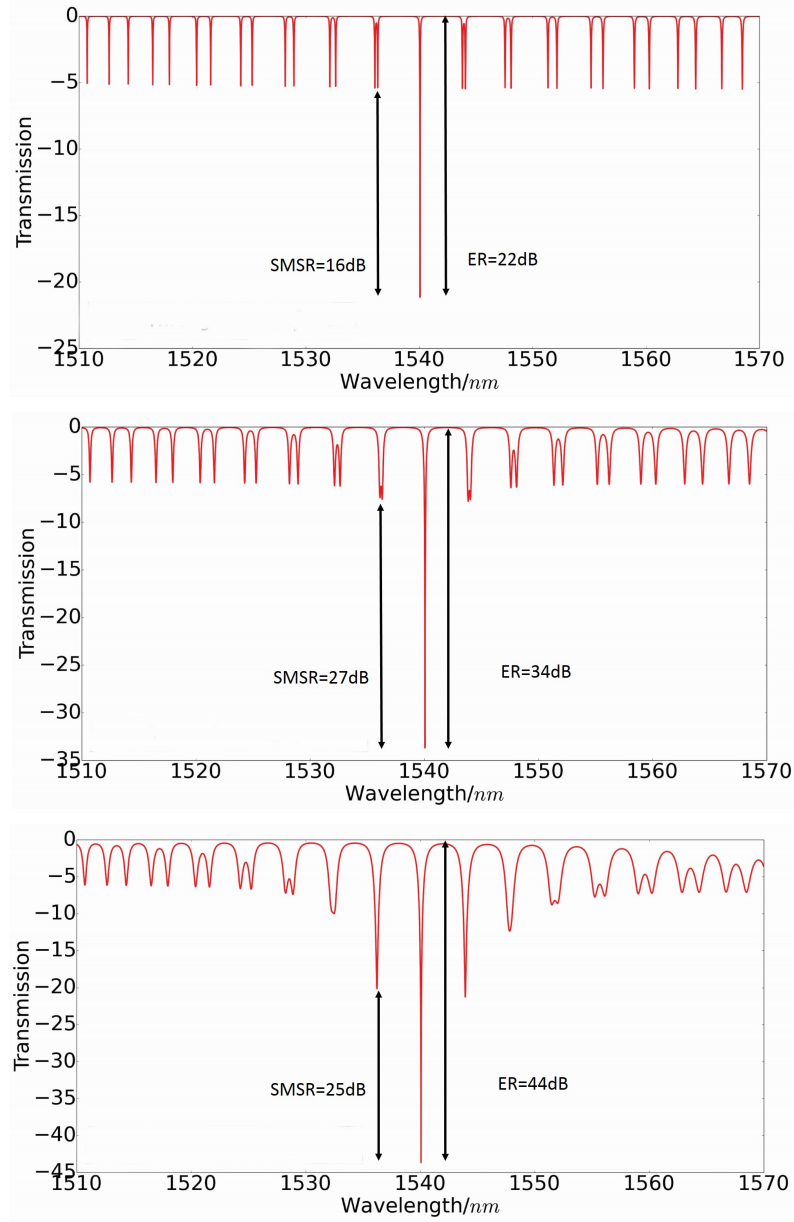


Figure 4.26: A simulated through port spectra of our device under different coupling conditions, $\kappa_i^2 = 0.05$ (a), $\kappa_i^2 = 0.2$ (b) and $\kappa_i^2 = 0.5$ (c). The order m is chosen to be 23, and the MRR is set at the normal coupling condition $\kappa_i^2 = \kappa_o^2$.

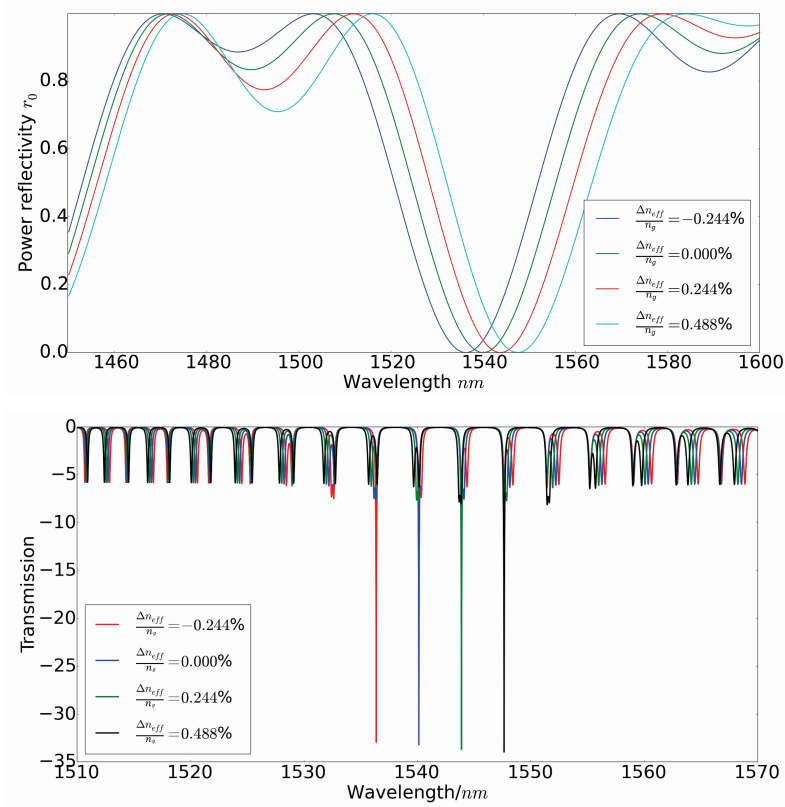


Figure 4.27: In common tuning configuration, the zero-reflection wavelength of the reflector (a) and the resonance wavelength of the MRR (b) shift at the same rate, and thus the MRR remains single mode. n_g is designed to be 4.2, so maximum $\Delta n = 0.488\% n_g \approx 0.02$

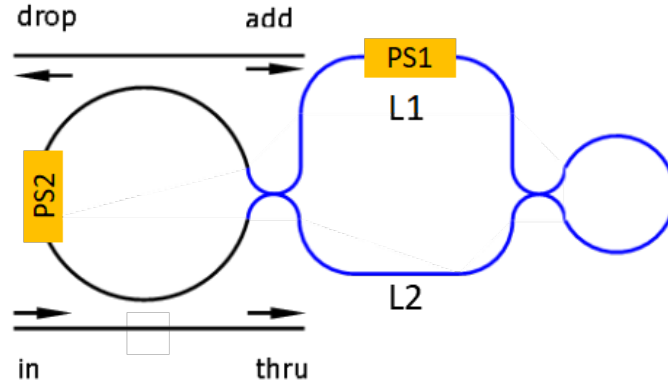


Figure 4.28: Instead of using one common phase shifter, we can implement two separate phase shifters to achieve individual tuning of the zero-reflection wavelength of the reflector and the resonance wavelength of the ring.

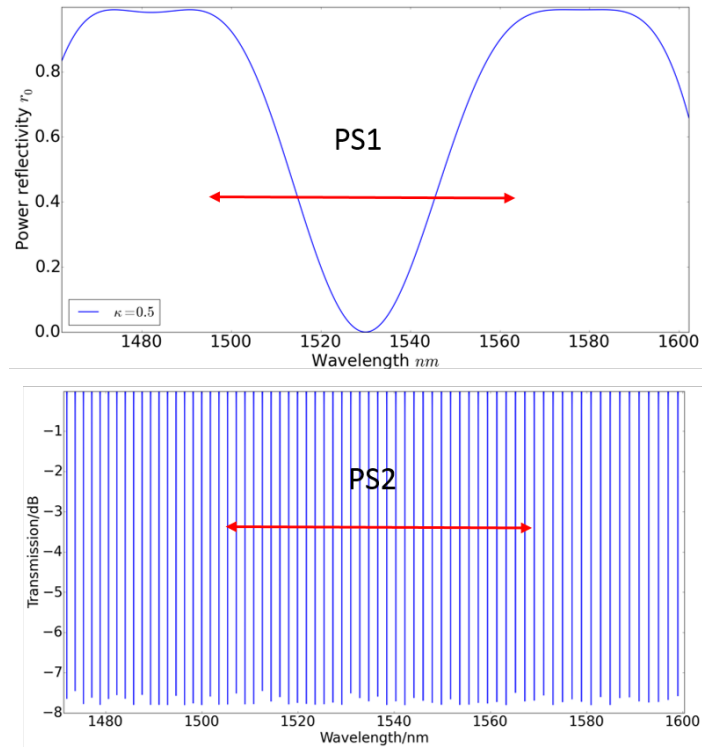


Figure 4.29: Brief illustration of the functionalities of PS1 and PS2 in Fig. 4.28. PS1 is in charge of shifting the zero reflection point of the reflector while PS2 performs the comb shift, to select one of the ring resonance to match the zero reflection point.

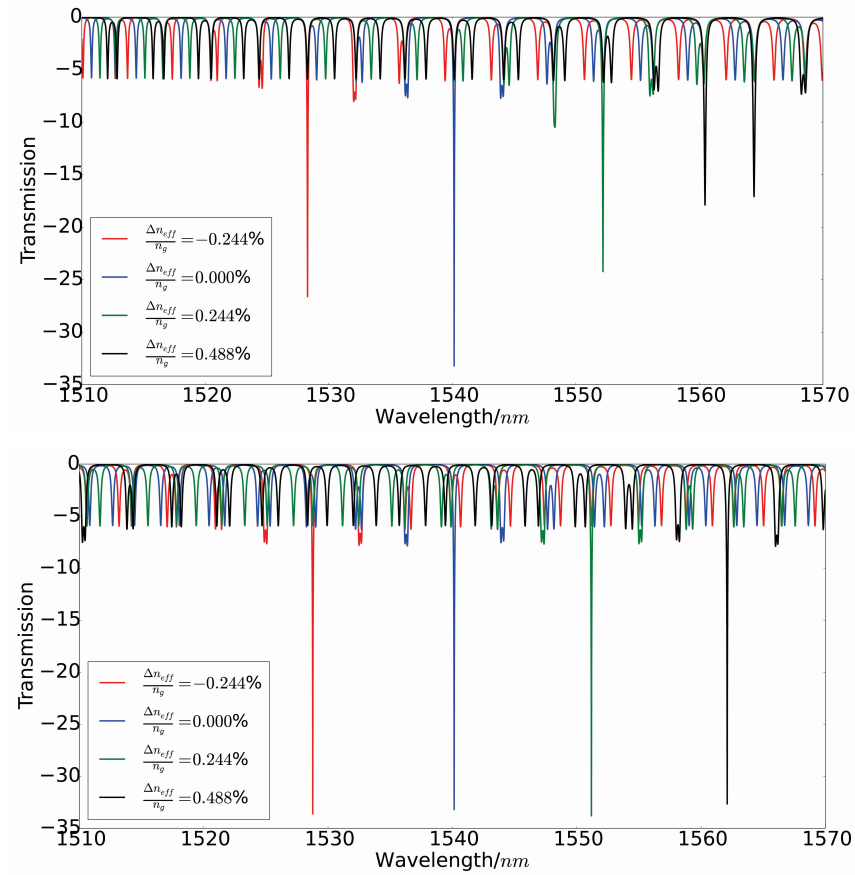


Figure 4.30: (a) Without PS2, tuning PS1 might result in degradation of the relocated single mode resonance as the local ring resonance doesn't match well with the zero reflection point. (b) With PS2 working, the performance of the relocated single mode resonance can be improved due to the good alignment between local resonance and zero reflection point. With the same index change, we achieve a 4 times larger wavelength shift compared to common tuning.

of the shift of the ring spectrum due to the index change at PS2 is given in equation (4.12).

$$\frac{\Delta\lambda_{ref}}{\lambda_0} = \frac{\Delta n_{ps1}}{n_g} \frac{L_{ps1}}{\Delta L} \quad (4.11)$$

$$\frac{\Delta\lambda_{ring}}{\lambda_0} = \frac{\Delta n_{ps1}L_{ps1} + \Delta n_{ps2}L_{ps2}}{n_g(L_{ps1} + L_{ps2}) + n_{eff}L_{rest}} \quad (4.12)$$

- λ_0 is the wavelength of the single resonance. At original state, this is the zero-reflection wavelength of the reflector and it matches one of the resonance wavelength of the ring resonator.
- Δn_{ps1} and Δn_{ps2} are the effective index change in PS1 and PS2 respectively. Similarly, L_{ps1} , L_{ps2} refer to the physical length of these two phase shifters.
- L_{rest} stands for the rest length of the ring resonator. $L_{rest} + L_{ps1} + L_{ps2}$ represents the total length of ring L .
- $\Delta\lambda_{ref}$ and $\Delta\lambda_{ring}$ are the shift of the zero-reflection wavelength of the reflector and the resonance wavelength of the ring resonator, respectively.

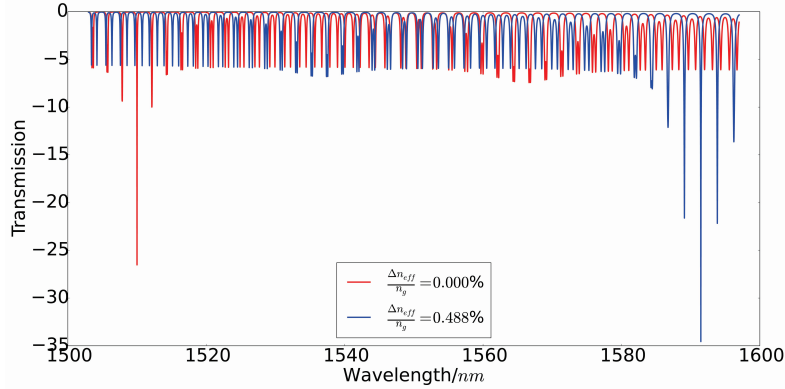


Figure 4.31: When optimizing for a larger tuning range (at the cost of smaller SMSR) we achieve a tuning rang almost as wide as 100 nm with the same index change.

Clearly shown in equation (4.11), the term $\frac{L_{ps1}}{\Delta L}$ acts like an amplification coefficient for the shift of the zero reflection point of the reflector, making it shift much further than a normal silicon ring resonator given the same index change. For instance, if L_{ps1} is designed to be 100 μm and $\Delta L = 7.3 \mu m$ (corresponding with $m = 23$), the tuning range of the zero-reflection wavelength is $14\times$ larger than a normal silicon ring resonance with the same index change Δn . This enables the possibility to achieve a wider tuning range of this single mode. After the

zero reflection point is shifted to a specific position, PS2 will be precisely tuned to arrive at a condition where $\Delta\lambda_{ref} = \Delta\lambda_{ring} + n\text{FSR}$, then one resonance of the ring will match this new zero reflection point, thus a single mode at the new location is generated. the evolution of this two step tuning mechanism is presented in Fig. 4.30. In this example, $L_2 = L_{ps2} = 10 \mu\text{m}$, $m = 23$, $L=150 \mu\text{m}$, we achieve a $4\times$ higher tuning efficiency. If these parameters are optimized for a even higher tuning efficiency, for instance, $L_2 = L_{ps2} = 50 \mu\text{m}$, $m=27$, $L=260 \mu\text{m}$, the tuning range can expand to almost 100 nm, covering the spectrum from 1500 nm to 1600 nm, as illustrated in Fig. 4.31.

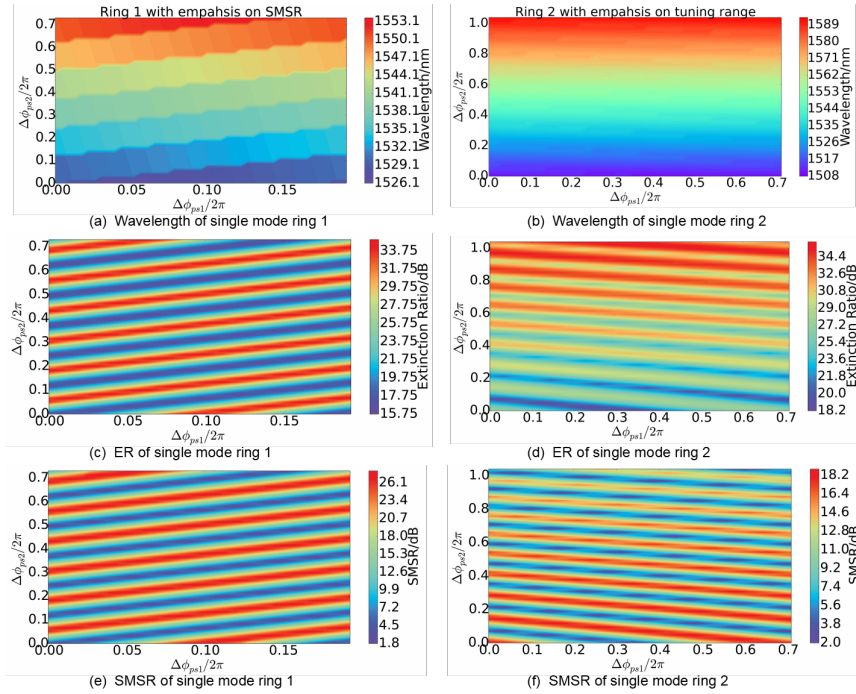


Figure 4.32: Tuning map for the two phase shifters PS1 and PS2 to achieve a continuous shift of the single mode resonance. Figures (a), (c) and (e) give the results of the first design, where the SMSR of each wavelength is larger than 28 dB while the tuning range is only 30 nm, 4 times wider than that of a normal silicon ring resonator; The results of the modified design are illustrated in figures (b), (d) and (f), where the design parameters are changed to achieve a much wider tuning range around 90 nm at the price of a smaller SMSR, but still, at each wavelength, a SMSR larger than 14 dB can be guaranteed. Note that, 85 nm tuning range comes with a $\Delta\phi_{ps1}$ that is less than $0.7 \times 2\pi$, an even wide range is feasible by increasing $\Delta\phi_{ps1}$.

In Fig. 4.32, we give a more straightforward way to illustrate how to tune the PS1 and PS2 in order to achieve a tuning of the single mode wavelength. Clearly,

by tuning the index change of PS1 and PS2 in a feasible range (0-0.02), we can address a continuous shift of the single mode wavelength in a 30 nm span or a 90 nm span, depending on the design parameters of the MZI reflector. And at each wavelength, an extinction ratio larger than 30 dB and a side mode suppression larger than 26 dB (14 dB for the 90 nm tuning span) can be guaranteed. In other words, a wide tuning range comes at the price of a smaller side mode suppression. However, the extinction ratio would be roughly independent of the length of PS1. Thus, the choice between a larger tuning range and a larger side mode suppression would depend on specific application. These figures actually reveal another important feature of our device, which is the tolerance to the design accuracy. In other words, it does not require a ridiculously precise design of the individual optical length, as the single mode condition can be always achieved by dynamic tuning PS1 and PS2.

As we commented on other approaches towards ultra wide FSR, the existence of stochastic backscattering and parasitic reflections inside a ring resonator shall not be neglected. So we also investigate how tolerant our device is to unintentional backscattering. To do this, we add lumped reflector with random phase and constant power reflectivity that is proportional to the total roundtrip length of the ring according to literature Ref. [28] and our own work. The parasitics of the directional coupler are also taken into account. The simulated outputs are plotted in Fig. 4.33.

Naturally, due to the presence of parasitics, the performance degrades in terms of a lower ER and SMSR. When the length grows from 150 μm to 300 μm , and the power reflectivity caused by backscattering increases from 0.00105 to 0.0021, the single mode condition is detuned when the ring is configured at $\kappa_i^2 = 0.2$ and $m = 23$. The reason is simple, due to the existence of the stochastic backscattering, the single mode resonance is not in the condition of zero internal reflection. But still, one could increase the performance by simply increasing the coupling coefficients and increasing the resonant number m , as illustrated in Fig. 4.33(b) and Fig. 4.33(c). Theoretically, we can also compensate backscattering by tuning the reflector's reflectivity as introduced and demonstrated in previous section in this chapter. However, it might be quite complicated as now the reflector is not designed as balanced. Any tuning of PS1 will lead to the shift of the zero reflection point. So another phase shifter PS3 on the other arm of the MZI is needed. Both PS1 and PS3 should work in order to compensate backscattering and tune the zero reflection point to the same location.

4.3.3 Experimental characterization

The devices shown in Fig. 4.34 are fabricated in IMEC's 200nm CMOS pilot line through the Europractice MPW service [29]. The substrate is a 220 nm thick SOI

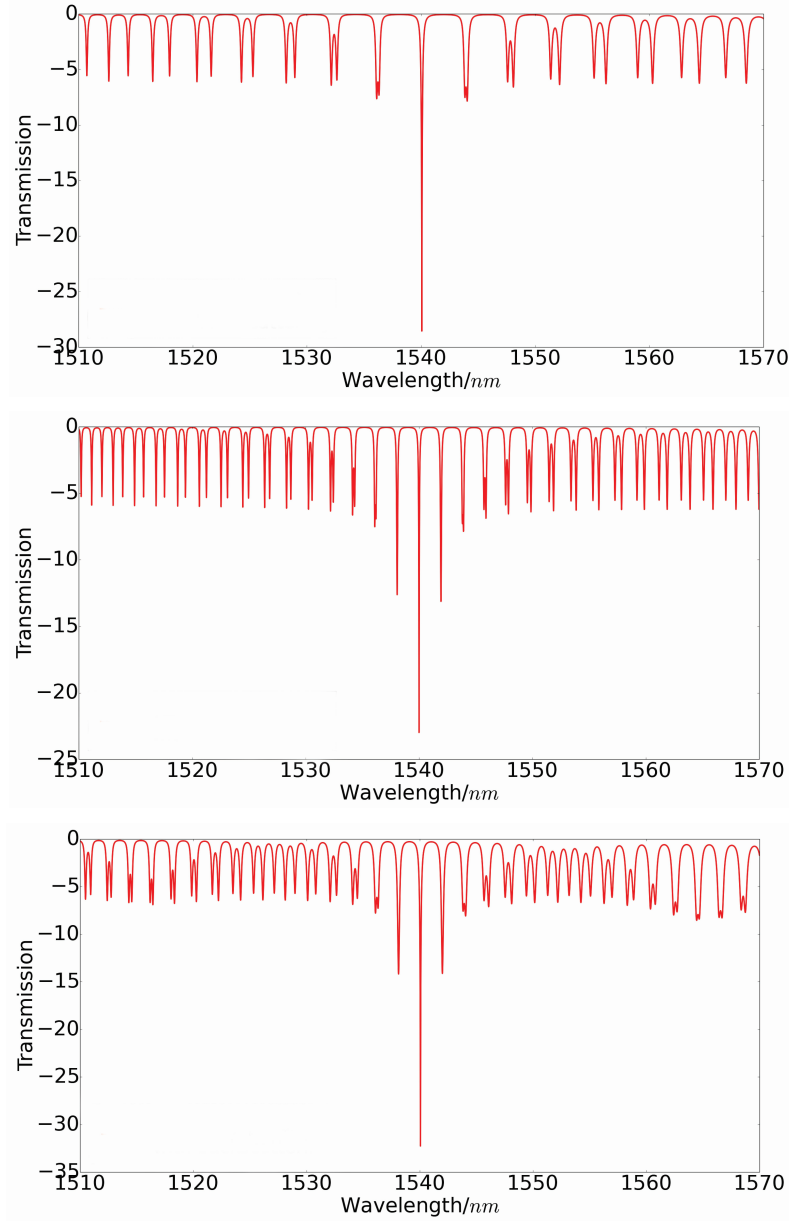


Figure 4.33: Effect of unintentional backscattering on the performance of the MRR. (a) $L = 150 \mu\text{m}$, $\kappa_i^2 = 0.2$, $R_{bs} = 7 \times L$. (b) $L = 300 \mu\text{m}$, $\kappa_i^2 = 0.2$, $R_{bs} = 7 \times L$. (c) $L = 300 \mu\text{m}$, $\kappa_i^2 = 0.4$, $R_{bs} = 7 \times L$ and $m = 55$. When the ring roundtrip length increases from $150 \mu\text{m}$ to $300 \mu\text{m}$, and the corresponding power reflectivity of backscattering grows to $7m^{-1} \times L = 0.0021$, the side mode suppression shows a significant decrease. But we could increase the κ_i and the resonant number m to compensate as in (c).

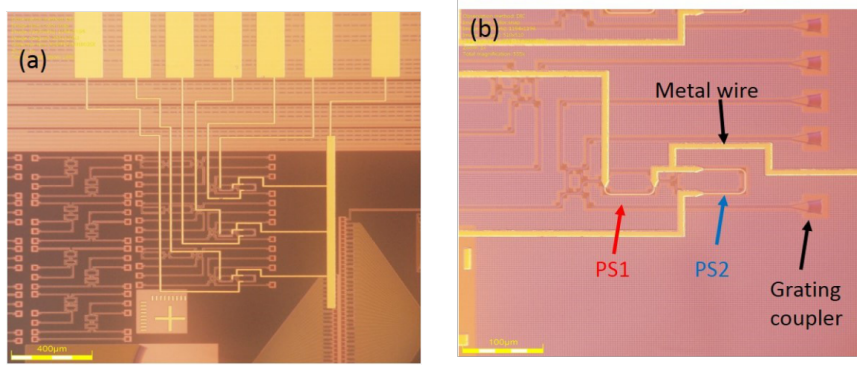


Figure 4.34: Microscope images of the fabricated device with two integrated phase shifters (metal heaters) (a) and a zoom view of a single device (b).

wafer and the devices are covered by $1.5\ \mu\text{m}$ thick planarized silicon dioxide layer, on top of which the integrated metal heaters are processed in the Ghent University clean rooms. Again, each heater consists of a titanium resistive element with $2\ \mu\text{m}$ width and $100\ \text{nm}$ thickness. The metal wires are based on Gold with $10\ \mu\text{m}$ width and $500\ \text{nm}$ thickness. All the waveguides are designed to have a width at $450\ \text{nm}$ to ensure single mode operation. Grating couplers are employed to achieve fiber-chip coupling. For the measurement, we still use an Agilent tunable laser ($1465\ \text{nm}$ to $1570\ \text{nm}$) to perform the wavelength sweep. And the two metal heaters (PS1 and PS2) are driven by two Keithley 2400 sourcemeters independently. PS1 is responsible for shifting the zero-reflection wavelength of the reflector while PS2 is in charge of shifting the ring spectrum.

In Fig. 4.35 we give the measured spectra of our device when $\text{PS1}=0\text{mW}$, meaning no power is injected into phase shifter 1. By tuning PS2 to correct condition, where one of the ring resonance matches the zero-reflection point (around $1505\ \text{nm}$), the SMSR and ER improve. The designed zero-reflection point is $1480\ \text{nm}$. This deviation is due to the fabrication variation that influences the effective index of the waveguides. Current devices shows a maximum SMSR around $12\ \text{dB}$, this can be further improved by multiple ways:

- Current ring roundtrip length is excessively long as each arm of the MZI reflector is designed to be $200\ \mu\text{m}$ to ensure adequate phase shift. Long roundtrip leads to small FSR, which means the side modes are very close to the single mode. As a results, a smaller SMSR is present. However, the experiment shows that each arm can be safely reduced to less than $100\ \mu\text{m}$. The total roundtrip length can be optimized to only 60% of the current value, meaning the FSR will be increased by more than 1.5 times. This will significantly increase the spacing between single mode and side modes, thus

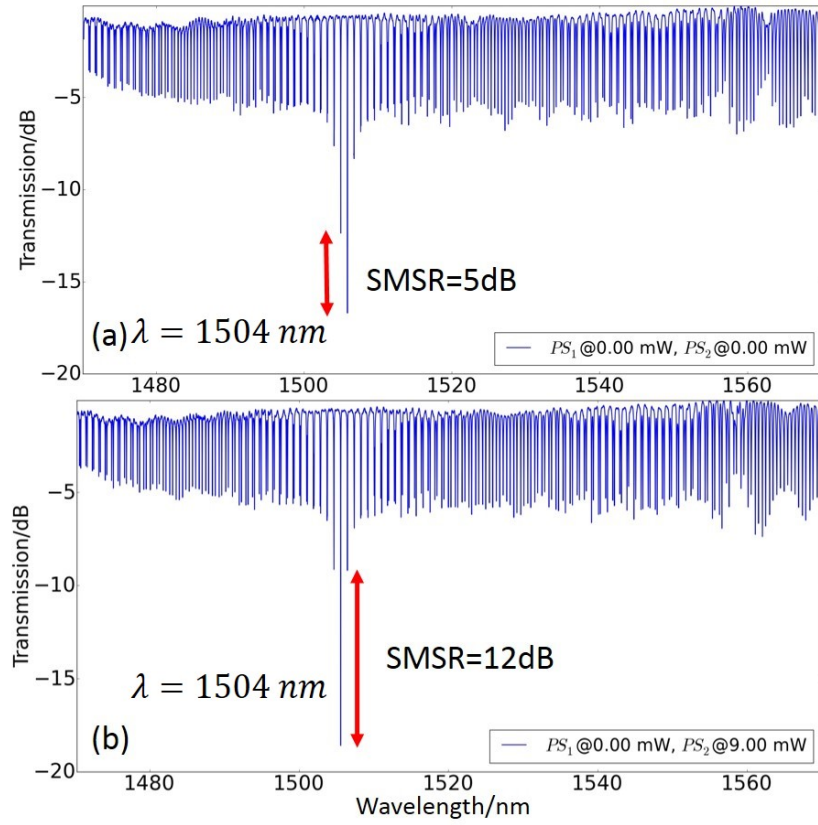


Figure 4.35: Measured spectra of our device. (a) shows the condition that the ring resonance doesn't match the zero-reflection point perfectly, so a resonance with small extinction ratio and side mode suppression ratio is observed. While (b) gives the results when PS_2 is tuned such that one resonance is well aligned to the zero-reflection point. The performance gets improved.

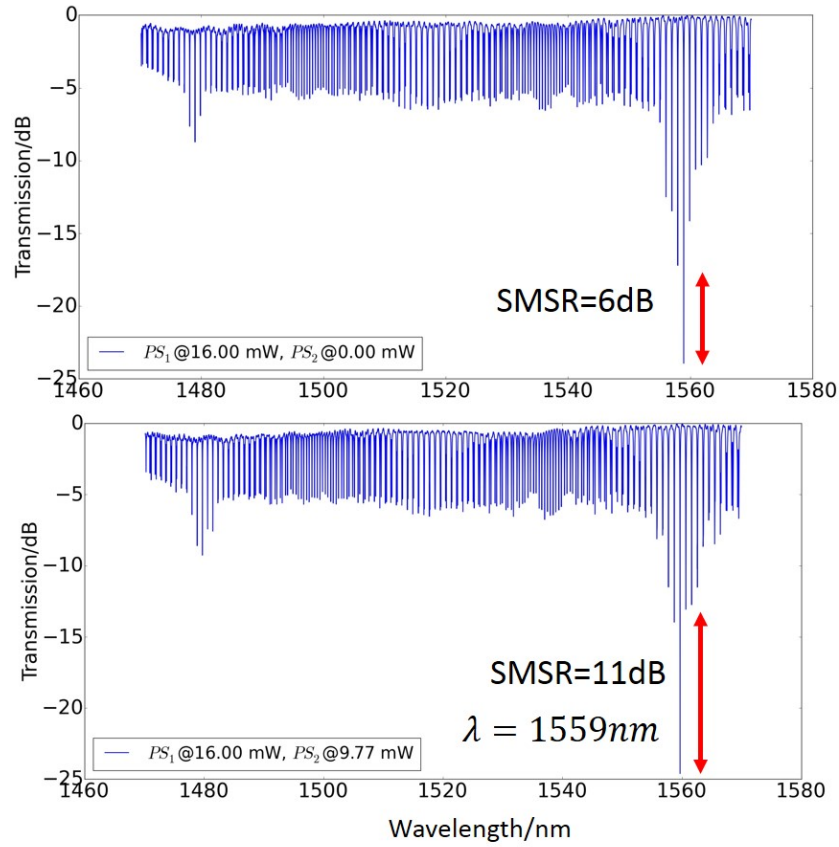


Figure 4.36: By controlling PS_1 , the zero-reflection point can be shifted. Then tuning PS_2 will again make one resonance match it to get a good ER and SMSR. 16 mW (around 0.0148 index change) can shift the single mode around 55 nm, which is $11\times$ more efficient than a normal silicon ring resonator.

increase the SMSR.

- As demonstrated in the theoretical part, SMSR can be simply increased by increasing the coupling coefficient of the ring resonator, at the price of lower Q factor.
- Also discussed in the theoretical section, SMSR can be further increased by increasing the m factor of the reflector. In this way, the slope of the reflection spectrum will be sharpened. But increasing m will slightly decrease the tuning range and it can not be too large to avoid extra zero reflection point. So there is certain compromise.

In Fig. 4.36 we show the shift of the single mode by injecting power into PS1. Still, PS2 needs to be controlled to get a good alignment between the ring resonance and the zero-reflection point. The measured results show that 16 mW can shift the resonance around 55 nm. According to Ref. [30], 18 mW for a Titanium heater leads to a temperature change around 93 K (corresponding index change 0.0167). So 16 mW can roughly generate a index change of 0.0148. Compared to a normal silicon ring resonator, such an index change will only shift the ring resonance around 5.5 nm assuming the group index to be 4.2. Usually the maximum power injected to a metal heater is limited in order to avoid burning heater, so this indicates that our device has a $11\times$ wider tuning range than a normal silicon ring resonator if the same heaters are used.

4.3.4 Drawbacks of this structure

There exist some drawbacks or problems of this kind of structure. Due to the strong internal reflections inside the ring cavity, both CW and CCW modes are activated. So there will be strong leakage to the *add* port and reflection to the *in* port as shown in Fig. 4.37. The reflection shows clear resonance pattern and the leakage at the *add* port is as high as the transmission at the *drop* port. Unfortunately, this is unavoidable for this structure. For applications, where a laser diode or semiconductor optical amplifier (SOA) will be connected directly to the *in* and *add* ports of this device, this reflection needs to be taken into consideration at the design stage as it might cause instabilities to the gain medium.

4.4 Other applications

This kind of structure can provide more applications than the two discussed above. Thanks to its fully tunable reflection conditions inside the ring cavity, almost all the applications relying on a ring resonator or some applications based on coupled ring resonators can be potentially realized using this structure, including a tunable microwave filter, novel sensing scheme based on resonance splitting etc.

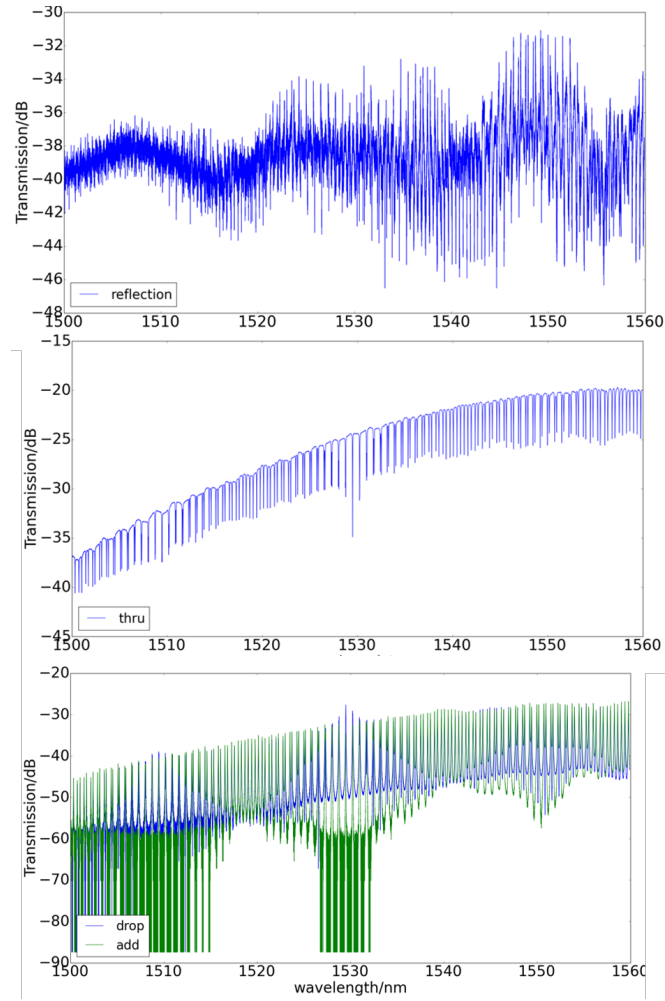


Figure 4.37: A measured spectra of a device with ultra wide FSR. It shows strong reflection to the in port and the leakage to the add port is as high as the transmission at the drop port.

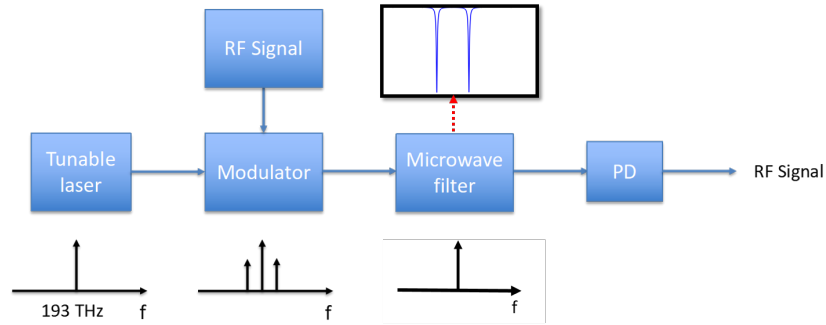


Figure 4.38: A brief illustration of the principle of a microwave photonics filter. When a microwave signal is applied to a modulator, there would be two sidebands generate at both sides of the optical carrier in the frequency spectrum. If this signal passes a notch filter, the two sidebands will be filtered out.

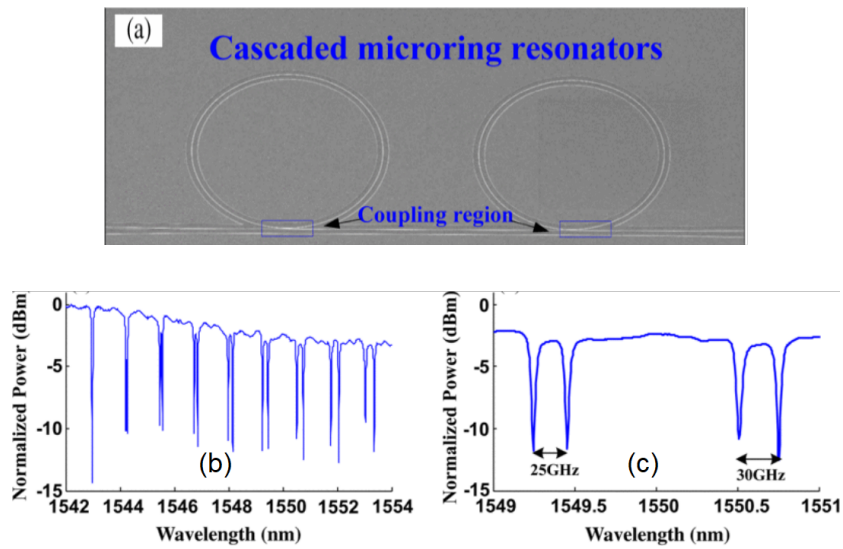


Figure 4.39: An example of making tunable microwave notch filter based on silicon PIC from Ref. [31].

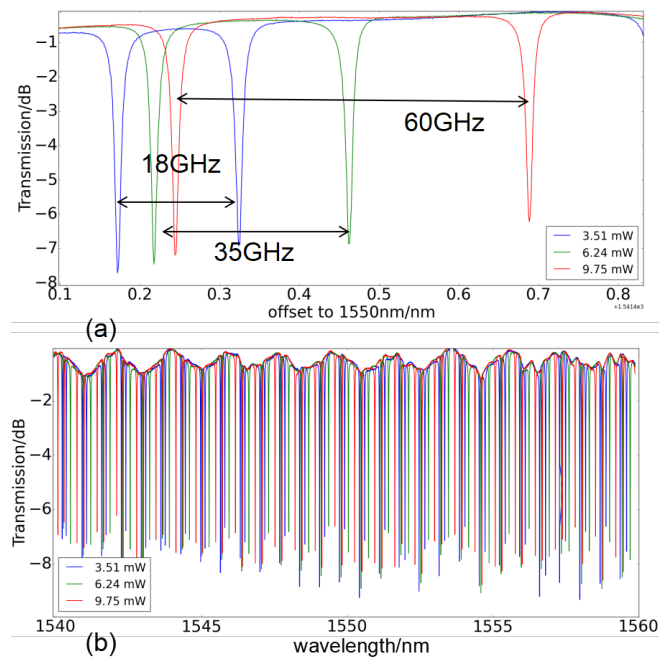


Figure 4.40: Static measurement of our device as a tunable MPF (a) and the whole spectrum (b). By tuning the metal heaters on top of one arm of the MZI reflector, the spacing between two adjacent peaks can be tuned over entire FSR. The asymmetry in two peaks is due to the ripples of the complete spectrum induced by parasitic reflections of the grating couplers and fiber/air facet.

4.4.1 Tunable microwave photonics filter

The advantage of large bandwidth, low loss, electromagnetic immunity as well as reconfiguration and tunability make photonics integrated circuit a wonderful choice for microwave application. Microwave filters using photonics technology, or in other words, microwave photonics filters (MPF) are now widely used for applications including wireless communication, radar system, satellite communication, sensor networks etc. It takes the functionality of filtering microwave component (in the frequency range from a few gigahertz to hundreds of gigahertz) from an incoming signal. As a filter, tunability of the central frequency and bandwidth of such a MPF is highly desirable to handle the random or unpredictable signals. And the ring resonator with an tunable reflector inside can be a great candidate for a tunable microwave notch filter, which is supposed to block unwanted frequency components or to monitor signals in channel. Various approaches based in fiber technology have been demonstrated [32–34]. While the demand for on chip MPFs is growing as chip scale solution always provides benefit in terms of low cost and high volume production, compactness as well as capability of integration with EICs.

The basic illustration of such a microwave notch filter is plotted in Fig. 4.38. When a microwave signal is applied to an optical carrier through modulator, two sidebands standing symmetrically to the carrier will be generated. The frequency spacing between each sideband and the carrier equals the frequency of the microwave signal. While a notch filter typically has a spectrum where two dips are present close to each other. If the frequency spacing between the two dips equal the spacing between two sidebands and the optical carrier frequency locates in the middle, then the microwave component will be filtered out when the modulated signal passes through this filter. That's why the tunability of such a notch filter is highly desirable.

J. Dong et al. proposed to make such a notch MPF based on a silicon PIC, where two indirectly coupled or cascaded silicon ring resonators with slightly different FSR are employed as shown in Fig. 4.39 [31]. By tuning individual rings, their respective resonances location can be shifted. Thus two adjacent resonances with different spacing between them can be achieved. Half of the spacing corresponds with the frequency of the to-be-filtered microwave signal. While this method is accompanied with one inevitable drawback that is the asymmetric peaks as clearly shown in Fig. 4.39(b) and (c). This is mainly due to the dispersion effect of the directional couplers. It's well known that within a single ring resonator's spectrum, each resonance may be quite different in terms of extinction ratio and bandwidth due to the dispersive feature of the coupling coefficient while the roundtrip loss is relatively wavelength independent. So using this cascaded ring resonator as a MPF will frequently lead to two adjacent resonances with asymmetric extinction ratio. This will cause unequal filter coefficient of the two sidebands.

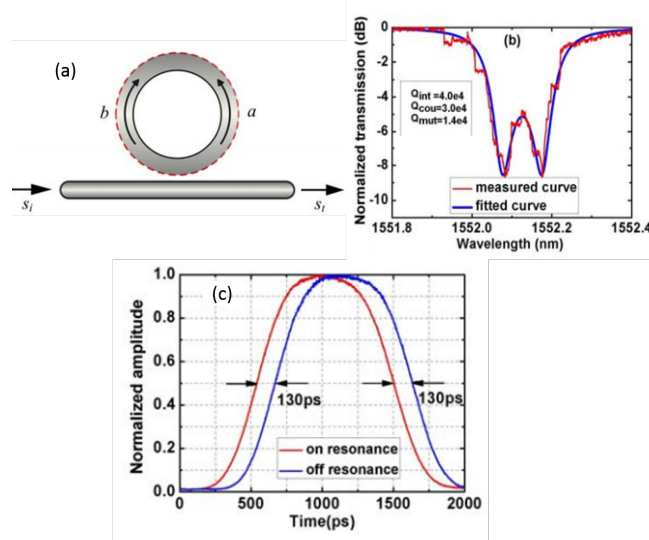


Figure 4.41: Schematic of a ring resonator with sidewall grating (a). Resonance splitting can be induced (b). This resonance splitting can be used to generate pulse advancement, which is so called fast light (c). Source: ref. [35].

Besides dispersive directional couplers, fabrication variation of the two ring resonators will also contribute to this problem. Moreover, it requires two heaters to work independently for each of the ring resonators. While our structure relies on a single ring resonator with symmetrical splitting induced by the reflector, the problem of asymmetry in the two peaks is fully avoided and it only requires one heater to tune the reflectivity. The static measurement is given in Fig. 4.40(a). Using a metal heater to tune the reflector's reflectivity, the spacing between the two peaks can be tuned over the entire FSR. The current ring has very long length around $600 \mu m$ as the MZI arm is designed to be $200 \mu m$, which gives a FSR less than 1 nm. So the maximum tuning range of this ring is around 120 GHz. But by reducing the MZI armlength, the FSR could be increased to around 1.8 nm, corresponding with a frequency spacing at 220 GHz. The little asymmetry in two peaks is due to the parasitic reflections taking place at the grating couplers and fiber/air facets that cause ripples on top of the transmission spectrum as shown in Fig. 4.40(b).

4.4.2 Tunable fast light

Slow and fast light techniques that can lead to modification of the group velocity of light have been attracting research attention recently. Potential applications of slow-light and fast-light include controllable optical delay lines, optical buffers, true time delay for synthetic aperture radars, and cryptography and imaging in the

quantum information field [36–39]. Fast light is particularly interesting as light can travel at a speed larger than c . And this superluminal signal velocities do not violate Einstein causality [40]. It can be achieved through dispersion engineering to get a very large anomalous dispersion at the frequency of interest, as indicated by the equation (4.13).

$$v_g = \frac{c}{n(\omega) + \omega \frac{dn(\omega)}{d\omega}} \Big|_{\omega=\omega_c} = \frac{c}{n_g} \quad (4.13)$$

Where $n(\omega)$ is the frequency dependent effective index of light in a guiding channel and ω_c refers to the central frequency. When $n_g > 1$, it's slow light while for fast light, n_g has to be smaller than 1.

It has been demonstrated using stimulated Brillouin scattering in fibers, coherent population oscillation in erbium-doped fiber amplifiers, electromagnetically induced absorption in atomic vapors and four wave mixing processes in SOA etc. [38, 41–43]. In terms of the demonstration in silicon photonics, people usually use ring resonators with resonance splitting as the splitting region can give anomalous dispersion. While the resonance splitting is usually achieved using either coupled resonators or sidewall grating along the ring waveguide as shown in Fig. 4.41 [35, 44]. The pulse advancement depends on the dispersion condition, which apparently depends on the splitting condition. While these two approaches have no control of the splitting condition, as the parameters that determine the splitting condition are not tunable. Our approach, as demonstrated in previous sections, can tune the splitting distance over entire FSR, thus in theory it is a wonderful candidate to demonstrate tunable fast light.

4.4.3 Novel sensing scheme based on Resonance Splitting

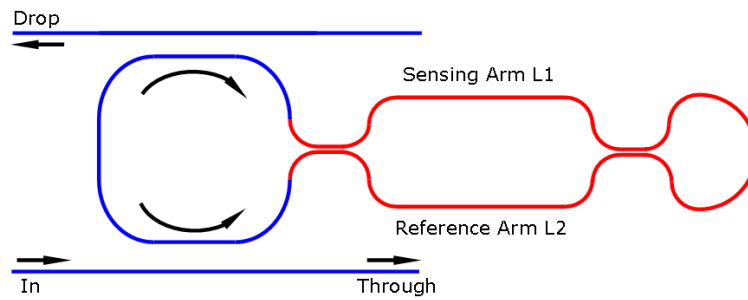


Figure 4.42: The schematic of the ring based sensor. One of the MZI reflector's arm will be exposed to the sensing environment.

Sensing is one of the most attractive applications of photonics integrated cir-

uits (PICs) [45–48], and silicon photonics has proven to be a quite promising platform for this application due to its high sensitivity and mass fabrication potential. Among silicon photonics devices, ring resonators and Mach-Zehnder-Interferometers (MZIs) are the most commonly used to demonstrate sensing applications. Ring resonators have advantages of a very narrow bandwidth, leading to a high sensitivity [49–51]. But sensing range is within the free spectral range (FSR), and rings can be sensitive to temperature-induced noise. MZI-based sensors can benefit from the temperature insensitivity as the temperature induced index change would cancel out if the MZI are designed to be balanced. However, they have the drawback of a broad bandwidth.

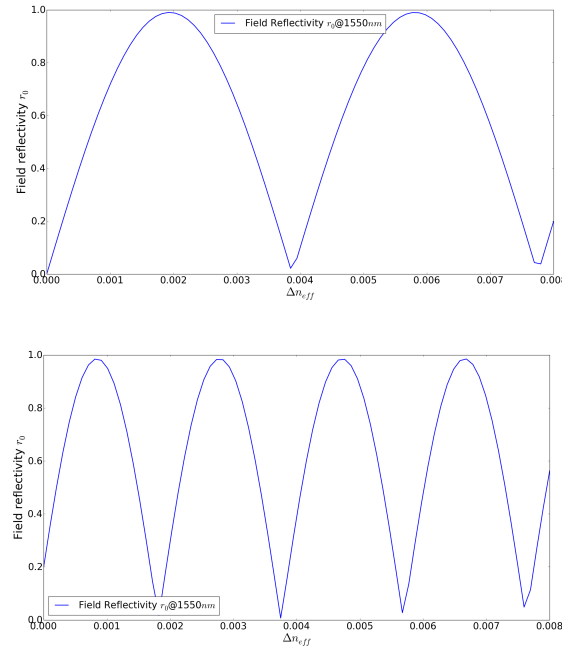


Figure 4.43: Field reflectivity r_0 as a function of index change. (a) $L_1 = L_2 = 200\mu\text{m}$ (b) $L_1 = L_2 = 400\mu\text{m}$. Increasing the arm length will lead to a smaller FSR but a sharper slope.

A novel sensing scheme can be developed with a silicon ring resonator with the tunable reflector inside, as shown in Fig. 4.42. The basic principle is the reflection induced resonance splitting of a ring resonator. The split distance is proportional to the reflection inside the ring, which couples the clockwise and counterclockwise mode. This idea of using resonance splitting for sensing application has already been adopted to detect the number of nanoparticles like viruses using a high Q

whispering-gallery-microcavity (WGM) [52], as the split distance reported is supposed to scale with the number of nanoparticles attached to the WGM.

In our sensing mechanism here the intentionally introduced loop-MZI reflector in the ring will incorporate the sensor waveguide. A small change in the sensor waveguide will introduce a significant change in its reflectivity, which will in turn affect the peak splitting in the ring transmission spectrum. Consequently we can track the split distance to detect the change of environment index. This kind of structure will combine both advantages of MZI based sensors and ring resonator based sensors. Since it is a ring resonator, it's accompanied with narrow bandwidth and high sensitivity and resolution. While the sensing element here is actually a MZI, which gives the robustness to temperature variation.

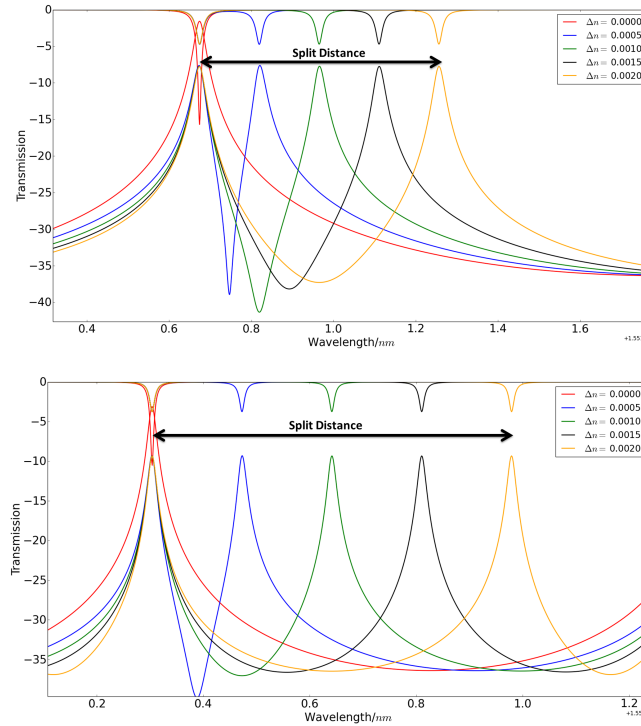


Figure 4.44: Simulated spectra of two devices, (a) $L_1 = L_2 = 100 \mu m$. (b) $L_1 = L_2 = 250 \mu m$. The red curve shows the original non-split resonance, while other colorful curves indicate how the split distance increases with increasing index change of the sensing arm. The result shows a efficiency around 350 nm/RIU .

Briefly speaking, the distance between the split peaks in the frequency domain $\Delta\omega$ is related to the reflectivity in the following equation:

$$\Delta\omega = 2 \frac{r_0 c}{n_g L} \cos\left(\frac{\phi_\mu}{2}\right) \quad (4.14)$$

Where r_0 is the field reflectivity, c light speed in vacuum, n_g group index of the waveguide and L ring's physical length. For simple coupling, we find that $\phi_\mu = 0$. A more straightforward equation (4.15) could be generated after simple transformations of (4.14):

$$\Delta\lambda = \frac{\lambda_1 \lambda_2}{\lambda_0^2} \frac{FSR}{\pi} r_0 \quad (4.15)$$

Where λ_0 is the original resonance wavelength, λ_1, λ_2 are the two wavelengths when the original resonance becomes split. $\Delta\lambda$ is the split distance between λ_1 and λ_2 , and FSR the free spectral range in the wavelength domain. All of the parameters in equation (4.15) can be extracted from the measured spectra by proper fitting introduced in chapter 3.

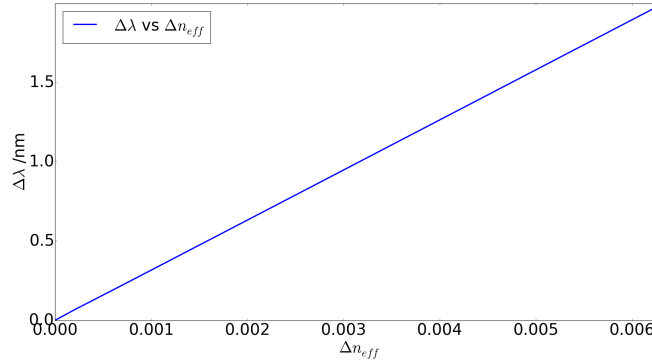


Figure 4.45: Simulated $\Delta\lambda$ as a function of Δn_{eff} .

In terms of the MZI based reflector, one arm L_1 is exposed to the sensing environment while the rest of the device is covered by proper cladding. A small change in the index of the sensing arm can already introduce a significant effect in the reflection of the reflector. It is this sensitivity which we use to create a sensor. Thus the change in environment index will lead to a change in effective index n_{eff} of arm L_1 , and a change in reflectivity, and as a consequence a change in the ring peak splitting $\Delta\lambda$.

The sensing efficiency is given in equation (4.16). Clearly, in order to achieve a large efficiency, we need a large FSR and a high sensitivity of reflectivity $\frac{dr_0}{dn}$. The first term is inversely proportional to ring's length L (including the total length of the reflector), while the second term is proportional to the length of MZI's arm L_1 as illustrated in Fig. 4.43. In summary, the sensing efficiency as a function

of sensing length L_1 is relative constant at a value around 350nm/RIU (refractive index unit) as shown in Fig. 4.44 and Fig. 4.45.

$$\frac{d\Delta\lambda}{dn_{eff}} = \frac{FSR}{\pi} \frac{dr_0}{dn_{eff}} \quad (4.16)$$

4.5 Summary

In this chapter, we thoroughly discussed reflection engineering in a silicon ring resonator using a single tunable reflector inside. We both theoretically prove and experimentally demonstrate a couple of applications of such a structure. First of all, this structure can be utilized to fundamentally suppress stochastic backscattering, which is an inevitable problem in silicon photonics. We demonstrate that, by tuning the reflector using metal heaters, not only the resonance splitting at the *drop* port and the *thru* port can be eliminated, but also the reflection to the *in* port and leakage to the *add* port can be significantly suppressed. Secondly, this kind of device can be used to generate a silicon ring resonator with ultra wide FSR and tuning range by introducing a small length difference to the two arms of the MZI reflector. Besides these two applications, we also briefly introduce the possibility of such a device to be used as tunable microwave photonic filter as well as a novel optical sensor which senses the environment by tracking the resonance splitting.

References

- [1] Adil Masood, M Pantouvaki, D Goossens, G Lepage, P Verheyen, Dries Van Thourhout, P Absil, and Wim Bogaerts. *Cmos compatible heater fabrication approaches for thermal tuning of photonics devices*. In 17th Annual Symposium of the IEEE Photonics Benelux Chapter, pages 307–310. IEEE, 2012.
- [2] Masao Kawachi. *Silica waveguides on silicon and their application to integrated-optic components*. Optical and Quantum Electronics, 22(5):391–416, 1990.
- [3] Isa Kiyat, Atilla Aydinli, and Nadir Dagli. *Low-power thermo-optical tuning of SOI resonator switch*. IEEE photonics technology letters, 18(2):364–366, 2006.
- [4] Reja Amatya, Charles W Holzwarth, Henry I Smith, and Rajeev J Ram. *Precision tunable silicon compatible microring filters*. IEEE Photonics Technology Letters, 20(20):1739–1741, 2008.
- [5] Maroof H Khan, Hao Shen, Yi Xuan, Lin Zhao, Shijun Xiao, Daniel E Leaird, Andrew M Weiner, and Minghao Qi. *Ultrabroad-bandwidth arbitrary radiofrequency waveform generation with a silicon photonic chip-based spectral shaper*. Nature Photonics, 4(2):117–122, 2010.
- [6] Ang Li and Wim Bogaerts. *Fundamentally cancel backscattering in silicon microrings*. In Lasers and Electro-Optics Europe & European Quantum Electronics Conference (CLEO/Europe-EQEC, 2017 Conference on), pages 1–1. IEEE, 2017.
- [7] Sam Werquin, Steven Verstuyft, and Peter Bienstman. *Integrated interferometric approach to solve microring resonance splitting in biosensor applications*. Optics express, 21(14):16955–16963, 2013.
- [8] Qiangsheng Huang, Keqi Ma, and Sailing He. *Experimental demonstration of single mode-splitting in microring with Bragg gratings*. IEEE Photonics Technology Letters, 27(13):1402–1405, 2015.
- [9] Amir Arbabi, Young Mo Kang, Ching-Ying Lu, Edmond Chow, and Lynford L Goddard. *Realization of a narrowband single wavelength microring mirror*. Applied Physics Letters, 99(9):091105, 2011.
- [10] GW Cong, K Suzuki, SH Kim, K Tanizawa, S Namiki, and H Kawashima. *Demonstration of a 3-dB directional coupler with enhanced robustness to gap variations for silicon wire waveguides*. Optics express, 22(2):2051–2059, 2014.

- [11] David AB Miller. *Perfect optics with imperfect components*. Optica, 2(8):747–750, 2015.
- [12] Ang Li, Thomas Vaerenbergh, Peter Heyn, Peter Bienstman, and Wim Bogaerts. *Backscattering in silicon microring resonators: a quantitative analysis*. Laser & Photonics Reviews, 10(3):420–431, 2016.
- [13] Ang Li, Qiangsheng Huang, and Wim Bogaerts. *Design of a single all-silicon ring resonator with a 150 nm free spectral range and a 100 nm tuning range around 1550 nm*. Photonics Research, 4(2):84–92, 2016.
- [14] Shankar Kumar Selvaraja, Wim Bogaerts, and Dries Van Thourhout. *Loss reduction in silicon nanophotonic waveguide micro-bends through etch profile improvement*. Optics Communications, 284(8):2141–2144, 2011.
- [15] Hao Shen, Li Fan, Jian Wang, Justin C Wirth, and Minghao Qi. *A Taper to Reduce the Straight-to-Bend Transition Loss in Compact Silicon Waveguides*. Photonics Technology Letters, IEEE, 22(15):1174–1176, 2010.
- [16] Magdalena S Nawrocka, Tao Liu, Xuan Wang, and Roberto R Panepucci. *Tunable silicon microring resonator with wide free spectral range*. Applied physics letters, 89(7):71110–71110, 2006.
- [17] Ashok M Prabhu, Alan Tsay, Zhanghua Han, and Vien Van. *Ultracompact SOI microring add-drop filter with wide bandwidth and wide FSR*. IEEE Photonics Technology Letters, 21(10):651–653, 2009.
- [18] Fengnian Xia, Lidija Sekaric, and Yurii a Vlasov. *Mode conversion losses in silicon-on-insulator photonic wire based racetrack resonators*. Optics express, 14(9):3872–86, May 2006.
- [19] Tin Komljenovic, Linjun Liang, Rui-Lin Chao, Jared Hulme, Sudharsanan Srinivasan, Michael Davenport, and John E Bowers. *Widely-Tunable Ring-Resonator Semiconductor Lasers*. Applied Sciences, 7(7):732, 2017.
- [20] Tom Claes, Wim Bogaerts, and Peter Bienstman. *Experimental characterization of a silicon photonic biosensor consisting of two cascaded ring resonators based on the Vernier-effect and introduction of a curve fitting method for an improved detection limit*. Optics express, 18(22):22747–22761, 2010.
- [21] JC Hulme, JK Doylend, and JE Bowers. *Widely tunable Vernier ring laser on hybrid silicon*. Optics express, 21(17):19718–19722, 2013.
- [22] Qiangsheng Huang, Keqi Ma, and Sailing He. *Experimental Demonstration of Single Mode-Splitting in Microring With Bragg Gratings*. Photonics Technology Letters, IEEE, 27(13):1402–1405, July 2015.

- [23] R Boeck, W Shi, L Chrostowski, and NAF Jaeger. *FSR-eliminated Vernier racetrack resonators using grating-assisted couplers*. IEEE Photonics Journal, 5(5):2202511–2202511, 2013.
- [24] Darius Urbonas, Armandas Balčytis, Martynas Gabalis, Konstantinas Vaškevičius, Greta Naujokaitė, Saulius Juodkasis, and Raimondas Petruškevičius. *Ultra-wide free spectral range, enhanced sensitivity, and removed mode splitting SOI optical ring resonator with dispersive metal nanodisks*. Opt. Lett., 40(13):2977–2980, Jul 2015.
- [25] Stephen J Emelett and Richard Soref. *Design and simulation of silicon microring optical routing switches*. Journal of lightwave technology, 23(4):1800, 2005.
- [26] J Komma, C Schwarz, G Hofmann, D Heinert, and R Nawrodt. *Thermo-optic coefficient of silicon at 1550 nm and cryogenic temperatures*. Applied Physics Letters, 101(4):041905, 2012.
- [27] Wim Bogaerts, Peter De Heyn, Thomas Van Vaerenbergh, Katrien De Vos, Shankar Kumar Selvaraja, Tom Claes, Pieter Dumon, Peter Bienstman, Dries Van Thourhout, and Roel Baets. *Silicon microring resonators*. Laser & Photonics Reviews, 6(1):47–73, 2012.
- [28] Francesco Morichetti, Antonio Canciamilla, Carlo Ferrari, Matteo Torregiani, Andrea Melloni, and Mario Martinelli. *Roughness induced backscattering in optical silicon waveguides*. Physical Review Letters, 104(January):1–4, 2010.
- [29] Philippe P Absil, Peter Verheyen, Peter De Heyn, Marianna Pantouvaki, Guy Lepage, Jeroen De Coster, and Joris Van Campenhout. *Silicon photonics integrated circuits: a manufacturing platform for high density, low power optical I/O's*. Optics express, 23(7):9369–9378, 2015.
- [30] Po Dong, Roshanak Shafiiha, Shirong Liao, Hong Liang, Ning-Ning Feng, Dazeng Feng, Guoliang Li, Xuezhe Zheng, Ashok V Krishnamoorthy, and Mehdi Asghari. *Wavelength-tunable silicon microring modulator*. Optics express, 18(11):10941–10946, 2010.
- [31] Jianji Dong, Li Liu, Dingshan Gao, Yuan Yu, Aoling Zheng, Ting Yang, and Xinliang Zhang. *Compact notch microwave photonic filters using on-chip integrated microring resonators*. IEEE Photonics Journal, 5(2):5500307–5500307, 2013.
- [32] JX Chen, Y Wu, J Hodiak, and PKL Yu. *A novel digitally tunable microwave-photonic notch filter using differential group-delay module*. IEEE Photonics Technology Letters, 15(2):284–286, 2003.

- [33] Yan Yin, Xiuge Che, Jun Hua Wang, and Kai Zheng. *Optical-fiber notch filter for storage ring transverse feedback system*. In Particle Accelerator Conference, 2007. PAC. IEEE, pages 4075–4077. IEEE, 2007.
- [34] Erwin HW Chan, Kamal E Alameh, and Robert A Minasian. *Photonic band-pass filters with high skirt selectivity and stopband attenuation*. Journal of lightwave technology, 20(11):1962, 2002.
- [35] Qiang Li, Ziyang Zhang, Jing Wang, Min Qiu, and Yikai Su. *Fast light in silicon ring resonator with resonance-splitting*. Optics express, 17(2):933–940, 2009.
- [36] Robert W Boyd, Daniel J Gauthier, and Alexander L Gaeta. *Applications of slow light in telecommunications*. Optics and Photonics News, 17(4):18–23, 2006.
- [37] Enrique Parra and John R Lowell. *Toward applications of slow light technology*. Optics and Photonics News, 18(11):40–45, 2007.
- [38] Lij // ijun J Wang, A Kuzmich, and Arthur Dogariu. *correction: Gain-assisted superluminal light propagation*. Nature, 411(6840):974–974, 2001.
- [39] Michael D Stenner, Daniel J Gauthier, and Mark A Neifeld. *The speed of information in a ‘fast-light’ optical medium*. Nature, 425(6959):695–698, 2003.
- [40] Raymond Y Chiao and Peter W Milonni. *Fast light, slow light*. Optics and Photonics News, 13(6):26–30, 2002.
- [41] Kwang Yong Song, Miguel González Herráez, and Luc Thévenaz. *Gain-assisted pulse advancement using single and double Brillouin gain peaks in optical fibers*. Optics express, 13(24):9758–9765, 2005.
- [42] A Schweinsberg, NN Lepeshkin, MS Bigelow, RW Boyd, and SI Jarabo. *Observation of superluminal and slow light propagation in erbium-doped optical fiber*. EPL (Europhysics Letters), 73(2):218, 2005.
- [43] Bala Pesala, Zhangyuan Chen, Alexander V Uskov, and Connie Chang-Hasnain. *Experimental demonstration of slow and superluminal light in semiconductor optical amplifiers*. Optics express, 14(26):12968–12975, 2006.
- [44] C Ciminelli, CE Campanella, F Dell’Olio, and MN Armenise. *Fast light generation through velocity manipulation in two vertically-stacked ring resonators*. Optics express, 18(3):2973–2986, 2010.
- [45] Richard Soref. *The past, present, and future of silicon photonics*. IEEE Journal of selected topics in quantum electronics, 12(6):1678–1687, 2006.

- [46] Adam Densmore, D-X Xu, Philip Waldron, Siegfried Janz, Pavel Cheben, J Lapointe, A Delge, Boris Lamontagne, JH Schmid, and Edith Post. *A silicon-on-insulator photonic wire based evanescent field sensor*. IEEE Photonics Technology Letters, 18(23):2520–2522, 2006.
- [47] Francesco Dell’Olio and Vittorio MN Passaro. *Optical sensing by optimized silicon slot waveguides*. Optics Express, 15(8):4977–4993, 2007.
- [48] Yu Chen, Hongtao Lin, Juejun Hu, and Mo Li. *Heterogeneously integrated silicon photonics for the mid-infrared and spectroscopic sensing*. ACS nano, 8(7):6955–6961, 2014.
- [49] Muzammil Iqbal, Martin A Gleeson, Bradley Spaugh, Frank Tybor, William G Gunn, Michael Hochberg, Tom Baehr-Jones, Ryan C Bailey, and L Cary Gunn. *Label-free biosensor arrays based on silicon ring resonators and high-speed optical scanning instrumentation*. IEEE Journal of Selected Topics in Quantum Electronics, 16(3):654–661, 2010.
- [50] Katrien De Vos, Irene Bartolozzi, Etienne Schacht, Peter Bienstman, and Roel Baets. *Silicon-on-Insulator microring resonator for sensitive and label-free biosensing*. Optics express, 15(12):7610–7615, 2007.
- [51] Gun-Duk Kim, Hak-Soon Lee, Chang-Hyun Park, Sang-Shin Lee, Boo Tak Lim, Hee Kyoung Bae, and Wan-Gyu Lee. *Silicon photonic temperature sensor employing a ring resonator manufactured using a standard CMOS process*. Optics express, 18(21):22215–22221, 2010.
- [52] Jiangang Zhu, Sahin Kaya Ozdemir, Yun-Feng Xiao, Lin Li, Lina He, Da-Ren Chen, and Lan Yang. *On-chip single nanoparticle detection and sizing by mode splitting in an ultrahigh-Q microresonator*. Nature photonics, 4(1):46–49, 2010.

5

Engineered reflections in silicon ring resonators with double tunable reflectors

5.1 General introduction of the device

In chapter refch4 we give two in-depth analyzed and a few briefly introduced applications of a silicon ring resonator with a single tunable reflector inside. Due to the broad tuning range and efficient control of such a reflector, we manage to get diverse reflection conditions inside a ring cavity. And it's quite natural to think one step further: what if we put two reflectors inside a ring resonator? The unique thing of putting an extra reflector lies in that two embedded Fabry-Perot cavities will be formed inside the ring resonator. So instead of a pure travelling wave cavity, now it becomes a mixed cavity system (two travelling modes and two standing wave modes). The interaction between these modes will generate multiple interesting phenomenon. In this chapter, we will thoroughly analyze such a device and show some phenomenon observed in experiments and give theoretical explanation.

The schematic of such a device is given in Fig. 5.1(a) and (c). it consists of a ring resonator with two reflectors placed symmetrically in the ring cavity. Each of the reflector is controlled by a PS on top of one of its arms. The illustration of this FP cavity formed by the two reflectors are presented in Fig. 5.1(b) and (d). Based on the working conditions of these two reflectors, the output of such a device can be categorized into three stages:

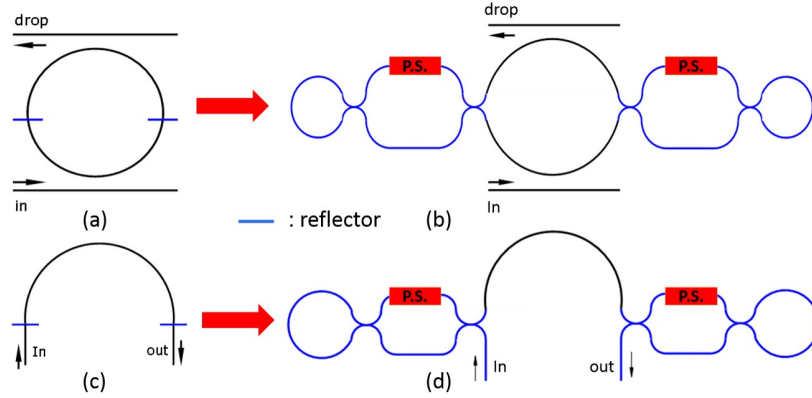


Figure 5.1: (a) and (c) give the conceptual illustrations of our device and the Fabry-Perot cavity formed by two reflectors, which are represented by blue lines. (b) and (d) show the schematics where the loop-ended MZI based reflectors replace the blue lines.

- Pure traveling wave cavity. It will become this case when both reflectors are tuned to introduce zero reflections. Thus this device is a pure ring resonator. The output at its drop port is then a Lorentzian shaped resonance as evident in Fig. 5.2(a). Note that in the simulations, the DCs of those reflectors are defined as perfect 50/50 splitters and the MZI is balanced, thus reflectors introduce zero reflections at the original state (without extra phase shift added to the PS). Even if the fabricated reflectors will for sure introduce certain reflectivity at the original state as the DCs will be deviated from 50/50 condition, it can always be tuned to zero reflection condition as explained in chapter 4.
- When one of the reflectors starts to introduce reflectivity by adding phase shift to its arm while the other one stays at zero reflection condition, normal resonance splitting will start to appear as shown in Fig. 5.2(a). And the split distance is proportional to the phase shift added. Under this circumstance, the device can be used to demonstrated applications mentioned in previous chapter, including tunable MPF, tunable fast light etc.
- When the second reflectors also start to increase its reflectivity, two embedded FP cavities will be constructed. And their outputs or their modes are determined by two reflectors. Now the device becomes a mixed cavity system whose output is a result of the interaction of the FP cavity and the ring cavity. Under different tuning conditions of the two reflectors (thus the FP mode), Fano resonance or electromagnetically induced transparency (EIT) will be generated as plotted in Fig. 5.2(c) and (d). Each of them can be fur-

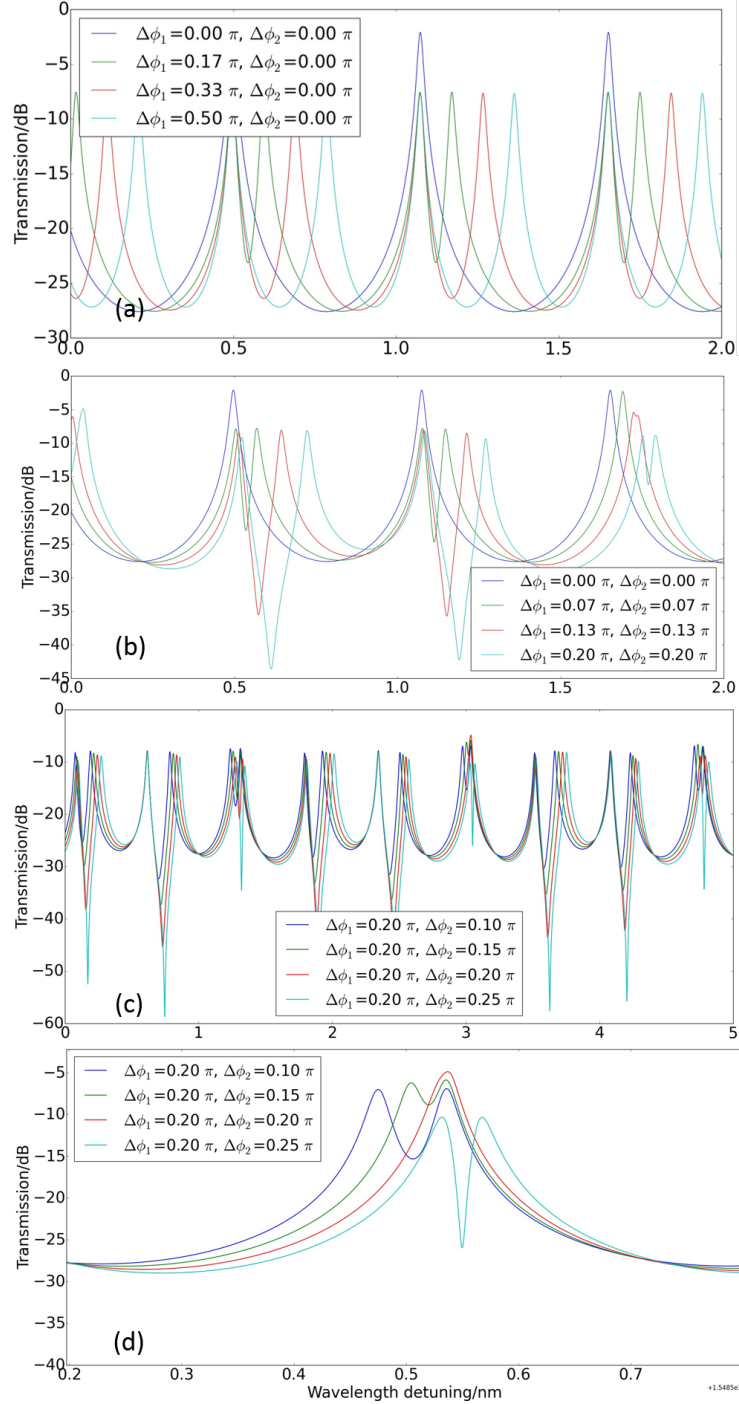


Figure 5.2: Simulated outputs at the drop port of the device. Without any reflections, we see a Lorentzian-shaped resonance. Increasing one reflector's reflectivity leads to normal resonance splitting (a); When the second reflector also introduces reflection, a Fano resonance appears from the interference between a FP mode and a ring resonance (b); An EIT like spectrum can be generated by precisely adjusting the reflectors' reflectivities (c). A zoom view of one resonance (d).

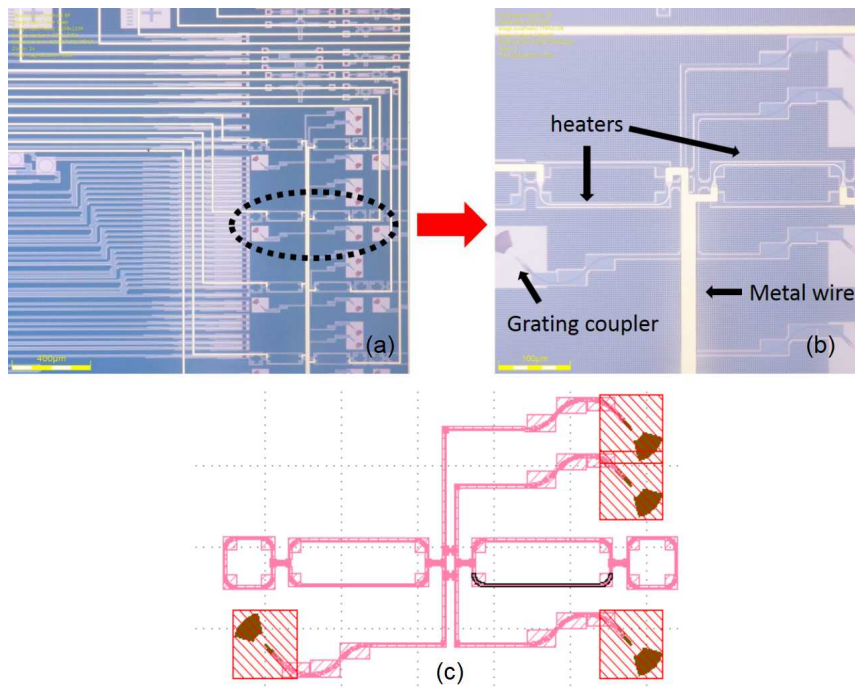


Figure 5.3: Microscopic images of our devices (a) and a zoomed view of the heaters (b). (c) gives the designed layout for this device.

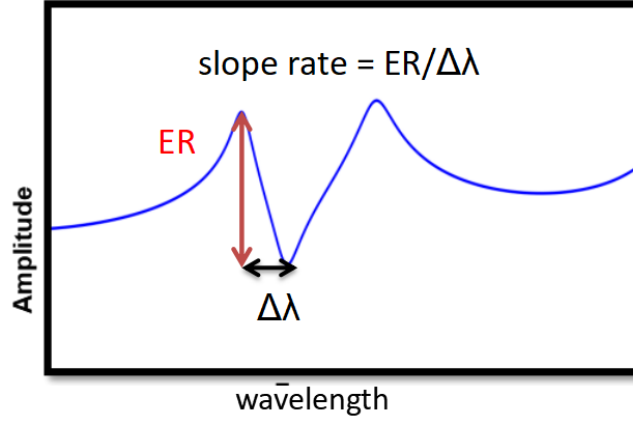


Figure 5.4: A basic introductory figure of a Fano resonance, with indication of its key parameters, including ER and slope rate.

ther tuned using metal heaters. The details about Fano resonance and EIT will be given later.

The microscopic figures of our devices are given in Fig. 5.3. The device is fabricated on IMEC's passive silicon photonics platform through the Europractice MPW service. As usual, the substrate is a 220 nm thick SOI wafer. We design the waveguide cross-section to be 450 nm×220 nm to ensure single mode operation. Grating couplers are employed to achieve vertical coupling between fibers and our chip. The structures are covered by planarized silicon dioxide protection layer, on top of which our metal heaters are processed in-house. The heaters are based on titanium resistive elements with a 2 μm width and 100 nm thickness connected with gold contact electrodes.

5.2 Fano resonance

5.2.1 Introduction and background

As mentioned above, in the third stage, one important phenomenon is the tunable Fano resonance generated by this device. Fano resonance was first proposed by U. Fano in 1961 [2]. It is a general phenomenon throughout nuclear, atomic and solid-state physics [3–8]. Overallly speaking, the Fano resonance line-shape is due to the interference between two scattering amplitudes, one due to scattering within a continuum of states (the background process) and the second due to an excitation of a discrete state (the resonant process). In photonics world, the origin for Fano resonance lies in the interference between two modes, one of which is very

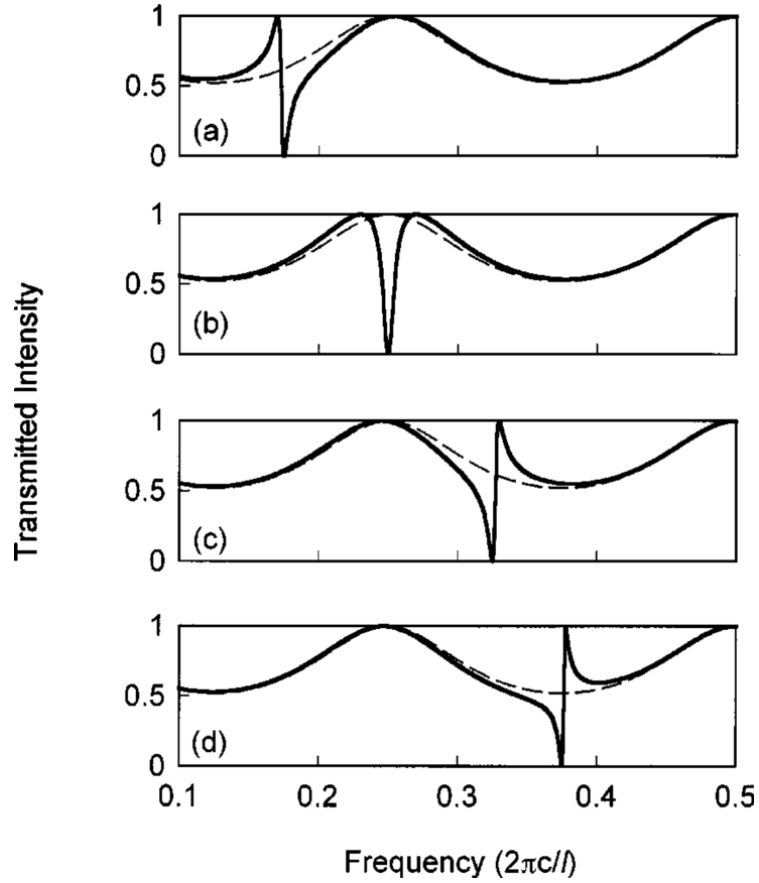


Figure 5.5: An example illustration of the asymmetric Fano resonance from Ref. [1]. Clearly shown in this figure, the Fano resonance originates from the interaction between a sharp resonance mode and a smooth background mode. In Ref. [1], this sharp resonance mode comes from a resonator side coupled to a bus waveguide while the smooth background comes from a Fabry-Perot cavity formed by two partial transmitting element on two sides of the bus waveguide.

smooth corresponding (low Q) with background mode while the other one can be a resonance (high Q) serving as the discrete state. Further speaking, around the resonance, the background mode varies smoothly both in amplitude and phase, while the resonance changes rather rapidly, especially in phase. For instance, a ring resonance can have almost π phase change around its resonance. Thus their interference pattern around the resonance will be very asymmetric due to the abrupt phase change accompanied by the resonance.

Fano resonances are considered interesting in photonics thanks to its extremely sharp slope and asymmetric shape in contrast to ordinary Lorentzian shaped resonance as shown in Fig. 5.4. These features make Fano resonance an attractive candidate for high efficiency sensors, low power consumption switches and modulators [9–12], as a much smaller wavelength shift is needed to generate the same transmission change. Recently ultra small laser cavities utilizing Fano resonances have also been demonstrated [13].

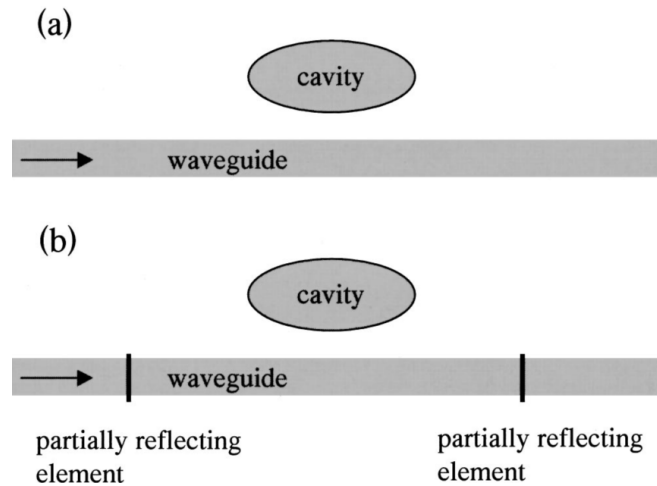


Figure 5.6: The conceptual schematic proposed by Fan for Fano resonance Ref. [1]. Two partial transmitting/reflecting elements are placed on the bus waveguide to form a Fabry-Perot cavity, which will interact with the ring resonance at the bus waveguide output.

For those applications like sensors and switches, it's highly desirable or necessary to function as an integrated circuit. Indeed, Fano resonances have already been demonstrated in integrated optics through various approaches, including embedded ring resonators, plasmonics and metamaterials, two beam interference in a ring resonator, two indirectly coupled WGMs, a ring resonator with coupled feedback waveguide, photonics crystal cavity etc. [13–19] And silicon photonics, as one of the most promising platforms for integrated optics, has also been heavily investigated for demonstration of Fano resonances. Unfortunately each of these

methods has its drawbacks. Either the devices are not fully integrated, or they suffer from relatively low extinction ratio (ER) and slope rate as well as poor tunability. If Fano resonance is considered to outperform ordinary Lorentzian shaped resonance as a candidate for high efficiency sensor and low power switch, its slope rate shall be at least higher than a normal Lorentzian resonance of silicon ring resonators, which can be approximated to 60 dB/nm (3 dB bandwidth of a silicon ring resonator resonance can be as narrow as 100 pm, so the slope rate is approximately $\frac{3 \text{ dB}}{50 \text{ pm}} = 60 \text{ dB/nm}$). However, Fano resonances demonstrated in silicon photonics so far have not yet shown superior performance.

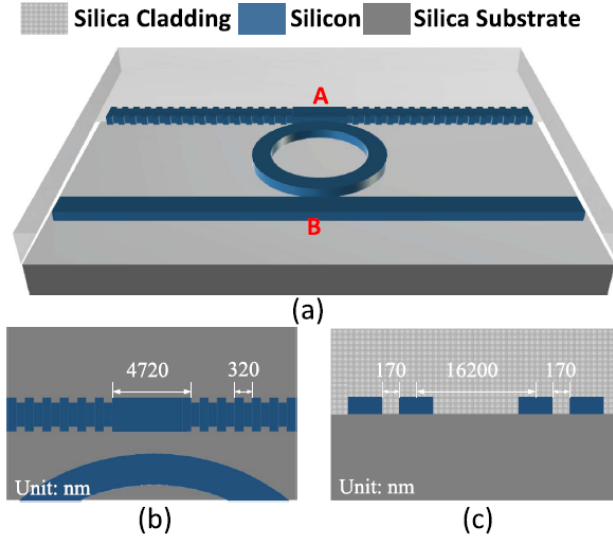


Figure 5.7: An experimental implementation of the structure proposed in Ref. [1] in silicon photonics reported in Ref. [17]. Two partial transmitting/reflecting elements are realized by sidewall grating along the bus waveguide.

Our device gets the Fano resonance through the interference of a low Q Fabry-Perot cavity mode and a high Q ring resonance. Fan theoretically proposed a similar approach in 2002, where two reflectors at the bus waveguide were used to form a FP cavity outside the ring cavity as shown in Fig. 5.6 [1]. Zhang et al. made an experimental implementation of the structure proposed by Fan in silicon photonics platform [17], where they used two sidewall gratings as the partially transmitting elements as given in Fig. 5.7. Unfortunately, the parameters of the Fabry-Perot cavity (grating period, cavity length etc.) formed by those sidewall gratings, which determine the properties of the Fano resonance, can only be physically adjusted instead of dynamically tuned. Thus they can only achieve tuning of the Fano resonance by injecting a high power pump laser to optically modify

the coupling strength between the Fabry-Perot cavity and the ring cavity. This is impractical for many applications and has a poor tuning range and efficiency. The maximum ER and slope rate reported is limited to 22.54 dB and 250.4 dB/nm, respectively. And the tuning range up to 90 pm is demonstrated.

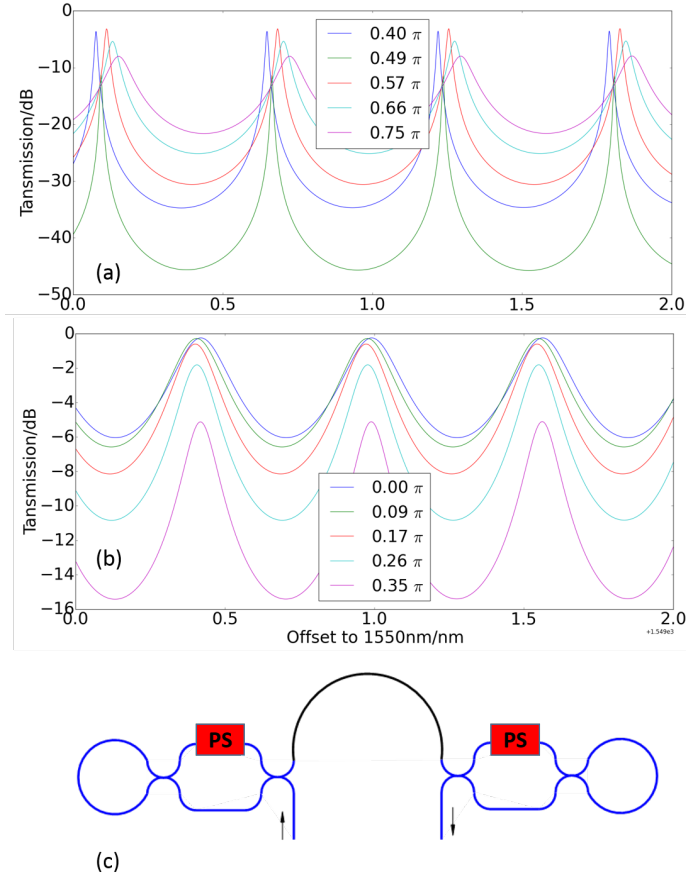


Figure 5.8: Simulated spectra of the embedded Fabry-Perot cavity (a),(b) and its schematic (c).

5.2.2 Principle and simulation

The structure proposed by us consists of a silicon ring resonator and two tunable reflectors inside as shown in Fig. 5.1(a) and (c). The Fano resonance comes from the interference of two modes, the background mode is from the Fabry Perot (FP) cavity formed by those two reflectors as illustrated in Fig. 5.1(b) and (d), while the other discrete mode is the ring resonance. The FP mode is dependent on the two

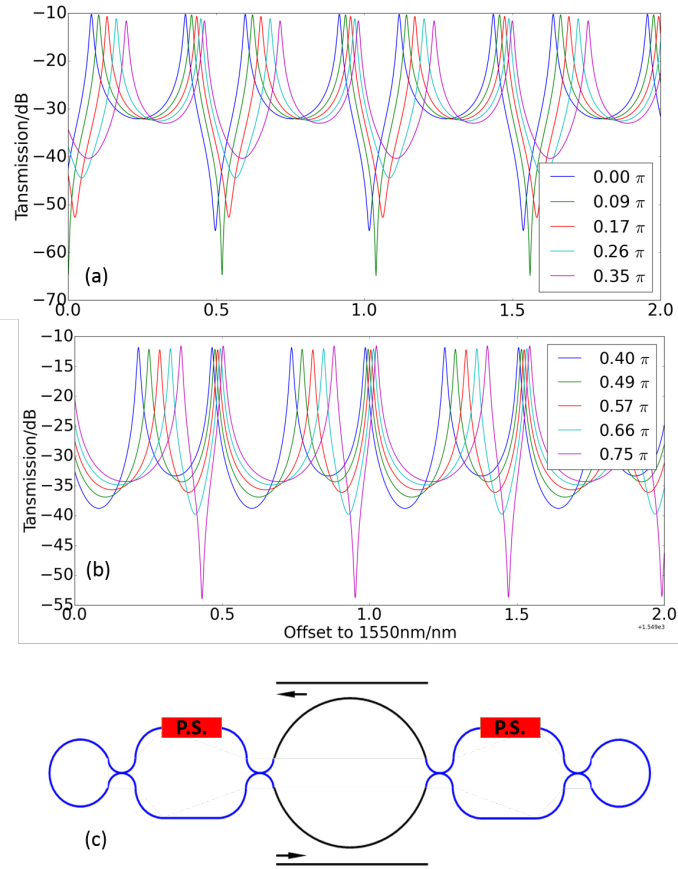


Figure 5.9: Simulated spectra of the complete device (a),(b), and its schematic (c). The tuning conditions are the same with those in Fig. 5.8.

reflectors which can be efficiently tuned using metal heaters, thus the generated Fano resonance exhibits good tunability in terms of ER and slope rate. It has been experimentally proven to generate a Fano resonance with over 40 dB maximum ER and over 700 dB/nm slope rate, which to our best knowledge, are the largest values realized so far.

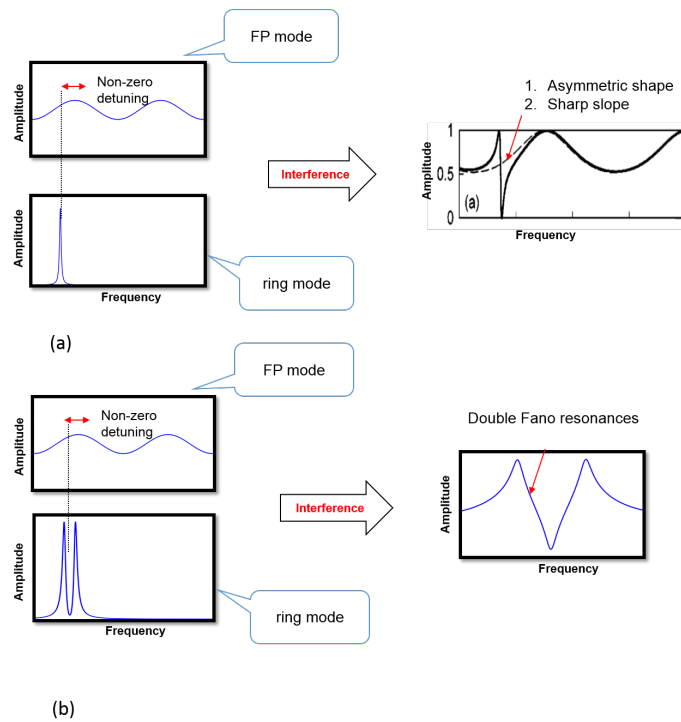


Figure 5.10: This figure gives the conceptual illustration of the generation of a double Fano resonance pattern from the interference between a continuous mode and a split resonance.

The reflector is already characterized in detail in chapter 3. Here both reflectors are designed to be identical with balanced MZI in order to provide flat reflection spectrum. The armlength is designed to be $200\ \mu m$ to ensure adequate phase shift induced by metal heaters. And they are placed symmetrically in the ring waveguide. In Fig. 5.8 we plot the simulated spectra of the Fabry-Perot cavity and the complete device in Fig. 5.9. As clearly shown in Fig. 5.8, by introducing different phase shifts to the reflectors to change their reflectivities, the Fabry-Perot mode can be tuned from quite sharp (high Q) to very smooth (low Q). The smooth mode can interfere with the discrete ring resonance mode to generate the Fano resonance, as exhibited in Fig. 5.9. It is somehow confusing as the resonance

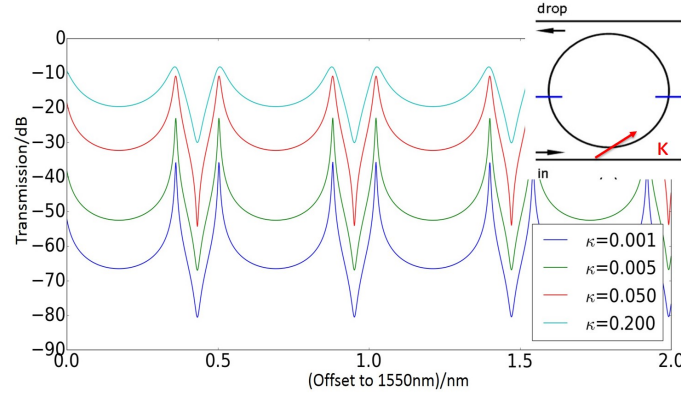


Figure 5.11: Simulation shows the influence of the power coupling coefficient of the ring resonator on the performance of the Fano resonance.

now shows a symmetric pattern around the dip while a Fano resonance shall be asymmetric as we always claim. It is easy to understand. The resonance pattern shown in Fig. 5.9 is not a single Fano resonance, instead, it consists of two identical Fano resonances standing back to back, which makes it symmetric with respect to the dip. Current ring resonance mode shows a resonance splitting due to the internal reflections inside the ring cavity which couple the clockwise circulating mode and counter-clockwise circulating mode and break their degeneracy [20]. So this Fano resonance is an interference between a continuous background mode (FP mode) with a split resonance (or two Lorentzian resonances standing back to back). Thus double Fano resonances are generated. If the reference point is set to the peak position (resonant wavelength), then the resonance is indeed asymmetric, with one side being a Lorentzian shape while the other side being quasi-linear. Fig. 5.10 gives the conceptual illustration of how this double Fano resonance is generated from the interference between the FP mode and a split resonance. For comparison, the generation of a normal single Fano resonance is also provided.

In these two simulations, we only tune one of those reflectors with another one fixed at specific reflection for simple demonstration, while in reality both reflectors can be controlled independently. Note that, the two peaks of the split resonance shift at slightly different rates. This phenomenon agrees well with our former observations [21], and has already been well explained in chapter 4.

We also investigate how the power coupling coefficient of the directional couplers in the ring resonator will influence the Fano resonance as coupling coefficient is one of the most common parameters to be engineered for a ring resonator. The results are plotted in Fig. 5.11. The ER of the Fano resonance can be increased by decreasing the power coupling coefficient (thus increasing the Q factor of the ring resonator) but this comes at the price of higher insertion loss. This is easy to

understand, as a higher Q factor will have a more abrupt phase change around a narrower optical bandwidth. Thus the interference between this resonance mode and the background mode will lead to a larger ER and sharper slope.

5.2.3 Measurement

The measurement of such a device is performed with the same setup introduced in previous chapters. First of all we give the overall measured spectra of the three stages in Fig. 5.12. Each spectrum in this figure corresponds with a tuning condition of the two phase shifters, which control the reflectivity of the reflectors. It shows good one-to-one correspondence with the three stages introduced and simulated in the introduction part as shown in Fig. 5.2. Clearly, all the three stages can be reproduced in experiments. In Fig. 5.12(a), we plot the spectra of Lorentzian-shaped resonances where both reflectors introduce zero or very low reflections as well as the normal resonance splitting case where only one reflector introduces strong reflection. If we further increase the second reflector's reflectivity by changing the power injection to the phase shifter, the Fano resonance starts to appear, as shown in Fig. 5.12(b). The spectra with EIT-feature is given in Fig. 5.12(c) and a zoom view of one EIT resonance is plotted in Fig. 5.12(d). EIT is generated on the basis of Fano resonance, by precisely controlling one phase shifter. As we can see from the legend in Fig. 5.12(c), the power injection to PS2 only changes from 0.0 mW to 0.8 mW, but a clear EIT peak appears.

In terms of the Fano resonance pattern, its specific measured spectra are exhibited in Fig. 5.13. Similar to the simulations, we fix one reflector and sweep the power injected to the other reflector. These measurements show the same resonance shapes and shift patterns as the simulation results in Fig. 5.9. Due to the disperse behavior of the directional couplers, which means that the coupling coefficients vary with wavelength, the measured resonances show different extinction ratios. The maximum ER can be over 40 dB within a 100 pm wavelength range, which gives a sharp slope with a rate over 400 dB/nm. While the maximum slope rate observed at some resonances can be over 700 dB/nm with an extinction ratio larger than 36 dB. Much less wavelength shift is needed to adequate extinction ratio if this Fano resonance is implemented as an optical sensor or switch. Such the efficiency will be increased and power consumption will be reduced. As for the tuning efficiency, less than 3 mW can tune the ER to reach its maximum. The tuning of the ER is always accompanied with the shift of the wavelength but this problem can be easily solved with an extra heater to control the ring resonance.

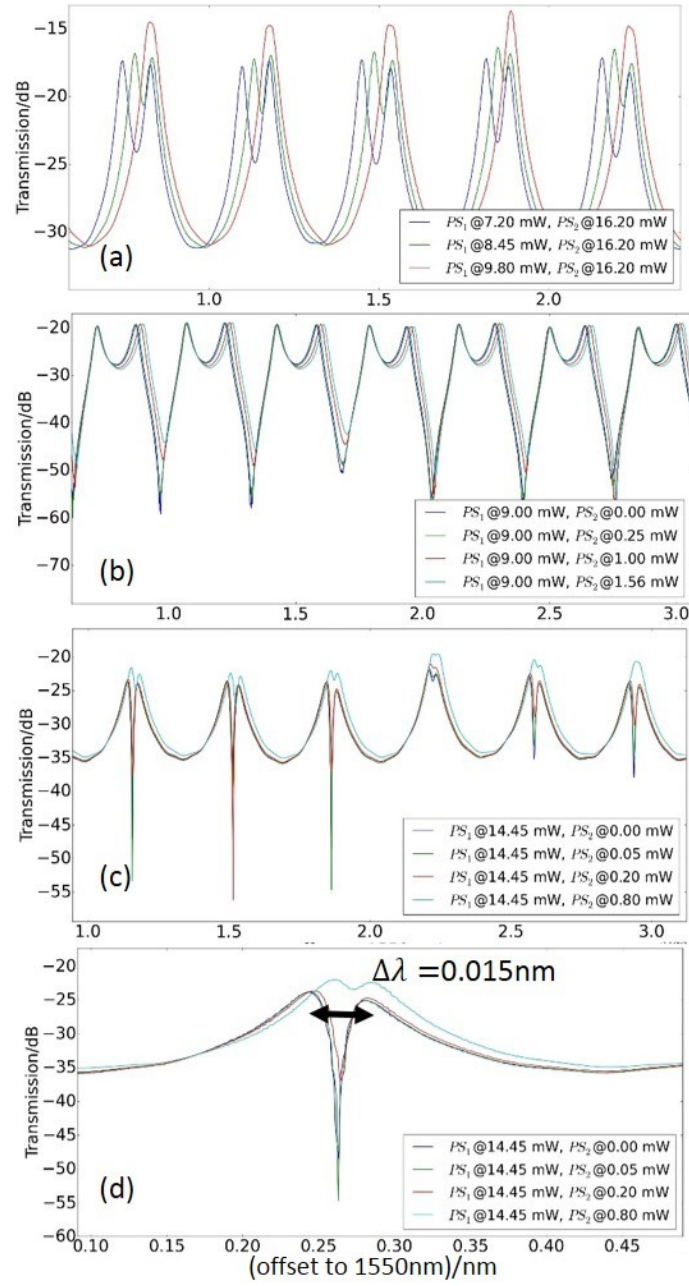


Figure 5.12: Overall measured spectra of our device with different tuning conditions of the two phase shifters. The figure presents a one-to-one correspondence with the three stages explained in the simulation part and plotted in Fig. 5.2.

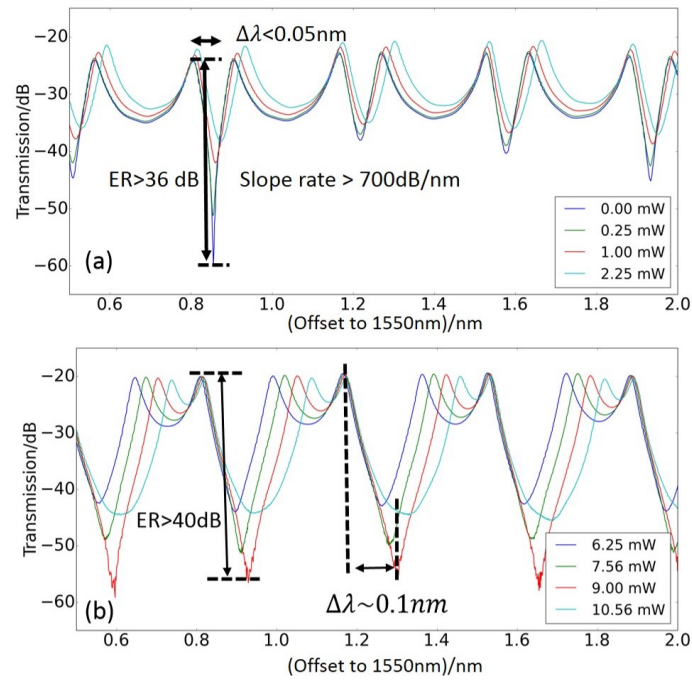


Figure 5.13: Measurements showing the tunability of the Fano resonance. One phase shifter is fixed with the other one receiving different power injection. The maximum ER can be larger than 40 dB with a corresponding slope rate over 400 dB/nm. While at other resonance, we observe a even sharper slope rate, which is over 700 dB/nm.

5.3 Optical analogue to electromagnetically induced transparency

5.3.1 Introduction

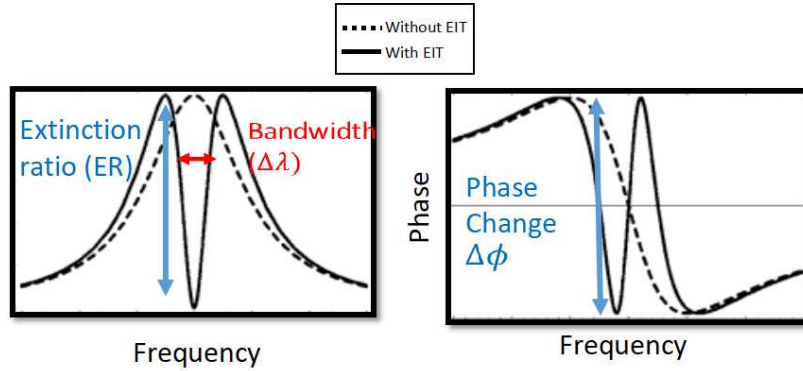


Figure 5.14: The spectral characteristics of EIT based on Fig. 1 from [22]. It will generate an ultra narrow window in the transmission or absorption spectrum. And the phase response or index profile shows an abrupt change within this window.

The same structure can also generate another phenomenon, which is called electromagnetically induced transparency (EIT). EIT is a fundamental phenomenon originally shown in atomic physics with a set of three energy states that is shown in Fig. 5.15 [22]. It will generate an ultra narrow "transparent window" in the transmission or absorption spectrum as shown in Fig. 5.14. Take the "lambda" scheme for example, to observe EIT in atomic states requires two lasers, one of them called "probe" is tuned to near the resonance between two of the energy states (from state "1" to state "2") to measure the transmission or absorption spectrum of these states. Ideally this will show a Lorentzian shape line as illustrated in dashed line in Fig. 5.14. If another laser called "pump" is present which is tuned to near resonance between the states "2" and "3", then a transparent window in the spectrum will be created by this "pump" laser. The principle behind this is the destructive interference of the transition probability amplitude of competing excitation pathways (from "1" directly to "2", or from "1" to "2" via "3" to "2"). Due to this, the electrons somehow are forbidden to transit between these two states, thus no absorption is present and a narrow transparent window is created. That is why EIT is also considered as a Fano resonance, from the interference between the probability amplitudes of these two excitation pathways.

The main benefit of demonstrating this in photonics lies in the utilization of the abrupt phase change within this ultra narrow window, which means extreme dispersion with very large group index n_g or low group velocity v_g . And this feature

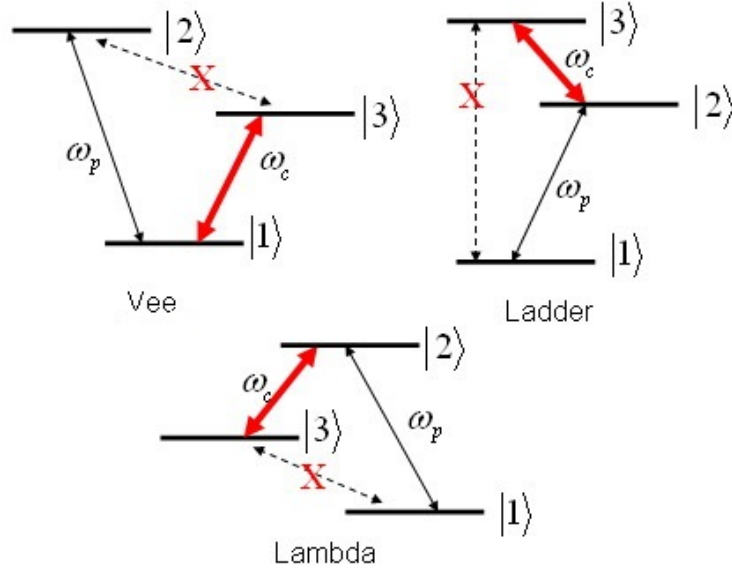


Figure 5.15: EIT level schemes can be sorted into three categories; vee, ladder, and lambda.

is very promising to further realize slow light or even stopped light [23]. Practically speaking, optical buffer or storage based on EIT becomes feasible and other applications like optical gyroscopes, laser cooling, optical switching or nonlinear optics can also be developed based on EIT [23–27]. Many efforts have been taken to generate EIT in an optical way through various platforms [28–31], including silicon photonics [32–39]. Among these approaches, coupled cavities are the most popular choice due to their similarity with atomic states. Each cavity is supposed to resonant at the frequency corresponding with energy state "2" (in other words, the two resonances need to have zero detuning). But they have to have different Q factors (photon lifetime), which refer to the two different transition pathways of "pump" and "probe". Ref. [32, 40] provide the mathematical prove of the similarity between a coupled resonator system with the atomic system for the generation of EIT and the mapping of those key parameters from each system.

5.3.2 Simulation

The simulated amplitude spectra in Fig. 5.2 already proves the ability of this device to generate an EIT peak. Fig. 5.16 further presents the simulated phase response of generated EIT peak and its tunability. By tuning the two reflectors, both of the extinction ratio of the EIT and the phase change can be tuned. In the simulation,

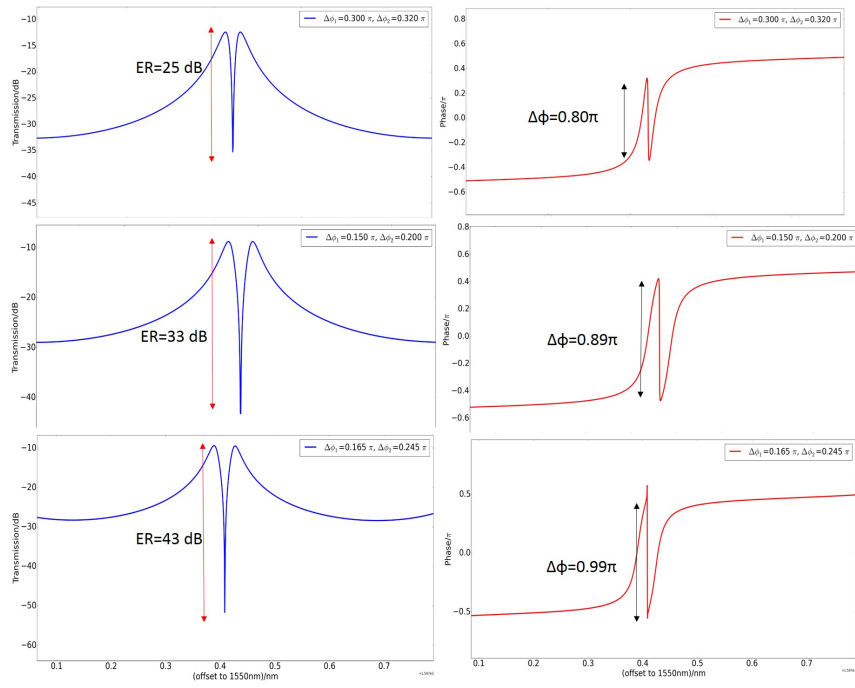


Figure 5.16: Tunability and phase response of the EIT peak generated by this ring with two reflectors. Left and right columns present the transmission in dB and the phase response normalized to π , respectively. By tuning the relative phase shift of the reflectors, we can get various EIT resonances.

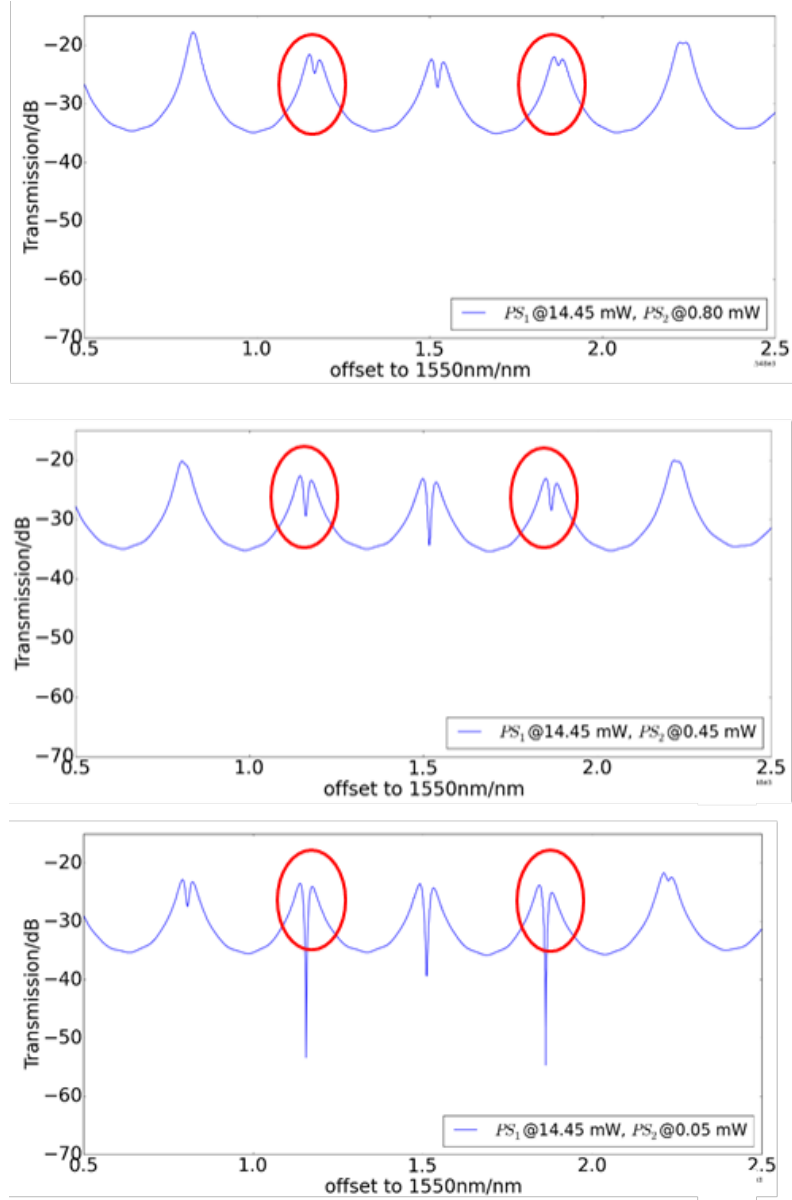


Figure 5.17: By precisely controlling one of the reflectors, a clear EIT peak emerges. Note the tiny change in the power injection shown in the legend.

we observe a phase change around 0.99π within less than 2 pm optical range.

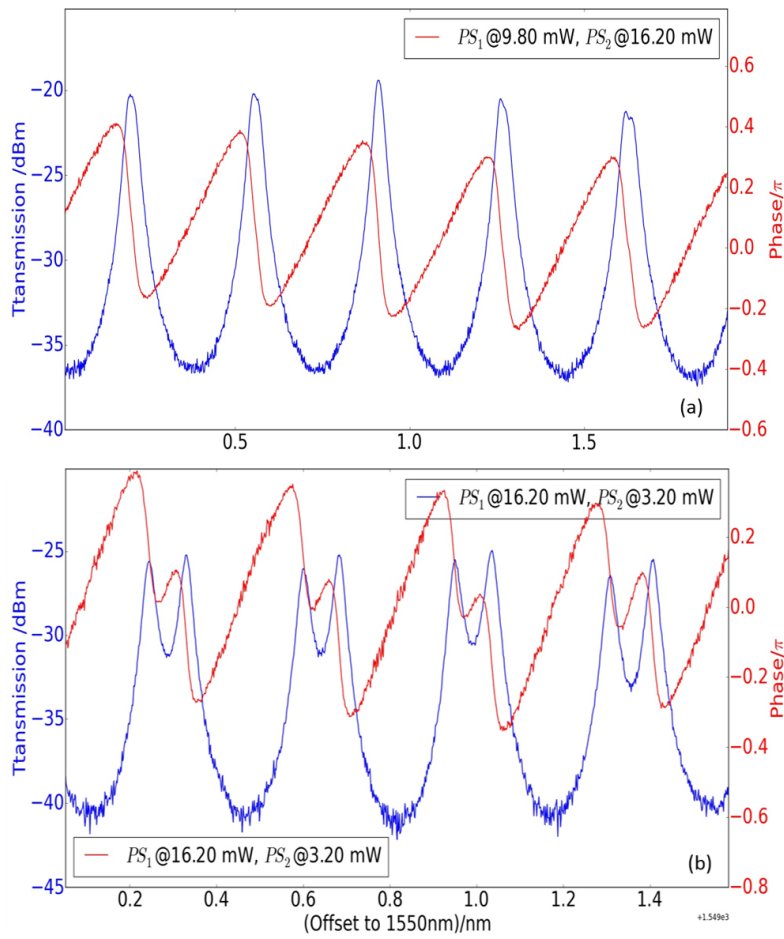


Figure 5.18: Measured phase response for the Lorentzian-shaped resonance (a) and normal resonance splitting (b).

5.3.3 Measurement

For the measurements, the overall measured spectra are already shown in previous section in Fig. 5.12. Clearly, the EIT peak is observed and importantly, we get the transition between Fano resonance and EIT in a single device, this is in consistence with other literature that theoretically proves EIT is fundamentally a Fano resonance [40]. In Fig. 5.17 it clearly shows that, only 0.4 mW change in the power injection into one of the phase shifters, the resonance pattern can be very

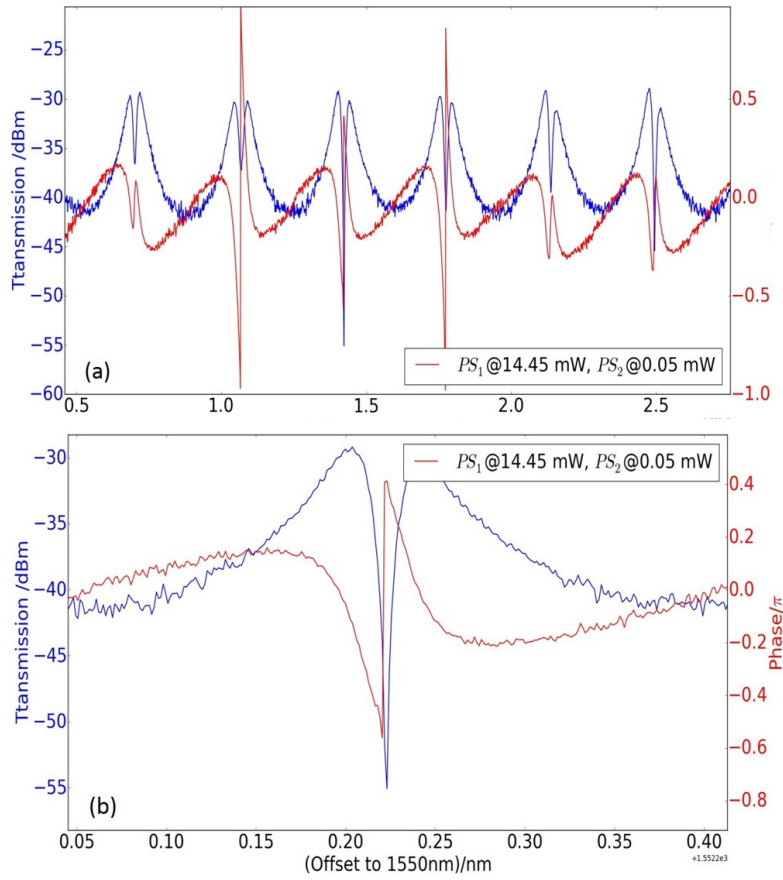


Figure 5.19: Measured phase response for the spectrum with EIT peaks (c) and a zoom view of one of the EIT peak (d). When EIT is present, an abrupt phase change happen within its ultra narrow bandwidth.

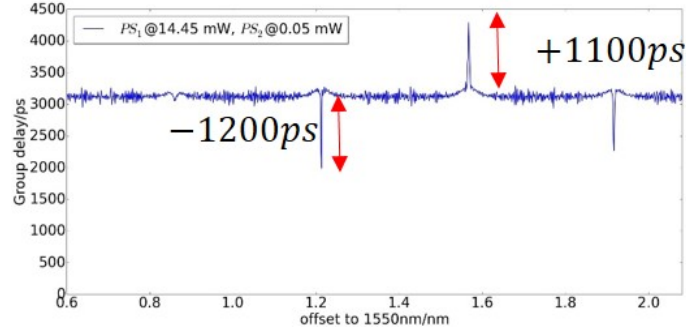


Figure 5.20: Measured group delay of the spectrum shown in Fig. 5.19. At the EIT peak, there is a larger group delay at 4100 ps, compared to the background level at 3200 ps, the EIT slows light down at 1100 ps. We also notice some dips at the delay spectrum at the resonances showing splitting. This is the so-called fast light phenomenon. Due to our tunability of the internal reflections, we can achieve both tunable fast light and slow light.

different. When $PS_2=0.05$ mW, EIT is quite obvious, while when $PS_2=0.45$ mW, the resonance pattern becomes quite different and the EIT peak disappears. This small power injection change in PS_2 won't change the reflectivity of this reflector very much, so is not the FP mode. But the slight frequency detuning between the FP mode and the ring resonance lead to the disappear of the EIT peak.

To get the phase response, we use an optical vector network analyzer (OVNA) from Luna Inc. to perform the measurements. It has an integrated interferometer that helps to extract the phase responses from our chip. The wavelength resolution is 1.5 pm. The results are given in Fig. 5.18 and Fig. 5.19. We list three sets of phase measurements, corresponding with the pure Lorentzian-shaped resonance pattern, normal resonance splitting pattern and EIT resonance pattern. Consistent with former literature, when it's pure ring resonance, the abrupt phase change only happens near the resonance wavelength [41]. While at the resonance splitting case, there is a gradual phase change in the splitting region. This phenomenon can be used to demonstrate fast light [42]. While at the EIT resonance, there is an abrupt phase change as large as 0.95π in an optical range less than 10 pm. We also give the measured group delay of such a device using the same equipment. Results of the spectrum shown in Fig. 5.19 are given in Fig. 5.20. Clearly, at the EIT peak, the group delay is 1100 -ps larger than the background level. What's more, for the other peak where it shows resonance splitting, we observe a smaller group delay, indicating a pulse advance. This is the so-called fast light effect introduced by resonance splitting [42], which has been introduced in chapter 4. Due our ability to fully control of the reflections inside the ring cavity (thus the resonance splitting conditions and the dispersion conditions within the splitting region), we are able to get a larger pulse advancement (1200 ps in our case) than former literature [42].

The tunability of the EIT resonance can also be viewed in Fig. 5.19.

5.4 Contour plot presentation

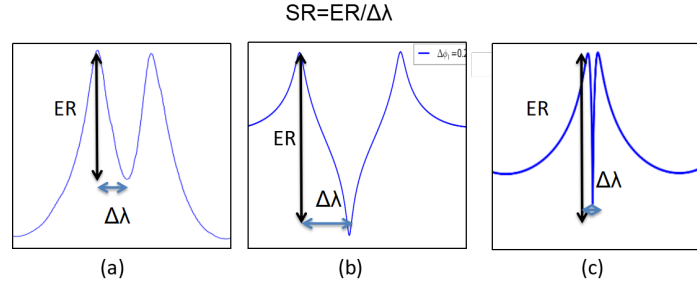


Figure 5.21: Definition of the two parameters to be characterized by the contour plots, namely extinction ratio and slope rate. (a), (b) and (c) present the case of normal resonance splitting, Fano resonance and EIT, respectively.

In sections above, we separately discussed the results of tuning of PS1 and PS2 for Fano resonance and EIT. Even if it's clear that the Fano resonance and EIT are both tunable by controlling PS1 and PS2, the tendency of how to tune PS1 and PS2 to get the desired performance of Fano resonance and EIT is not shown. Next we will provide two contour plots based on simulation results. The first one characterizes the dependency of the extinction ratio (ER) of the split resonance (defined in Fig. 5.21) on the PS1 and PS2, note that the split resonance can be anyone among the Fano resonance, EIT and normal resonance splitting. The second one is about the approximated slope rate (SR, also defined in Fig. 5.21). The contour plots are given in Fig. 5.22. In the simulations, the DCs of the reflectors are designed to be 50/50, so at the beginning state ($PS1=PS2=0$), both reflectors introduce zero reflection. When PS1 increases to 0.5π , the reflectivity also increases to 100% accordingly. So the x and y axis in the contour plots also represent the reflectivity of the reflector from 0 to 100% (with varying phase). Besides the two contour plots, four examples of from 4 different regions in the contour plot are also given. They refer to Lorentzian resonance, normal resonance splitting, Fano resonance and EIT, respectively. The former two belong to the large space of blue in the contour plots, where both ER and SR are low. Also we get a conclusion from this plots that, if $PS1=PS2$, then the resonance splitting disappears.

In this simulation, the two phase shifters of the reflectors are placed according to the schematic shown in Fig. 5.1. In this configuration, the two reflectors are not exactly point symmetric with respect to the ring center. So the contour plots don't show any symmetry with respect to the diagonal. If we place the two reflectors according to the schematic shown in top figure in Fig. 5.23, then the contour plots

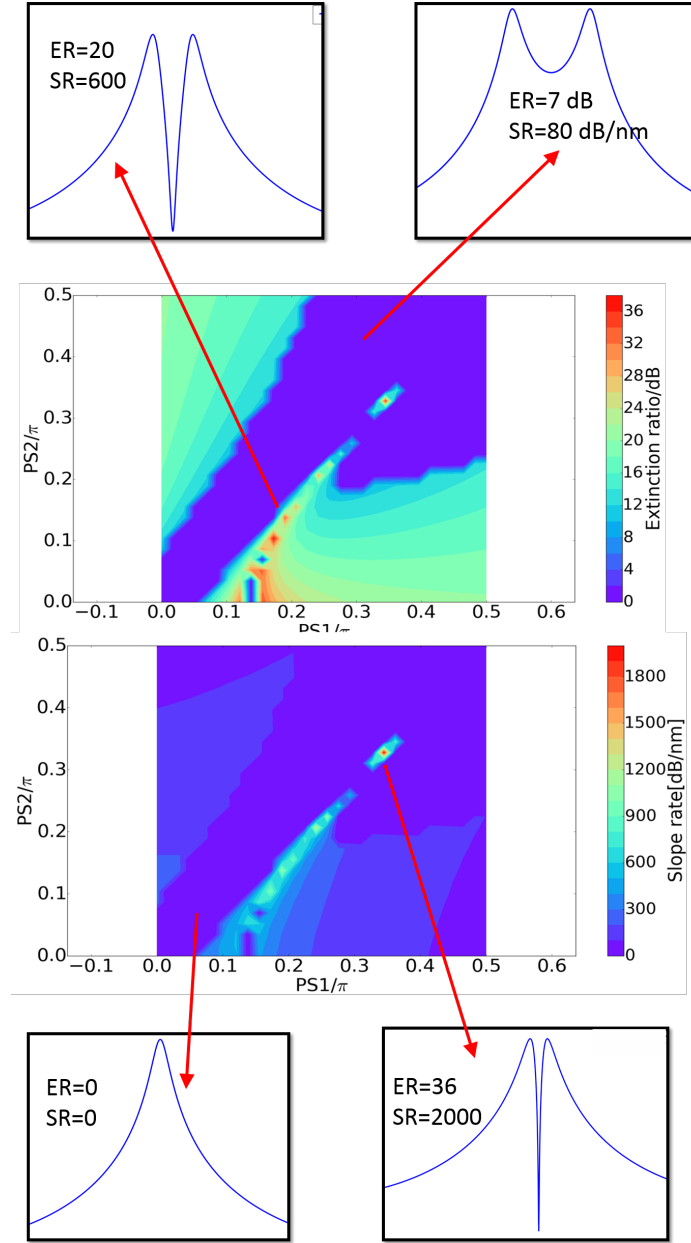


Figure 5.22: Contour plots of extinction ratio and slope rate vs $PS1$ and $PS2$. The x and y axis refer to the tuning range from 0 to 0.5π of two phase shifters. They also present the reflectivity of the reflectors from 0 to 100%.

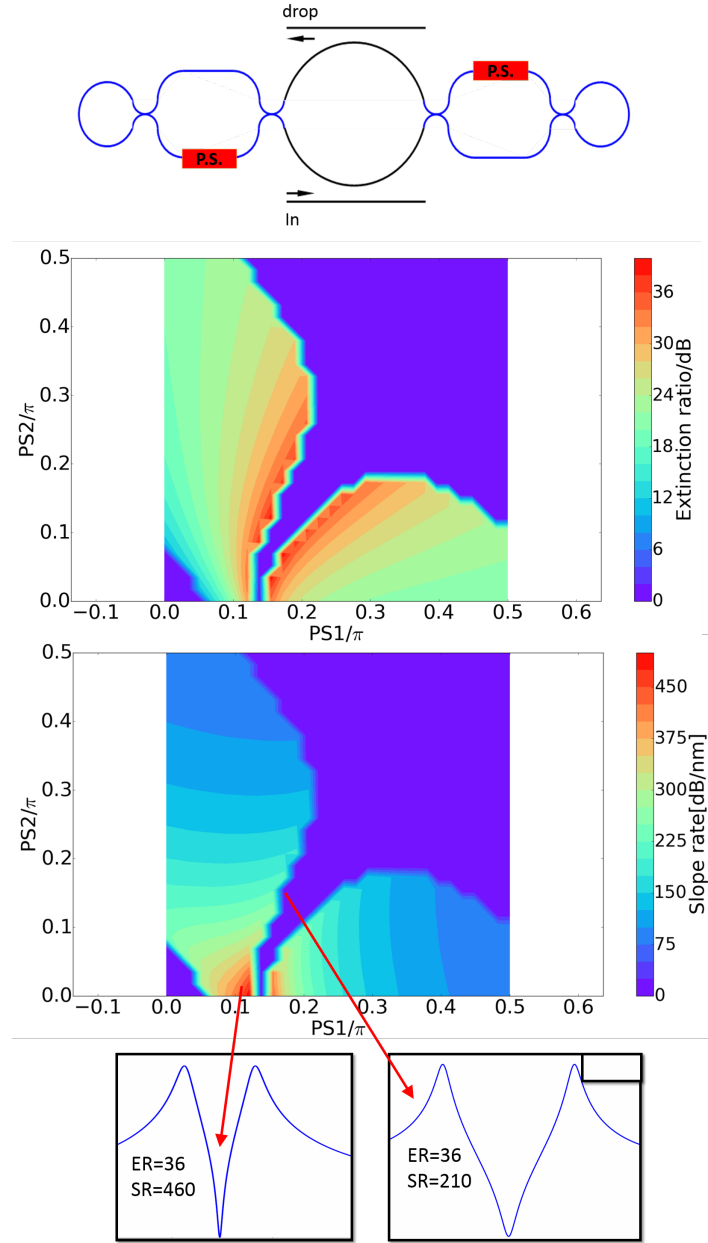


Figure 5.23: The two reflectors are now rearranged to make the two reflectors symmetric with respect to the center of the ring cavity. Now the two contour plots show certain symmetry with respect to the diagonal.

are more or less symmetric with respect to the diagonal as evident in Fig. 5.23. But it's interesting to notice that, in this configuration, EIT can not be generated as the maximum SR observed in the contour plot is less than 500 dB/nm. While typically a resonance with EIT peak should have a SR over 1000 dB/nm due to the extreme narrow optical range. The reason lies in the symmetric position of the two reflectors. This can be understood with following simulations.

As we mentioned above, when the two phase shifters change, both the amplitude and phase of their reflections change. To reduce the number of varying parameters, we perform another simulation where the two MZI based reflectors are replaced with dimensionless lumped reflectors, whose phase is constant. Their power reflectivity are noted with r_1 and r_2 . We plot the contour plots of ER and SR as a function of r_1, r_2 , respectively. The results are given in Fig. 5.24. They look quite similar with the contour plots shown in Fig. 5.23, as in both cases, the two reflectors are point symmetric with respect to the center of the ring. Moreover, in this configuration, we also notice that the EIT can not be generated due to the limited SR observed in the contour plot, which is also limited to 500 dB/nm, exactly the same with previous simulation.

5.5 Summary

In this chapter, we discussed two applications of a silicon ring resonator with two integrated tunable reflectors inside, namely Fano resonance and electromagnetically induced transparency (EIT). Each of them is systematically discussed including theory explanation, simulation characterization and experimental demonstration. Basically speaking, they are generated as a result of interaction between an embedded Fabry-Perot cavity formed by the two reflectors and the silicon ring cavity. Depending on the frequency detuning of these two cavities, either Fano resonance (non-zero detuning) and EIT (zero detuning) can be generated. And their respective parameters can also be tuned by controlling the two reflectors.

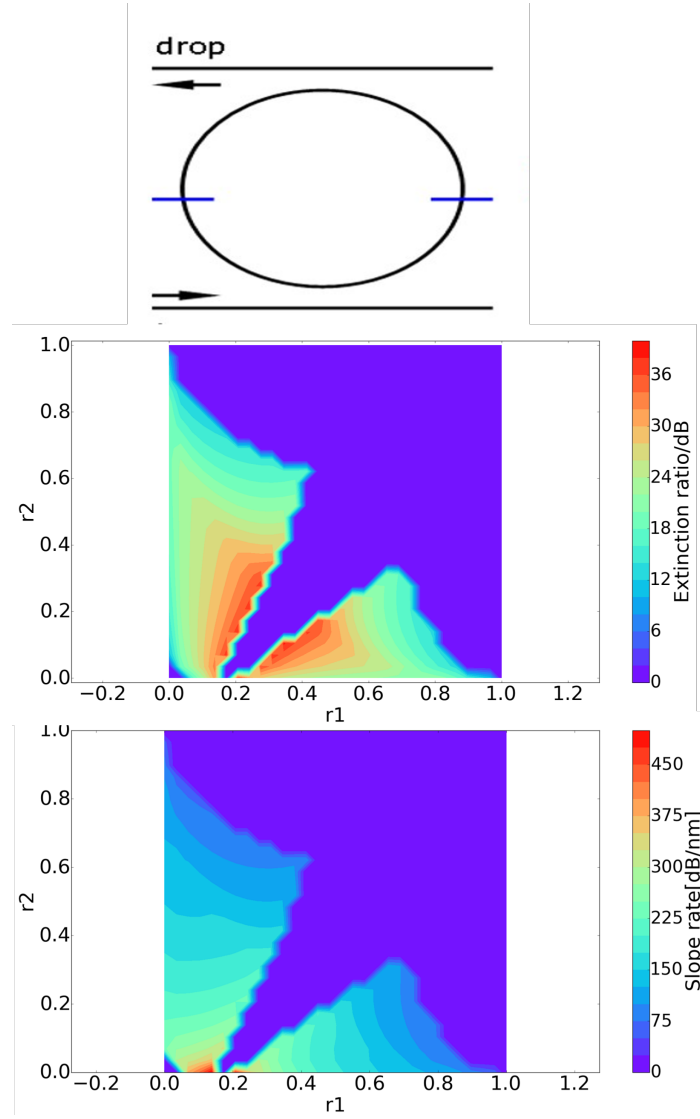


Figure 5.24: The two reflectors are now replaced with two dimensionless lumped reflectors, with constant reflection phase. The contour plots show similar pattern with those in Fig. 5.24.

References

- [1] Shanhui Fan. *Sharp asymmetric line shapes in side-coupled waveguide-cavity systems*. Applied Physics Letters, 80(6):908–910, 2002.
- [2] Ugo Fano. *Effects of configuration interaction on intensities and phase shifts*. Physical Review, 124(6):1866, 1961.
- [3] John Markus Blatt and Victor Frederick Weisskopf. *Theoretical nuclear physics*. Springer Science & Business Media, 2012.
- [4] RP Madden and K Codling. *New autoionizing atomic energy levels in He, Ne, and Ar*. Physical Review Letters, 10(12):516, 1963.
- [5] U Fano and JW Cooper. *Spectral distribution of atomic oscillator strengths*. Reviews of Modern Physics, 40(3):441, 1968.
- [6] Jan M Rost, K Schulz, M Domke, and G Kaindl. *Resonance parameters of photo doubly excited helium*. Journal of Physics B: Atomic, Molecular and Optical Physics, 30(21):4663, 1997.
- [7] Jonathan A Fan, Chihhui Wu, Kui Bao, Jiming Bao, Rizia Bardhan, Naomi J Halas, Vinodhan N Manoharan, Peter Nordlander, Gennady Shvets, and Federico Capasso. *Self-assembled plasmonic nanoparticle clusters*. science, 328(5982):1135–1138, 2010.
- [8] Andrew R Schmidt, Mohammad H Hamidian, Peter Wahl, Focko Meier, Alexander V Balatsky, JD Garrett, Travis J Williams, Graeme M Luke, and JC Davis. *Imaging the Fano lattice to ‘hidden order’ transition in URu₂Si₂*. Nature, 465(7298):570–576, 2010.
- [9] Jin-Hui Wu, Jin-Yue Gao, Ji-Hua Xu, L Silvestri, M Artoni, GC La Rocca, and F Bassani. *Ultrafast all optical switching via tunable Fano interference*. Physical review letters, 95(5):057401, 2005.
- [10] Landobasa Y Mario, S Darmawan, and Mee K Chin. *Asymmetric Fano resonance and bistability for high extinction ratio, large modulation depth, and low power switching*. Optics express, 14(26):12770–12781, 2006.
- [11] Feng Hao, Yannick Sonnefraud, Pol Van Dorpe, Stefan A Maier, Naomi J Halas, and Peter Nordlander. *Symmetry breaking in plasmonic nanocavities: subradiant LSPR sensing and a tunable Fano resonance*. Nano letters, 8(11):3983–3988, 2008.

- [12] Boris Luk'yanchuk, Nikolay I Zheludev, Stefan A Maier, Naomi J Halas, Peter Nordlander, Harald Giessen, and Chong Tow Chong. *The Fano resonance in plasmonic nanostructures and metamaterials*. Nature materials, 9(9):707–715, 2010.
- [13] Yi Yu, Weiqi Xue, Elizaveta Semenova, Kresten Yvind, and Jesper Mork. *Demonstration of a self-pulsing photonic crystal Fano laser*. Nature Photonics, 2016.
- [14] Gencheng Wang, Tingge Dai, Jianfei Jiang, Hui Yu, Yinlei Hao, Yuehai Wang, Yubo Li, Xiaoqing Jiang, and Jianyi Yang. *Slope tunable Fano resonances in asymmetric embedded microring resonators*. Journal of Optics, 19(2):025803, 2017.
- [15] Chen Qiu, Ping Yu, Ting Hu, Fan Wang, Xiaoqing Jiang, and Jianyi Yang. *Asymmetric Fano resonance in eye-like microring system*. Applied Physics Letters, 101(2):021110, 2012.
- [16] Bei-Bei Li, Yun-Feng Xiao, Chang-Ling Zou, Xue-Feng Jiang, Yong-Chun Liu, Fang-Wen Sun, Yan Li, and Qihuang Gong. *Experimental controlling of Fano resonance in indirectly coupled whispering-gallery microresonators*. Applied Physics Letters, 100(2):021108, 2012.
- [17] Weifeng Zhang, Wangzhe Li, and Jianping Yao. *Optically tunable Fano resonance in a grating-based Fabry–Perot cavity-coupled microring resonator on a silicon chip*. Optics letters, 41(11):2474–2477, 2016.
- [18] Guolin Zhao, Ting Zhao, Huifu Xiao, Zilong Liu, Guipeng Liu, Jianhong Yang, Zhaoyu Ren, Jintao Bai, and Yonghui Tian. *Tunable Fano resonances based on microring resonator with feedback coupled waveguide*. Optics Express, 24(18):20187–20195, 2016.
- [19] Ting Hu, Ping Yu, Chen Qiu, Huiye Qiu, Fan Wang, Mei Yang, Xiaoqing Jiang, Hui Yu, and Jianyi Yang. *Tunable Fano resonances based on two-beam interference in microring resonator*. Applied Physics Letters, 102(1):011112, 2013.
- [20] Ang Li, Thomas Vaerenbergh, Peter Heyn, Peter Bienstman, and Wim Bogaerts. *Backscattering in silicon microring resonators: a quantitative analysis*. Laser & Photonics Reviews, 10(3):420–431, 2016.
- [21] Ang Li and Wim Bogaerts. *Fundamentally cancel backscattering in silicon microrings*. In Lasers and Electro-Optics Europe & European Quantum Electronics Conference (CLEO/Europe-EQEC, 2017 Conference on), pages 1–1. IEEE, 2017.

- [22] Michael Fleischhauer, Atac Imamoglu, and Jonathan P Marangos. *Electromagnetically induced transparency: Optics in coherent media*. Reviews of modern physics, 77(2):633, 2005.
- [23] Kouki Totsuka, Norihiko Kobayashi, and Makoto Tomita. *Slow light in coupled-resonator-induced transparency*. Physical review letters, 98(21):213904, 2007.
- [24] Chao Peng, Zhengbin Li, and Anshi Xu. *Optical gyroscope based on a coupled resonator with the all-optical analogous property of electromagnetically induced transparency*. Optics express, 15(7):3864–3875, 2007.
- [25] Jacob B Khurgin. *Optical buffers based on slow light in electromagnetically induced transparent media and coupled resonator structures: comparative analysis*. JOSA B, 22(5):1062–1074, 2005.
- [26] CF Roos, D Leibfried, A Mundt, F Schmidt-Kaler, J Eschner, and R Blatt. *Experimental demonstration of ground state laser cooling with electromagnetically induced transparency*. Physical review letters, 85(26):5547, 2000.
- [27] MD Lukin and A Imamoglu. *Controlling photons using electromagnetically induced transparency*. Nature, 413(6853):273, 2001.
- [28] Mikhail D Lukin, Michael Fleischhauer, Marlan O Scully, and Vladimir L Velichansky. *Intracavity electromagnetically induced transparency*. Optics letters, 23(4):295–297, 1998.
- [29] Tohru Oishi and Makoto Tomita. *Inverted coupled-resonator-induced transparency*. Physical Review A, 88(1):013813, 2013.
- [30] H Jing, Şahin K Özdemir, Z Geng, Jing Zhang, Xin-You Lü, Bo Peng, Lan Yang, and Franco Nori. *Optomechanically-induced transparency in parity-time-symmetric microresonators*. Scientific reports, 5, 2015.
- [31] Hao Lü, Yajing Jiang, Yu-Zhu Wang, and Hui Jing. *Optomechanically induced transparency in a spinning resonator*. Photonics Research, 5(4):367–371, 2017.
- [32] David D Smith, Hongrok Chang, Kirk A Fuller, AT Rosenberger, and Robert W Boyd. *Coupled-resonator-induced transparency*. Physical Review A, 69(6):063804, 2004.
- [33] Qianfan Xu, Sunil Sandhu, Michelle L Povinelli, Jagat Shakya, Shanhui Fan, and Michal Lipson. *Experimental realization of an on-chip all-optical analogue to electromagnetically induced transparency*. Physical review letters, 96(12):123901, 2006.

- [34] Lin Zhang, Muping Song, Teng Wu, Lianggang Zou, Raymond G Beausoleil, and Alan E Willner. *Embedded ring resonators for microphotonic applications*. Optics Letters, 33(17):1978–1980, 2008.
- [35] Xiaodong Yang, Mingbin Yu, Dim-Lee Kwong, and Chee Wei Wong. *All-optical analog to electromagnetically induced transparency in multiple coupled photonic crystal cavities*. Physical review letters, 102(17):173902, 2009.
- [36] Y Zhang, S Darmawan, LYM Tobing, T Mei, and DH Zhang. *Coupled resonator-induced transparency in ring-bus-ring Mach-Zehnder interferometer*. JOSA B, 28(1):28–36, 2011.
- [37] Xiaodong Yang, Mingbin Yu, Dim-Lee Kwong, and Chee Wei Wong. *Coupled resonances in multiple silicon photonic crystal cavities in all-optical solid-state analogy to electromagnetically induced transparency*. IEEE Journal of Selected Topics in Quantum Electronics, 16(1):288–294, 2010.
- [38] Qingzhong Huang, Zhan Shu, Ge Song, Juguang Chen, Jinsong Xia, and Jinzhong Yu. *Electromagnetically induced transparency-like effect in a two-bus waveguides coupled microdisk resonator*. Optics express, 22(3):3219–3227, 2014.
- [39] Zecen Zhang, Geok Ing Ng, Ting Hu, Haodong Qiu, Xin Guo, Mohamed Saïd Rouifed, Chongyang Liu, and Hong Wang. *Electromagnetically induced transparency-like effect in microring-Bragg gratings based coupling resonant system*. Optics express, 24(22):25665–25675, 2016.
- [40] Bo Peng, Sahin Kaya Ozdemir, Weijian Chen, Franco Nori, and Lan Yang. *What is-and what is not-Electromagnetically-Induced-Transparency in Whispering-Gallery-Microcavities*. arXiv preprint arXiv:1404.5941, 2014.
- [41] Wim Bogaerts, Peter De Heyn, Thomas Van Vaerenbergh, Katrien De Vos, Shankar Kumar Selvaraja, Tom Claes, Pieter Dumon, Peter Bienstman, Dries Van Thourhout, and Roel Baets. *Silicon microring resonators*. Laser & Photonics Reviews, 6(1):47–73, 2012.
- [42] Qiang Li, Ziyang Zhang, Jing Wang, Min Qiu, and Yikai Su. *Fast light in silicon ring resonator with resonance-splitting*. Optics express, 17(2):933–940, 2009.

6

Backcoupling manipulation of silicon ring resonator

6.1 Introduction

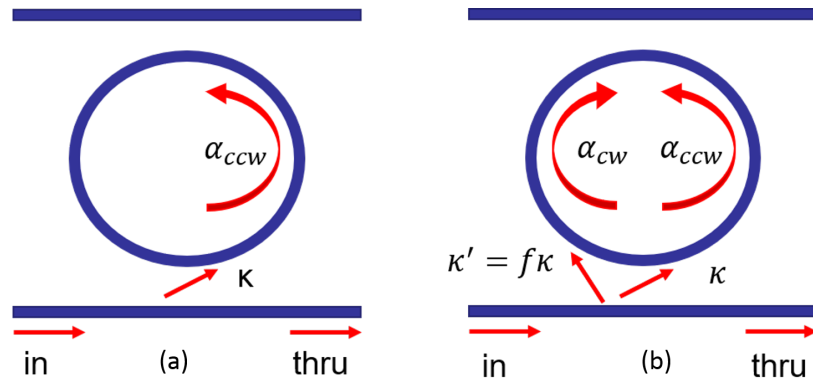


Figure 6.1: Brief illustration of the concept of backcoupling. Left one shows the case of an ideal ring resonator, where the incoming light will only contribute to one of the two circulating modes. If backcoupling exists, both modes will be coupled from the incoming light as illustrated in the right part.

Previous chapters talk about novel applications or enhanced performance of silicon ring resonators by means of internal reflections engineering. The devices

with one or two reflectors and their applications have been systematically discussed. However, based on our work presented in chapter 3, there is another degree of freedom that impacts ring resonators performance and has been so far neglected, which is the so-called backcoupling. It is the contribution from the input light to the counter circulating mode (CW in Fig. 6.1) besides the normal circulating mode (CCW in Fig. 6.1). In this chapter, we will demonstrate the manipulation of the backcoupling using two kinds of structures, one of which has a standard silicon ring resonator with only stochastic backscattering inside while the other one has a tunable reflector inside.

6.2 Theory

For an ideal ring resonator without internal reflections, the backcoupling has no effects on the outputs of a ring resonator as the two circulating modes are degenerate and resonant at the same frequency. Something interesting happens at the case with internal reflections. Their degeneracy will be broken due to the coupling between them and the resonance of the ring resonator will show split. Under this circumstance, the backcoupling will strongly impact the outputs as mathematically proven in equation (3.13) in chapter 3, which is also written here:

$$\frac{S_d}{S_i}|_{bs} = \frac{A_0}{2} \left[\frac{\frac{BW_0}{2}(1-f)^2}{j(\omega - \omega_1) + \frac{BW_1}{2}} + \frac{\frac{BW_0}{2}(1+f)^2}{j(\omega - \omega_2) + \frac{BW_2}{2}} \right] \quad (6.1)$$

This equation describes the transmission at the drop port of an add-drop ring resonator with internal reflections inside. Two peaks start to emerge instead of a single resonance due to resonance splitting. $f = \frac{\kappa'}{\kappa}$ is a dimensionless factor to indicate backcoupling κ' . It can be a complex number, whose amplitude is the strength of the backcoupling normalized to forward coupling κ of a directional coupler, while its phase describes the phase difference between backcoupling and forward coupling. For instance, if they are in phase, f is a positive real number, while if they have a π phase difference, f is a negative real number. And f will strongly influence the heights of these two peaks in a split resonance. Thus a tunable f or backcoupling can make the two peaks in a split resonance controllable.

To make it more clear, we also derive the transmission equation at the *thru* port as shown in equation (6.2) and replace the f factor with the normal backcoupling factor κ' . As in equation (3.13), it will become not so easy to understand when $f = \infty$ (for instance, κ very small with respect to κ').

$$\frac{S_t}{S_i}|_{bs} = 1 - \frac{1}{2} \left[\frac{(\mu_i - \mu'_i)^2}{j(\omega - \omega_1) + \frac{1}{\tau_{tot}}} + \frac{(\mu_i + \mu'_i)^2}{j(\omega - \omega_2) + \frac{1}{\tau_{tot}}} \right] \quad (6.2)$$

$$\omega_1 = \omega_0 + \mu_r, \omega_2 = \omega_0 - \mu_r \quad (6.3)$$

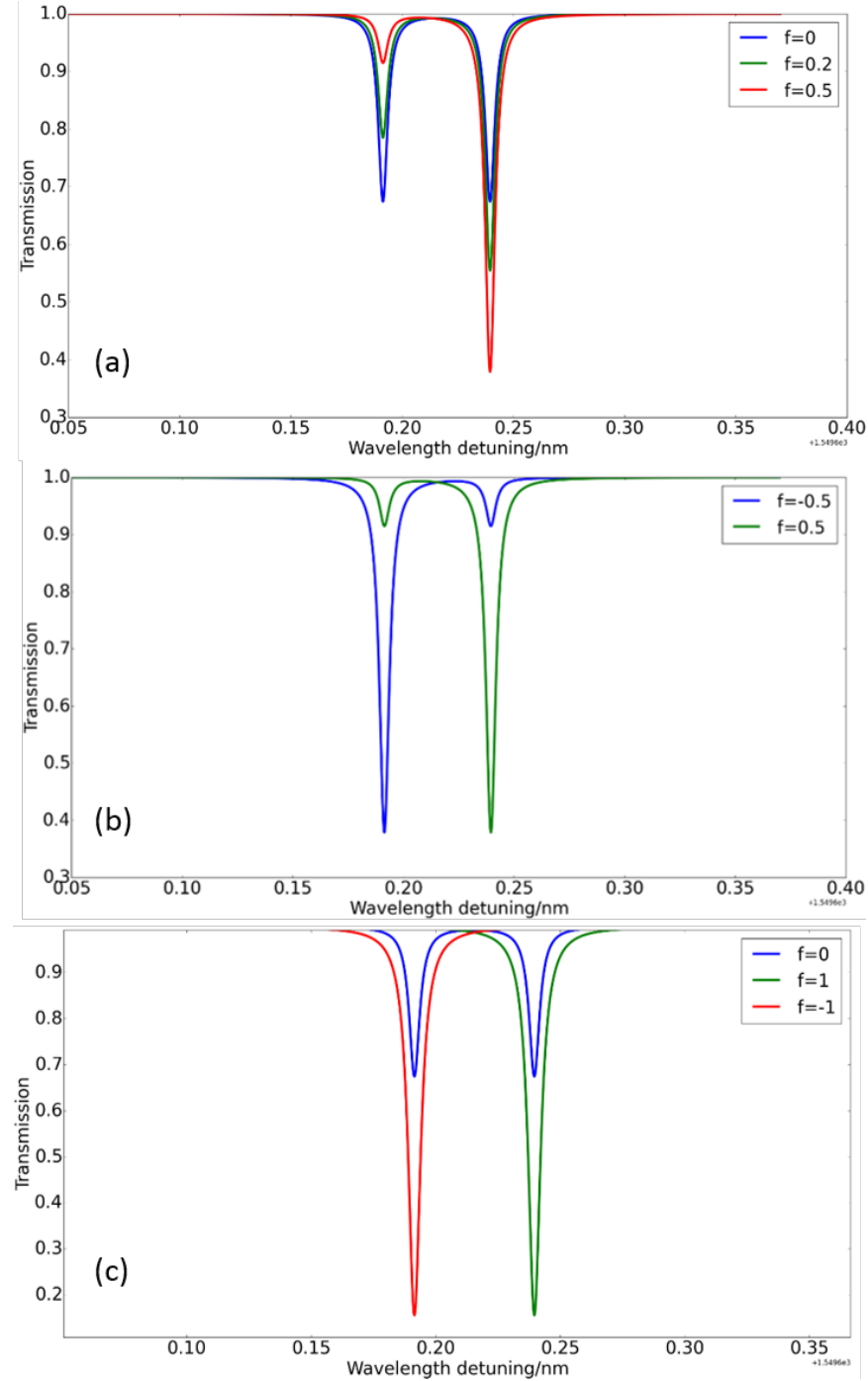


Figure 6.2: Simulated through port spectra of a circuit shown in Fig.6.1(b) with backcoupling induced at the directional coupler. (a) presents the results when $f=0, 0.2$ or 0.5 . When $f=0$, i.e. no backcoupling is present, the spectrum shows asymmetric resonance splitting. By varying the backcoupling strength ($f=0.2$ or 0.5), the peak asymmetry can be adjusted. (b) shows the case when $f=0.5$ and -0.5 . The minus sign indicates a π phase difference between κ and κ' . (c) gives the results when $f=1$ and -1 , namely the amplitude of backcoupling equals that of forward coupling. Under such condition, one peak will be suppressed. So resonance splitting will be eliminated even the backscattering is still present.

$$\mu_r = r \frac{c}{n_g L} \quad (6.4)$$

$$\mu_i = \kappa^2 \frac{c}{n_g L} = \frac{2}{\tau_i} \quad (6.5)$$

$$\mu_i' = \kappa'^2 \frac{c}{n_g L} = \frac{2}{\tau_i'} \quad (6.6)$$

$$\frac{1}{\tau_{tot}} = \frac{1}{\tau_i} + \frac{1}{\tau_i'} + \frac{1}{\tau_l} \quad (6.7)$$

All the concepts of these terms are explained in chapter 3. Clearly, the individual contribution from the input to CW and CCW modes will strongly affect the peak heights of the split resonance, as κ and κ' both stand in the numerator.

6.3 Conceptual simulation

We use Caphe to perform the simulation of this conceptual device. The simulated manipulation of backcoupling of a circuit shown in Fig. 6.1(b) is given in Fig. 6.2. It contains internal reflection (a lumped reflector) that leads to resonance splitting and directional couplers that include backcoupling. For simplicity, we mark the two peaks in a split resonance with P_b and P_r , respectively. P_b refers to the blue shift one while P_r refers to the red shift one. As shown in Fig. 6.2(a), symmetric splitting ($P_b = P_r$) happens when $f = 0$, namely without backcoupling. By varying the strength of the backcoupling, the peak asymmetry can be adjusted. This would be useful to demonstrate single sideband filter. While adding a minus sign to f , or physically speaking, introducing π phase difference between backcoupling and forward coupling, the individual peak to be manipulated can be switched as shown in Fig. 6.2(b). Under special condition, when $f = \pm 1$ ($\kappa = \kappa'$), one of those two peaks will be fully suppressed as evident in equation (3.13) and Fig. 6.2(c).

The manipulation of the internal reflection can control the splitting distance between P_b and P_r . While manipulation of backcoupling can further allow the control of the individual peak height. In summary, by combining these two degrees of freedom, we manage to get full control of a split resonance.

6.4 Practical circuit design and simulation

In the simulation performed above, we manage the backcoupling by means of manually modifying the scatter matrix of a directional coupler, which is not feasible in reality and it can not simulate every possible cases of backcoupling in order to make the directional coupler's scatter matrix unitary. For instance, the f in our current circuit mode can not be pure imaginary ($\frac{\pi}{2}$ phase difference between κ and

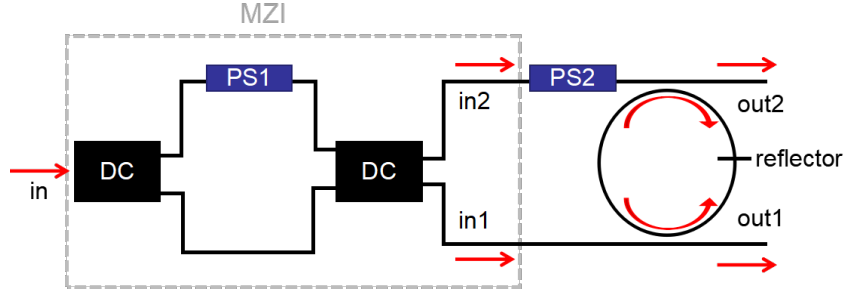


Figure 6.3: A designed circuit in order to introduce and manipulation backcoupling in a realistic way. A MZI is placed in front of a ring resonator to dynamically control the intensity of light at two inputs of a ring resonator. Each of the input will couple to one circulating mode in the ring. Thus the manipulation of the MZI split ratio will lead to the manipulation of the coupling ratio from input light to the two circulating modes of the ring resonator. A tunable reflector introduced in chapter 4 and 5 is implemented inside the ring cavity to couple the two circulating modes and induce resonance splitting. PS indicates phase shifter and DC refers to directional coupler.

κ'), otherwise the circuit would introduce gain, which makes no sense. In order to fully investigate the backcoupling in a practical way, we design a circuit shown in Fig. 6.3. It can be considered as two parts, a Mach-Zehnder-Interferometer (MZI) that splits incoming light into two paths (in1 and in2) and a ring resonator that accepts both of these two paths. Each of these two inputs will contribute to one circulating mode of the ring resonator (CW and CCW). Thus the split ratio of the MZI determines how much incoming light will be coupled to each circulating mode. There is also a tunable reflector introduced in chapter 4 implemented in the ring cavity, in order to couple these two modes and induce resonance splitting to visualize the impacts of backcoupling. Two phase shifters are placed in the circuit. One of them (PS1) is on the arm of the MZI and the other one (PS2) is on one access waveguide of the ring resonator. PS1 is responsible for tuning the split ratio of the MZI, alternatively speaking, it controls the magnitude of f or backcoupling. While PS2 changes the relative phase difference between two inputs of the ring resonator, in other words, it takes control of the phase of f which is the phase difference between κ and κ' . There is actually a third phase shifter within the reflector to tune its reflectivity, for simplicity it's omitted in the figure.

It can be also mathematically proven that this circuit is identical with a pure ring resonator that has internal backscattering and backcoupling at the directional couplers. In the view of tCMT for this circuit, there are two modes α_{cw} and α_{ccw} in the ring cavity. Each of them resonant with the same angular frequency ω_0 , which is the eigenfrequency of the resonator. Also each mode has the same total decay rate $\frac{1}{\tau_{tot}}$, that includes loss rate $\frac{1}{\tau_l}$, coupling rates $\frac{1}{\tau_i}, \frac{1}{\tau_o}$ due to the coupling to two bus waveguides. These two modes are coupled with each other through

internal reflections μ_r . They are fed by the external incoming light at ports in1 and in2, respectively, marked with S_{in1} and S_{in2} . S_{in1} and S_{in2} are dependent with each other, as $S_{in1}^2 + S_{in2}^2 = S_{in}^2$, where S_{in} is the original input at the port in. So the mode amplitude equations based on tCMT for this circuit ((6.8) and (6.9)) are identical with the equations for a single ring resonator with backscattering and backcoupling given in chapter 3.

$$\frac{d\alpha_{ccw}}{dt} = j(\omega_0 + j\frac{1}{\tau_{tot}})\alpha_{ccw} - j\mu_i S_{in1} - j\mu_r \alpha_{cw} \quad (6.8)$$

$$\frac{d\alpha_{cw}}{dt} = j(\omega_0 + j\frac{1}{\tau_{tot}})\alpha_{cw} - j\mu_i S_{in2} - j\mu_r \alpha_{ccw} \quad (6.9)$$

S_{in1} can be replaced with mS_{in} and S_{in2} replaced with nS_{in} , where $m^2 + n^2 = 1$. So varying the ratio between S_{in1} and S_{in2} is the same with varying the ratio between backcoupling and forward coupling of the directional couplers.

To characterize this structure, we build a corresponding circuit model in caphe. The reflector is tunable in its reflectivity, which can range from 0 to 100%. The MZI is designed to be balanced in its two arms and its DCs are designed as 50/50 splitter. At the original state without any phase shift added to PS1, all the light from port in will be directed to port in2. While adding π phase shift into PS1, all the light will be directed to port in1. in1 and in2 will have identical transmission when $PS1=0.5\pi$. The two input waveguides of the ring resonator are also designed to be identical. For simplicity, we omit the dispersive behavior of all the directional couplers and only focus on one resonance to observe its evolution and the impacts of backcoupling. The parasitics of the directional couplers including its lumped backcoupling and reflections are also neglected as the internal reflection is dominant by the tunable reflector and the external backcoupling introduced by the MZI is also dominant over the lumped backcoupling induced at the directional couplers.

We continue to use the optical circuit simulator Caphe to perform the characterization of such a device. We start with the case when the reflector introduces zero reflectivity and confirm that under such circumstance, the backcoupling has no impacts on the outputs. The results are plotted in Fig. 6.4. (a) and (c) show the output at out1 while (b) and (d) present the results at out2. (a) and (b) give the manipulation of PS1 with PS2=0 while (c) and (d) shows the results of changing PS2 with PS1 fixed at 0.2π (in order to make light split into both in and in2). Clearly, when there is no internal reflections and resonance splitting, varying backcoupling (both amplitude and phase) doesn't modify the resonance shape. The change in the transmission level shown in Fig. 6.4(a) and (b) is due to the change in the MZI's split ratio when PS1 is working. In detail, when $PS1 = 0$, all the light coming from MZI is in in2, thus there is no transmission from out1 as shown in (a). Besides, when $PS1 = \pi$, ideally only in1 of the MZI has light thus only out1 has

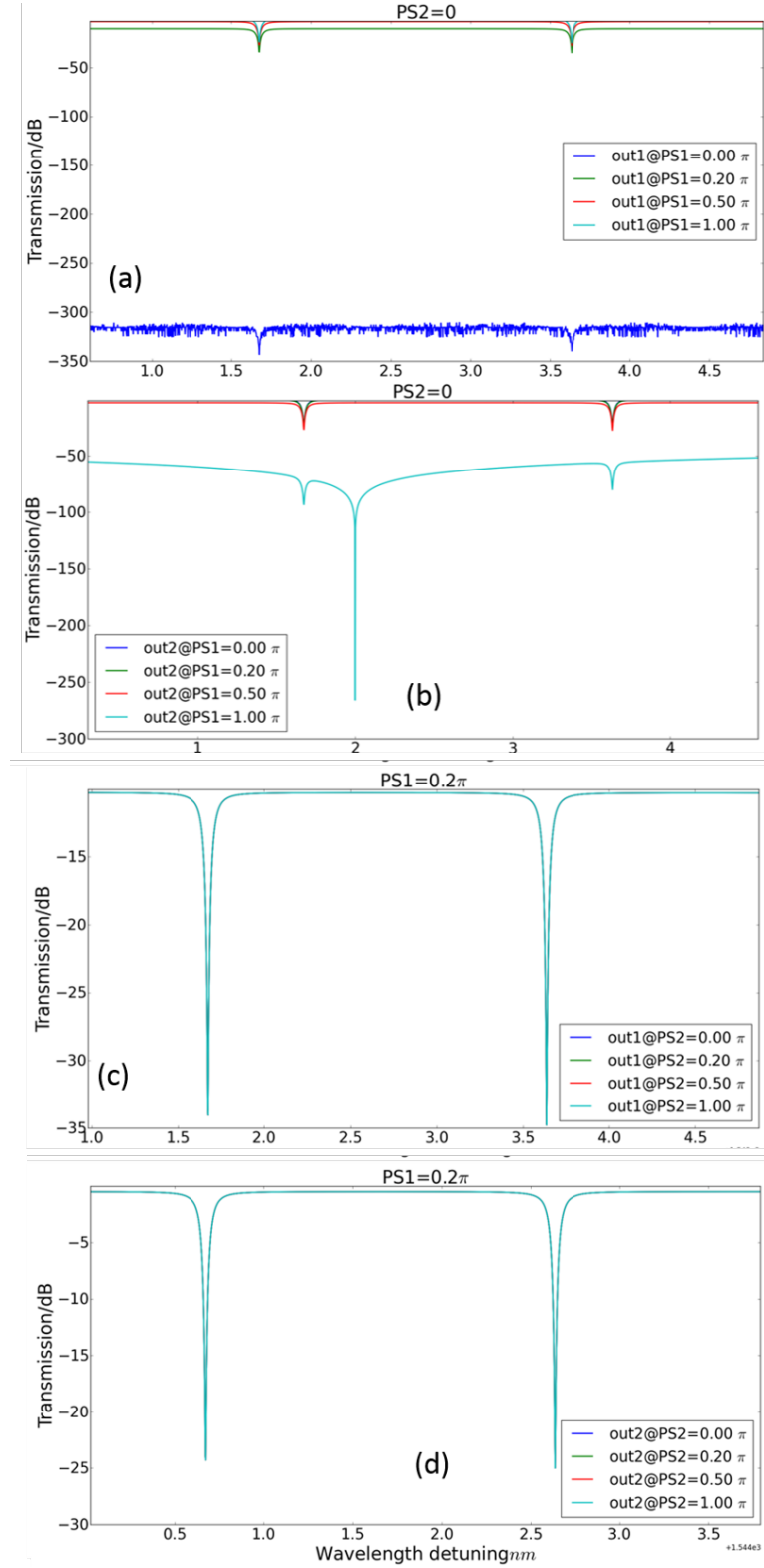


Figure 6.4: Simulated spectra of the circuit in Fig.6.3 at the condition when the reflector introduces 0 reflectivity. Left column refers to out1 and right column presents the results at out2. Clearly, when there is no internal reflection thus no resonance splitting, manipulating backcoupling doesn't modify the resonance shape. The change in the transmission level is due to the change in the split ratio of the MZI.

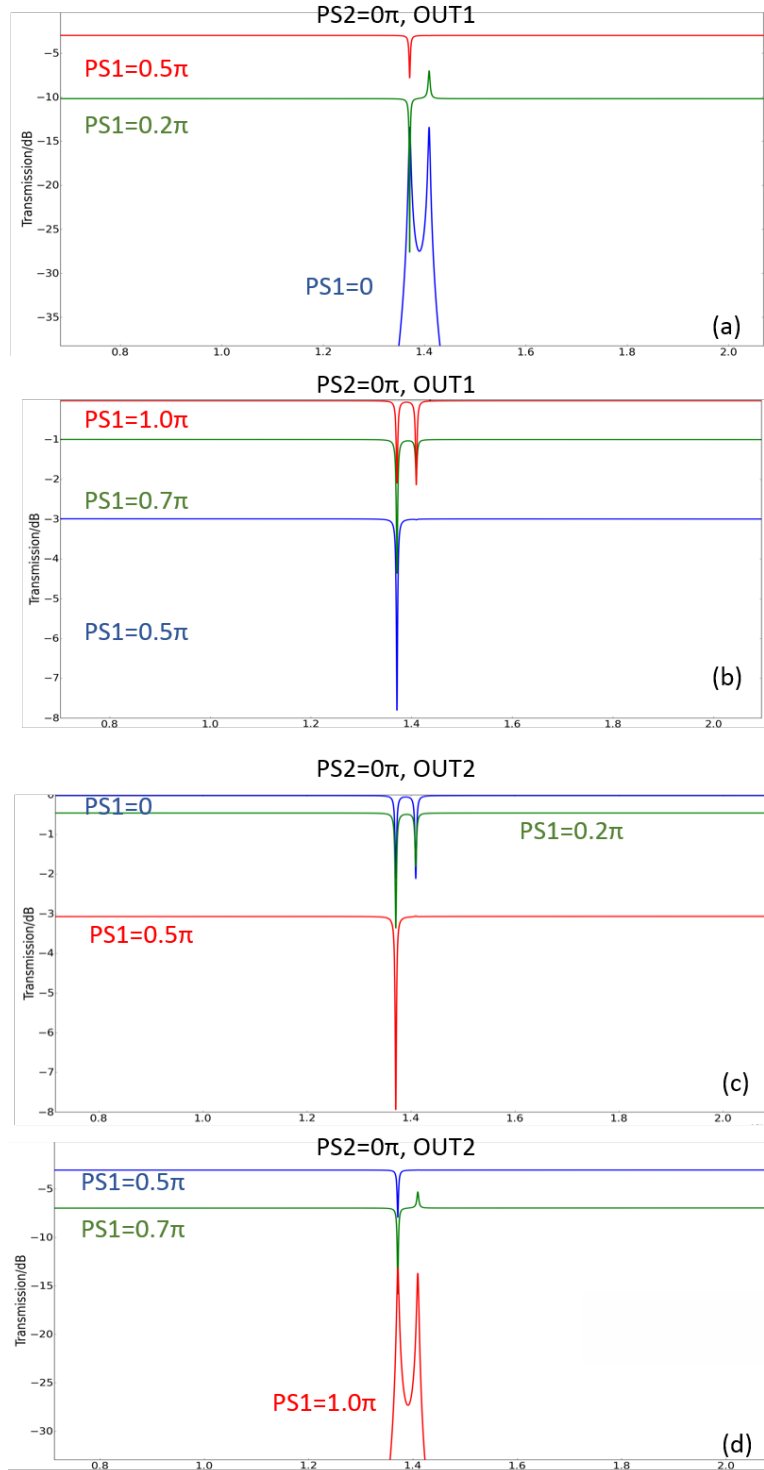


Figure 6.5: When resonance splitting is present, the impacts of backcoupling will become visible. These figures show the results of manipulating $PS1$ with $PS2=0$. (a) and (b) show the outputs at out1 while (c) and (d) present the results at out2.

light with no transmission at out2. However, the phase added into a phase shifter is wavelength dependent. Thus in Fig. 6.4(b) the transmission spectrum at out2 is approaching 0 only at one wavelength point.

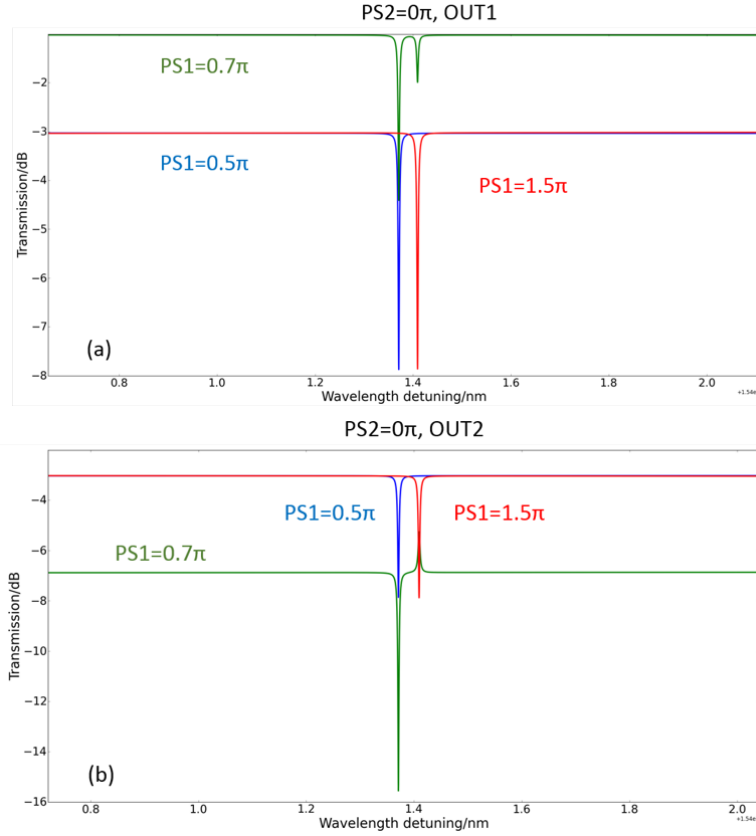


Figure 6.6: When backcoupling equals forward coupling ($in1=in2$), one of the two peaks in a split resonance can be suppressed. And by adding either 0.5π or 1.5π phase shift to $PS1$, we can also choose which peak to be suppressed.

The impacts of backcoupling start to appear when there is certain reflection inside the ring cavity that is strong enough to cause resonance splitting. The results of manipulating $PS1$ when $PS2=0$ is shown in Fig. 6.5. Top two panels show the spectra at out1 while bottom two give the outputs at out2.

From the figure some useful information can be extracted. First of all, resonance splitting is eliminated when $PS1 = 0.5\pi$ as shown in all panels. This confirms the conclusion obtained above, that is when the amplitude of backcoupling equals that of the forward coupling, one peak of the split resonance will be suppressed. By adding either 0.5π or 1.5π phase shift to $PS1$, we can also choose

which peak to be suppressed as shown in Fig. 6.6.

Another observation is that, by manipulating the ratio between in1 and in2 through changing PS1, the peak asymmetry can be adjusted as evident in Fig. 6.5. This is also consistent with former simulation and theoretical analysis. The ratio between in1 and in2 in this circuit is similar to ratio between the amplitudes of forward coupling and backcoupling, thus by changing PS1 the peak asymmetry can be adjusted.

We also notice that under some conditions, the two peaks of the split resonance (P_b, P_r) point to opposite directions (peak or dip). For instance, at the beginning state ($PS1 = 0.05\pi$), the resonance in out1 shows asymmetry in the peak directions as shown in Fig. 6.5(a). One of them (P_b) points down (dip) with the other (P_r) pointing up (peak). By adding more than 0.5π to PS1, both peaks will point down as evident in Fig. 6.5(b). There are multiple reasons behind this phenomenon. In the ring cavity, CW and CCW modes are activated simultaneously. They are coupled through the internal reflection and CW is supported through external incoming light at in2 while CCW is fed by external port in1. And the output at out1 contains two contributions. One is from in1 and happens through the coupling of the CCW mode supported by in1, which is a dip feature in spectrum as out1 serves as the *thru* port for in1. The other one is from in2 through coupling of the CCW mode supported by in2, which is a peak in the spectrum as out1 serves as the *add* port for in2. In other words, with only incoming only from in1, spectrum at out1 shows dips, while with only in2 working, it shows peaks. So the relative light intensity at in1 and in2 will determine the overall behavior of the output at out1 and out2. This is one of the reasons. Moreover, in1 and in2 are not independent with each other. According to equation (3.13), their ratio also determine the relative peak height of the split resonance. That's why the out1 spectrum show both peak and dip patterns.

Now we start to control PS2 to see the impacts of phase manipulation of backcoupling. To do this, we fix PS1 at 0.2π in order to split light into two ports (in1 and in2). The results are present in Fig. 6.7. (a) and (b) show the output at out1 while (c) and (d) present the results at out2. In summary, by changing PS2, the peak asymmetry can also be adjusted and the pointing direction can also be reversed depending on which region PS2 is in, $(0, 0.5\pi)$ or $(0.5\pi, \pi)$. When $PS2=0.5\pi$, the resonance again becomes symmetric as shown in Fig. 6.7.

6.5 Experimental results

6.5.1 Ring with tunable reflector

We designed two kinds of circuits as shown in Fig. 6.8. The only difference between them lies in the source of the internal reflection of the ring resonator. In one

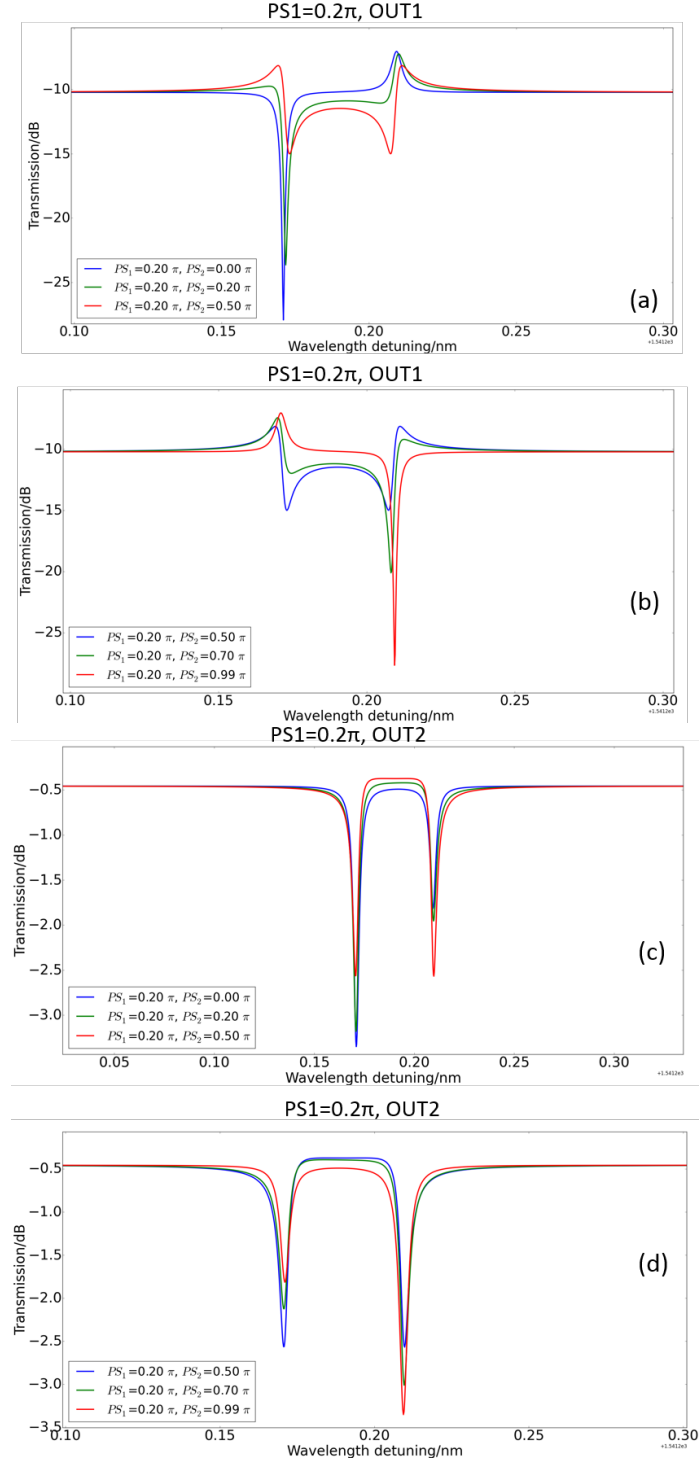


Figure 6.7: We fix $PS_1=0.2\pi$ and vary PS_2 to change the phase difference between backcoupling and forward coupling. (a) and (b) show the output at out1 while (c) and (d) present the results at out2.

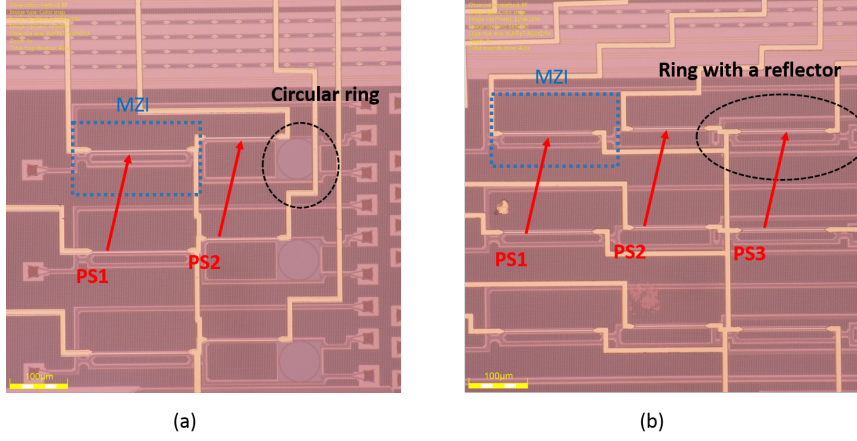


Figure 6.8: Microscopic images of the devices to manipulate backcoupling. (a) is the circuit with a circular ring resonator; whose internal reflection is induced by stochastic backscattering. (b) presents the circuit with a ring resonator that has a tunable reflector inside.

circuit (Fig. 6.8(a)), the ring cavity is a circular ring resonator with a bend radius of $35 \mu m$. The internal reflection is caused by the stochastic backscattering while in the other one (Fig. 6.8(b)), there is a tunable reflector inside the ring cavity. For each kind of circuit, we designed three instances with different coupling coefficients of the ring cavity. For the ring with reflector inside, we vary the coupling coefficients by changing the coupling length, from $1 \mu m$ till $5 \mu m$ with a fixed gap at $200 nm$. While for the circular ring resonator, this is done by changing its coupling gap, from $200 nm$ to $400 nm$. We first show the experimental characterization of the circuit with a tunable reflector.

We start with the demonstration of the tunability of the internal reflection using a phase shifter (PS3) within the reflector, which is shown in Fig. 6.8(b). The results of such a device under different working conditions of PS1 are exhibited in Fig. 6.9. At both cases, the resonance splitting can be eliminated under correct tuning condition, which means zero internal reflections. Next we characterize the manipulation of backcoupling (both in amplitude and phase) by changing PS1 and PS2 under the condition when internal reflections become 0. To check whether it matches the simulation or not. Fig. 6.10 plots the results. Clearly, without internal reflections and resonance splitting, backcoupling imposes no influence on the output resonance, which is in consistency with former simulations. The change in PS1 only lead to the change in the overall transmission level, due to the change in the split ratio of the MZI.

After this, we start to investigate how the manipulation of backcoupling would

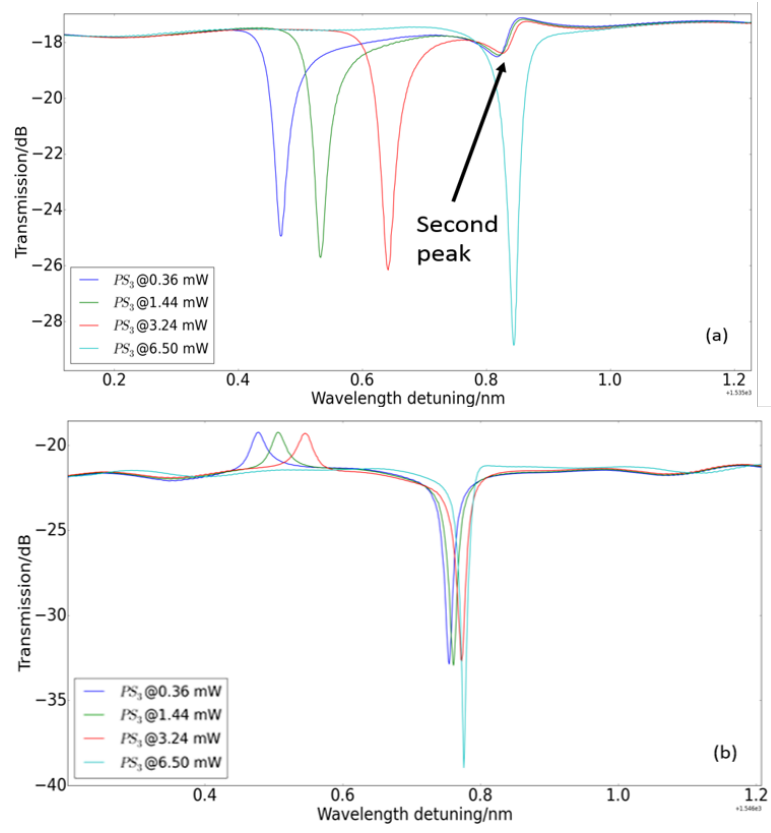


Figure 6.9: Demonstration of the tunability of internal reflections using PS3 shown in Fig. 6.8(b). (a) and (b) present the tunability under different conditions of PS1.

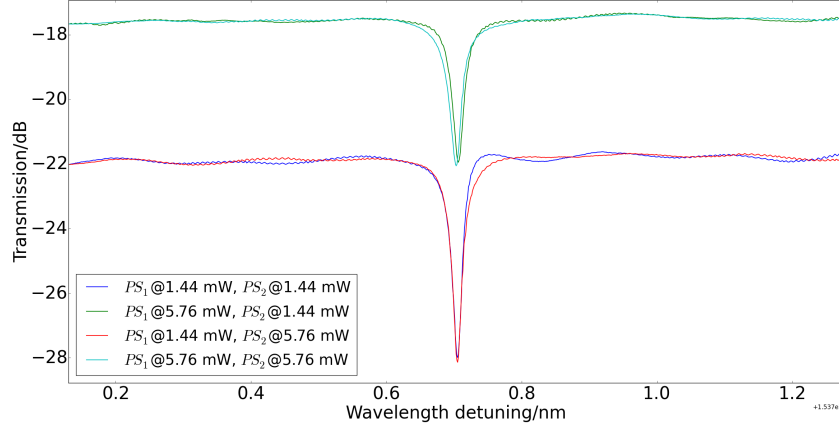


Figure 6.10: Without internal reflections and resonance splitting, varying PS_1 and PS_2 do not impact the resonance shape, which is consistent with former simulation results.

affect the output through measurement results. Similar with the procedure in the simulation part above, we first isolate PS_2 ($PS_2=0\text{mW}$) and gradually change PS_1 to observe its impacts. The measured spectra plotted in Fig. 6.11 perfectly match the simulated spectra presented in Fig. 6.5. First of all, changing PS_1 indeed adjusts the peak asymmetry, which confirms the potential application as a single sideband filter. And under specific point, one of the peaks disappears as shown in the red curves in Fig. 6.11(a) and (b), indicating the equal amplitude of backcoupling and forward coupling ($in_1=in_2$). Moreover, we also observed the transition in the pointing direction of one peak.

Following the same procedure with simulation part, we start to investigate the influence of PS_2 , which is the change in the relative phase between backcoupling and forward coupling. We fix PS_1 to be 0 and gradually increase PS_2 . Different with the configuration in simulation, where we need to fix PS_1 not to be 0 in order to split light both into in_1 and in_2 as the directional couplers (DCs) are perfect 50/50 splitters. While in the experiments, when $PS_1=0$ there are already transmission to both in_1 and in_2 due to fabrication variation which makes the DCs deviated from 50/50. The results are plotted in Fig. 6.12. The resonances show good one to one matching with the simulations exhibited in Fig. 6.7. Changing PS_2 could significantly modify the resonance shape. When $PS_2=4.41\text{ mW}$, the resonance becomes symmetric splitting, indicating 0.5π phase difference between backcoupling and forward coupling.

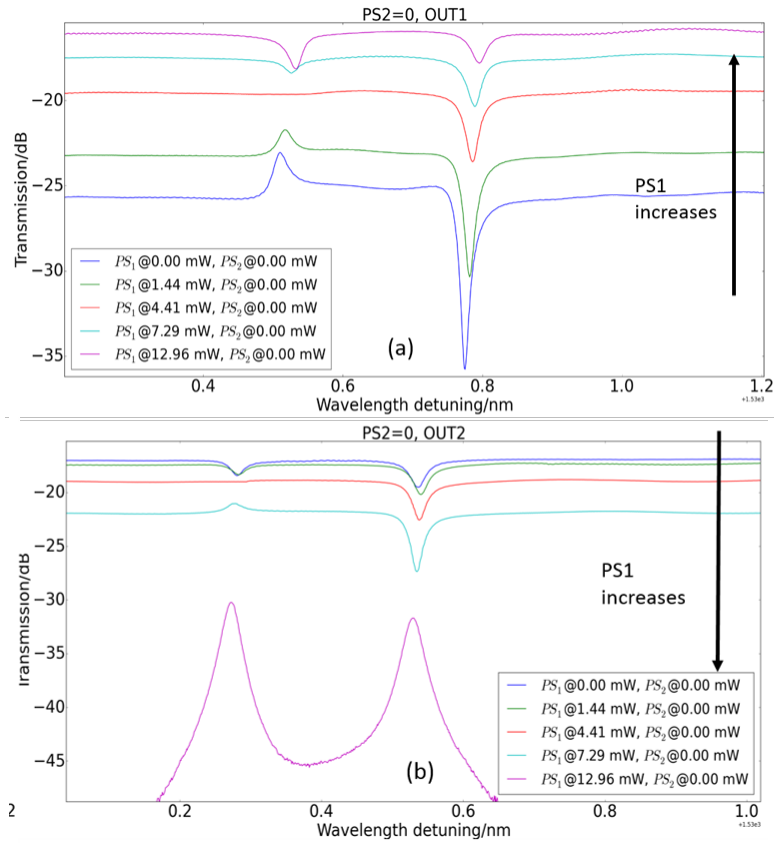


Figure 6.11: Measured spectra at out1 and out2 at fixed $PS_2=0$ with varying PS_1 . They show good match with simulation results plotted in Fig. 6.5.

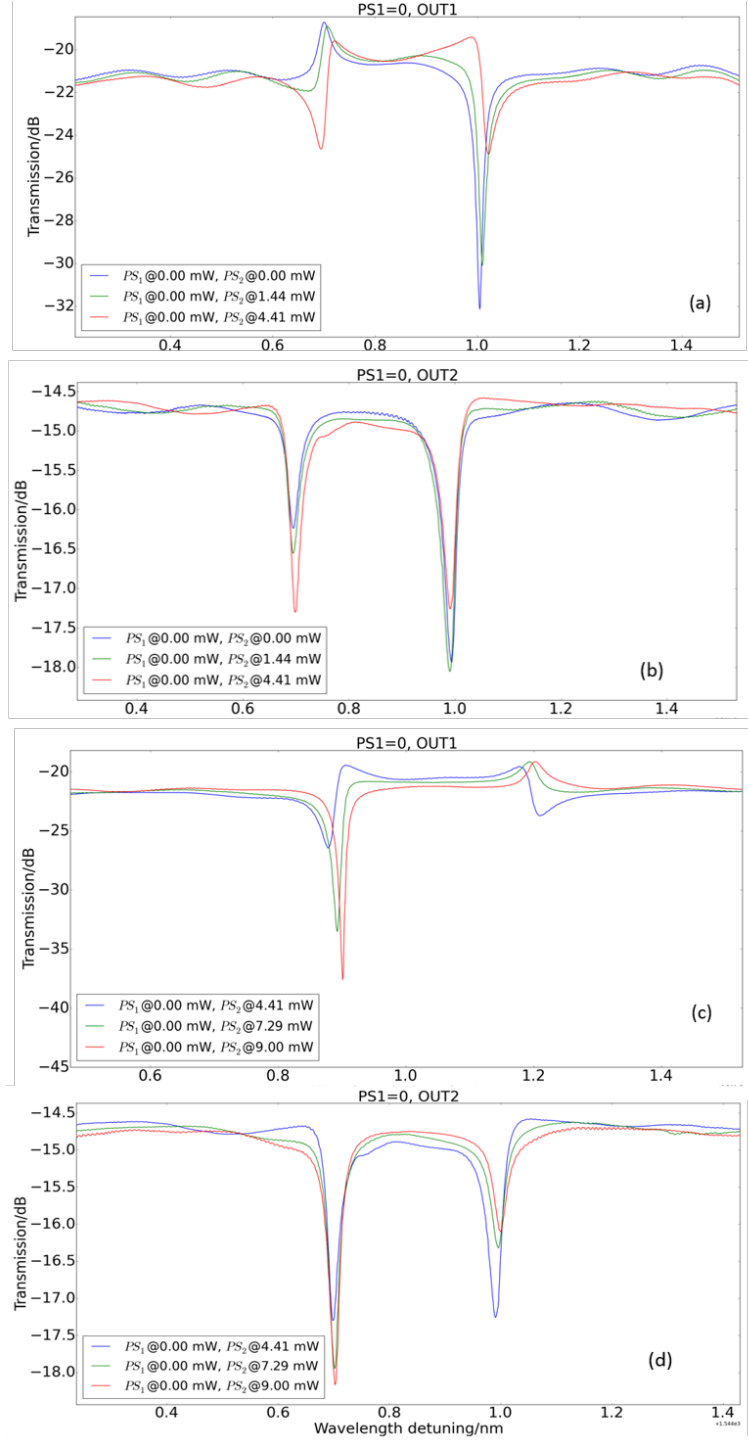


Figure 6.12: Measured spectra at out1 and out2 at fixed $PS_1=0$ with varying PS_2 . They show good match with simulation results plotted in Fig. 6.7.

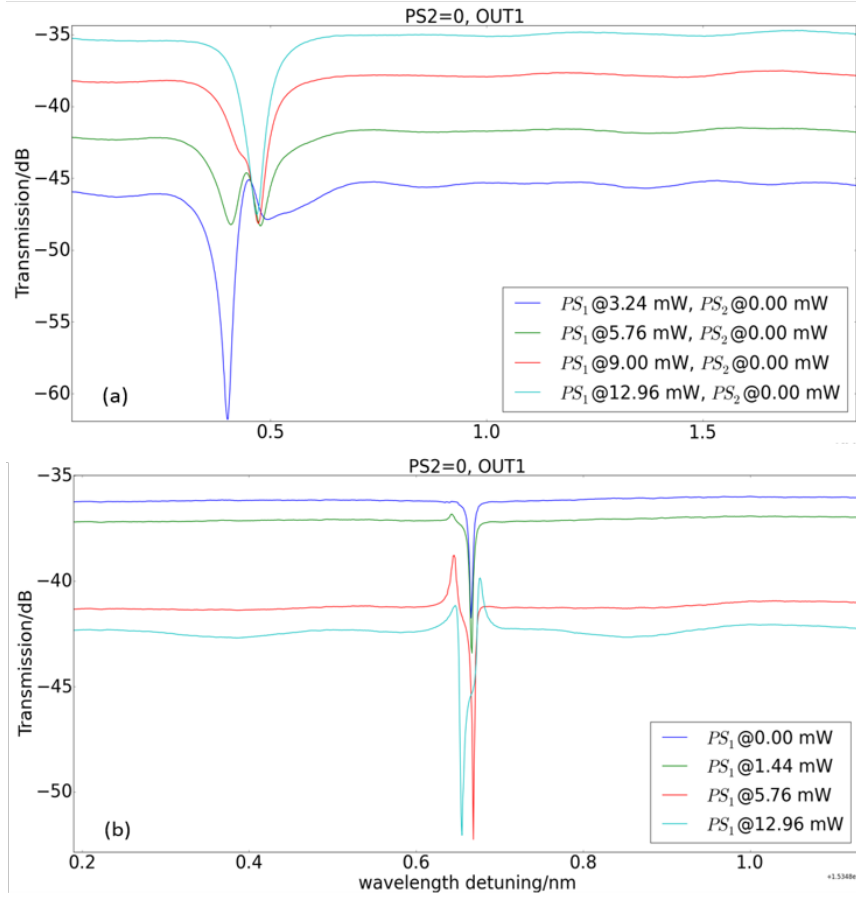


Figure 6.13: Measured spectra with varying PS_1 and fixed $PS_2=0$ of two circuits. They both have circular ring resonators (without tunable reflector) but with different coupling coefficients ((a) low Q and (b) high Q). Resonance splitting due to stochastic backscattering is present in both case and it can be suppressed by varying PS_1 .

6.5.2 Circular ring resonator

In previous subsection, we show the experimental demonstration of a backcoupling manipulation in a ring that has a tunable reflector inside. Based on the results, multiple potential applications can be achieved, including single sideband filter, Fano resonance etc. Here we are going to show the experimental characterization of another similar circuit, where the ring with a tunable reflector is replaced with a circular ring resonator, whose internal reflections are purely induced by parasitic reflections and stochastic backscattering. We want to investigate the manipulation of backcoupling on this kind of circuit as we believe it to be an alternative method to solve the problem of backscattering induced resonance splitting. Compared to the method introduced in chapter 4, it's biggest advantage lies in that this method doesn't increase the total roundtrip length of a ring resonator. Thus the FSR of a ring resonator wouldn't be sacrificed in order to avoid resonance splitting.

The manipulation of PS1 at PS2=0 mW of two rings with different coupling coefficients (Q factor) are given in Fig. 6.13. Both resonances show clear splitting due to stochastic backscattering. And by varying PS1, one of the peaks can be suppressed, which is consistent with former observations and it confirms the potential to manipulate backcoupling to avoid resonance splitting. Also the transition in the pointing direction of one peak is observed. Similarly, varying PS2 can also suppress one of the peaks and eliminate splitting as evident in Fig. 6.14.

Another very interesting and surprising observation is the ultra high Q and ultra large Finesse of the resonances of the ring resonator with smallest coupling coefficients (coupling gap at 400 nm). Zoomview of different resonances of such a ring resonator in Fig. 6.15 all show a bandwidth less than 5 pm, with corresponding Q factors all larger than 300,000, even approaching 400,000. Moreover, they are all accompanied with satisfying extinction ratio (ER), ranging from 6 dB to 11 dB. The FSR of such a resonator is around 2.5 nm and the corresponding Finesse is in the range between 500 and 625. The FSR and Finesse can be further increased by using smaller bend radius. The reason we chose it to be 35 μm is to make sure the stochastic backscattering to be strong enough to cause resonance splitting. While for practical use, it can be safely reduced.

Q factor is a measure of the sharpness of the resonance, defined as $Q = \frac{\lambda}{FWHM}$, where FWHM is the 3-dB bandwidth of the resonance. It represents the number of oscillations of the field before the circulating energy is depleted to 1/e of the initial energy [1]. More simply, it determines how long the light can resonant in the cavity before attenuated to a very low level. Thus a high Q factor is very critical for ring resonator based nonlinear optics, like frequency comb, wavelength conversion, four wave mixing, optical logic operation etc., as it means long photon lifetime. It's also desirable to have a high Q factor for ring based practical devices including (de-)multiplexers, laser cavities, sensors, filters etc. As a high Q factor means a narrow resonance bandwidth, and the narrow bandwidth

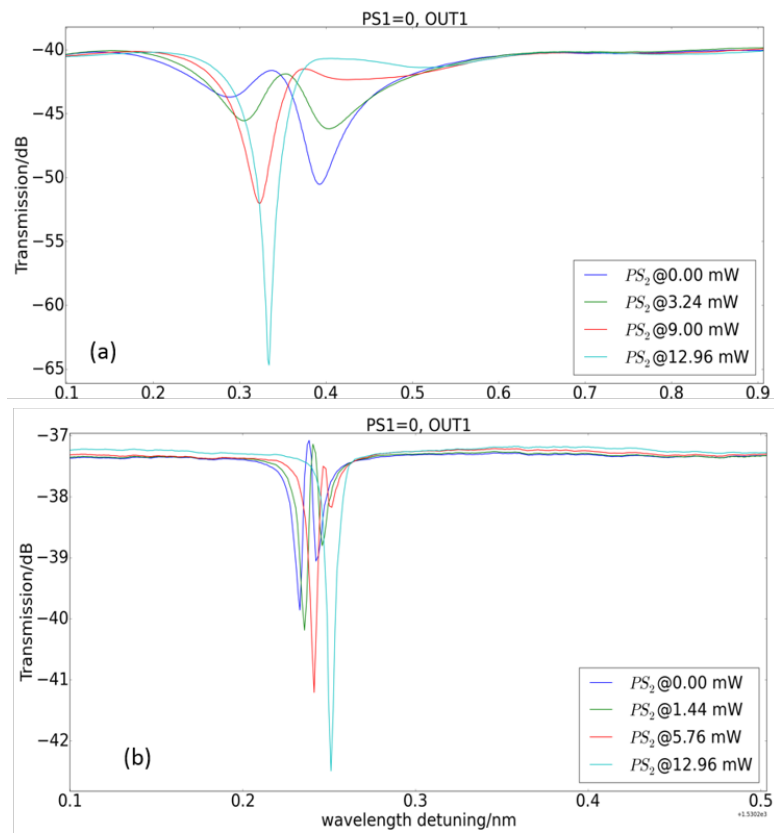


Figure 6.14: Measured spectra with varying PS_2 and fixed $PS_1=0$ of two circuits with circular ring resonators that have different coupling coefficients ((a) low Q and (b) high Q). Resonance splitting due to stochastic backscattering is present in both case and it can be suppressed by varying PS_2 .

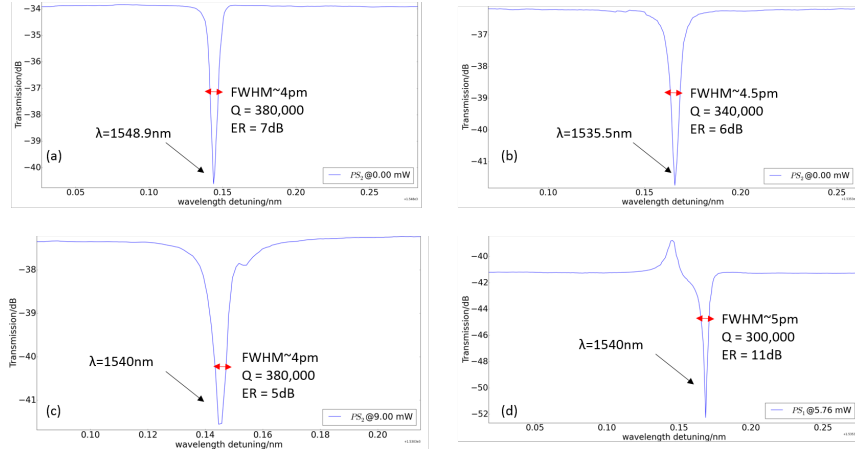


Figure 6.15: Some zoomview of resonances measured of a ring resonator with coupling gap at 400 nm. All resonances show Q factor larger than 300,000 and large ER. The FSR of such a resonator is about 2.5 nm. The calculated Finesse is around 600.

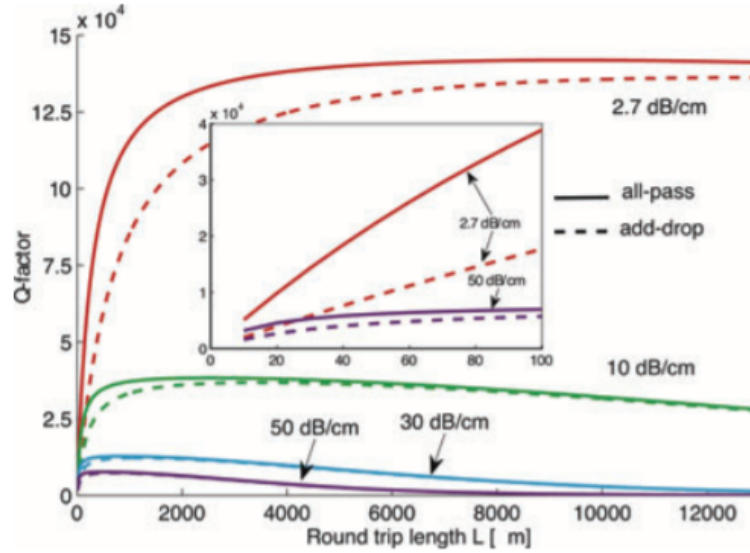


Figure 6.16: Quality factor as a function of cavity length for four propagation loss figures from Ref. [1].

can provide high resolution and efficiency. But for ring based modulators, the Q factor can not be too high in order to get a high modulation speed.

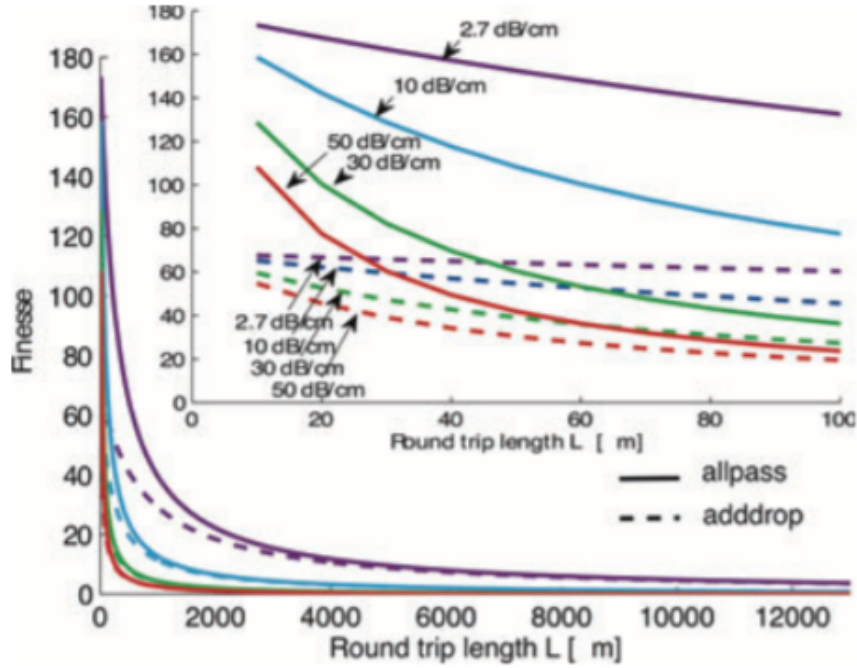


Figure 6.17: Finesse as a function of cavity length for four propagation loss figures from Ref. [1].

The Q factor is limited by the total loss in the cavity. Here, the loss includes both the propagation loss (radiation loss, absorption loss, bend loss, substrate leakage etc.) and the coupling loss to the bus waveguides. As a consequence, there are two terms describing the Q factor of a cavity, namely loaded Q (Q_l) and intrinsic Q (Q_i). The former one refers to the Q factor with coupling loss to the bus waveguide included, while the second one applies to the case where the cavity is isolated from external world. When the ring resonator is critically coupled, in other words, coupling loss equals the propagation loss, then $Q_l = 0.5Q_i$. According to Ref. [1], the Q factor of an add-drop ring resonator is given by following equation:

$$Q = \frac{\pi n_g L \sqrt{r_1 r_2 a}}{\lambda_0 (1 - r_1 r_2 a)} \quad (6.10)$$

Where n_g and L refers to the group index and roundtrip length of this ring. λ_0 is the resonant wavelength. r_x is the self-coupling coefficient, or the transmission coefficient of the directional couplers in the ring. Its relationship with coupling

coefficient κ is $r^2 + \kappa^2 = 1$ if coupling loss is neglected. a represents transmission coefficient per roundtrip, it depends on the propagation loss coefficient $\alpha[m^{-1}]$ ($\alpha[dB/m] = 4.34\alpha[m^{-1}]$) as $a^2 = \exp(\alpha L)$, here $\alpha[m^{-1}]$ refers to the propagation loss in the ring waveguide and doesn't include the coupling loss to the bus waveguides. From this equation, it is known that Q factor depends on three physical parameters, namely roundtrip length, propagation loss per unit length $\alpha[dB/cm]$ and coupling coefficients.

Increasing length seems to be the easiest method to increase Q factor, but its contribution is limited as increasing L will also increase roundtrip loss. And at some point, the benefit brought by increasing L would be cancelled by the high roundtrip loss. This is verified by Fig. 6.16 from Ref. [1]. Moreover, increasing L is detrimental to other important parameters, including FSR and Finesse. The importance of large FSR has been explained in chapter 4. It is also beneficial to obtain a relatively large Finesse. Finesse, which is defined as the ratio of FSR and FWHM $Finesse = \frac{FSR}{FWHM}$, is a measure of the sharpness of resonances relative to their spacing. Physically speaking, Finesse is supposed to represent with a factor of 2 the number of round-trips made by light in the ring before its energy is reduced to 1/e of its initial value. Quite similar with Q factor, it is very crucial to have a large Finesse for ring based nonlinear optics applications, where it is necessary for light to stay in the cavity as long as possible. To improve the Q factor by means of increasing roundtrip length would always sacrifice the FSR and Finesse, as evident in Fig. 6.17. As seen from Fig. 6.16, if $\alpha = 2.7 dB/cm$, which is close to the propagation loss of standard strip silicon waveguides fabricated at CMOS fabs, the maximum loaded Q factor for an add-drop ring resonator by increasing L is limited to 136,000 with a roundtrip length longer than 13 mm. The experimental demonstrations of silicon ring resonators with ultra high Q using this approach all show a very long length and small FSR (<100 pm) [2, 3]. This is ok for applications like microwave photonics, but it's unacceptable for other applications like WDM filters, sensors, laser cavities etc., where FSR and Finesse are also important.

If we only consider the case where L is in a reasonable range in order to get a satisfying FSR and Finesse, the intrinsic Q factor can be approximately estimated based on the propagation loss factor $\alpha[m^{-1}]$. For intrinsic Q, we first replace r_1, r_2 in equation (6.10) with 1. And based on Taylor expansion, we get approximations for \sqrt{a} and $1 - a$:

$$1 - a = 1 - \exp\left(\frac{\alpha L}{2}\right) \approx \frac{\alpha L}{2} \quad (6.11)$$

$$\sqrt{a} = \exp\left(\frac{\alpha L}{4}\right) = 1 - \frac{\alpha L}{4} = 1 \quad (6.12)$$

Then the equation for intrinsic Q can be derived:

$$Q_i = \frac{2\pi n_g}{\alpha \lambda_0} = \frac{\lambda_0}{\alpha \times FSR \times R} \quad (6.13)$$

Where R refers to the bend radius of the ring resonator if it's circular. So minimizing the propagation loss is the most fundamental way to increase the Q factor. However, even if the silicon doesn't absorb light with wavelength longer than $1.1\ \mu\text{m}$, the inevitable sidewall roughness serves as the main source for the propagation loss. So far, the silicon strip waveguide fabricated at mature CMOS fabs using deep UV (DUV) lithography are reported to have a propagation loss around 2 dB/cm [4, 5]. Even if fabricated using ebeam lithography, which is supposed to provide higher resolution than DUV lithography, the silicon strip waveguide also exhibits loss around 1 dB/cm [6], as the etching procedure also contributes to sidewall roughness. This is why the ring resonator using strip waveguides only show moderate Q factors of a few 10k. Unless the fabrication technology sees a fundamental upgrade, for instance, using extreme UV (EUV) instead of DUV, the propagation loss of silicon strip waveguides is not supposed to show an abrupt improvement.

One way to reduce the propagation loss of silicon strip waveguide is to use TM polarization. As explained in chapter 3, TM polarization exhibits weak discontinuities of the electric field at the vertical sidewall, thus it's less vulnerable to the roughness and suffers lower propagation loss. A circular ring resonator using TM polarization has been demonstrated and shows a maximum Q factor at 340,000 [7], which is comparable with our results. The ring has a bend radius of $20\ \mu\text{m}$ with a corresponding FSR around 5.5 nm, which is larger than our results. But their FSR can not be further increased as the bend radius for TM polarization can not go as tight as that for TE polarization due to the weaker confinement of TM polarization. But in our approach, the bend radius can be safely reduced down to sub $5\ \mu\text{m}$ (corresponding with a FSR around 20 nm). Moreover, in the approach using TM polarization, resonance splitting still happens occasionally from resonance to resonance and have no way to eliminate it. While in our approach, this problem can be dynamically solved.

In our analysis, the Q factor measured in our device is approaching the intrinsic Q factor. First proof comes from the 3D FDTD simulation of the directional coupler shown in Fig.6.18. Such a DC consisting of a bus waveguide and a $35\ \mu\text{m}$ bend radius arc with a 400 nm gap in between has a coupling coefficient less than 0.003 according to the simulation, which is very close to 0. Moreover, an intrinsic Q factor of 380,000 corresponds with a propagation loss around 2.02 dB/cm, which matches the mainstream cognition of the propagation loss for silicon strip waveguides based on current fabrication technology (standard 200 mm wafer with DUV lithography).

Usually, the loaded Q factor can be increased towards the intrinsic Q factor by decreasing the coupling coefficients of the directional couplers, as the coupling loss to bus waveguides will be suppressed. However, this will decrease the extinction ratio of the resonance, which is supposed to reach its maximum when the ring

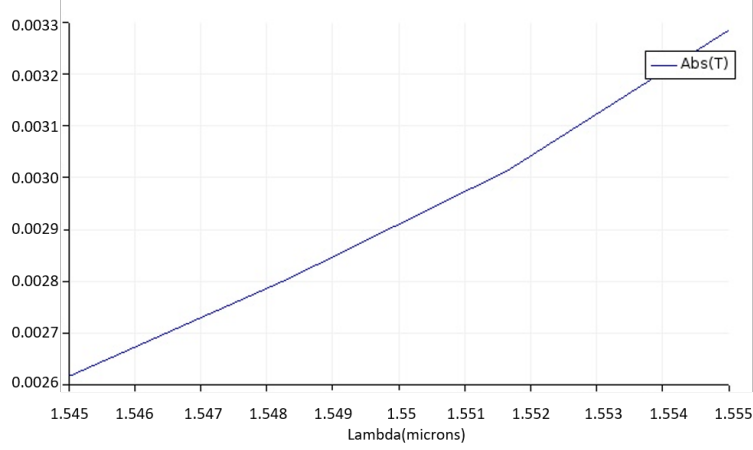


Figure 6.18: FDTD simulation of the transmission of the directional coupler consisting of a circular arc with $35 \mu\text{m}$ bend radius and a bus waveguide with 400 nm gap in between. The coupling coefficient is less than 0.003.

is critically coupled. We simulate a circular add-drop ring resonator with the same bend radius of $35 \mu\text{m}$, the propagation loss at 2.02 dB/cm and the coupling coefficients at 0.0025. The resonance shows a similar Q factor at 300,000 but with an ER less than 3.5 dB at the non-split condition and 1.5 dB with resonance splitting (Fig. 6.19). While in our measured results, the ER can be as large as 11 dB. The reason is that the manipulation of backcoupling through PS1 and PS2 enhances the ER as evident in both simulation (Fig. 6.5 and Fig. 6.5) and measurements (Fig. 6.11 and Fig. 6.12). The further principle behind this is assumed to the Fano resonance, which comes from the interference between the MZI mode and the ring resonance mode.

Another series of simulation are performed to further confirm this. We put all the parameters above into the simulation of the circuit shown in Fig. 6.3. The results of manipulating PS1 (thus the amplitude of the backcoupling) are provided in Fig. 6.20. When $PS1 = \pi$, this refers to the case without backcoupling, as all the light is at "in1". In this case, the output shows a symmetric resonance splitting, with an ER at 1.5 dB, which matches with the output of a pure circular ring with backscattering inside (Fig. 6.19(b)). When $PS1 = 0.5\pi$, this means the backcoupling now has the equal amplitude with the forward coupling, thus the resonance splitting disappears. And the resonance shows an ER at 3.5 dB, which matches the with the output of a pure circular ring without backscattering inside (Fig. 6.19(a)). But when $PS1$ has other values, for instance, 0.2π , the ER of the resonance is much larger, can be around 10 dB, which matches our measurements.

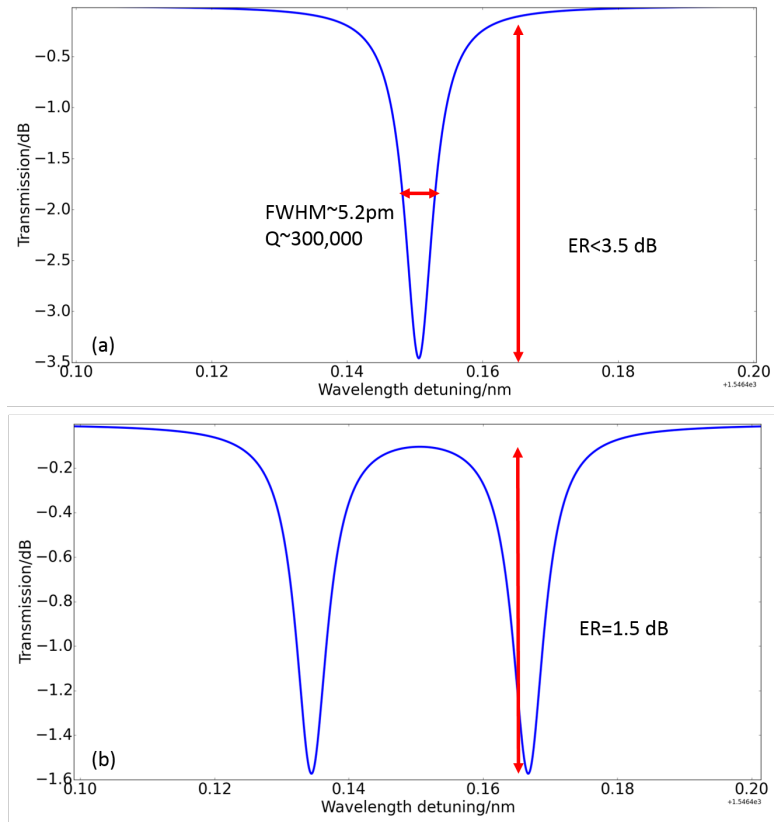


Figure 6.19: FDTD simulation of the transmission of the directional coupler consisting of a circular arc with $35 \mu\text{m}$ bend radius and a bus waveguide with 400 nm gap in between. The coupling coefficient is around 0.003.

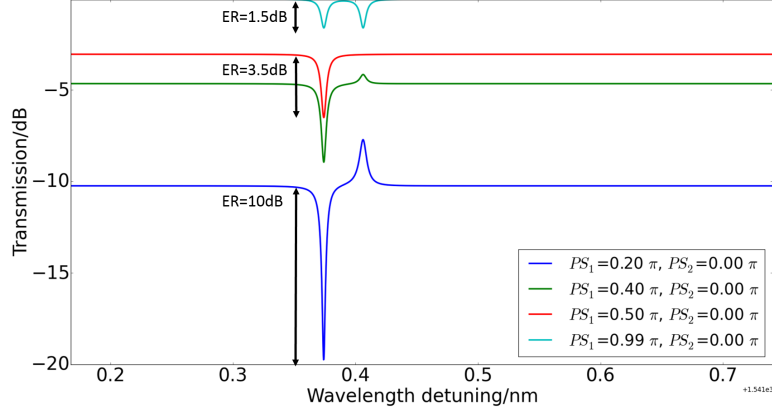


Figure 6.20: Simulated outputs of the circuit shown in Fig. 6.3 but with the same parameters in the simulation of a pure circular ring above. Manipulating the backcoupling can increase the extinction ratio of the resonance.

6.6 Summary

In this chapter we demonstrate the manipulation of another degree of freedom for silicon ring resonator, namely the backcoupling. Manipulation the backcoupling is to allocate the contributions from the input to the two coupled circulating modes in the ring resonator, i.e CW and CCW modes. Due to any kind of internal reflections, they are coupled and resonance splitting will be induced. Without any backcoupling, they are supposed to be symmetric. Manipulating the backcoupling can adjust their relative peak asymmetry and under correct condition (backcoupling equals forward coupling), one of the peaks will be suppressed, thus it is an effective method to eliminate resonance splitting. Moreover, the fabricated circuit with a $35 \mu\text{m}$ bend radius pure circular ring resonator shows ultra high Q factor and large Finesse.

References

- [1] Wim Bogaerts, Peter De Heyn, Thomas Van Vaerenbergh, Katrien De Vos, Shankar Kumar Selvaraja, Tom Claes, Pieter Dumon, Peter Bienstman, Dries Van Thourhout, and Roel Baets. *Silicon microring resonators*. Laser & Photonics Reviews, 6(1):47–73, 2012.
- [2] Maurizio Burla, Benjamin Crockett, Lukas Chrostowski, and José Azaña. *Ultra-high Q multimode waveguide ring resonators for microwave photonics signal processing*. In Microwave Photonics (MWP), 2015 International Topical Meeting on, pages 1–4. IEEE, 2015.

- [3] Aleksandr Biberman, Michael J Shaw, Erman Timurdogan, Jeremy B Wright, and Michael R Watts. *Ultralow-loss silicon ring resonators*. Optics letters, 37(20):4236–4238, 2012.
- [4] Pieter Dumon, Wim Bogaerts, Vincent Wiaux, Johan Wouters, Stephan Beckx, Joris Van Campenhout, Dirk Taillaert, Bert Luyssaert, Peter Bienstman, Dries Van Thourhout, et al. *Low-loss SOI photonic wires and ring resonators fabricated with deep UV lithography*. IEEE Photonics Technology Letters, 16(5):1328–1330, 2004.
- [5] Wim Bogaerts, Roel Baets, Pieter Dumon, Vincent Wiaux, Stephan Beckx, Dirk Taillaert, Bert Luyssaert, Joris Van Campenhout, Peter Bienstman, and Dries Van Thourhout. *Nanophotonic waveguides in silicon-on-insulator fabricated with CMOS technology*. Journal of Lightwave Technology, 23(1):401–412, 2005.
- [6] M Gnan, S Thoms, DS Macintyre, RM De La Rue, and M Sorel. *Fabrication of low-loss photonic wires in silicon-on-insulator using hydrogen silsesquioxane electron-beam resist*. Electronics Letters, 44(2):115–116, 2008.
- [7] Peter J De Heyn, Bart Kuyken, Diedrik Vermeulen, Wim Bogaerts, and Dries Van Thourhout. *High-performance low-loss silicon-on-insulator microring resonators using TM-polarized light*. In Optical Fiber Communication Conference, page OThV2. Optical Society of America, 2011.

7

Conclusion

7.1 Conclusion

I started my Ph.D at the beginning of the maturization stage of silicon photonics. Initially, I focused my studies on the issue of parasitics in silicon PICs, as understanding and modelling them is one of the key steps for large scale silicon PICs. The outcome of this work is presented in chapter 2, where we give our study of the most important and frequent forms of parasitics in silicon photonics, such as spurious reflections at the grating couplers, substrate leakage and coupling to other components, distributed backscattering caused by sidewall roughness and unintended evanescent coupling. Their impacts and origins are discussed through simulations and measurements.

During the study of these parasitic effects, I spent quite some time and efforts in modelling the backscattering in silicon waveguides and ring resonators. This is induced by the sidewall roughness of the waveguides, which is unavoidable in silicon photonics based on current fabrication technology. Besides the stochastic reflections and extra radiation loss induced by the backscattering, our research revealed that the backscattering will also induce rapid and strong fluctuations in its transmission spectrum. And these fluctuations are dependent on the waveguide length. For a 2 cm long WG, the maximum fluctuation is about 6.5 dB, and it grows to over 14 dB for a 7 cm long WG, which is absolutely unacceptable for a guiding channel. We built an optical circuit model to confirm the connection between backscattering and the fluctuations. We also use a straightforward mathematical

model to explain this.

The impacts of backscattering are more severe in resonant devices such as ring resonators, as the backscattering per roundtrip length will coherently build up due to the high Q factors and long photon lifetime in ring resonators. At the time when I studied the backscattering in silicon ring resonators, this issue had already attracted a lot of attention and it was concluded that the internal backscattering will lead to resonance splitting, as it couples two originally degenerate modes (clockwise and counter-clockwise circulating modes). This phenomenon can be explained in analogue to Zeeman or Stark effect, where the spectral lines of atoms will split in the presence of an external electric or magnetic field. But simple resonance splitting that has symmetric peak power can be well explained and modelled, while diverse asymmetric resonance splitting shapes we observed in rings could not be explained in a satisfactory manner. What's more, based on our measurements of over 1000 resonances, we found that asymmetric resonance splitting comprised over 80% of all split resonances, which made it quite compelling to explain and model the asymmetric resonance splitting. During our study we identified and experimentally confirmed the origin for this asymmetric splitting, concluding that can be attributed to the backcoupling in the directional couplers. Also, we built a model based on tCMT for a ring resonator with both backscattering and backcoupling. All kinds of resonances could be well fitted using this model. We applied the model to over 1000 resonances from different ring resonators to extract the backscattering strength of each resonance. With this rich data, we performed a quantitative analysis of the dependency of backscattering strength on some important physical parameters of a ring resonator, including the coupler gap, coupling length and ring roundtrip length.

During the work of modeling the backscattering in silicon ring resonators, the idea that the internal reflections should be manipulated was gradually taking shape. After all, backscattering is just a form of uncontrollable internal reflections, and it proves to significantly impact the performance of a ring resonator. So in chapter 4, we proposed a method to get full control of the internal reflections by incorporating a tunable reflector inside a ring cavity, and we proposed the internal reflection as another degree of freedom when designing a silicon ring resonator. The reflector is based on a loop-ended MZI, and with only a $\pi/2$ phase shift it can provide a change in its reflectivity from 0 to almost 100%. With such a reflector, manipulating the internal reflections by tuning its reflectivity can lead to multiple applications. First of all comes the fundamental suppression of backscattering. The simulated and measured results all confirm this. Not only can we eliminate the resonance splitting under correct tuning condition, but also suppress the leakage to the *add* port and reflection to the *in* port. Another application lies in the generation of a ring resonator with an ultra wide FSR and tuning range. There is only one resonance with an outstanding extinction ratio in over 150 nm optical range, while all the

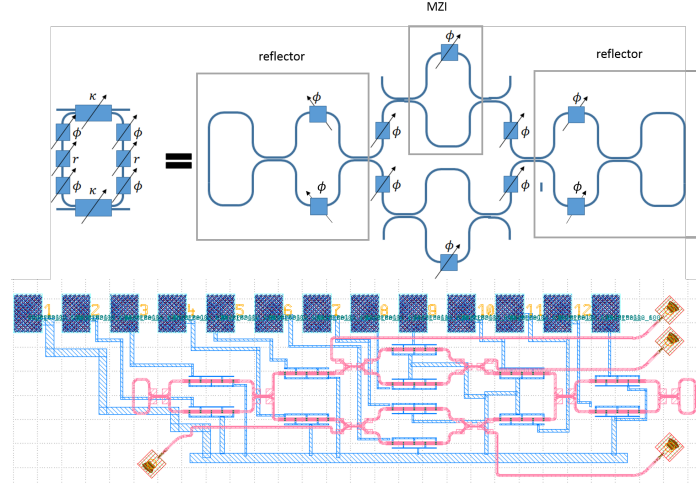


Figure 7.1: The design of a generic programmable ring resonator. Top part shows the schematic and bottom part presents the designed layout.

other resonances show splitting and have only very limited extinction ratio. What's more, the tuning range of this resonance is 11 times larger than that of a normal silicon ring resonator. This is realised using two-step tuning mechanism. Besides the two applications mentioned above, this device is also eligible for applications such as tunable microwave photonics filters, tunable fast light and optical sensors.

Since we've proven the value of engineering the internal reflections in silicon ring resonator using a single tunable reflector inside, it's quite natural to think one step further: what if we put two reflectors inside a ring cavity. In chapter 5, we investigate such a device. In this case, it becomes more complicated and interesting. As these two reflectors will form embedded Fabry-Perot cavities inside the ring cavity. The interaction of these two cavities will generate two different phenomena, namely Fano resonance and electromagnetically induced transparency (EIT). Fano resonances have very sharp slope and can be used as high efficiency sensors and switches. It can be generated by the interference of two modes, one of which is supposed to be a very smooth background mode (low Q) while another one should be a discrete mode (high Q). And these two modes need to be different in their resonance frequency (non-zero detuning). In terms of EIT, its features include an ultra narrow window in the amplitude transmission spectrum and an abrupt phase change within this ultra narrow window. This extreme dispersion leads to large group index and slow group velocity. So it is very promising to demonstrate slow light applications, like optical buffer and storage. In our circuit, the FP mode can be tuned to be very smooth by controlling the two reflectors and the detuning between the FP mode and ring resonance can also be controlled in the same way.

When they show a certain detuning, Fano resonances can be generated, with tunable extinction ratio and slope rate. We observed a slope rate over 700 dB/nm, which is one order of magnitude higher than a silicon ring resonance. When these two modes have zero detuning, EIT will emerge. The experiments show that we get an EIT peak with 0.95π phase change within a 0.01 pm span. Also we demonstrate a time delay of 1100 ps due to the EIT peak.

Also originating from the work of modelling backscattering in silicon ring resonators, we were aware that the backcoupling at the directional couplers also served as an influential factor for the outputs of a ring resonator. But the backcoupling at a conventional directional couplers is usually very weak and uncontrollable. In chapter 6, we propose a novel method to manipulate the backcoupling and propose it to be another degree of freedom for silicon ring resonators. The simulations and measurements prove the manipulation of the backcoupling. And it can be used to eliminate stochastic backscattering induced resonance splitting. Moreover, using this approach we manage to get a pure circular ring resonator, whose resonances all show Q factors over 300,000 (max. 380,000) and extinction ratios larger than 6 dB (max. 11 dB). And the ring has a large FSR around 4.5 nm, the corresponding Finesse is in the range of 500 to 625.

7.2 Future work

We can take it one step further. As a continuation of our work on silicon ring resonators, we designed a so-called generic programmable ring resonator as shown in Fig. 7.1. Generally speaking, it is an add-drop ring resonator but with many tunable degrees of freedom. First of all, it contains two tunable reflectors, whose reflectivity and phase can be adjusted using the four phase shifters (2 for each reflector) in their arms. Moreover, the optical length of the ring resonator can be tuned using the four phase shifters on the ring waveguide, thus the resonance location can be controlled. This will also control the detuning between the FP cavity (formed by the two reflectors) and the ring cavity. Finally, the coupling coefficients that influence the extinction ratio and Q factor of the resonance can also be tuned as the fixed directional couplers have been replaced by a tunable Mach-Zehnder interferometer. Because the phase relations between the 4 functional elements in the ring (the two couplers and the two reflectors) can also be adjusted, it is not possible to manipulate the phases at each of these elements. This structure adds tunability to most of the functional parameters of the ring resonator, taking exception of the backcoupling.

We expect it to perform all the functions introduced in this thesis as well as many other applications based on ring resonators or coupled resonators. For instance, as this ring is a 4-port device, it has 16 elements in its Scattering matrix. Due to reciprocity, 10 of those are independent. As this ring also has 10 degrees of

freedom, the ambition is to take full control of the scattering matrix of this device, effectively creating a programmable 4-port (for a given wavelength).

References

